UNIVERSITY OF READING

Department of Meteorology

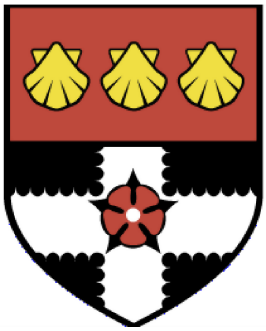

Conservation Properties of an Offline Global Tracer Advection Model and the Evolution of the Chemical Background State

Stephanie A. Higgs

A thesis submitted for the degree of Doctor of Philosophy

July 2011

Declaration

I confirm that this is my own work and the use of all material from other sources has been properly and fully acknowledged.

Stephanie A. Higgs

Abstract

This thesis investigates the conservation properties of a 3D global tracer advection model and how the model output can be used in the development of a tracer-relative chemical transport model (CTM). The global tracer advection scheme is based on the finite volume NIRVANA scheme. Shape preservation is improved with the inclusion of a reduced grid at the polar regions. When solid body rotation acts on uniform mass and tracer fields then mass conservation is observed. If a cosine bell tracer distribution is used then mass non-conservation is observed, with the magnitude depending on the angle of rotation relative to the grid (-1.9$\times10^{-3}$C%$<x<$6.6$\times10^{-4}$C% per revolution, where C is the maximum Courant number).

Advection of a passive ozone tracer by analysed winds results in a numerical mass change that is increased when using a coarser temporal and spatial resolution. The global non-conservation arises from the difference in treatment of the mass continuity equation by the offline tracer model and the NWP model producing the analyses. Due to the effects of spatial truncation it is better to use re-analyses produced at low resolution than to take high resolution operational analyses and truncate them. As a result of temporal truncation of the winds any offline tracer scheme is expected to violate global conservation. A comparison with the chemical change in the global ozone burden obtained using an ozone photochemistry parameterisation quantifies the relative importance of this numerical change. This comparison also reveals the importance of a global diagnostic (e.g. global burden) over a local diagnostic (e.g. ozone hole minimum) in determining the most accurate numerical scheme.

The numerical mixing rate in the model was also determined by representing the volcanic eruption of Sarychev Peak in 2009. This was then compared to a mixing rate determined from observations and was found to be too fast in the upper troposphere lower stratosphere region of the atmosphere. However, the numerical diffusivity is within the range of those determined in the atmosphere.

The output from the global tracer advection model is then used to investigate the feasibility

of a tracer-relative CTM. This CTM uses a reference tracer that is almost inert, such as potential vorticity, and describes the evolution of all other tracer species relative to it, under the assumption that all tracer contours are parallel. The dominant source of error in this method is the assumption that the 3D tracer distribution can be described using the background state (determined from the reference tracer) and the parallel contour approximation. A secondary error is introduced by the assumption that the heating field also aligns with the background state, but greatly simplifies the steps required for this new model.

Acknowledgements

First and foremost I would like to thank my supervisor, John Methven, whose support over the last few years has been invaluable and without whom this thesis would not have been possible. I also give my thanks to Keith Shine and John Thuburn for being my examiners and diligently reading my thesis and asking insightful and challenging questions regarding my work. Also, to Helen Dacre who, along with Keith Shine, made certain that I stayed on track throughout my degree and provided many useful insights into my work along the way. I also owe my gratitude to all those who provided me with invaluable data and support required in the completion of this thesis.

A mention must also be made of everyone I have shared an office with (you know who you are) and gotten to know in the department over the years. When the stress got too much the laughs that we shared were invaluable and will always be remembered. I have met some great people and have many fantastic memories of my time in the department that will be treasured. Last, but definitely not least, I would like to thank all my friends and family who have supported and encouraged me over the years. A special mention must be made of my housemates, Karen and Rachel, who have provided me with a wonderful and supporting place to come home to at the end of the day, somewhere where I can put aside the stresses of work and relax.

Contents

Chapter 1

Introduction

Numerical models are essential in atmospheric science. The governing equations of fluid flow are non-linear and complex and as a result only a few analytic special solutions are known. Numerical models allow us to test and refine theories as well as predict future weather and climate. However, they are limited by their formulation and finite truncation and as a result the models are not always accurate or realistic. In cases where properties of the exact system behaviour are known, numerical divergence from the true result can be identified. One of the easier numerical properties to investigate is conservation. Both global and material conservation are fundamental properties of fluids.

1.1 Tracer Properties in the Atmosphere

In this instance the definition of a tracer can be taken from Rind (2009) where it is stated that tracers are "substances (trace gases, aerosols) that are advected by atmospheric motions. From observations of the time variations of tracers, one can deduce the air motions responsible for their distribution".

1.1.1 Global and Material Conservation

The key properties of tracers in the atmosphere are global and material conservation. The best way to visualise these is to consider a tank of water into which a finite amount of dye is dropped. Global conservation states that there can be no loss or gain of dye amount (e.g. number of molecules) with time. Material conservation refers to properties that are invariant following fluid parcels, such as the mixing ratio of tracer within a fluid parcel. This essentially means that over time the maximum and minimum tracer concentration

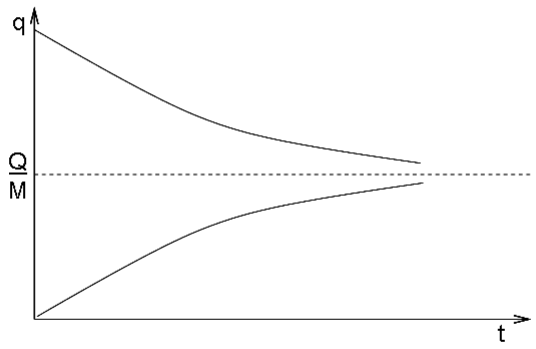

Figure 1.1: *Schematic of global conservation of tracer in a fluid. Over time the tracer maximum and minimum mixing ratios (the curves) tend towards the same value as a result of mixing i.e. homogeneous distribution with respect to mixing ratio. This value can be determined from the global mass of tracer, Q, and the mass of fluid, M.*

Figure 1.2: *Image of two different coloured dyes in a rotating tank of water. As stretching and folding of tracer parcels occurs and filaments form mixing between fluid parcels is inevitable. Image by Prof. J Marshall, Massachusetts Institute of Technology.*

will converge to a specific value determined by the mass of tracer and the mass of fluid, as shown in figure 1.1. This occurs due to the mixing between fluid parcels which is inevitable as tracer parcels are stretched and folded, as shown in figure 1.2 for two coloured dyes in a rotating tank of water. Lastly, it is not possible for extrema to develop that are outside of the initial range of tracer values.

Conservation of fluid mass and tracer mass can be expressed in flux form:

$$\frac{\partial \rho}{\partial t} + \nabla . \rho \underline{v} = 0 \tag{1.1}$$

$$\frac{\partial (\rho q)}{\partial t} + \nabla . \rho q \underline{v} = 0 \tag{1.2}$$

Equation (1.1) represents the conservation of fluid mass where ρ is the density, $\underline{v}$ is the velocity and t is time. The tracer conservation is then represented by equation (1.2) where q is the tracer mixing ratio. The formulation and truncation used in solving these equations results in numerical models that can diverge from the true solution.

If equation (1.1) is integrated over the entire atmosphere and Gauss' Theorem is used then:

$$\frac{d}{dt}\iiint \rho dV + \iint \rho \underline{v}.d\underline{S} = 0$$

In the absence of fluxes at the boundaries the second term is zero so that global conservation is obtained as $dM/dt = 0$, where $M = \iiint \rho dV$. Alternatively, combining equations (1.1) and (1.2) obtains:

$$\frac{\partial q}{\partial t} + \underline{v}.\nabla q = 0$$

This can also be written as:

$$\frac{Dq}{Dt} = 0$$

This is a statement of material conservation, where D/Dt represents the rate of change following an air parcel.

1.1.2 Transport of Tracers in the Stratosphere

Of considerable interest for the work presented in this thesis is the behaviour of tracers in the stratosphere. The stratospheric part of the mean meridional circulation in the atmosphere is also known as the Brewer-Dobson circulation. A schematic of this circulation is shown in figure 1.3. The key features of the Brewer-Dobson circulation are as follows. Above the tropical tropopause, where there is an exchange of air between the troposphere and the stratosphere, the air in the stratosphere ascends on average. This air is then transported towards higher latitudes in the winter hemisphere until it descends over the winter pole.

The dominant motion of the Brewer-Dobson circulation results in two features in the tropical stratosphere that are exploited by many numerical models as a test. The first of these is the stratospheric tape recorder which arises due to the exchange of water vapour across the tropopause, as well as the fact that water vapour behaves like a conserved tracer in the stratosphere (Mote *et al.*, 1996). Figure 1.4 shows the tape recorder as observed by

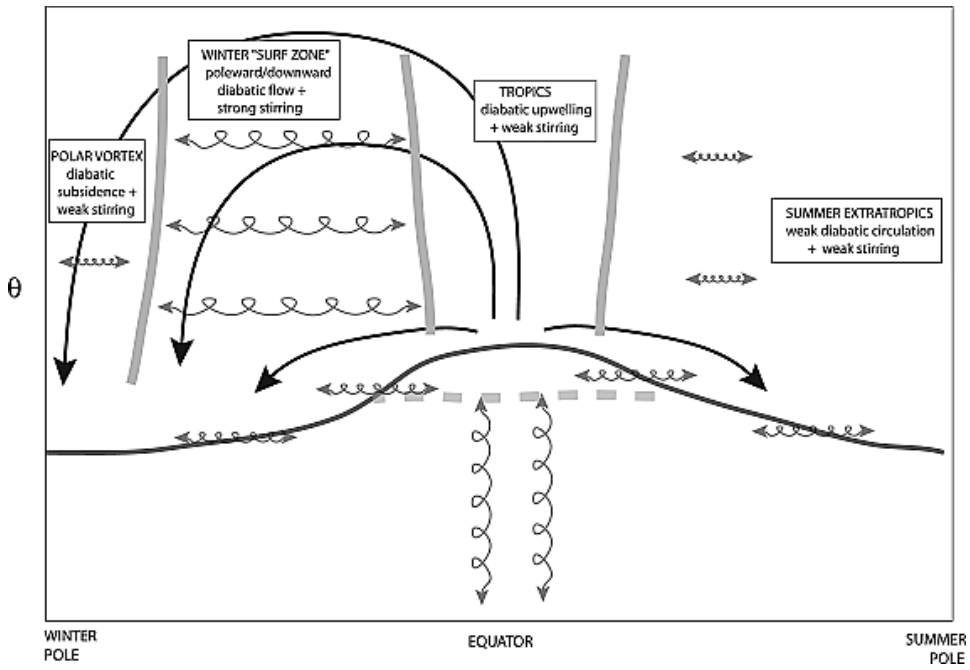

Figure 1.3: *Schematic of the meridional atmospheric circulation. The curve extending between poles represents the tropopause. Curves with a single arrow represent the mean circulation. Double headed arrows show isentropic mixing and the vertical grey bands denote the transport barriers that inhibit mixing between regions. Note the circulation in the stratosphere is otherwise known as the Brewer-Dobson circulation. Taken from Plumb (2007).*

the Halogen Occultation Experiment (HALOE) and presented in Gregory and West (2002). Essentially the tape recorder arises because the amount of water vapour that crosses the tropical tropopause into the stratosphere varies seasonally. The air is relatively moist in the Northern Hemisphere summer and dry in the Northern Hemisphere winter and is shown in figure 1.4 as alternating regions of white and grey. This signal in water vapour is defined as the head of the stratospheric tape recorder. Its progression is then determined by the Brewer-Dobson circulation and the diabatic heating in the stratosphere. Since both of these processes are slow and the lateral mixing is weak the water vapour signal is observable for some time. The representation of the signal in a 1D model was investigated in Mote *et al.* (1998).

The other feature is known as the age-of-air which was first presented by Bischof *et al.* (1985), with detailed work also presented by Hall and Plumb (1994) and Waugh and Hall (2002). The age-of-air makes use of the relationship between pairs of tracers with differing lifetimes. By knowing the different lifetimes of the two tracers and the ratio of the tracers then mixing can be accounted for. With these factors known it is then possible to determine the transport time between two locations, this is then referred to as the age. By accounting

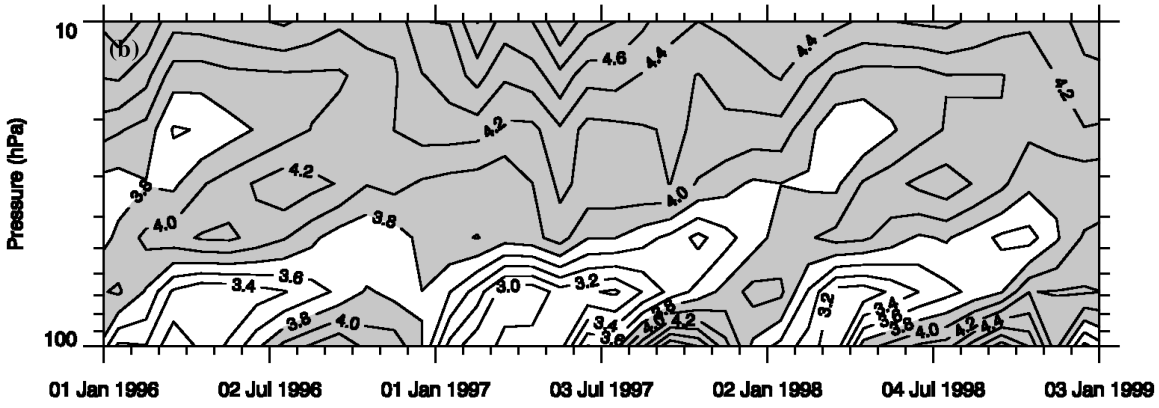

Figure 1.4: *Height-time cross sections of tropical (15S-15N) mean specific humidity from HALOE (1996-1998) showing the stratospheric tape recorder. Specific humidity is shown with contours in ppmv. Taken from Gregory and West (2002).*

for the mixing process between air parcels of varying ages a spectrum of ages is calculated. The stratospheric age-of-air refers specifically to the time since crossing the tropopause.

The Effect of the Polar Vortex on Tracers

One of the more significant features of the stratosphere is the polar vortex, which is shown schematically over the South Pole in figure 1.5. Climatologies show that in the summer the winds in the stratosphere are generally easterly and in the winter are westerly (Labitzke and van Loon (1999) and Dessler (2000)). At the start of winter the stratosphere over the polar region cools. As the polar air cools radiatively the magnitude of the meridional temperature gradient increases and thermal wind balance implies that the zonal winds surrounding the pole become more westerly. The gradient in cooling also increases the magnitude of the potential vorticity (PV) in the polar PV reservoir. Rossby wave breaking sharpens the PV gradients at the polar vortex edge which, through PV inversion, is consistent with even stronger westerlies around the vortex.

These strong westerlies are referred to as the polar night jet, with the fastest winds located in the upper stratosphere near the stratopause. The winds then decay and extend down into the stratosphere and up into the mesosphere. The vortex acts as a transport barrier (e.g. Dahlberg and Bowman (1994), Haynes and Shuckburgh (2000)) as well as a source of mixing, time-dependent straining and filamentation of the tracer field. With the return of spring and the end of polar night the radiative cooling ends and the winds weaken allowing the polar vortex to collapse.

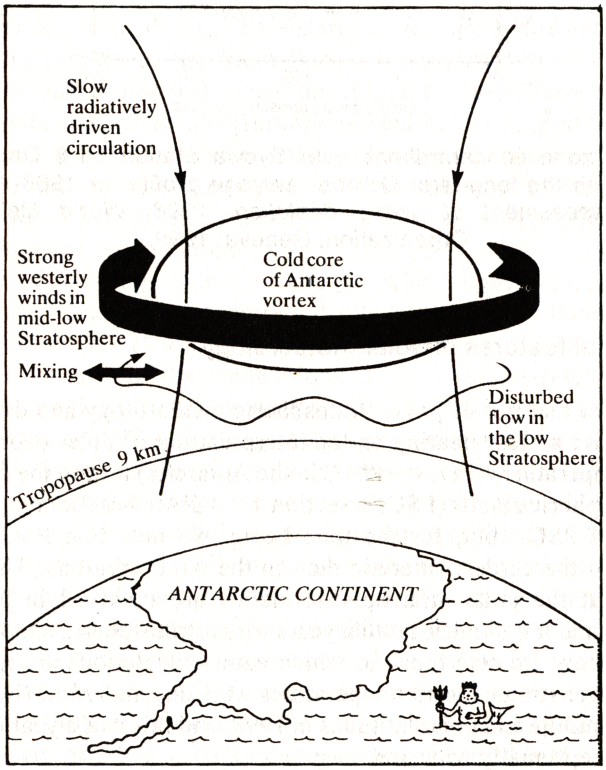

Figure 1.5: *Schematic of the stratospheric polar vortex (Wayne, 1991).*

The processes described above are true for both the Southern and Northern Hemisphere winters. However, the two hemispheres do differ in that colder temperatures can be reached and maintained over the Southern Hemisphere polar region than the Northern Hemisphere. This occurs due to the fact that the Rossby wave propagation that dynamically disturbs the atmosphere in the Northern Hemisphere also serves to transport heat to the cold Arctic and act as a balance to the radiative cooling. Therefore, the radiative cooling in the Northern Hemisphere polar region is partly offset by eddy stirring and mixing of warmer air into the vortex. The Southern Hemisphere is dominated by ocean and has less zonal asymmetry as a result. This results in a Rossby wave propagation that is considerably weaker in the Southern Hemisphere, which in turn means that the stratosphere is less dynamically disturbed and experiences a weaker offset to the radiative cooling. It must also be noted that the descent of air within the polar vortex is an additional source of heating in the polar atmosphere.

Due to these colder temperatures over the Antarctic than the Arctic during their respective winters a stronger and more stable vortex is formed over the Antarctic. As a result of this the vortex exists up to two months longer in the Southern Hemisphere than the Northern Hemisphere (Labitzke and van Loon, 1999). It is during these additional couple of months

that the conditions are suitable for the chemistry to take place that results in large scale ozone destruction and hence the formation of the ozone hole over Antarctica.

Equivalent Latitude

In this area of study the equivalent latitude, rather than latitude, is commonly used. The equivalent latitude is determined by calculating the area contained within a tracer contour and then making it zonally symmetric and centering it on the pole. The latitude to which it extends is called the equivalent latitude. Two of the earliest papers published on equivalent latitude are McIntyre (1980) and Butchart and Remsberg (1986). Norton (1994) presented potential vorticity equivalent latitudes as a co-ordinate system that could follow the stratospheric polar vortex. Other papers such as Allen and Nakamura (2003) detail the benefits of using equivalent latitude when considering isentropic transport. The focus is specifically on the advantages of using chemical tracer equivalent latitude which contains less noise than the use of potential vorticity equivalent latitude.

Waugh and Randel (1999) use equivalent latitude whilst creating a climatology of the winter polar vortex, as do Karpetchko *et al.* (2005) who study vortices as represented in ERA-40. Lary *et al.* (1995) also investigate the use of an equivalent latitude-potential temperature co-ordinate system for diagnostics, as well as the potential of remapping tracer fields onto this co-ordinate in order to initialise a model. The main advantage of this is that it reduces spin-up times in models. The independent evolution of the field when mapped onto this equivalent-latitude-potential temperature co-ordinate system has not been attempted to date. This means mapping the initial state onto this co-ordinate system, evolving the mass and tracer fields without additional input from a model and then investigating whether an accurate evolution of the tracer field can be obtained.

1.1.3 Emergence of Tracer-Tracer Correlations

In the atmosphere it is sometimes possible to use relationships between tracers to identify where chemistry is active and where mixing is occurring. All of this is based on the assumption that all tracers in the atmosphere have their distribution partially determined by advection. Therefore, a strong correlation between tracers will represent tracer alignment.

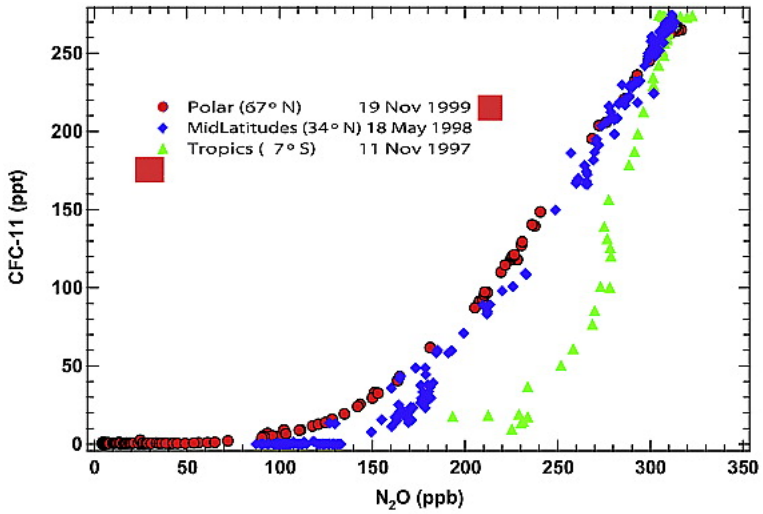

Figure 1.6: *Plot of CFC-11 (pptv) against N_2O (ppbv) from balloon-borne LACE data (Moore* et al.*, 2003). This highlights the different tracer relationships that develop in different regions, in this case the tropics, mid-latitudes and polar vortex. Taken from Plumb (2007), where it was provided by James Elkins and Fred Moore.*

It is not uncommon to see these correlations used with tracers in the stratosphere. For example, Waugh *et al.* (1997) and Plumb *et al.* (2000) used tracer-tracer relationships to diagnose mixing within and around the polar vortex. Both of these papers show that when long-lived tracers are plotted on a tracer-tracer scatter plot it is expected that the data will show a smoothly varying compact curve with different tracers creating different correlations. These compact relationships will be maintained as straight lines as long as mixing is the only process occurring. The introduction of slow processes such as photochemistry will result in the formation of non-linear curves in the tracer-tracer correlations. Hence, the relationships between tracers can act as an identifier of mixing and chemistry.

Plumb (2007) takes an in depth look at tracer-tracer relationships within the stratosphere. When describing the properties of stratospheric tracers it is stated that for long-lived tracers, where sources and sinks act slowly relative to the dynamics, gradients are determined by the competition between horizontal mixing (produces straight lines in tracer-tracer plots) and the overturning circulation. These two processes affect all tracers in the same way. Plumb (2007) discusses different flows including ones where a permeable barrier is present. An example of a tracer-tracer correlation is shown in figure 1.6 (Plumb, 2007). This figure shows the correlation between two gases in three different regions of the atmosphere: tropics, mid-latitudes and polar vortex. The different correlations are in part maintained by the fact that barriers (figure 1.3) inhibit mixing between the regions. An increased curvature in the relationship develops with increased levels of photochemistry destroying CFC-11 at

higher altitudes (low N_2O).

1.1.4 The Background State and a Tracer Relative Chemical-Transport Model

One concept that sometimes appears when modelling the atmosphere is the background state. The background state is a vague quantity that is rarely defined precisely. In general terms the background state can be considered as the long term, slowly evolving atmospheric composition. In numerical models this can be used as the nominal atmospheric state to which a model can be relaxed, or with which mixing can occur. The correlations mentioned above that arise between tracers in the atmosphere, if considered all together, can be considered as representing this background state of the atmosphere. The tracer distributions are primarily determined by advection and therefore global mean advection plays a role in determining the background state of the atmosphere. The other contributing factor to determining the atmospheric background is chemical in origin. This allows short-lived tracers, which do not exist long enough to align with long-lived tracers, to influence the atmospheric background state. The chemical interactions that contribute to the background state are referred to as global chemical modes, which are specific spatial and temporal variations in the atmosphere.

Global chemical modes exist in the atmosphere due to the coupling of chemical and transport processes. These modes vary in time, space and with chemical species. Therefore, each mode will describe a specific chemical and transport combination where shorter lifetime modes can be either transport-chemistry modes or just transport modes. Together these modes represent an alternative definition of the atmospheric background state. Both Prather (1994) and Wild and Prather (2000) describe in detail how these chemical modes can be determined and focus on the $CH_4 - CO - OH$ mode since this is the primary mode in the troposphere. Specifically, it summarises the reaction of $OH + CH_4$ then multiple other reactions before $CO +$ products is obtained.

A more recent study (Wild and Prather, 2000) determined this primary mode to have a lifetime of 14.2 years, 4.5 years longer than the lifetime of CH_4 (9.7 years) determined from the loss reaction with OH. The lifetime of this mode varies only slightly in the vertical due to the chemical lifetimes being much longer than the lifetime of the convective

overturning in the troposphere. The primary mode is typically excited due to a perturbation to the OH field. Due to this a short lived chemical species can create a long term and global perturbation to the atmosphere and in essence alter the background state. When the stratosphere is considered as well the tropospheric primary mode couples with the $N_2O - NO_y - O_3$ mode. The lifetime of this combined mode is on a century scale and Prather (1994) calculated a value of approximately 110-120 years.

The theory of the background state and tracer-tracer correlations form the basis of a new tracer-relative chemical transport model (CTM). A tracer-relative CTM is a new concept that will be discussed in detail in Chapter 6, along with a precise definition of the background state. Briefly, the tracer-relative CTM uses a reference tracer, such as PV, from which the background state is calculated by using the tracer-tracer correlations. This derived background state can then potentially act as the basis for the tracer-relative CTM. The main advantage of this model over a traditional CTM is that it would be much quicker to run due to a co-ordinate system defined as $C(q, \theta, t)$ rather than $C(x, y, \theta, t)$.

The use of one less dimension means that the tracer-relative CTM would be faster to integrate, this would be especially beneficial as the number of modelled tracers increases. This is important when considering climatological runs that are now used in some studies as well as when more complex chemical systems are incorporated into models. Analyses would be needed to calculate the distribution of the reference tracer in a fully three dimensional model, but all the other tracers will be modelled relative to the reference tracer in the tracer-relative CTM.

1.2 Numerical Methods

The features described above are often investigated using offline CTMs. Before an advection scheme can be used in a CTM the numerical properties of the scheme need to be quantified in order to determine its accuracy and influence on modelled features, such as long term trends in the global burden of greenhouse gases. Therefore, this section discusses some of the various types of advection schemes used in CTMs before some of the properties of CTMs and the analyses used to drive them are considered in the next section.

The main types of schemes are Eulerian, Lagrangian and semi-Lagrangian schemes. Eu-

lerian schemes consider the evolution of a tracer field at a point and Lagrangian schemes consider the evolution of a tracer following air parcels. Semi-Lagrangian schemes are similar to Lagrangian schemes but consider a new set of tracer parcels arriving on a prescribed grid at each time step. One factor that is commonly considered for Eulerian schemes is the Courant-Friedrichs-Levy (CFL) criterion. It is specified using the Courant number defined as $C = u\Delta t/\Delta x$ where u is the velocity, Δt is the time step and Δx is the grid spacing. The Courant number is representative of how many grid spaces a parcel will travel in one time step. For this reason a Courant number $\leq$1, or on the order of 1, is often necessary in order to obtain a stable scheme (i.e. a parcel only travels one grid space in one time step).

1.2.1 Eulerian Finite Difference Methods

Chapter 25 of Zdunkowski and Bott (2003) details the basic methods used in Eulerian schemes, in particular finite difference methods. When using finite difference methods the solution to the equation under consideration, specifically the derivatives ($\partial/\partial t$, $\partial/\partial x$, etc.), undergoes a Taylor expansion about points on a fixed grid and the higher order terms are then ignored, i.e. the solution is truncated. The stability of the scheme is often determined by the Courant number.

1.2.2 Finite Volume Methods

A specific type of Eulerian scheme are finite volume schemes, which are presented in detail by Durran (1999). These schemes are widely used since they are inherently conservative. In finite volume schemes a finite grid spacing is used but the equations are expressed as integrals in order to ensure conservation over each grid cell. The integrals are used in the calculation of the fluxes which themselves represent the time average flux across a face of the grid cell, $\bar{F}_j$. This method is particularly good for discontinuous solutions. Starting from equation (1.2), the equation is integrated over the grid cell volume, δV, and then one time step, Δt:

$$\int_t^{t+\Delta t} \int_V \left[\frac{\partial(\rho q)}{\partial t} + \nabla.\mathbf{F} \right] dV dt = 0$$

$$\int_t^{t+\Delta t} \left[\frac{d}{dt} \langle \rho q \rangle \, \delta V + \sum_j \mathbf{F}_j . \mathbf{n}_j \delta S_j \right] dt = 0$$

$$\left(\langle \rho q \rangle^{n+1} - \langle \rho q \rangle^n \right) \delta V + \sum_j \bar{\mathbf{F}}_j . \mathbf{n}_j \delta S_j \Delta t = 0$$

where $\langle \rho q \rangle$ is the volume-weighted average over the grid cell.

Monotonic Schemes

It is sometimes desirable to have a scheme that is monotonic. Monotonicity means that the numerical scheme will not produce spurious extrema outside the range of the initial data. Most monotonic schemes are only first order accurate and hence highly diffusive near extrema. However, as well as not producing random extrema, monotonic schemes avoid the production of 'spurious ripples' in the tracer field near to a discontinuity or a gradient that is poorly resolved.

Care must be taken when using a monotonic scheme as it can degrade the numerical solution if a high enough horizontal resolution is used and a well resolved solution exists. If there are no discontinuities in the numerical solution then the use of a monotonic scheme can be extraneous. On the other hand a monotonic scheme can convert errors that appear in the form of undershoots and overshoots into a more acceptable type of error. This is important in meteorological models as an overshoot or undershoot can have a significant impact by coupling with other processes. An example provided by Durran (1999) is the creation of cloud due to positive anomalies in the water vapour field. The formation of the cloud releases latent heat into the atmosphere which in turn affects the atmospheric circulation. The formation of negative values in a tracer field can make instabilities and non-physical chemical processes occur.

One method used to create a monotonic scheme is flux corrective transport (FCT). The flux corrector works by putting a condition on the fluxes such that no new extrema are created and the existing extrema are not enhanced so that the material conservation is ensured by calculating a second low order solution to the equations. A flux limiter method is similar, but does not calculate the low order solution. An alternative method to a flux limiter is to approximate the solution at a grid cell as a sum of piecewise-linear, piecewise-continuous polynomials or piecewise-constant functions. These functions are then evolved forward in

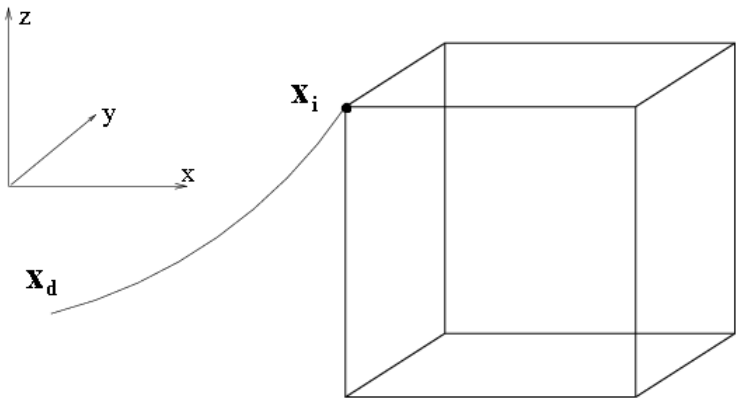

Figure 1.7: *Schematic of the departure point for a semi-Lagrangian scheme. For any particular point, x_i, the scheme will determine one departure point, x_d, in three dimensional space.*

time using the finite volume method in order to produce an accurate numerical solution.

Positive Definite Schemes

The other property that is sometimes desired in a scheme is for it to be positive definite. If a scheme is positive definite then it will not generate negative tracer values in an initially non-negative tracer field (note that a monotone scheme is positive definite but vice versa is not true). The earliest and simplest methods used to ensure a scheme is positive definite simply involves filling in any negative tracer values that appear. In order to ensure mass conservation a corresponding amount of tracer has to be removed from regions of positive tracer. Some schemes remove mass from points local to the negative value and others are more complex by removing tracer globally by multiplying each grid point by the ratio of total original mass to total non-negative mass at that time. This method has the disadvantage that regions of highest tracer concentrations are damped. An FCT method can also be used to ensure a positive definite scheme by limiting the fluxes so that negative concentrations cannot be formed.

1.2.3 Semi-Lagrangian Methods

Durran (1999) also presents a chapter on semi-Lagrangian schemes. Semi-Lagrangian methods are widely used in numerical modelling and have a distinct advantage over Lagrangian methods. When a Lagrangian method is used then over time the parcels that are being

tracked can cluster together resulting in large portions of the system not being represented unless new parcels are added and old parcels removed as the system evolves. By using the semi-Lagrangian method and choosing a new set of parcels at each time step the parcels remain evenly distributed and the problems observed when using a Lagrangian method are avoided. These schemes also have the advantage that they enable a longer time step by lifting the CFL criterion present in Eulerian schemes, but semi-Lagrangian schemes are not mass conservative.

Semi-Lagrangian schemes require the calculation of short back trajectories at each time step to determine departure points. The departure point is defined as where the parcel arriving at a grid point originates, a schematic of this is shown in figure 1.7. For each grid point, x_i, one departure point, x_d, is calculated. For a first order in time scheme it is assumed that the material derivative can be approximated as:

$$\frac{Dq}{Dt} \simeq \frac{q^{n+1}(x_i) - q^n(x_d)}{\Delta t}$$

where Δt is the time step. Errors in the calculation of the departure point, x_d, can arise if the velocity along the trajectory is not constant. There are various methods that can be used to calculate the trajectories and as such will not be detailed here. The order of the interpolation used in the scheme for the determination of the mixing ratio at the departure point, $q(x_d)$, is of importance as a linear interpolation produces a lot of diffusion and so a higher order interpolation is used. A higher order, often cubic, interpolation allows for a smooth solution as a polynomial can be fitted to the grid points surrounding the departure point. Overall semi-Lagrangian schemes are stable and independent of the CFL criterion, however, as with Eulerian schemes, care must be taken when on a sphere due to the convergence of the grid at the polar regions.

Semi-Lagrangian schemes will generally not maintain a positive definite distribution if a quadratic or higher order polynomial interpolation is used to determine the mixing ratio at the departure points, $q(x_d)$. A positive definite scheme can be obtained if the interpolation step is instead considered as a parameterised advection problem that uses a positive definite scheme. If a strict positive definite scheme is not required then a flux limiter can be used in the parameterised advection step to reduce the overshoots and undershoots that develop. Recent implementations of semi-Lagrangian schemes will be discussed in Section 2.6.1.

1.3 Chemical Transport Models

Thuburn (2008) considered in detail some of the various conservation properties that should be considered in the construction of numerical models and their wide reaching effects. The quantities that Thuburn (2008) considers include mass, angular momentum, energy and entropy. Care needs to be taken with respect to the unresolved part of the field for quantities that involve a cascade to smaller scales with time. It is shown how this is especially true when considering energy conservation. Thuburn (2008) states that the properties that are slowly varying are the ones that should be focused on in terms of conservation, an important example being the mass of dry air. Due to the influence of atmospheric mass on surface pressure the potential for influence on a wide range of atmospheric features exists. It is also noted that many other conservation laws have an inherent dependence on the conservation of mass. In climate models in particular the conservation of mass for water and greenhouse gases would be desirable.

A numerical scheme that is mass conservative under a prescribed flow, such as solid body rotation or deformational flow, may not be so when advection is driven by analyses. This is not always due to problems with the numerical model but can be a direct consequence of the analyses themselves which are not always accurate and conservative. This can be significant when considering realistic winds or global circulation model (GCM) output that is coupled with chemistry such as in the Chemistry-Climate Model Validation Activity (CCMVal) project (`www.pa.op.dlr.de/CCMVal/`) where there can be an accumulation of errors. These errors are not always noticeable as at any given time features such as stretching, folding, spiral evolution, etc. can be seen in the tracer field due to the use of analyses to drive advection. However, these features are not necessarily accurate and errors can be due to the analyses and/or how the numerical model uses the analyses.

In many numerical models it is often re-analyses that are used to drive the advection. Dee (2009) provides a concise description of how re-analyses are made and can be used. In essence re-analyses make use of modern advances in data assimilation to reprocess past atmospheric observations as well as additional data produced by models. Since re-analyses are produced by one data assimilation system and model, artificial trends in the data due to system upgrades are removed and as a result there is increased homogeneity in the long timescale variability. However, trends can arise due to changes in the observing system. As

a check the re-analyses must be evaluated against independent observations and, obviously, obey the laws of physics. The overall aim of the re-analyses is to represent the atmospheric state and its evolution over a long period by using all the available information (models and observations) in a way whereby uncertainties are exposed and reduced as much as possible. As an example, the data and assimilation processes used in the development of ERA-Interim is presented in Dee *et al.* (2011). Details of some of the parameterisations used in the forecast model are also presented along with comparisons of ERA-Interim to observations and ERA-40.

Rind (2009) presented information on how tracers can be used in the evaluation of a numerical model. Since transport in a model is often determined by a wind field that can be difficult to visualise (e.g. ageostrophic circulations, convection, turbulence) the formation of a discrepancy in a passive tracer field will provide information on where there may be a potential problem. However, it must be noted that pinpointing the source of an error can be complex due to the interaction of different processes in the atmosphere. The use of tracers in this way can be hindered by a lack of information about the tracers themselves, such as incomplete knowledge of the sources and sinks and general observations.

Transport processes where tracers can be used include inter- and intra-hemispheric transport, troposphere-stratosphere exchange, transport within the stratosphere and vertical mixing within the troposphere. Due to the range in timescales on which these transport processes act tracers with different lifetimes are required. A good example is vertical transport in the troposphere where tracers with longer lifetimes are required as many tracers (including water) have sources and sinks at the ground and so if they have a short lifetime then boundary layer mixing and convection become the most important processes. If a suitable tracer is chosen, one with a lifetime comparable to the timescale of the transport process that is of interest, then it can be used effectively as a tool in studying and testing numerical schemes.

1.3.1 Conservation in Global Analyses

Berrisford *et al.* (2011) carried out studies in order to investigate how well atmospheric mass, energy and angular momentum are conserved within ERA-Interim. The mass in the re-analyses shows long timescale variations similar to other re-analyses. However, when in

direct comparison with its predecessor (ERA-40), ERA-Interim shows smaller magnitude variations in mass from month to month. The ECMWF model used to produce ERA-40 and ERA-Interim is a semi-Lagrangian, semi-implicit spectral model with a hybrid vertical co-ordinate as presented by Simmons and Burridge (1981). The use of the hybrid co-ordinate means that each model level is defined as $\eta = f(p, p_s)$ where p_s is the surface pressure and p is pressure. On each half level:

$$\frac{p_{l+1/2}}{p_0} = A_{l+1/2} + B_{l+1/2}\frac{p_s}{p_0} \tag{1.3}$$

where A and B are coefficients, and p_0 is a constant of 10^5Pa. The full model levels are then defined as $p_l = 0.5(p_{l-1/2} + p_{l+1/2})$. ERA-40 and ERA-Interim differ due to the evolution of the ECMWF model via updates to parameterisations, use of available data, data assimilation methods, etc. Dee *et al.* (2011) compare the parameterisations used in development of ERA-40 and ERA-Interim and the resulting differences in the re-analyses.

If the ERA-Interim model is permitted to run without data assimilation taking place a mass gain of 0.3% per year is observed. The evolution of the total mass and dry air mass is shown in figure 1.8(a) and (c) respectively and is compared to ERA-40 showing the similarity between them. However, ERA-Interim does have some problems in regards to the cross-equatorial mass flux where the fluxes seem to be biased towards flow into the Southern Hemisphere (see figure 4 Berrisford *et al.* (2011)). This bias is due to problems in the divergent wind along the equator.

Conservation in global analyses is also considered by Trenberth and Smith (2004) who investigate the role of water vapour in the total mass of the atmosphere. Water vapour loading in the atmosphere is at a maximum in the Northern Hemisphere summer and a minimum in the Northern Hemisphere winter. Therefore the total mass of the atmosphere is not constant and has a corresponding maximum and minimum in the Northern Hemisphere summer and winter respectively. The reason for the dominance of the Northern Hemisphere is due to the fact that the average temperature is higher in the Northern Hemisphere and the atmosphere is therefore able to hold more water vapour.

The total global mass of air will also have an interannual variation due to differences in water vapour loading such as those that occur due to El Niño. It is the dry mass of the atmosphere that is approximately conserved and so can be used as a measure of how well mass conservation is met in numerical models. Due to the release of gases into the

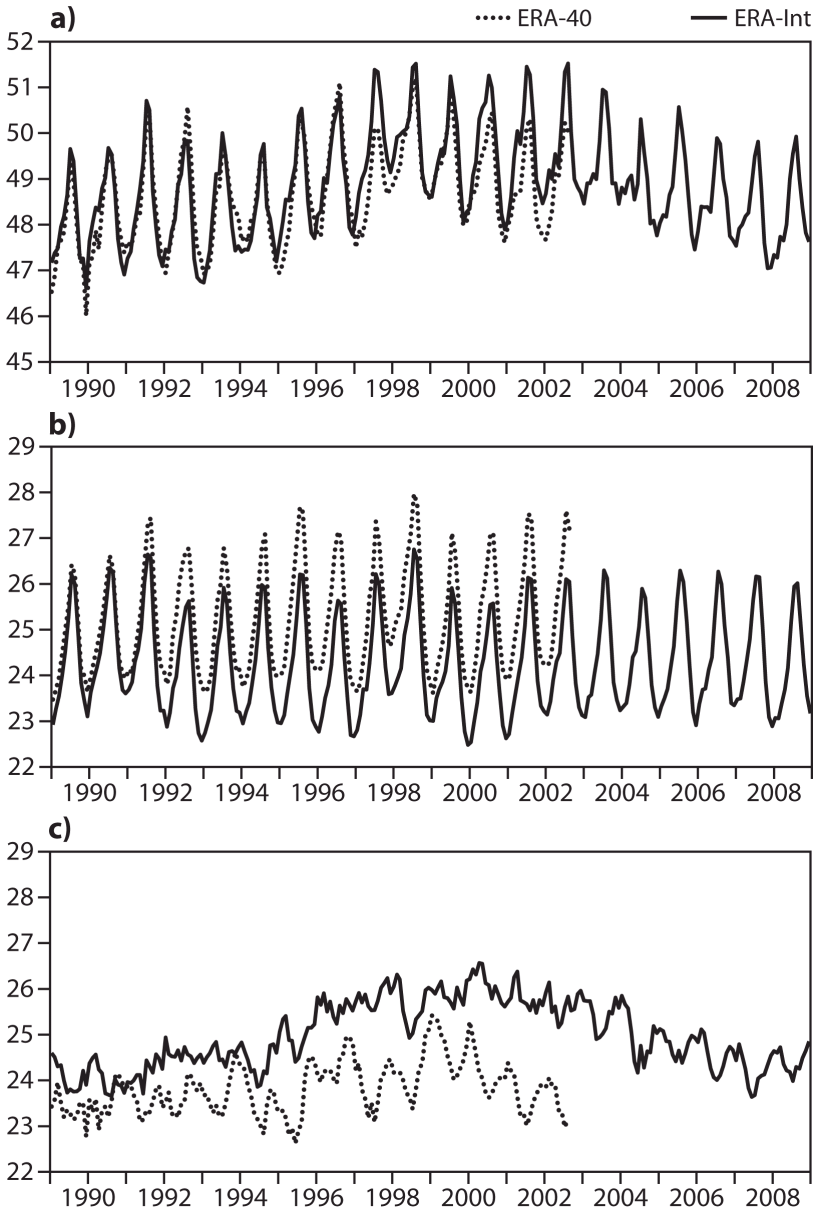

Figure 1.8: *Vertically integrated global monthly mean time series from 1989 to 2008 for ERA-Interim (solid) and ERA-40 (dashed) of (a) mass, (b) total column water vapour and (c) dry mass. The units are* kgm^{-2}*-10000 for (a) and (c) and* kgm^{-2} *for (b). Taken from Berrisford* et al. *(2011)*

atmosphere the dry air mass fluctuates over time. However, Trenberth and Smith (2004) state that the effect of this pollution on the dry air mass will be on the order of less than 0.1 hPa, which is smaller than the accuracy at which the mass of dry air is known (±0.1 hPa). Estimates of dry air mass have a large range due to different topographies used in the various studies as well as changing observing systems. This last fact will have a significant impact in re-analyses and the mass of dry air will change throughout the period covered by the re-analyses.

The mass of dry air in ERA-40 was calculated by Trenberth and Smith (2004) as 5.1352 $\pm 0.0003 \times 10^{18}$ kg with a corresponding surface pressure of 983.05 hPa. The mean surface pressure in ERA-40 calculated by Trenberth and Smith (2004) was 985.50 hPa, which corresponds to a global mass of 5.1480×10^{18} kg. The difference between these numbers arises due to water loading in the atmosphere. The mass of dry air in ERA-40 can be compared with values taken from Berrisford *et al.* (2011) for the mass of dry air calculated from ERA-Interim and the NCEP/DOE re-analyses (NRA2). The average mass of dry air calculated from ERA-Interim is 10024.7 kgm^{-2} which is equivalent to 5.1132×10^{18} kg if multiplied by the area of the Earth. The dry air mass presented for NRA2 is stated as being 0.08% smaller than the other analyses, which equates approximately to a mass of 5.1092×10^{18} kg. Considering the different data assimilation processes and data etc. used in the three different re-analyses there is a high degree of agreement between them.

The way in which analyses are used, e.g. temporal and spatial truncation of analyses, can also have an impact on the conservation of a model. The effect of the wind update frequency has been investigated by Bregman *et al.* (2006) who use ERA-40 and the ECMWF operational analyses to compare the use of 6 hourly and 3 hourly wind updates in a 3D Eulerian CTM. A comparison between instantaneous (assume winds are constant between wind updates) and interpolated winds (interpolate winds between updates) is also presented. The majority of numerical models use interpolated winds to drive advection. Using 3 hourly wind updates produces a better representation of the stratosphere and is closer to observations. For example, the polar vortex shows a stronger gradient at the vortex edge and older ages are achieved in the mean age-of-air experiment if 3 hourly interpolated winds are used. This set up also shows improved hemispheric transport and reduced vertical dispersion allowing sharper gradients in the tracer field. An increase in the variability is also permitted with the 3 hourly winds which allows a more accurate representation of the

true variability in the observations. Overall better results are obtained when interpolated, rather than instantaneous, winds are used. This is also true when using the operational analyses from the ECMWF. One final point to be noted is the amount of dispersion observed when using the different analyses. This was achieved by plotting the end points of a set of trajectories showed a greater spread, and more dispersive winds, when using ERA-40 than when using the operational analyses. This could be linked to the data assimilation method used, with the dispersive ERA-40 using 3D-Var and the less dispersive operational analyses using 4D-Var.

A comparison of four different model spatial resolutions between T21 and T106 in a CTM with 3 hourly wind updates and chemically active tracers was carried out by Wild and Prather (2006). It was found that the change in resolution has different impacts for different tracers, making the source of the errors difficult to pinpoint. In the case of tropospheric ozone the global burden varied with resolution, with a higher resolution having a lower global burden. Wild and Prather (2006) state that these changes are due to differences in gross production, increase in deposition and reduction in stratospheric input of ozone. If the troposphere is split into layers then below 4 km net ozone production decreased with increasing resolution but increased in the 4-10 km range. This was hypothesised as due to improved representation of pollution plumes with increasing resolution, more efficient chemistry, better representation of convection and differences in mixing. The change in resolution did not have a consistent effect everywhere, with different regions experiencing different changes mainly due to the effects of resolution on chemistry. Wild and Prather (2006) note that a change to lower resolution means that advective fluxes are averaged over adjacent grid boxes resulting in the removal of high frequency variability in the analyses causing slower transport in the region of strong tracer gradients. Due to this the changing resolution alters the relative importance of various transport mechanisms. One of these mechanisms being convection, which is exaggerated at lower resolutions. This is especially important for shorter lived tracers where convection has a significant impact on their distribution.

Even if a specific set of analyses are chosen, Ploeger *et al.* (2010) noted that the choice of vertical transport scheme can have a noticeable impact on results. They carried out experiments using ERA-Interim and the ECMWF operational analyses in the Chemical Lagrangian Model of the Stratosphere (CLaMS) trajectory model, for details see e.g.

McKenna *et al.* (2002), Konopka *et al.* (2007). Particular attention was placed on the tropical tropopause as vertical transport across this region is of importance to transport into and out of the stratosphere. Two different types of vertical transport scheme were considered by Ploeger *et al.* (2010); diabatic and kinematic schemes. A diabatic velocity scheme uses an isentropic co-ordinate system with diabatic heating rates from the thermodynamic equation determining the cross-isentropic flow. Kinematic velocity schemes consider horizontal flow with the vertical motion determined from the mass continuity equation. Ploeger *et al.* (2010) observed a range in the amount of dispersion, with the kinematic schemes producing larger dispersion than the diabatic schemes.

A noticeable difference was also observed by Ploeger *et al.* (2010) when the same velocity scheme was used but different analyses. Specifically, the operational analyses show a larger vertical dispersion in the end points of a set of model trajectories than ERA-Interim and in general ERA-Interim shows less noise in the wind field than the operational analyses. Liu *et al.* (2010) note that ERA-40 is also more dispersive than ERA-Interim. The effect of the increased dispersion is that the operational analyses produce a faster upwelling in the tropical tropopause layer than ERA-Interim. The result of the slower vertical transport in ERA-Interim is that there is a greater spread in the horizontal as the trajectories can be seen to reach the regions where jets form. This work highlights that, especially in the vertical, it is the combination of numerical scheme and analyses that needs to be considered when designing a CTM or trajectory model.

1.3.2 Stratospheric Tape Recorder and Age-of-Air Diagnostics

As mentioned earlier (Section 1.1.2) stratospheric tape recorder and age-of-air diagnostics are widely used to test numerical models driven by analyses. It must be kept in mind that it is not always the analyses that introduce errors but the way in which the analyses are used that can result in inaccuracies, even if the driving data were perfect. Some examples of the tape recorder and age-of-air experiments will be considered now in order to give a brief overview of how these experiments are used.

Eluszkiewicz *et al.* (2000) use age-of-air diagnostics in a comparison of advection schemes, including an Eulerian, semi-Lagrangian and Lagrangian advection scheme. Eluszkiewicz *et al.* (2000) state that prior to their work the difference in the ages calculated were linked

to differences in the winds used, however there is a dependence on the numerics of the model used. The following values can be compared to a mean age-of-air for the stratosphere of approximately 4 years. The oldest ages, 4-5 years too old, were obtained for the non-diffusive centred-difference schemes. This suggests that these schemes are the best for multi-year runs. The youngest, and most unrealistic, ages on the order of 1 year were found for the semi-Lagrangian schemes due to the high degree of numerical diffusion. A test suppressing the numerical diffusion by removing the vertical interpolation was carried out and resulted in older ages of air. This is in support of the suggestion that numerical diffusion is partly responsible for some models producing ages that are too young. A finite volume scheme was also found to produce young ages and a monotonic version of the scheme produces even younger ages. The young ages were obtained with an Eulerian scheme due to a too fast diabatic dispersion (but not as fast as a semi-Lagrangian scheme).

A comparison of vertical co-ordinates is also shown by Eluszkiewicz *et al.* (2000) for a Lagrangian trajectory model. If $\dot{\sigma}$ (where σ is a hybrid co-ordinate presented in Fels *et al.* (1980)) is used as the vertical velocity then interpolation errors cause the vertical velocity to be too fast. In comparison using $\dot{\theta}$ produces slightly younger ages than those observed with a centred-difference scheme. Eluszkiewicz *et al.* (2000) theorised that a higher resolution will produce older ages due to a reduction in numerical diffusion for all of the schemes. This is supported by the fact that an increase in vertical resolution is observed to reduce the differences between the Eulerian and semi-Lagrangian schemes. However, for the centred-difference scheme it is suggested that an increase in resolution does not necessarily decrease the errors since the source of the error is at higher wavenumbers.

Monge-Sanz *et al.* (2007) compare a range of analyses using the mean age-of-air experiment, a trajectory test and the stratospheric tape recorder in an offline CTM. Two models were used in order to compare a difference in the model co-ordinate system. TOMCAT uses σ-p levels and SLIMCAT uses $\sigma - \theta$ hybrid levels but both are 3D CTMs. The analyses used were ERA-40, the ECMWF operational analyses, the UK Meteorological Office (UKMO) winds and the system used in a series of short experiment re-analyses in preparation for ERA-Interim. In Monge-Sanz *et al.* (2007) this is referred to as EXP471 and for simplicity the same will be done here. Monge-Sanz *et al.* (2007) immediately noted that the newer ECMWF winds have a more realistic horizontal and vertical transport. In the mean age-of-air test it was found that ERA-40 results in a mean age-of-air on the order of 1-2 years

(2-3 years too young) and the latitudinal gradient in the ages is too weak. In the same test the UKMO winds showed excessive transport between the tropics and the sub-tropics. Older ages were obtained using the ECMWF operational analyses and EXP471 due to an improved vertical advection, in particular less noise in the wind field. The improvement in age when using EXP471 is associated with improvements in horizontal mixing and, more importantly, a more realistic vertical advection. The choice of co-ordinate system was also observed by Monge-Sanz *et al.* (2007) to have an effect as TOMCAT produced younger ages than SLIMCAT for the same analyses.

From experiments using the trajectories of released particles Monge-Sanz *et al.* (2007) found that those analyses resulting in a younger tracer age have greater vertical dispersion as well as a faster mean velocity, in agreement with what was found by Eluszkiewicz *et al.* (2000). In particular the differences between ERA-40 and the EXP471 analyses are mainly due to the vertical dispersion. Also, reduced latitudinal dispersion in the EXP471 analyses means that there is an improved latitudinal gradient compared to that for ERA-40. The final test that Monge-Sanz *et al.* (2007) present is the stratospheric tape recorder experiment. Using the EXP471 analyses produced results closest to the observations and the UKMO analyses produced the worst results. The reason why one set of analyses is better than the others is difficult to pin down due to the range of differences between analyses. However, many of the improvements are linked to the use of 4D-Var data assimilation as it produces analyses that are more consistent in time. The increase in available data and changes in the forecast model are also important. These small differences can have a significant impact when using them in a model, as shown by Liu *et al.* (2010) when using a trajectory model to investigate cross-isentropic transport of stratospheric water vapour. The results presented by Liu *et al.* (2010) showed that small differences in dispersion, troposphere-stratosphere transport, temperature and wind fields can have a noticeable impact on water vapour distribution and evolution.

The stratospheric tape recorder is again considered in Gregory and West (2002) and it was observed that different schemes cause a different propagation rate. The Heun (or improved Euler) scheme produced a tape recorder with a realistic speed, but it was unphysically strong due to the development of an unphysical numerical oscillation in the tracer field. The non-monotonicity of the Heun scheme is stated as being the source of this oscillation. The total variation diminishing (TVD, see Durran (1999)) scheme tested produced

a propagation rate approximately 250% faster due to vertical diffusion. Unlike the Heun scheme no unphysical oscillation was observed with the TVD scheme. The TVD scheme was improved by calculating fluxes using local velocities, rather than upstream velocities, as well as removing the entropy fixer in the scheme. The final scheme that Gregory and West (2002) considered was the NIRVANA scheme, which will be presented in more detail in the next chapter. It was found that the phase speed of the tape recorder had a dependence on the vertical diffusion. The order of the interpolation polynomial in the NIRVANA scheme can be used to alter the vertical diffusion, with higher order polynomials producing less dispersion and a slower phase speed. The scheme also formed weak numerical instabilities that resulted in unphysical oscillations in the tape recorder. The use of a monotonic limiter was found to slightly increase the tape recorder speed but was also more diffusive. However, it also removed the previously seen oscillations with a resulting decrease in the amplitude of the tape recorder at higher levels. This highlights the difficulties in choosing a numerical scheme that gives the most accurate result.

1.3.3 Tracer Mass Conservation in GCMs using Mass Fixers

As mentioned above global mass conservation is not necessarily built into numerical schemes. If a scheme does not conserve mass then one way in which mass conservation can be obtained is to implement a mass fixer. There are several ways in which a mass fixer can work: relax the mass back to some value to counter a mass gain, add mass at each time step to counter a mass loss, or redistribute mass within the model to smooth out spurious maxima and minima. Even though mass conservation may be achieved, mass is often redistributed in an ad hoc manner that creates unrealistic changes to the tracer fields. When a relaxation is carried out the use of a background may not be suitable since over a long enough period of time this background may also evolve.

One example of a mass fixer is outlined by Rotman *et al.* (2001) when using a semi-Lagrangian advection scheme. The scheme uses a hybrid vertical co-ordinate that is terrain following in the troposphere and a pressure co-ordinate in the lower stratosphere (see Rasch and Williamson (1991) for more details of the scheme). In this mass fixer the correction to the mass is made by considering the tracer column, rather than the tracer mixing ratio within a grid box, and is applied at the end of each time step. The mass error arises

due to a deviation between the column mass in the model ($P(CTM)$) and the surface pressure from the analyses, (P(met field)) such that $P(err) = P(CTM) - P$(met field). One suggested method to remove this error is to reset the surface pressure in the CTM when the new analyses file is read (e.g. every 6 hours), as is done in the model used in this thesis. However, Rotman *et al.* (2001) state that this can lead to errors in the tracer field due to the jump in surface pressure creating an artifical flow in the vertical as the changing surface pressure will act like a source/sink.

The alternative method suggested by Rotman *et al.* (2001) is in the form of a wind field, (u, v), to correct for $P(err)$ by creating a resolved wind flow that carries tracer and thereby conserves global tracer mass and mixing ratio. The first stage of the mass fixer is to maintain the two surface pressure fields, $P(CTM)$ and P(met field), separately. When the analyses are updated the two surface pressures are compared in order to determine $P(err)$. The $P(err)$ field is filtered in order to determine a (u,v)-corrected wind field which is added to the original wind field in order to reduce $P(err)$. Prather *et al.* (1987) also published details on this mass fixer method and include equations for the two wind components:

$$u = 0.125\,[P(err)_{i,j} - P(err)_{i+1,j}]\,\frac{1}{g}\frac{\Delta x \Delta y}{\Delta t}$$

$$v = 0.125\,[P(err)_{i,j} - P(err)_{i,j+1}]\,\frac{1}{g}\frac{\Delta x \Delta y}{\Delta t}$$

where u represents the eastward flux between grid box (i, j) and its neighbour and v is the northward flux, g is the acceleration due to gravity and Δx and Δy represent the dimensions of the grid box. The factor of 0.125 arises due to the removal of an eighth of the difference in the pressure error between neighbouring grid cells. The negative side to this method is that the error is not completely removed, merely decreased. More data storage is also need to independently store the two surface pressure fields.

There are many other examples of mass fixers available in the literature such as that presented by Rasch and Williamson (1990) and Brasseur *et al.* (1998). Both of these present similar approaches in the creation of a mass fixer which makes adjustments to the tracer field that are proportional to the tracer mass per unit volume. This spreads the effects of the mass fixer across the model domain rather than creating strong localised effects. Jöckel *et al.* (2001) present an alternative type of mass fixer that uses a hybrid grid in order to account for any discrepancy between surface pressure and model mass. One final method that will quickly be mentioned is that of Bregman *et al.* (2003) that utilises a corrective

flux to balance the advective fluxes and the mass tendency. This is a similar principle to that outlined by Prather *et al.* (1987), but Bregman *et al.* (2003) use a different method. These examples show the range of mass fixer methods that exist and can be found in the literature.

When considering mass conservation within a GCM or CTM there are several different factors that need to be taken into account. Firstly, the mass conservation of the analyses being used to drive the model (as shown in Section 1.3.1). The second consideration is whether the model itself conserves both atmospheric mass and tracer mass. The last point to consider is whether the mass field in the model is consistent with the mass field derived from the analyses being used. This last point is considered in the mass fixer of Prather *et al.* (1987) presented above.

1.4 Thesis Aims and Outline

Although advection schemes may produce qualitatively realistic tracer structures, such as filaments, when run over long timescales they can accumulate numerical errors. An additional problem is that it is difficult to evaluate simulations of trace gases against observations due to uncertainties in sources and sinks. However, passive tracers provide information about properties of the transport in a numerical scheme, specifically global and material conservation. Therefore, both passive and active tracers will be used in this thesis to evaluate a numerical model.

Details of the new offline global CTM used in this thesis are presented in Chapter 2 as well as a comparison to some pre-existing numerical schemes. The remainder of this thesis addresses the following scientific questions:

1. Even if mass is conserved by an advection scheme when driven by a prescribed wind field, will it still be observed when driven offline by analyses? In particular, can this be achieved without the use of an ad hoc mass fixer that unrealistically redistributes mass within the tracer field? How does the mass conservation vary with different analyses? What are the ramifications for simulations of long-lived greenhouse gases?

2. Can the numerical model realistically represent small scale features and filamentation

of a tracer field as characterised by the decay of tracer mixing ratios following air masses away from a source? Numerical advection schemes introduce artificial mixing into tracer evolution which has significant impacts for point source tracers. Therefore, what is the numerical mixing rate in the model and is this comparable to true atmospheric mixing?

3. The output from the numerical model will be used further in investigating the concept of a background state. Specifically, how much of the 3D tracer distribution is encoded in equivalent latitude-theta co-ordinates and the passive reference tracer? Can this system then be evolved without the need for 3D calculations of many tracers?

The first question is of particular interest due to the fact that climate model runs focus on small changes in tracers over long periods that could be dwarfed by numerical mass changes (for example a change in the global burden of methane). Being able to quantify or limit the numerical mass change would be extremely beneficial.

Chapters 3 and 4 address question 1. In particular, Chapter 3 investigates the global mass conservation within the numerical model outlined in Chapter 2. Two test cases are considered: solid body rotation (prescribed wind field) and a passive tracer initialised as ozone and advected by analysed winds. Chapter 4 then compares the numerical changes in global burden of the passive ozone tracer in Chapter 3 with photochemical changes in global burden. This is achieved by incorporating a parameterised stratospheric ozone photochemistry scheme into the numerical model.

Question 2 is addressed in Chapter 5 which focuses on the smaller scale and is concerned with shape preservation and the numerical mixing rate of the model. This work makes use of the rare case of a point source release (Sarychev Peak volcanic eruption) with global observations of the tracer as it is advected away from the source over a month to estimate the numerical mixing rate in the upper troposphere.

Lastly, Chapter 6 looks at calculating the background state in a tracer-relative framework in answer to question 3. The degree to which the background state might be predicted without explicit calculation of all of the active species in 3D is also tested. All of the work presented in this thesis is summarised in Chapter 7, as well as providing suggestions on where this work could be taken next.

Chapter 2

Development of a Global Tracer Advection Model

As discussed in the Introduction, global conservation and shape preservation are desirable properties of a numerical scheme. Global conservation is of particular importance for the long term evolution of the distribution of tracers. Shape preservation means that during the evolution of the global distribution no spurious extrema are created by the numerical scheme. The requirement of mass conservation naturally led to the use of an inherently conservative finite volume scheme in this global tracer advection model. This avoids the use of a mass fixer to enforce mass conservation.

2.1 The Advection Scheme

2.1.1 The NIRVANA Scheme

A scheme of note for this thesis is the Non-oscillatory Integrally Reconstructed Volume-Averaged Numerical Advection (NIRVANA) scheme presented by Leonard *et al.* (1995). The NIRVANA scheme is a conservative finite volume scheme and Leonard *et al.* (1995) also study the scheme when monotonicity is enforced. The NIRVANA scheme is stable for any Courant number since the time step is semi-Lagrangian in nature and works on the basis of a departure point calculation to estimate the location of an air parcel one time step before. However, care must be taken in the meridional direction due to the boundary conditions at the polar regions placing a restriction on the meridional Courant number. More details are given on the meridional boundary conditions later.

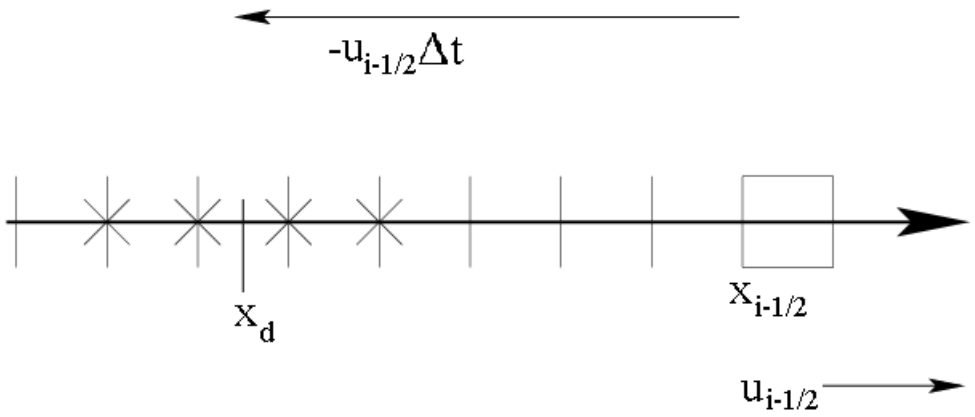

Figure 2.1: *Schematic of an interpolation stencil used in the NIRVANA scheme. In this example a cubic interpolation stencil (represented by a 4-point stencil) is centred on the departure point, x_d, not on the face of interest, $x_{i-1/2}$, and as such the scheme is stable even though the Courant number is $5 < C < 6$.*

Leonard *et al.* (1995) detail the use of different interpolants to determine the fluxes in each direction integrated over the model time step and the effects on the accuracy of the scheme. Among the interpolants considered are upwind and downwind (both linear and quadratic as well as weighted), piecewise linear and cell-centred. The interpolation is described as upwind when the stencil has more points upwind of the grid point being considered than downwind. By analysing the use of the different interpolants it was noted that the higher order interpolants result in reduced numerical dispersion during the advection. However, only the linear scheme is non-oscillatory.

A time step restriction would arise in the NIRVANA scheme if extrapolation in space was used in order to calculate the value of the tracer field at the departure point, $q(x_d)$, for each grid cell. The departure point is the point that reaches the upwind side of the grid cell under consideration at time n+1. If information local to the departure point, as in figure 2.1, is used in the interpolant to determine $q(x_d)$ then there is no Courant number limitation to the time step. For example, figure 2.1 shows a case where the Courant number has a value between 5 and 6, but the scheme is still stable. It is only when this interpolant is calculated using the velocity local to the face being considered, i.e. $x_{i-1/2}$, that the Courant number will act as a restriction in the numerical scheme. This is because the points used in the stencil would then not be representative of the tracer flux.

In order to obtain shape preservation within the scheme for higher than first order interpolation a limiter is required, several of which are discussed. It is shown that numerical

distortions in the field are most likely to occur where there is a sharp gradient in the tracer field. The NIRVANA scheme is also considered in three dimensions where Leonard *et al.* (1995) note that there are potential difficulties. Specifically, calculating the flux integral accurately and estimating the sub-cell behaviour of the tracer in a way that is accurate and shape preserving. The diffusion and other terms are also briefly considered. Source terms, for example, can simply be averaged over a grid cell. To second order, advection and diffusion terms can be treated independently and simply added to the advection update. To third order this is no longer true as the diffusion term alters the face values and the advection term alters the gradients and so multi-dimensional formulae would need to be used.

2.1.2 Advection Scheme Formulation

The NIRVANA scheme was used as the basis of the global tracer advection model that is used in this thesis. Andrew Gregory developed a global version used online within the Met Office Unified Model v3.2 which was a finite difference model (Cullen, 1993). Some details of the advection scheme can be found in Gregory and West (2002). This scheme was altered further by John Methven (University of Reading) to be used offline with chemistry-climate or forecast model output. Throughout the development of the model the hydrostatic approximation is used. For the work that follows the model is driven either by a prescribed wind field or by 6-hourly analyses from the ECMWF (European Centre for Medium-Range Weather Forecasts).

As stated in Section 1.2.2, in finite volume schemes the tracer conservation equation in flux form is integrated over each grid box (V) and then a time step (Δt):

$$\int_t^{t+\Delta t} \int_V \left(\frac{\partial(\rho q)}{\partial t} + \nabla . \mathbf{F} \right) dV dt = 0 \tag{2.1}$$

becomes

$$m^{n+1} - m^n + \sum_j \mathbf{F}_j \delta S_j \Delta t = 0 \tag{2.2}$$

where $m = \int_V \rho q dV$, $\mathbf{F}$ is the time average flux across the faces of each grid cell and δS is the face area. As stated in the Introduction, a finite volume scheme is inherently conservative, in an integral sense, since it ensures that conservation is obeyed within each individual grid cell and therefore globally as well. This global conservation is the main advantage of a

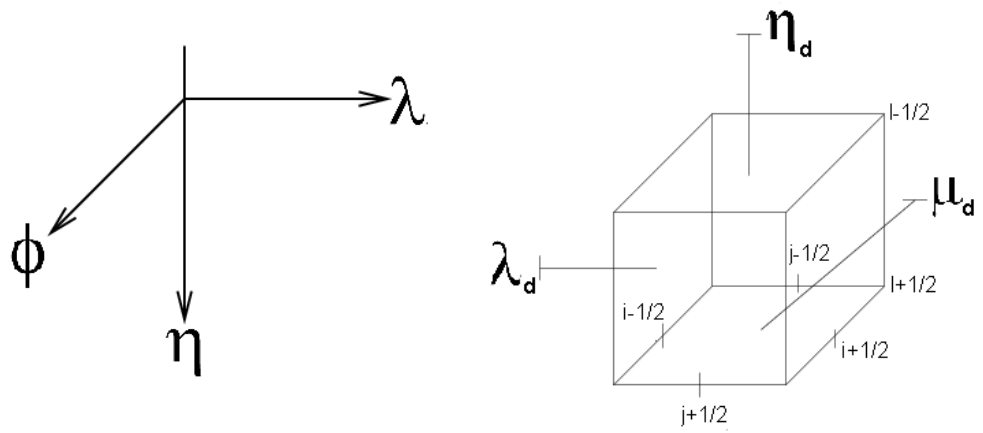

Figure 2.2: *Schematic of the co-ordinate system used and the corresponding departure points assuming positive wind flow in all three directions.*

finite volume scheme. The main disadvantage is that spurious maxima and minima can occur when using this method (for more information see Durran (1999)), but these can be remedied e.g. through the use of flux limiters.

NIRVANA uses a dimension splitting scheme whereby advection is carried out in sequence, first in the zonal direction, then the meridional direction and finally in the vertical. The co-ordinate system is shown in figure 2.2, and it is noted that the index in the zonal direction (i) increases eastward from 0E, the index in the meridional direction (j) increases from the North Pole to the South Pole and the vertical index (l) increases from the top, $\eta = 0$, to the bottom boundary, $\eta = 1$. As a result of the dimension splitting the NIRVANA scheme differs from a traditional semi-Lagrangian scheme due to the use of three departure points rather than one. This is shown by a comparison of figure 1.7, where one departure point in 3D space is used, and figure 2.2, where one departure point is used for each dimension.

The basic equations for the model, in spherical co-ordinates in the horizontal and η co-ordinates in the vertical, are equations (2.3) and (2.4). The first equation represents the conservation of mass on the sphere and the second is the conservation of tracer. If a material source or sink were to be included then this would be on the right-hand side of the equation.

$$\frac{\partial \rho}{\partial t} + \frac{\partial}{\partial \lambda}\left(\frac{\rho u}{a cos\phi}\right) + \frac{1}{cos\phi}\frac{\partial}{\partial \phi}\left(\frac{\rho v cos\phi}{a}\right) + \frac{\partial}{\partial \eta}\left(\rho \dot{\eta}\right) = 0 \tag{2.3}$$

$$\frac{\partial (\rho q)}{\partial t} + \frac{\partial}{\partial \lambda}\left(\frac{\rho u q}{a cos\phi}\right) + \frac{1}{cos\phi}\frac{\partial}{\partial \phi}\left(\frac{\rho q v cos\phi}{a}\right) + \frac{\partial}{\partial \eta}\left(\rho \dot{\eta} q\right) = 0 \tag{2.4}$$

where q is the tracer mixing ratio, $\rho = g^{-1}\partial p/\partial\eta$ is pseudo-density in η co-ordinates and a is the radius of the earth and is assumed to be constant. The hybrid co-ordinate used in the vertical, η, mixes pressure and surface pressure as described in Simmons and Burridge (1981). The winds in the zonal direction, meridional direction and vertical are u, v and $\dot{\eta}$ respectively, with i and j the longitude-latitude indices and l the vertical index. The sizes of the grid boxes are given by $\Delta\lambda$ (zonal direction), $\Delta\mu_j$ (meridional direction) where μ=sinϕ and $\Delta\eta_l$ (vertical), with the mass and velocities arranged on an Arakawa C-grid.

Integration of equation (2.3) over one time step and the grid cell volume, $\Delta\lambda\Delta\mu_j\Delta\eta_l$, in each dimension in turn produces the following three equations (using the operator splitting method as in Easter (1993)):

$$m^{*}_{ijl} = m_{ijl} - [m_{up}U_{i+\frac{1}{2},j,l} - m_{up}U_{i-\frac{1}{2},j,l}]\frac{\Delta t}{\Delta\lambda} \tag{2.5}$$

$$m^{**}_{ijl} = m^{*}_{ijl} - [m_{up}V_{i,j+\frac{1}{2},l} - m_{up}V_{i,j-\frac{1}{2},l}]\frac{\Delta t}{\Delta\mu_j} \tag{2.6}$$

$$m^{+}_{ijl} = m^{**}_{ijl} - \left[\left(\dot{\eta}\frac{\partial p}{\partial\eta}\right)_{i,j,l+1/2} - \left(\dot{\eta}\frac{\partial p}{\partial\eta}\right)_{i,j,l-1/2}\right]\Delta t \tag{2.7}$$

Once advection in the zonal direction has been carried out quantities are denoted by $(*)$, after the successive advection in the meridional direction this becomes $(**)$ and after the final advection in the vertical $(+)$. The $(+)$ sign therefore represents the quantity at time $t + \Delta t$. Note that all of the equations have been divided by the term $(-\Delta\lambda\Delta\mu_j/g)$. The indices on the terms in the square brackets are dependent on the direction of the flow. As the indices are currently written they are accurate for a flow in the direction of increasing indices in all directions. It must be noted that the densities used in the equations, m_{up}, are the densities of the grid boxes adjacent to each face on the upwind side. m_{up} is always determined from the mass field at the start of the time step and not the updated mass field. Also, $U = u/acos\phi$ represents the face average zonal flow, $V = vcos\phi/a$ represents the face average meridional flow and $m \equiv \Delta p$. m is determined from the analyses or prescribed wind field at the start of each time step, i.e. the model does not carry an internally evolving mass field throughout the duration of a model run.

Equation (2.5) is the mass update in the zonal direction, (2.6) is the mass update in the meridional direction and (2.7) is in the vertical. In each case the second term on the right-

hand side represents the fluxes across the faces of the grid cell in the respective directions. Note that the grid size in the meridional and vertical directions is not constant. It should also be noted that, contrary to mass, the velocities use half integers in the indices as values midway between cell centres (i.e. on the faces) are used.

In the case of the vertical (equation 2.7) the discretisation of the continuity equation contains a partial derivative. This term can be defined as (following Simmons and Burridge (1981)):

$$\left(\dot{\eta}\frac{\partial p}{\partial \eta}\right)_{l+\frac{1}{2}} = -\frac{\partial p_{l+\frac{1}{2}}}{\partial t} - \sum_{r=1}^{l} \nabla \cdot (\mathbf{v}_r \Delta p_r) \tag{2.8}$$

In order to solve this equation we follow the same method as implemented in the ECMWF model and outlined by Simmons and Burridge (1981), which involves calculating the discrete vertical integrals of divergence to find $\partial p_{l+1/2}/\partial t$. Once done $\dot{\eta}\partial p/\partial \eta$ can be used in equation (2.7).

If operator splitting is again used the tracer continuity equation (2.4) can be re-written as:

$$m_i^* q_i^* = m_i q_i + \left(F_{i-\frac{1}{2}}(q) - F_{i+\frac{1}{2}}(q)\right)\frac{1}{\Delta\lambda_i} \tag{2.9}$$

$$m_j^{**} q_j^{**} = m_j^* q_j^* + \left(G_{j-\frac{1}{2}}(q) - G_{j+\frac{1}{2}}(q)\right)\frac{1}{\Delta\mu_j} \tag{2.10}$$

$$m_l^{+} q_l^{+} = m_l^{**} q_l^{**} + H_{l-\frac{1}{2}}(q) - H_{l+\frac{1}{2}}(q) \tag{2.11}$$

where q is the tracer mass mixing ratio and m is the same mass per grid box as in equations (2.5)-(2.7). For this reason the mass update has to be calculated before the tracer update. The tracer fluxes in λ, μ and η are F, G and H respectively. The fluxes are calculated using an explicit method in one dimension at a time:

$$F_{i+\frac{1}{2}} = \int_{t-\Delta t}^{t} \rho q u dt$$

If it is assumed that u can be approximated as $Dx/Dt \simeq dx/dt$ (i.e. the trajectory has a uniform velocity given by the value at the face), then this becomes:

$$F_{i+\frac{1}{2}} \simeq \int_{x_{up}}^{x_{i+1/2}} \rho q dx \tag{2.12}$$

$$\simeq \rho_{up} \int_{x_{up}}^{x_{i+1/2}} q dx \tag{2.13}$$

The integral is determined by integrating the tracer, q, over the domain and then subtracting the value of the integral interpolated to the departure point from the value at the face being considered. This is an upwind interpolation and, as mentioned previously, is similar to a semi-Lagrangian method but in one dimension at a time. This process lifts the CFL restriction for the NIRVANA scheme, as shown by figure 2.1, and gives rise to the "integrally reconstructed" part of the scheme name. Using this method the flux becomes:

$$F_{i+\frac{1}{2}} = m_{up}\left(\int_0^{x_{i+\frac{1}{2}}} q dx - \int_0^{x_{up}} q dx\right) \tag{2.14}$$

$$= m_{up}\left(I_{i+\frac{1}{2}} - I_{x_{up}}\right) \tag{2.15}$$

where

$$I_{i+\frac{1}{2}} = \sum_{k=1}^{i} q_k \Delta x_k \tag{2.16}$$

$$x_{up} = x_{i+\frac{1}{2}} - u_{i+\frac{1}{2}}\Delta t \tag{2.17}$$

Note that an alternative method exists whereby the approximation made in equation (2.13) is not applied. In this case ρ is retained within the integral and the tracer flux is $\int \rho q dx$ (equation 2.12). The schemes with and without this approximation (2.13) will be referred to as schemes v2 (i.e. version 2) and v3 respectively.

As before, m_{up} represents the mass in the neighbouring grid box upstream and does not use the updated mass field. The location of the departure point at time $t - \Delta t$ is x_{up}. Equation (2.17) again assumes that there is a uniform wind in one direction. $I_{x_{up}}$ is the value of the integral interpolated to x_{up}, but the flux formulation ensures the conservation of tracer mass. Defining the integral in this form means that it is monotonic and smooth in x. Since I is monotonic the resulting interpolation is smooth, with undershoots and overshoots less likely to arise from interpolation.

The quintic polynomial used in the zonal direction to calculate the $I_{x_{up}}$ term is represented schematically in figure 2.3. Note that since the interpolation is fifth order, six points are used. This arises since any interpolation order requires one additional point. For example a linear interpolation requires two points in order for the interpolation to work, and so on. In the meridional and vertical directions a cubic interpolation is used.

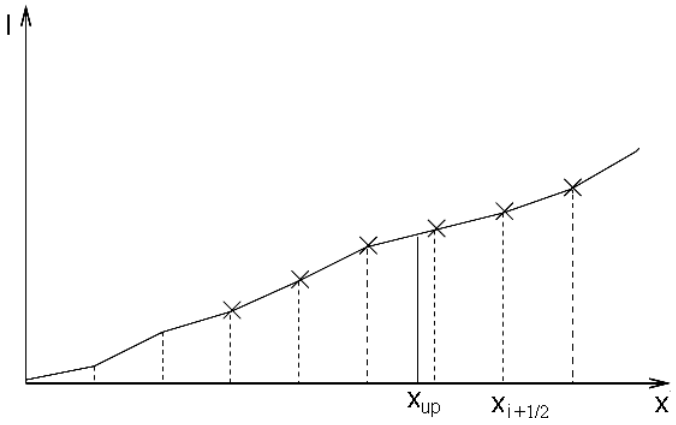

Figure 2.3: *Schematic of quintic interpolation for x_{up} (determined for point $x_{i+1/2}$). Dashed lines represent the faces of the grid boxes and the crosses are the points used in the interpolation.*

Equation (2.15) is also used to calculate G with a corresponding change in Δx and the indices. In the case of the vertical flux the equation becomes:

$$H_{l+\frac{1}{2}} = \frac{\Delta p_{up}}{\Delta \eta_{up}} \left(\int_0^{\eta_{l+\frac{1}{2}}} q d\eta - \int_0^{\eta_{up}} q d\eta \right) \tag{2.18}$$

$$= \frac{\Delta p_{up}}{\Delta \eta_{up}} (I_{i+\frac{1}{2}} - I_{\eta_{up}}) \tag{2.19}$$

With a corresponding change to the calculation of the upwind departure point:

$$\eta_{up} = \eta_{l+\frac{1}{2}} - \left(\frac{\partial p}{\partial \eta} \dot{\eta} \right)_{l+1/2} \frac{\Delta \eta_{up}}{\Delta p_{up}} \Delta t \tag{2.20}$$

The value of $\Delta \eta_{up} / \Delta p_{up}$ is taken from the grid box adjacent to the face, in this case $l+1/2$, on the upwind side where $\Delta \eta_{up}$ is the height of the upwind grid box. Note that in the meridional direction and the vertical, $\Delta \mu_j$ and $\Delta \eta_l$ respectively, will vary depending on position as the grid is not uniform.

It needs to be noted that the tracer advection equations stated above use the initial tracer distribution in the calculation of the tracer fluxes. The scheme as documented by Gregory and West (2002) uses the updated tracer field in the flux calculations, i.e. $G(q^*)$ and $H(q^{**})$, and will be referred to as scheme v1. The scheme using the initial mass and tracer fields in the tracer flux calculations (as detailed above) will be referred to as scheme v2. The reason for this alteration will be explained in Section 2.3.

The model is driven offline by analyses from the ECMWF which are interpolated linearly in time so that the wind field evolves between tracer time steps. The scheme can also

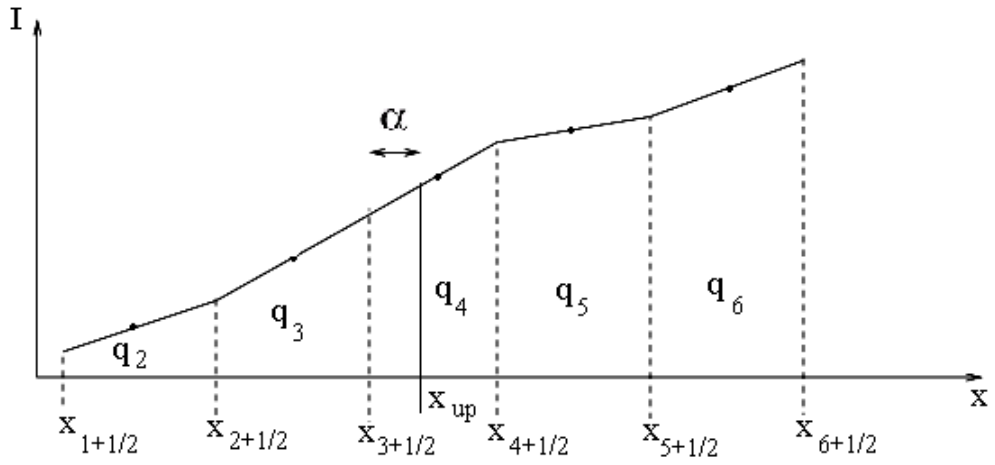

Figure 2.4: *Schematic of a monotonic flux limiter. The dashed lines represent the faces of the grid boxes ($x_{i+1/2}$) and the tracer values represent the grid box average tracer values and are located at the centre of grid boxes (q_i). x_{up} represents the location of the departure point.*

be forced to be monotonic (introduce no new maxima and minima into the tracer field) and/or positive definite (ensure no negative values in the tracer field). The reason for making the scheme positive definite is because even though the scheme is conservative, any interpolation higher in order than linear introduces weak oscillations into the tracer distribution. The positive definite feature will then systematically remove any negative values by setting them to zero, thereby increasing the global integral of the tracer. For this reason forcing the scheme to be positive definite with such a simple method should be avoided if possible.

2.1.3 Monotonic and Positive Definite Schemes

Figure 2.4 is similar to figure 2.3 and shows the essential grid points that will be required in order to outline how the monotonic limiter works. The values of $I(x_{i+1/2})$ are given for the grid box faces and the tracer values, q_i, are grid box average values and are given for the centre of the grid boxes. The difference in location of the two values must be noted. In the grid box where the departure point, x_{up}, is located the tracer distribution in that box will fall into one of two possible categories: extrema or no extrema. In the case of an extrema being located in the grid box then a linear interpolation is carried out across the

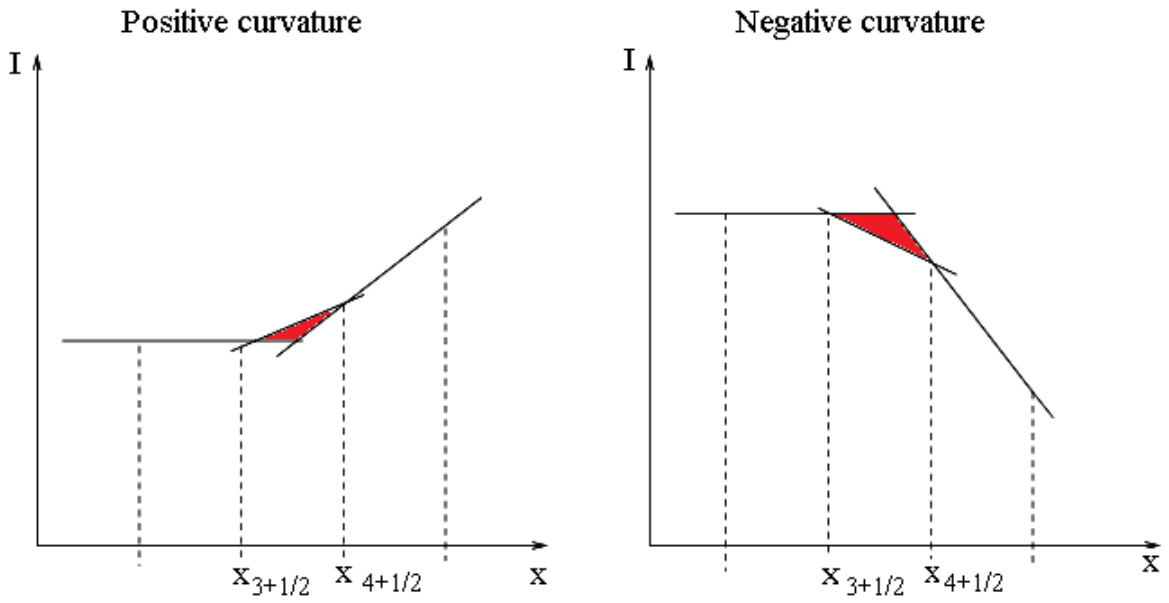

Figure 2.5: *Schematic of a monotonic flux limiter when there is positive or negative curvature at the grid box where x_{up} is located. The monotonic limiter acts to restrict $I(x_{up})$ to the region highlighted in red.*

grid box in order to determine $I(x_{up})$. The presence of an extrema is determined:

$$\begin{aligned} q_3 &= I(x_{3+1/2}) - I(x_{2+1/2}) \\ q_4 &= I(x_{4+1/2}) - I(x_{3+1/2}) \\ q_5 &= I(x_{5+1/2}) - I(x_{4+1/2}) \end{aligned}$$

The differences between the tracer value in the box where x_{up} is located, q_4, and the tracer values on either side are:

$$\begin{aligned} dleft &= q_4 - q_3 \\ dright &= q_5 - q_4 \end{aligned}$$

If the multiple of these two numbers is negative then an extrema is located in the grid box of interest and $I(x_{up})$ is determined via linear interpolation:

$$I(x_{up}) = I(x_{3+1/2}) + \alpha q_4 \tag{2.21}$$

where α is the distance between $x_{3+1/2}$ and x_{up}.

When there is not an extrema (i.e. dleft*dright is positive) then there can be a positive or negative curvature of the integral, I, in the departure point grid box. This is shown

schematically in figure 2.5. In this case there are two stages to the monotonic limiter. The first stage involves extrapolating the value of q_3 from the grid points on the left and right:

$$\begin{aligned} qleft &= I(x_{3+1/2}) + \alpha q_3 \\ qright &= I(x_{4+1/2}) - (1-\alpha) q_5 \end{aligned}$$

The second stage is to calculate a linear interpolation across the grid point of interest (equation 2.21). These three values (qleft, qright and equation 2.21) then form the boundaries of the red highlighted region in figure 2.5. The limiter then acts to ensure that $I(x_{up})$ is located within this highlighted region. As a result of this limiter $I(x)$ is also bound to be almost monotonic (a higher order interpolation can cause slight 'wiggles' in the integral).

In this work the scheme is made positive definite by setting $q = 0$ where $q < 0$. This is the simplest method that can be used to make a scheme positive definite and will inherently result in an increase in the global burden of a tracer. More complex positive definite schemes exist, as mentioned in the Introduction (Section 1.2.2).

2.2 Mass Advection Considerations

This section aims to test the dimension splitting approach used in the advection scheme. At the same time two different versions of the mass update scheme are compared. Both of the schemes use equation (2.5), but only one uses equation (2.6) where the mass flux is calculated using the original mass, m. The other case is where the mass fluxes are calculated using the updated mass, m^*, as in Gregory and West (2002). In this case equation (2.6) then becomes:

$$m^{**}_{ijl} = m^*_{ijl} - [m^*_{up} V_{i,j+\frac{1}{2},l} - m^*_{up} V_{i,j-\frac{1}{2},l}] \frac{\Delta t}{\Delta \mu_j} \tag{2.22}$$

Relative motion about a point can be partitioned into three components (Batchelor (1967) and figure 2.6). These components can be considered in the form of a divergent flow, a deformation flow and rotation. Each of these cases will be considered in turn to see whether the ratio of final mass to initial mass after horizontal advection (m^{**}/m) is equal to the analytical solution for each flow or not.

In all three cases the simplest scenario of a uniform mass (m_{ijl}) is used so that deviations are clearly a result of numerical errors in the case of deformation and rotation. The planar

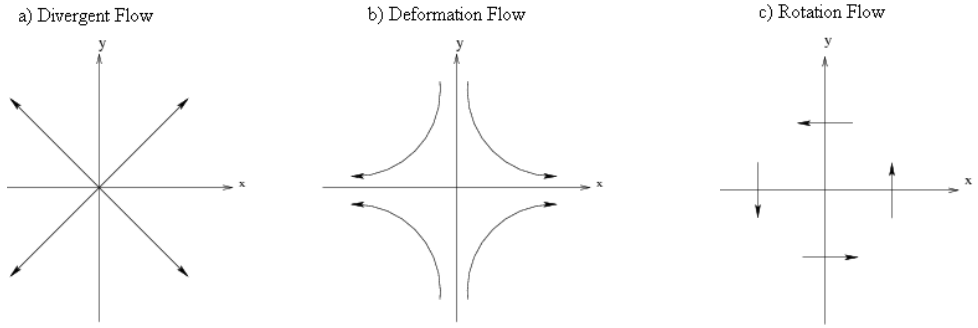

Figure 2.6: *Schematic of the three types of analytical flows considered.*

approximation is also used which assumes that the grid is regular so that $\Delta\lambda = \Delta\mu_j =$ constant. Vertical advection is not considered at this point for the sake of simplicity. If all of these assumptions are then included, equations (2.5) and (2.6) can be combined to give (2.23). Similarly equations (2.5) and (2.22) combine to give (2.24).

$$\frac{m^{**}_{ijl}}{m_{ijl}} = 1 - \frac{\Delta t}{\Delta x}[u_{i+\frac{1}{2},j,l} - u_{i-\frac{1}{2},j,l} + v_{i,j+\frac{1}{2},l} - v_{i,j-\frac{1}{2},l}] \tag{2.23}$$

$$\begin{aligned}\frac{m^{**}_{ijl}}{m_{ijl}} &= 1 - \frac{\Delta t}{\Delta x}[u_{i+\frac{1}{2},j,l} - u_{i-\frac{1}{2},j,l} + v_{i,j+\frac{1}{2},l} - v_{i,j-\frac{1}{2},l}] \\ &+ \frac{\Delta t^2}{\Delta x^2}\,[v_{i,j+\frac{1}{2},l}(u_{i+\frac{1}{2},j,l} - u_{i-\frac{1}{2},j,l}) - v_{i,j-\frac{1}{2},l}(u_{i+\frac{1}{2},j-1,l} - u_{i-\frac{1}{2},j-1,l})]\end{aligned} \tag{2.24}$$

where $u_{i+\frac{1}{2},j,l}$ can be considered as u evaluated at $x+(1/2)\Delta x$ and so on.

Divergent flow

In this case the winds serve to spread out the tracer from one point, here taken as the origin ij, as shown in figure 2.6(a). The winds can be defined using the simple equations $u = \beta$x and $v = \beta y$, where β is the rate of divergence and is taken as a constant. If both of these are substituted into equation (2.23) then the following is obtained:

$$\frac{m^{**}_{ijl}}{m_{ijl}} = 1 - 2\beta\Delta t$$

The mass within a grid box decreases for a divergent flow as expected. This can be compared with the exact solution, the derivation of which is shown below.

Equation (2.3) for a uniform density can be rearranged to give:

$$\frac{\partial\rho}{\partial t} + \rho\nabla.\mathbf{u} = 0$$

Integrating this equation over a grid box then becomes:

$$\frac{\partial M}{\partial t} + \rho \int \nabla.\mathbf{u} dx dy = 0$$

The second term in the equation can be expanded and, using the velocities defined above, becomes:

$$\begin{aligned} \int \nabla.\mathbf{u} dA &= \int \left(\frac{\partial u}{\partial x} + \frac{\partial v}{\partial y} \right) dA \\ &= \int (\beta + \beta) dA \\ &= 2\beta \int dA \\ &= 2\beta \Delta x^2 \end{aligned}$$

This can then be substituted into the full equation and leads to:

$$\frac{M^+ - M}{\Delta t} \simeq -2\beta\rho\Delta x^2 + O(\Delta t)$$

Rearrange, noting that $M{=}\rho\Delta x^2$, to obtain:

$$\frac{M^+}{M} = 1 - 2\beta\Delta t + O(\Delta t^2)$$

Equation (2.24) (scheme v1) explicity produces an additional term, $\alpha^2\Delta t^2$, where α is a scaling factor. This term is not produced when using equation (2.23) (scheme v2), but otherwise agrees with the analytical solution. The absence of the higher order term suggests that scheme v2 is not as accurate as scheme v1 when considering a divergent flow.

Deformation flow

For a deformation flow, figure 2.6(b), the tracer is stretched along the x-axis and compressed along the y-axis. The winds can be defined as $u = \beta x$ and $v = -\beta y$, and once again substituted into equation (2.23). In this case the resulting equation is:

$$\frac{m^{**}_{ijl}}{m_{ijl}} = 1$$

For a deformation flow the scheme should therefore conserve mass. If scheme v1 is again considered (equation 2.24) then an additional term, $-\alpha^2\Delta t^2$, appears on the right-hand side and the scheme deviates from the analytical solution. These two results can both be compared with the actual solution as in the previous case of a deformation flow. In this case it is simpler as it can be quickly seen that the divergence of the wind field is zero and therefore dM/dt is zero. Which means that the ratio of the masses should equal one.

Rotation

In the final case of the tracer undergoing a rotation, figure 2.6(c), the tracer is turned about its centre. Once again the winds can be simply defined as $u = -\beta y$ and $v = \beta x$ and the analytical solution is:

$$\frac{m^{**}_{ijl}}{m_{ijl}} = 1$$

Therefore, whilst undergoing rotation the mass should be conserved since, as in the previous case of a deformation flow, the divergence of the flow is zero. In this case the same result is obtained regardless of whether equation (2.23) or (2.24) is used. This is because in the latter case the final term cancels to zero when substituting in the wind equations. Therefore, in either case the numerical scheme should be mass conservative when undergoing rotation. From these three simple tests it can be seen that equation (2.23) should be used rather than (2.24). However, note that these test cases do not evaluate the tracer part of the scheme.

2.3 Tracer Advection Considerations

The same requirement of no mass change over a time step will now be considered for the tracer equations in the horizontal. The two different versions of the tracer advection scheme previously mentioned will be considered. As a reminder, scheme v2 uses equations (2.9) and (2.10) where the tracer flux in all directions is calculated using the original tracer field, q. In comparison, the tracer fluxes in scheme v1 are calculated using the updated tracer field, $G(q^*)$, as in Gregory and West (2002).

Scheme v2 will be considered first as the same method is used in both the mass and tracer fluxes in this version and the mass update has already been shown to be accurate. The flux equation (2.14) will also be needed in the equations that follow. Zonal advection (equation 2.9) is carried out first with the flux terms written in integral form. Note that the j index has been left out for simplicity.

$$\begin{aligned} m^*_i q^*_i &= m_i q_i - \Bigg[m_{up_{i+1/2}} \left(\int_0^{x_{i+1/2}} q dx - \int_0^{x_{up_i}} q dx \right) \\ &\quad - m_{up_{i-1/2}} \left(\int_0^{x_{i-1/2}} q dx - \int_0^{x_{up_{i-1}}} q dx \right) \Bigg] \frac{1}{\Delta x_i} \end{aligned}$$

Since q is assumed uniform it can be taken outside of the integral in order to obtain:

$$\begin{aligned} m_i^* q_i^* &= m_i q_i - \left[m_{up_{i+1/2}} q \left(\int_0^{x_{i+1/2}} dx - \int_0^{x_{up_i}} dx \right) \right. \\ &\quad \left. - m_{up_{i-1/2}} q \left(\int_0^{x_{i-1/2}} dx - \int_0^{x_{up_{i-1}}} dx \right) \right] \frac{1}{\Delta x_i} \\ &= m_i q_i - \left[m_{up_{i+1/2}} q \left(x_{i+1/2} - x_{up_i} \right) \right. \\ &\quad \left. - m_{up_{i-1/2}} q \left(x_{i-1/2} - x_{up_{i-1}} \right) \right] \frac{1}{\Delta x_i} \end{aligned}$$

Due to the use of a uniform mass field $m_{up_{i+1/2}} = m_{up_{i-1/2}} = m$ and a regular grid means that $\Delta x_i = \Delta x$. This, along with equation (2.17), produces:

$$\begin{aligned} m_i^* q_i^* &= mq - \frac{mq}{\Delta x} \left(U_{i+1/2} \Delta t - U_{i-1/2} \Delta t \right) \\ \frac{m_i^* q_i^*}{mq} &= 1 - \frac{\Delta t}{\Delta x} \left(U_{i+1/2} - U_{i-1/2} \right) \end{aligned}$$

This is then the same expression that was obtained for the mass updates (equation 2.23), which is known to be conservative.

The meridional advection then uses equation (2.10). Making the same assumptions of uniformity in mass, tracer and a regular grid (where $\Delta y = \Delta x$) means that the following is obtained:

$$\frac{m_j^+ q_j^+}{mq} = 1 - \frac{\Delta t}{\Delta x} \left(V_{j+1/2} - V_{j-1/2} \right)$$

Once again this reflects the result for the mass update. Therefore, after the zonal and meridional advection the scheme is mass conservative as:

$$\frac{m_{ij}^+ q_{ij}^+}{m_{ij} q_{ij}} = 1 \tag{2.25}$$

If scheme v1 is considered, with identical initial conditions to those above, then the same result is obtained. This suggests that both schemes (v1 and v2) will produce the same conservative result and as such both need to be considered further. Recall, both schemes use equation (2.5)-(2.7) and equation (2.9). The difference arises in equations (2.10) and (2.11) where scheme v1 uses $G(q^*)$ and $H(q^{**})$ instead. Note that equation (2.22) is never used because it causes lumping in the density field.

2.4 Polar Grid

Figure 2.7(a) shows the distortion after one rotation that occurs in the cosine bell distribution when it is advected over the pole if the fluxes are calculated as in equations (2.9) and (2.10) (scheme v2). In order to correct this distortion an alteration in the grid in the polar regions was carried out. This concept of a grid reduction at the poles was referred to as an extended polar zone in Prather *et al.* (1987) and referencing articles. The reduced grid works by increasing the zonal length of the grid cells closest to the pole by using fewer cells around a latitude circle. This reduces the zonal Courant number, which is at a maximum at this point due to the convergence of the grid at the poles. At the poles this is of particular importance due to the meridional boundary conditions creating a purely zonal flow at the most poleward latitude (see Section 2.5.2 for more details).

This grid reduction is achieved by grouping the existing grid cells into equal sized groups, for example at a horizontal resolution of T159 use five groups at the most poleward latitude, and then doubling the number of groups at each successive latitudinal band as shown in figure 2.9. Within each group, for example the highlighted section in figure 2.9, the grid cells contained in it are averaged over and the averaged value assigned to the new larger grid cell. These large grid cells are considered for the zonal advection. Due to the reduced number of grid points, especially at the most poleward latitude, the previous quintic interpolation has been reduced to a linear interpolation to reduce the stencil size on the reduced grid.

Once the zonal advection has been carried out, the large cell is split back up into its original number of cells and the tracer and mass values obtained after the zonal advection are assigned equally to each of these smaller grid cells. This is the same method used by Li and Chang (1996) and the reasons for their choice will be discussed in more detail later. The meridional and vertical advection steps are carried out on the original grid and introduce varying values into each grid box. These are then averaged out at the start of the next time step by the zonal advection. The grid reduction is only carried out when undergoing the zonal advection because the grid boxes have the smallest dimension in the zonal direction and hence the largest Courant number.

These modifications result in the dent in the cosine bell seen in figure 2.7(b) rather than the previously seen trench in (a) when using scheme v2. The alternative method to obtain

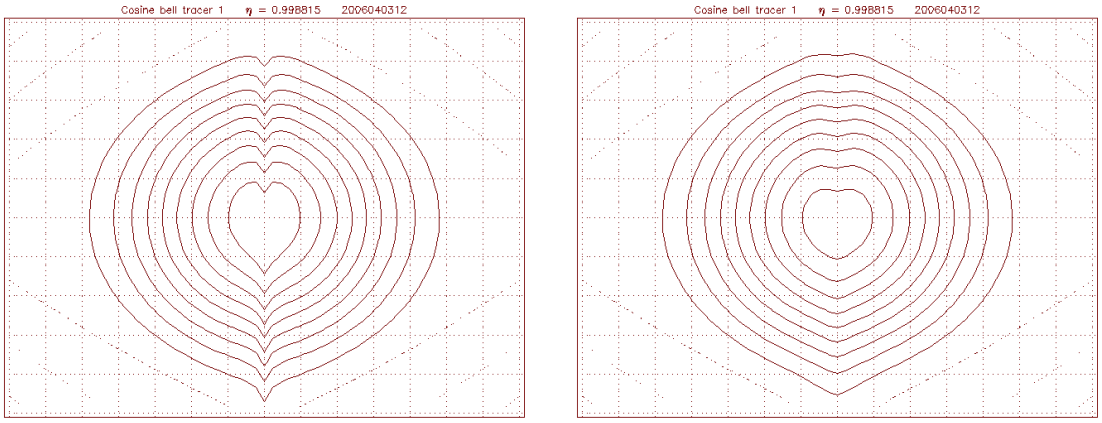

(a) Without reduced grid (b) With reduced grid

Figure 2.7: *Cosine bell advected by solid body rotation at α=90 after one complete rotation using scheme v2 at a horizontal resolution of T159. The wind is advecting from the bottom to the top of the figure. (a) advection when the polar grid is unaltered (maximum Courant numbers of 21.4 and 0.32 in the zonal and meridional directions respectively), and (b) advection when the reduced grid is included (maximum Courant numbers of 2.43 and 0.32 in the zonal and meridional directions respectively). Dotted line is zero, contour spacing of 0.1.*

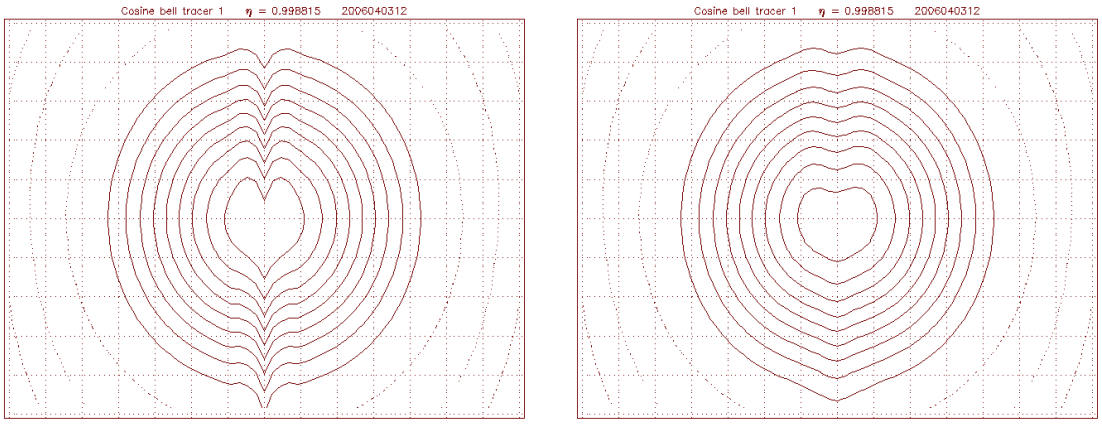

(a) Without reduced grid (b) With reduced grid

Figure 2.8: *Cosine bell advected by solid body rotation at α=90 after one complete rotation using scheme v1 at a horizontal resolution of T159. The wind is advecting from the bottom to the top of the figure. (a) advection when the polar grid is unaltered (maximum Courant numbers of 21.4 and 0.32 in the zonal and meridional directions respectively), and (b) advection when the reduced grid is included (maximum Courant numbers of 2.43 and 0.32 in the zonal and meridional directions respectively). Dotted line is zero, contour spacing of 0.1.*

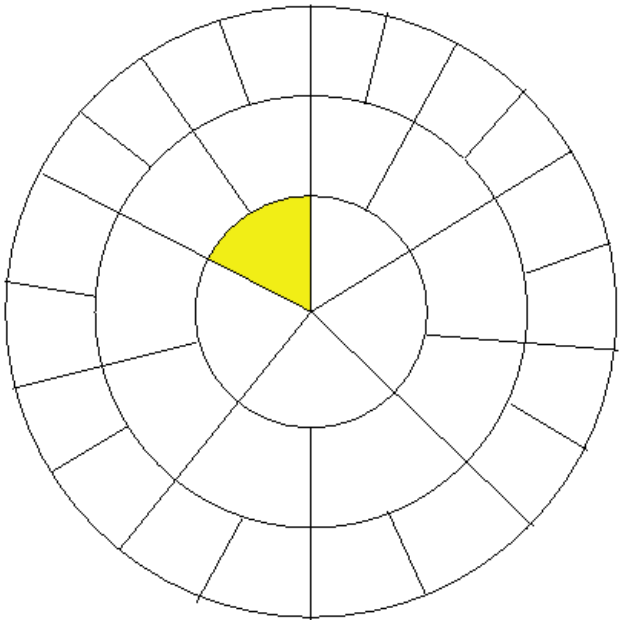

Figure 2.9: *Schematic of the reduced grid at T159. The highlighted yellow cell is averaged over 64 original cells. With each successive latitude the number of cells doubles until the original 320 is obtained.*

this result is to decrease the size of the time step. However, this is impractical for long model runs and shows the benefit of the polar grid. Figure 2.8 shows the same images as in figure 2.7, but for scheme v1. The reduced grid has a similar effect for both schemes. However, the figures do show the initial differences observed between the two schemes, with scheme v2 producing a cosine bell that is stretched in the zonal direction relative to scheme v1, despite using the same interpolation (quintic in the zonal direction and cubic in the meridional direction).

2.5 Boundary Conditions

2.5.1 Vertical

The boundary conditions in the vertical were implemented in order to force the condition of $\dot{\eta} = 0$ at the boundaries ($\eta = 0, 1$), which ensures no flux. At the same time this ensures that when the departure point is calculated it lies within the model domain. Figure 2.10 demonstrates this along with a schematic of the grid discretisation in the vertical. If the zero velocity boundary condition is not enforced then it is possible for the dashed line to represent the velocity profile which is then used to calculate the departure point D_1. This point is outside of the model domain. With zero velocity ensured the solid curved line

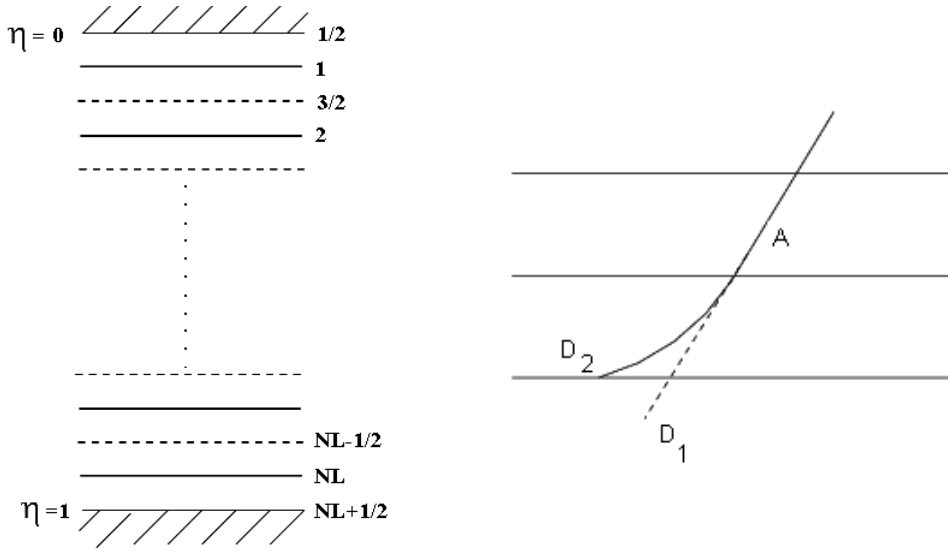

Figure 2.10: *Left: Grid discretisation in the vertical. The dashed levels are the half levels where $\dot{\eta}$ is defined. m and q are defined on the full levels. Right: Schematic of the boundary conditions in the vertical. Without enforcing $\dot{\eta} = 0$ then the dashed line is possible where the departure point is calculated outside of the model levels (D_1). With the new conditions the exponential decay in velocity retains the departure point within the model range (D_2).*

now represents the velocity profile and departure point D_2 is calculated within the model domain. The equations needed to achieve this will now be presented.

At the uppermost boundary the condition $\dot{\eta}|_0 = 0$ needs to be met. The departure point (η_d) is then calculated using this condition and the velocity at the half level closest to the boundary ($\eta_{3/2}$ as shown in figure 2.10). Using these produces:

$$\begin{aligned} \frac{D\eta}{Dt} &= \frac{\eta - 0}{\eta_{3/2} - 0}\dot{\eta}_{3/2} \\ \int \frac{d\eta}{\eta} &= \int_{t-\Delta t}^{t} \frac{\dot{\eta}_{3/2}}{\eta_{3/2}} dt \\ [ln\eta]_{\eta_d}^{\eta_{3/2}} &= \frac{\dot{\eta}_{3/2}}{\eta_{3/2}}\Delta t \\ \eta_d &= \eta_{3/2} e^{\frac{-\dot{\eta}_{3/2}\Delta t}{\eta_{3/2}}} \end{aligned} \tag{2.26}$$

At the lowermost boundary the condition becomes $\dot{\eta}|_1 = 0$. Once again using the velocity

on the closest half level ($\eta_{nl-1/2}$) results in the departure point equation:

$$\begin{aligned}
\frac{D\eta}{Dt} &= \frac{1-\eta}{1-\eta_{nl-1/2}}\dot{\eta}_{nl-1/2} \\
\int \frac{d\eta}{1-\eta} &= \int \frac{\dot{\eta}_{nl-1/2}}{1-\eta_{nl-1/2}}dt \\
[-ln(1-\eta)]_{\eta_d}^{\eta_{nl-1/2}} &= \frac{\dot{\eta}_{nl-1/2}\Delta t}{1-\eta_{nl-1/2}} \\
ln\left(\frac{1-\eta_d}{1-\eta_{nl-1/2}}\right) &= \frac{\dot{\eta}_{nl-1/2}\Delta t}{1-\eta_{nl-1/2}} \\
\eta_d &= 1-(1-\eta_{nl-1/2})e^{\frac{\dot{\eta}_{nl-1/2}\Delta t}{1-\eta_{nl-1/2}}} \qquad (2.27)
\end{aligned}$$

These equations echo work presented in Wood *et al.* (2009) which demonstrates the use of applying a similar boundary condition. A linear interpolation is used at the lowermost and uppermost grid box if the flow is away from the boundary. Cubic interpolation is used at all interior grid boxes.

2.5.2 Meridional Direction

Figure 2.11 shows the grid discretisation used in the meridional direction (the same grid is used at the South Pole with the requisite increase in the indices). As in the vertical the velocities are defined on the half levels and m and q on the full levels.

The boundary condition in the meridional direction states that $V = 0$ at both poles. Therefore, when there is no cross-polar flow, all tracer at the most poleward latitude is advected by the zonal scheme around the pole. As in the vertical, the interpolation is reduced to a linear scheme at the boundary, i.e. the most poleward latitude.

The inclusion of a polar cap, similar to that detailed by Hundsdorfer and Spee (1995), was also considered by J. Methven during initial modifications to the advection scheme. This was found to have a detrimental impact on the performance of the scheme and so was not considered further. An extrapolation of the departure point across the pole was also considered but found to create inaccuracies when used with the NIRVANA scheme.

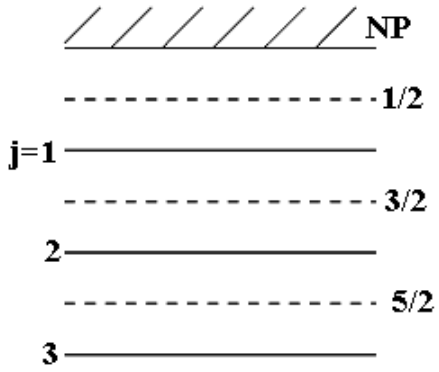

Figure 2.11: *Schematic of the grid in the meridional direction at the North Pole. Velocities are defined on the half levels. m and q are defined on the full levels.*

2.6 Comparison with other Numerical Schemes

There are many global advection schemes that have been published and a sample of these will be discussed now. A summary of the key aspects of these schemes is shown in table 2.1. The following comparison makes it possible to see what properties the NIRVANA scheme has in common with others, as well as demonstrating some aspects of other schemes that it might be advantageous to include in the NIRVANA scheme. The results from some of the experiments using these published schemes will be considered in Chapter 3 in comparison with some results from the model used in this thesis.

2.6.1 Details of Some Semi-Lagrangian Advection Schemes

The first type of numerical scheme to be considered will be the semi-Lagrangian advection schemes such as those by Gravel and Staniforth (1994), Lin and Rood (1997) and Yabe *et al.* (2001). As stated in the Introduction, semi-Lagrangian schemes have many advantages over Eulerian schemes. They have the potential for longer time steps, generally have less dispersion, can handle discontinuities in tracer distributions better and tend to develop fewer overshoots and undershoots. However, semi-Lagrangian schemes suffer from numerical dissipation due to the interpolation used. Some highly accurate and conservative semi-Lagrangian schemes are documented below. These semi-Lagrangian schemes are also fundamentally different to the NIRVANA scheme, making a direct comparison difficult.

Scheme name	Author	SL	Global cons.	Local cons.	CFL	Flux limiter	Mass fixer	Polar av.
NIRVANA	Leonard *et al.* (1995)	✗	✓	✓	✗	✗	✗	✗
SLICE	Zerroukat *et al.* (2002), Zerroukat *et al.* (2004), Zerroukat *et al.* (2005), Zerroukat *et al.* (2009)	✓	✓	✓	✗	✓	✗	✓
LMCSL	Kaas (2008)	✓	✓	✓	✓	✓	✗	✗
CISL	Nair and Machenhauer (2002)	✓	✓	✗	✓	✗	✗	✓
CCS	Nair *et al.* (2002)	✓	✓	✗	✓	✗	✗	✓
extended CCS	Nair (2004)	✓	✓	✗	✗	✗	✗	✓
CIP-CSL	Yabe *et al.* (2001)	✓	✓	✗	✓	✗	✓	N/A
FFSL	Lin and Rood (1996)	✓	✓	✓	✗	✓	✗	✗
GETTM	Li and Chang (1996)	✗	✓	✗	✓	✓	✗	✓
	Walcek (2000)	✗	✓	✗	✓	✓	✗	✗
	Hundsdorfer and Spee (1995)	✗	✗	✗	✗	✓	✗	✓
	Hubbard and Nikiforakis (2003)	✗	✗	✗	✗	✓	✗	✗
Second-order moments	Prather (1986)	✗	✓	✗	✓	✓	✗	✗
	Bott (1989), Bott (1992)	✗	✗	✗	✓	✓	✗	✗

Table 2.1: *Comparison of some aspects of the various numerical schemes mentioned. Along with the scheme name and the author it is stated whether the scheme is semi-Lagrangian (SL), globally and locally conservative, CFL limited, includes a flux limiter or mass fixer, and carries out polar averaging.*

The first scheme to be mentioned, and the second detailed in table 2.1, is the two dimensional mass conservative Semi-Lagrangian Inherently Conserving and Efficient (SLICE) scheme. This scheme was first published by Zerroukat *et al.* (2002), and was later adapted to spherical co-ordinates in Zerroukat *et al.* (2004). The scheme only requires a slight adjustment at each time step to accommodate the polar regions and the stability is independent of the CFL criterion. The SLICE scheme involves a remapping between Eulerian and Lagrangian grids using a cascade interpolation. Cascade interpolation involves dimension splitting and interpolation through the use of a sequence of intermediate grids, for details of cascade interpolation see, for example, Purser and Leslie (1991) and Nair *et al.* (1999).

The initial step in the SLICE scheme carries out the zonal advection on the Eulerian grid. The mass is then transferred from the Eulerian to the Lagrangian control volumes via Eulerian and Lagrangian intermediate control volumes. The advection in the meridional direction is then carried out on the Lagrangian grid. The mass is then transferred back to the corresponding Eulerian control volume for the next time step. The different treatment of the zonal and meridional directions arises due to the use of the cascade interpolation. In order to account for the polar region the polar cap is extended and an adjustment to the density field is carried out for all latitudes within the polar cap whilst maintaining mass conservation. The details of a filter to ensure that the SLICE scheme is monotonic and positive definite was developed by Zerroukat *et al.* (2005). Zerroukat *et al.* (2009) further develop the SLICE scheme to work on an Arakawa C-grid (rather than an Arakawa B-grid).

Kaas (2008) details a locally mass conserving semi-Lagrangian (LMCSL) scheme that is a potential alternative to SLICE. In this LMCSL scheme the mass conservation is obtained by modifying the interpolation weights that act on the upstream departure point. The weights are dependent on the interpolation used and define the remapping of the tracer from the departure points to the Eulerian grid points. Kaas (2008) provides details about how the traditional weights in a semi-Lagrangian scheme are modified in order to locally conserve mass. The main change to the weights is that instead of just considering the change in grid point values, like a traditional scheme, it is the change in the grid box average that is considered.

The new weights act to ensure that the total mass that goes to all the surrounding departure points from a Eulerian grid point is equal to the mass lost at that grid point. In effect

the changes to the weights approximate the effects of divergence and convergence. It is explained that, due to the use of a polynomial in the weighting, a number of Eulerian grid points are used in the remapping to departure points. Therefore, for higher order polynomials the scheme becomes less local and equivalent to what is seen in many finite volume schemes, such as NIRVANA.

The final property discussed by Kaas (2008) is the ability to combine the LMCSL scheme with a semi-implicit scheme (SI-LMCSL) in order to permit longer time steps in a test using the shallow water equations. The SI-LMCSL scheme produces solutions that are smooth and stable for longer time steps (Courant number order of 5-10) than are permitted using the traditional semi-implicit semi-Lagrangian scheme. There is also a reduction in noise in the tracer field in a shallow water model when using the SI-LMCSL scheme rather than a traditional scheme. Despite the differences, the new scheme presented evolves a tracer field in a very similar way to traditional semi-Lagrangian schemes and is not monotonic or positive definite. Kaas (2008) states that ultimately the stability of the LMCSL scheme is dependent on the order of the Taylor expansion used in the calculation of the trajectories. The second value on which the stability depends is the value assigned to the reference geopotential thickness. For both of these terms a number that is too small will result in instability, but for differing reasons (see Kaas (2008)).

Another semi-Lagrangian scheme that is mass conservative is the cell-integrated semi-Lagrangian (CISL) scheme for the sphere detailed by Nair and Machenhauer (2002). This scheme does not require time splitting or have a CFL restriction. The cell-integrated part of the scheme refers to the fact that instead of using a grid point value it is the average value of a grid box that is used, as was also seen in the LMCSL scheme and NIRVANA. This is an inherently mass conservative method and global mass conservation is shown for two dimensional advection on a sphere. Furthermore, the integral form of the continuity equation states that mass is conserved along a trajectory. Nair and Machenhauer (2002) detail the remapping that is required between the Eulerian and Lagrangian grids when using the CISL scheme. The distribution within each Eulerian grid cell is represented by quasi-parabolic functions which, when integrated, give the mass in each Lagrangian grid cell. To work in spherical co-ordinates special consideration has to be made for the poles. In the Lagrangian latitude belt that encompasses a Eulerian pole the first step is to calculate the total mass within that belt. This mass is then distributed throughout the grid cells

within this belt using weights determined using a semi-Lagrangian scheme described by Nair and Machenhauer (2002). As a result, local mass in this latitude belt is not conserved but total mass is.

A conservative cascade scheme (CCS) is detailed by Nair *et al.* (2002). In this scheme a finite volume method is combined with a semi-Lagrangian scheme using a cascade method as in SLICE. This scheme is restricted to cases where the polar meridional Courant number is less than one, but there is no dependence on the Courant number in the zonal direction. As is true for the NIRVANA scheme, the restriction on the meridional Courant number means that the Lagrangian pole is located within, or on, the polar most latitude circle on the Eulerian grid. The reason for the use of the cascade method is that it can be used to replace more computationally expensive multidimensional methods traditionally used and is generally more accurate that dimension splitting.

The basis of the cascade method as described by Nair *et al.* (2002) is that intermediate grid cells are explicitly defined. The grid points of this intermediate grid are defined as the intersection between the Lagrangian latitudes and Eulerian longitudes. These are then used to transfer the cell-averaged density between grids. As with the CISL scheme described above, when near the poles the method is not locally mass conservative but global mass is conserved. When using the cascade method a piecewise parabolic polynomial is constructed that represents sub-cell behaviour of each Eulerian grid cell variable. This method also allows for monotonicity and positive definiteness. There are set steps that make up the cascade process: define the intermediate grid as previously stated, determine the intermediate and computational (Lagrangian) cells, transfer the mass from the Eulerian cell to the intermediate cell, transfer mass from the intermediate cell to the computational cell.

Due to the convergence of the grid on a sphere, and the fact that this is a cell based scheme, the extension of the CCS to the sphere is problematic unless adjustments are made. Nair *et al.* (2002) describe the formation of a polar cap on the Lagrangian grid that encompasses the Eulerian pole. The mass contained within the polar cap on the intermediate grid is the same as that contained in the polar cap on the computational (Lagrangian) grid. To improve accuracy the Lagrangian latitude circle that contains the polar region can be split up into cells.

As noted previously the CCS scheme as described in Nair *et al.* (2002) is restricted by the meridional Courant number near to the pole. Nair (2004) published an extension to the scheme in order to allow large Courant numbers by combining the CCS and CISL schemes to form the extended CCS. The CCS method is used on the majority of the model domain with the CISL scheme being used over the polar regions. The previously defined singular belt used in the CISL scheme is used as the interface between the two methods. In the case of solid body rotation the extended CCS method is equivalent to the CCS method in terms of accuracy.

Yabe *et al.* (2001) detail a cubic-interpolated propagation method (Takewaki *et al.* (1985), Takewaki and Yabe (1987)) for a conservative semi-Lagrangian scheme (CIP-CSL) in one dimension. The mass conservation is obtained by continuously modifying the shape of the interpolation function. The cubic interpolation is used because linear interpolation results in numerical diffusion and a quadratic polynomial in the interpolation results in overshooting. These inaccuracies arise due to fact that the sub-cell behaviour of the solution to the equations is not taken into account. The cubic polynomial can interpolate the tracer profile between two grid points and better resolve the sub-cell behaviour. Yabe *et al.* (2001) show that the CIP method produces little numerical dispersion and is able to capture sharp gradients in tracer profiles.

In order to obtain mass conservation with the cubic interpolation Yabe *et al.* (2001) explain that, as in the NIRVANA scheme, the interpolation must act on the integral of the tracer rather than the tracer itself. This new method will also work for large Courant numbers (up to CFL=5) on the condition that the integral is calculated over the grid cell that contains the departure point. Alternatively, a fourth-order polynomial can be used with the CIP method which produces a less diffuse solution. In the case of time evolution the conservative equation is split into two parts: advection and non-advection. The advection part is the standard advection and obeys the continuity equation. The non-advection part is concerned with just the time evolution of the physical field. The non-advection part is solved using the result of the advection part. The mass conservation is maintained as a sub-cell spatial profile at every time step.

A flux form semi-Lagrangian (FFSL) scheme extended to multiple dimensions is described by Lin and Rood (1996). The scheme can be made monotonic and the additional ability to allow large time steps is also shown. Tests on the scheme demonstrate that it is conservative

and also maintains tracer correlations. In order to remove the error that arises due to the use of operator splitting a term that appears similar to a cross-derivative is introduced into the advection. The additional term includes the result of the meridional advection being carried out on the tracer field that has evolved after the zonal advection. This has the result that a field with an initially uniform mixing ratio remains so. It is possible that the inclusion of such a term in the scheme presented in Section 2.1 might alleviate the dilemma over whether scheme v1 or v2 should be used as it essentially uses a combination of the two schemes. Lin and Rood (1996) detail the scheme development and compare different zonal and meridional operators in order to optimise the scheme. One feature that is detailed is the use of a dual grid (Arakawa C and D-grids) since it is beneficial to have the divergent wind and rotational wind components on the C and D grids respectively.

2.6.2 Details of Some Eulerian Advection Schemes

Some Eulerian schemes will now be considered and have also been listed in table 2.1 in order to compare some of the features with the above semi-Lagrangian schemes and the NIRVANA scheme. Bott (1989) describes a positive definite flux form advection scheme that is mass conservative for all order of polynomials used in the interpolation. Less numerical diffusion is observed if a higher order interpolation can be implemented when using an upstream scheme. The rate of improvement is not constant but decreases with increasing order of interpolation. In order to obtain the numerical solution to the one dimensional advection of a non-diffusive tracer, $\psi(x,t)$:

$$\frac{\partial \psi}{\partial t} = -\frac{\partial (u\psi)}{\partial x}$$

Bott (1989) details the need for weighting factors on the fluxes (especially when using a polynomial higher than second order) when carrying out this advection. The weights act on the tracer field in order ensure that the total flux out of a grid box is positive and that this remains true for any order of interpolation. A flux limiter is also defined and acts on the weighted fluxes in order to produce a completely positive definite scheme. The flux calculations and limiter can be applied to any flux form scheme. However, the integrals defined are dependent on the Courant number being less than, or equal to, one. The results from a rotational and deformational flow test are presented in which the scheme reproduces the analytical solution with a high degree of accuracy. Walcek (2000) states that in long term runs with a deformational flow weak numerical instabilities do form and as a result of

the time splitting undershoots and overshoots develop.

Bott (1992) develops the scheme further by considering a monotonic version derived for one dimension. For this version to work the previously defined positive definite flux limiters are replaced by ones that ensure monotonicity (see Introduction for details on monotonic schemes). As is true for the majority of schemes, Bott (1992) states that the scheme is only truly monotonic in uniform flow fields. In the case of a three dimensional flow small undershoots and overshoots form and the scheme can only be monotonic if the flow in each direction is constant. The size of these anomalies depends on the Courant number and the strength of the deformation in the flow field, but remains of a small amplitude relative to the tracer field. In order to account for the deformation of the tracer field a correction term is added to the fluxes (see Bott (1992) for details).

The use of a high order polynomial resulted in an initially sharp gradient in the tracer field being smoothed at the initial advection step. However, after this initial step the smoother field is advected with high accuracy and is overall better than a low order polynomial. Also, this scheme tends to produce a larger numerical diffusion in many of the tests, but the previously seen undershoots and overshoots have been either reduced or removed. In uniform flows Bott (1992) noted that larger amplitude and phase errors arise with this monotonic version of the Bott (1989) scheme due to more restrictive limiters.

Easter (1993) references the work published by Bott (1989) and modifies his positive definite advection scheme. In particular two different modified versions are described. One is a conservative flux form ($\partial\psi/\partial t = -\nabla.(\underline{\mathbf{v}}\psi)$, where ψ is the tracer per unit volume) and one is a non-conservative advective form ($\partial q/\partial t = -\underline{\mathbf{v}}.\nabla q$, where $q = \psi/\rho$ is the tracer mixing ratio). The advective form is potentially beneficial when using analyses where continuity may not be obeyed due to the use of interpolation in the wind field. The use of a finite volume approach for the advective form means that in the case of a purely rotational flow the flux-form and advective form algorithms are the same. Particular attention is given by Easter (1993) to the dimension splitting used and the fact that in deformational flows the advection in the two horizontal directions separately results in an error due to the exclusion of cross-derivative terms.

It is suggested by Easter (1993) that this dimension splitting error can be avoided if tracer is advected as a mixing ratio, q. The advection of the tracer as a mixing ratio is also used

in the NIRVANA scheme. For rotational and deformational flows the algorithm used is the same for both the flux form and advective form of the scheme. Each grid cell is considered in three parts: two regions are the tracer that will flow into the grid boxes on either side in one time step and the third is the tracer that remains in the grid box. After advection the new tracer value in the grid box is calculated as a sum of these parts. Following McRae *et al.* (1982) the order in which the advection in the horizontal (zonal and meridional directions) is carried out is alternated at each time step. This alternation was used with schemes v1 and v2 but was found to reduce the accuracy of the scheme and as such was not used further.

Li and Chang (1996) take the work of Bott (1989) and Easter (1993) one step further by applying it to spherical co-ordinates and onto a non-uniform grid. This non-uniformity occurs in part due to the convergence of longitudes at the poles. In order to account for this the number of grid cells in the polar regions is reduced by averaging together existing grid cells to create larger ones, as in Prather (1986) and Section 2.4, to create an extended polar zone (EPZ). The fluxes in the zonal and meridional directions are calculated as the total mass transfer amounts during a time step through each boundary/face of a grid cell. This definition accounts for the variation in spacing in the latitudinal direction. It also maintains the equality that the flux out of a grid cell will equal the flux into the downstream grid cell in order to obtain mass conservation within the scheme. The scheme contains two constraints, the first of these being a limiter in order to ensure a positive definite scheme and the second being that the Courant number is ≤ 1.

In the tests presented by Li and Chang (1996) it is shown that the method used to redistribute the mass within the polar grid cells plays a role in the conservation of the numerical scheme. If the mass within each polar grid cell is simply set so that the mass is equal to the mass in the equivalent EPZ cell (i.e. $M_j = M_i^{EPZ}$) then tracer mass is conserved. If a linear or higher-order mass redistribution process is used then tracer mass is not conserved. It was also found that tracer conservation was easier to obtain if the redistribution was carried out using the tracer mass rather than the tracer mixing ratio (which is the method used in Section 2.4).

Walcek (2000) investigates the development of a monotonic advection scheme that acts on a tracer as a mixing ratio. This scheme is mass conservative, upstream, positive definite (but can advect negative values) and uses monotonic limiters. The method used here to

make the scheme monotonic involves adjusting the fluxes at the two cell edges around an extremum. This has the effect of aggregating mass at the extrema in order to counter the numerical diffusion. The order in which the grid cells are updated during the advection is dependent on the direction of flow. Ideally the advection begins in a grid cell where there is only outflow and updates the masses with the direction of flow. In the case of analyses, for example, there will need to be two sweeps around a line of grid cells. The first sweep updating tracer values in the positive direction and the second updating the tracer values in the negative direction.

The multi-dimensional version of the scheme presented by Walcek (2000) uses the density field at the start of the time step in all flux calculations. However, the mixing ratio is calculated using the updated density field in order to smooth out any perturbations that may occur due to the dimension splitting. This is the same method used in scheme v2 presented in Section 2.1.2. The process of using sweeps along a line of grid cells during advection could have potential benefits when used with the NIRVANA scheme, especially when advection is by analyses. At present the direction of the wind is determined at each grid point prior to the calculation of the advection at that point, and so requires frequently alternating the direction of the advection. The method of advection by Walcek (2000) is potentially more efficient as, once the grid points with positive and negative wind values are determined, it does not require this alternation. However, without applying this method it is difficult to estimate how much of an impact it will have with regards to mass conservation.

Hundsdorfer and Spee (1995) present a finite volume type scheme for horizontal advection on a sphere. The scheme described is shape preserving and positive definite. The advection scheme is derived in detail beginning with advection on a plane before considering the adjustments that are required for a sphere. For the meridional advection the tracer fluxes are calculated using the updated tracer field from the zonal advection, as in scheme v1. As detailed in Section 2.5, at the pole a no flux condition is applied so that all flow is around the pole, a common feature of Eulerian schemes. For a grid box that is downstream of the pole such that the flux calculation requires points on the other side of the pole then extrapolation is used rather than interpolation across the pole. This method was also mentioned in Section 2.5 and was found to degrade the accuracy of the NIRVANA scheme.

When there is advection over the pole a strong deformation to the tracer distribution is observed which is significantly improved with the inclusion of the polar cap. The polar cap

is described as being a grid cell with a uniform tracer distribution that also allows a larger time step due to reducing the Courant number. The negative side of using polar caps is that they introduce diffusion and therefore it is recommended that the polar caps be kept as small as possible. As was previously mentioned in Section 2.5, the inclusion of a polar cap was found to be detrimental to the accuracy of the NIRVANA scheme. Also, in essence, the polar cap had the same effect on the results as the reduced grid in Section 2.4.

Further improvement was found by Hundsdorfer and Spee (1995) if after each time step a process called polar mixing is carried out. Polar mixing involves mixing the tracer values in the grid cells that are adjacent to each other across the pole. This process almost completely removes the diffusion that arises due to the advection over the pole using a polar cap. The polar mixing also further reduces the distortion caused from advection over the pole. An alternative method to the mixing is the implementation of a deformation correction which corrects for the dimension splitting. However, it is stated that this method does not exactly conserves mass.

Similarly, Hubbard and Nikiforakis (2003) detail a three dimensional flux-based finite volume scheme that uses the weighted average flux (WAF) method and an adaptive mesh refinement (AMR) algorithm. Since this is a finite volume scheme, due to the use of the conservation law in integral form and calculating flux integrals over grid boxes, it is inherently mass conservative. The operator splitting that is applied is not a full splitting since the velocity divergence term in each direction is always calculated using the tracer distribution at the start of the time step. In order to demonstrate this clearly the advection equations provided by Hubbard and Nikiforakis (2003) are shown below.

$$\begin{aligned}
q^{*}_{ijk} &= q^{n}_{ijk} - \frac{\Delta t}{V_{ijk}}\Big[\left(Aq^{n}u^{n+1/2}\right)_{i+1/2,j,k} - \left(Aq^{n}u^{n+1/2}\right)_{i-1/2,j,k} \\
&\quad + q^{n}_{ijk}\left(Au^{n+1/2}\right)_{i+1/2,j,k} - q^{n}_{ijk}\left(Au^{n+1/2}\right)_{i-1/2,j,k}\Big] \\
q^{**}_{ijk} &= q^{*}_{ijk} - \frac{\Delta t}{V_{ijk}}\Big[\left(Aq^{*}v^{n+1/2}\right)_{i,j+1/2,k} - \left(Aq^{*}v^{n+1/2}\right)_{i,j-1/2,k} \\
&\quad + q^{n}_{ijk}\left(Av^{n+1/2}\right)_{i,j+1/2,k} - q^{n}_{ijk}\left(Av^{n+1/2}\right)_{i,j-1/2,k}\Big] \\
q^{***}_{ijk} &= q^{**}_{ijk} - \frac{\Delta t}{V_{ijk}}\Big[\left(Aq^{**}w^{n+1/2}\right)_{i,j,k+1/2} - \left(Aq^{**}w^{n+1/2}\right)_{i,j,k-1/2} \\
&\quad + q^{n}_{ijk}\left(Aw^{n+1/2}\right)_{i,j,k+1/2} - q^{n}_{ijk}\left(Aw^{n+1/2}\right)_{i,j,k-1/2}\Big]
\end{aligned}$$

where q is the tracer mixing ratio, V is the volume of the grid box and A is the area of

the grid cell face. The use of q^n in each direction is what is of note. The reason given for this formulation is that it maintains the conservative nature of the scheme and takes into account both the tracer flux and divergence. In particular, this method accounts for the development of convergence or divergence in one dimension which can then be compensated for in the other dimensions. If the dimension splitting is not carried out in this way then this may not be true. It is the use of this method that also necessitates solving the advection equation ($q_t + \underline{\mathbf{u}}.\nabla q = 0$) rather than the continuity equation in flux form (equation 1.2).

In essence this method uses a combination of schemes v1 (use of q^* in meridional fluxes and q^{**} in vertical fluxes) and v2 (use of q^n in meridional and vertical fluxes), as was also seen in the semi-Lagrangian scheme of Lin and Rood (1996). This suggests that there may be potential benefits in using this combination of the schemes. The WAF method refers to the flux calculation method used and incorporates a flux limiter that in essence tunes the local value of the numerical diffusion (see Hubbard and Nikiforakis (2003) for details).

In order to accommodate the convergence of the model grid at the poles Hubbard and Nikiforakis (2003) use a cell-centre flux-based approach. In order to accommodate flow near the pole a dummy cell is placed at the pole that contains the value from the cell directly opposite the cell of interest and acts as a boundary to the grid. No value is actually stored at the pole. This is a slightly different method than that currently used with the NIRVANA scheme and described in Section 2.5. However, as was stated previously, tests using an extrapolation across the pole proved to create additional deviations from mass conservation and shape preservation and this method is liable to result in the same.

Hubbard and Nikiforakis (2003) go into some detail on the AMR method with additional details on how it needs to be modified to apply to a sphere. In essence a hierarchical system of grids that are embedded within each other are used. This allows the use of a higher resolution grid around features that require it, such as sharp gradients or filaments in tracer fields. In order for the scheme to function accurately the time step used on the higher resolution grids also has to be scaled accordingly. By having the grids embedded there is a smoother transition from the coarser to the more refined grid. Using multiple advection steps (by decreasing the time step) in the zonal direction during operator splitting and increasing the number of advection steps as the pole is approached allows for increased efficiency and accuracy. Multiple advection steps can be used as a replacement for increasing the size (reducing the number) of grid cells. However, caution must be used as it is shown

that if too many advection steps are used then the error that is introduced by using this method will begin to dominate. If a point source was being considered, or there was a keen interest in filamentation, for example then this method could prove to be beneficial.

The time splitting used in a numerical scheme has a significant impact on its accuracy and conservation. One example of a recent in depth look at the effects of time splitting is Bott (2010). In many cases the error is seen to arise due to the fact that transport into neighbouring grid cells on the diagonal is not carried out. As in Easter (1993), Bott (2010) alternates the order of the advection at every time step, which was noted earlier as having a detrimental effect on the accuracy of schemes v1 and v2. Flux limiters are also applied to ensure a positive definite and shape preserving scheme.

The modification to the time splitting suggested by Bott (2010) involves the inclusion of a deformational correction term. In terms of equations (which are very similar to equations (2.5)-(2.7) for the NIRVANA scheme):

$$\begin{aligned} \psi^{*} &= \psi^{n} - F(\psi^{n}, u) \\ \psi^{**} &= \psi^{*} - F(\psi^{*}, v) \\ \psi^{n+1} &= \psi^{**} - F(\psi^{**}, w) \end{aligned}$$

becomes

$$\begin{aligned} \psi^{*} &= \psi^{n} - \left(F(\psi^{n}, u) - \psi^{n} \frac{\partial u}{\partial x} \Delta t \right) \\ \psi^{**} &= \psi^{*} - \left(F(\psi^{*}, v) - \psi^{n} \frac{\partial v}{\partial y} \Delta t \right) \\ \psi^{n+1} &= \psi^{**} - \left(F(\psi^{**}, w) - \psi^{n} \frac{\partial w}{\partial z} \Delta t \right) - \psi^{n} \nabla . \mathbf{v} \Delta t \end{aligned}$$

where ψ is the tracer and F is the net flux. In essence the deformation correction is added in the first two directions and then subtracted off at the end. The resulting scheme produces a low level of numerical diffusion, but develops undershoots and overshoots in regions of strong gradients in the tracer field. The concept of a deformation correction term being included during advection has been noted several times in the papers presented here. The NIRVANA scheme does not use a correction or cross-derivative term, but this literature suggests that it may be of benefit to the scheme. This method would also more accurately account for flow on the diagonal than is currently possible.

In order to make the scheme positive definite Bott (2010) applies a flux limiter that must act on the deformation correction terms as well as on the fluxes. The second limiter placed

on the scheme to produce shape preservation suppresses overshoots and undershoots to a high degree. However, some undershoots do still occur and therefore the scheme is not strictly monotonic. In order to avoid the production of large Courant numbers, whenever the maximum Courant number in a grid column exceeds one the time step is reduced in that column to $\Delta t/(n+1)$ where n is the integer part of the Courant number. Bott (2010) noted that this did not affect the mass conservation or positive definite property of the scheme.

Details on various other schemes have been published, such as the method of Prather (1986) which considers the conservation of second-order moments. In particular the method conserves the second-order moments of tracer spatial distributions. This method is used in CTMs such as SLIMCAT/TOMCAT (Chipperfield, 2006) and one used by Hsu *et al.* (2005) in the investigation of stratosphere-troposphere fluxes of ozone. Prather (1986) lists five advantageous features of this advection scheme: conservation of tracer, positive definite, stable for large time steps up to the limit of the Courant number $\leq$1, accurate for a non-divergent flow and resolves and advects tracer features on the order of the grid size. In this method each grid box is considered a separate entity and discontinuities across the boundaries between grid boxes are expected. Within each individual grid box the tracer concentration is represented by a second-order polynomial and the fluid density is considered uniform.

The basic method described by Prather (1986) involves splitting the grid box into two or more smaller ones, with each sub-grid box corresponding to a fraction of the grid box that is either advected to an adjacent grid box or remains in the original, similar to the method of Easter (1993). The second order polynomial describing the tracer used in the original grid box is maintained in the sub-grid boxes. Each sub-grid box now has new local moments that depend on its centre of mass and after the advection a new polynomial of the tracer distribution is determined from the moments of the sub-grid cells. This method conserves the zeroth-order moment (total tracer abundance), the first-order moment (mean slope of tracer distribution) in each dimension and the second-order moments (curvature in the tracer distribution). The scheme is made positive definite by placing limits on the zeroth moment (total amount of tracer) creating slight numerical diffusion.

2.7 Summary

This chapter outlined the advection scheme that is used throughout this thesis. The global advection model is a finite volume scheme based on the NIRVANA scheme of Leonard *et al.* (1995) and is inherently mass conservative. One alteration made to the scheme involved an adjustment to the grid in the polar regions by decreasing the number of grid points and therefore increasing the grid spacing (following Prather *et al.* (1987)). This significantly reduced the distortions to the tracer distribution when advected over the polar regions, thereby maintaining as high a degree of shape preservation as possible. Boundary conditions in the vertical were also altered to ensure zero vertical velocity at the boundaries and that the calculated departure points remained within the range $0 < \eta < 1$ (following Wood *et al.* (2009)).

Finally, in the mass continuity equation the fluxes use the mass from the start of each time step otherwise the dimension splitting results in an error for a deformation flow. In three simple case studies of divergent flow, deformation flow and rotation (with a uniform initial mass field) the mass advection scheme produces the exact solution. The tracer advection schemes v1 and v2 differ only by whether the updated tracer mixing ratio is used in the tracer fluxes or not. Scheme v1, using the updated tracer field, follows the tracer flux method of Gregory and West (2002). A third version of the scheme was also introduced that follows the same method as scheme v2 but does not include the assumption that mass can be taken outside of the integral used in the tracer flux calculations (2.12). For a steady flow and uniform tracer field the tracer advection scheme also shows mass conservation and produces the exact solution, independent of whether scheme v1 or v2 is used. As a consequence both schemes will be considered in the next stage of this thesis. The mass conservation in particular is studied further in the next chapter.

Chapter 3

Global Mass Conservation

The Introduction discussed the two properties of tracer transport that are important: shape preservation (no spurious maxima and minima) and global mass conservation. Global mass conservation is particularly important since a numerical model will potentially be used to study small changes in tracer concentrations over a long period of time (e.g. climatological timescales). Therefore, any mass changes that occur as a result of the numerics need to be accounted for. The previous chapter showed that both the mass and tracer advection schemes are conservative in idealised simple cases. The mass conservation of the numerical scheme is considered further in this chapter with experiments that carry out advection using both a prescribed wind field and analyses.

3.1 Solid Body Rotation Tests

In the initial set of experiments prescribed winds are used to carry out solid body rotation at a horizontal resolution of T159 ($\Delta\lambda$=$\Delta\phi$ $\approx$1.125 degrees). Solid body rotation is the simplest test case that can be used on a sphere and has many advantages when considering conservation within a numerical scheme. The primary advantage is that the exact solution is known; after one complete rotation of the sphere the final distribution should look identical to the initial distribution. This experiment is analogous to having a spot on a ball and then rotating the ball; the spot is invariant but moves relative to a grid that does not rotate. Since the advection on the sphere is steady and non-divergent, and there are no sources or sinks, the model should be mass conservative.

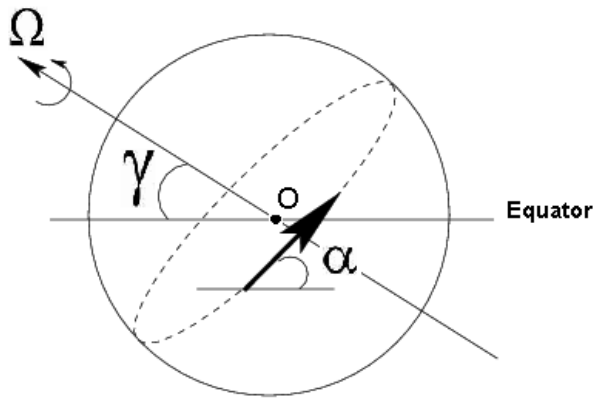

Figure 3.1: *Schematic of solid body rotation showing the relevant angles involved, where γ is the angle between the equatorial plane and the rotation vector and $\alpha = \frac{\pi}{2} - \gamma$.*

The equations for solid body rotation (e.g. Williamson *et al.* (1992)) are:

$$u = U_0[cos(\alpha) + tan(\phi_j)cos(\lambda_i)sin(\alpha)] \tag{3.1}$$

$$v = -U_0 sin(\lambda_i)sin(\alpha) \tag{3.2}$$

$$\dot{\eta} = 0 \tag{3.3}$$

where

$$U_0 = \frac{2\pi a}{\tau} \tag{3.4}$$

where λ_i is the longitude and ϕ_j is the latitude. The angular velocity is specified by U_0, where a is the radius of the Earth and τ is the period. In these experiments the rotation rate is set so that one complete revolution is completed in τ=2.5 days. The angle of advection to the equator is represented by α, which is shown schematically in figure 3.1. In this figure it can be seen that γ is the angle between the equatorial plane and the rotation vector and $\alpha = \frac{\pi}{2} - \gamma$. The atmospheric mass, m_{ijl}, is set to a constant value of 1 in all of the solid body rotation experiments and is set at the start of every time step.

One quantity that will be mentioned throughout the solid body rotation experiments is the Courant number which was originally presented in the Introduction (Section 1.2). The Courant number is defined as C=u$\Delta t/\Delta x$, and in order to ensure stability within a numerical scheme this number is often required to be $\leq$1. Using the notation for this numerical scheme the Courant number is defined in the zonal and meridional directions as $C_\lambda = \dot{\lambda}\Delta t/\Delta\lambda$ and $C_\mu = \dot{\mu}\Delta t/\Delta\mu$ respectively.

The NIRVANA scheme is designed to be stable for any Courant number (for a uniform velocity), but it becomes increasingly inaccurate as the Courant number increases above 1. For this reason, it is advantageous to run the model with as small a Courant number as possible given the experiment. For example, if a model is concerned with climatological timescales a small time step is not reasonable. It should also be noted that there are a range of Courant numbers across the globe due to the varying grid spacing in all directions, the time step being governed by the largest value.

3.1.1 Uniform Tracer Distribution

The first set of solid body rotation experiments used a uniform tracer distribution where the tracer mixing ratio was set to a value of 1 at all model grid points. Since the tracer distribution is uniform, any distortion to the tracer field must be a numerical error. The experiment was carried out using both versions of the tracer advection scheme: v1 using the updated tracer field in the tracer flux calculations, and v2 using the tracer field at the start of each time step in the tracer flux calculations (equation 2.14).

Both versions of the tracer advection scheme resulted in a mass conservative model where the mass conservation observed is independent of the angle of rotation. In the case of scheme v2, oscillations in the tracer field develop downwind of both poles as in figure 3.2 which shows the oscillations downwind of the North Pole. This figure is for the specific case of α=70, and a time step of 332 seconds (maximum C=3.74 and 0.49 in the zonal and meridional directions respectively). As mentioned in the Introduction (Section 1.3.2), Gregory and West (2002) also noted the formation of unphysical oscillations in the tracer field when studying the stratospheric tape recorder. If a small enough time step, with maximum C<2.53 and 0.33 in the zonal and meridional directions respectively, is used then these oscillations do not develop.

When fringes do form then the cubic interpolation in the meridional direction amplifies them and the model run becomes unstable. If the meridional interpolation is reduced to linear then no amplification of the oscillations occurs. The reduction of the zonal interpolation to linear has no additional impact on the stability and as such the quintic interpolation is retained. Due to the additional stability using a linear meridional interpolation, and the practical considerations of a small time step, this reduced interpolation will be used in the

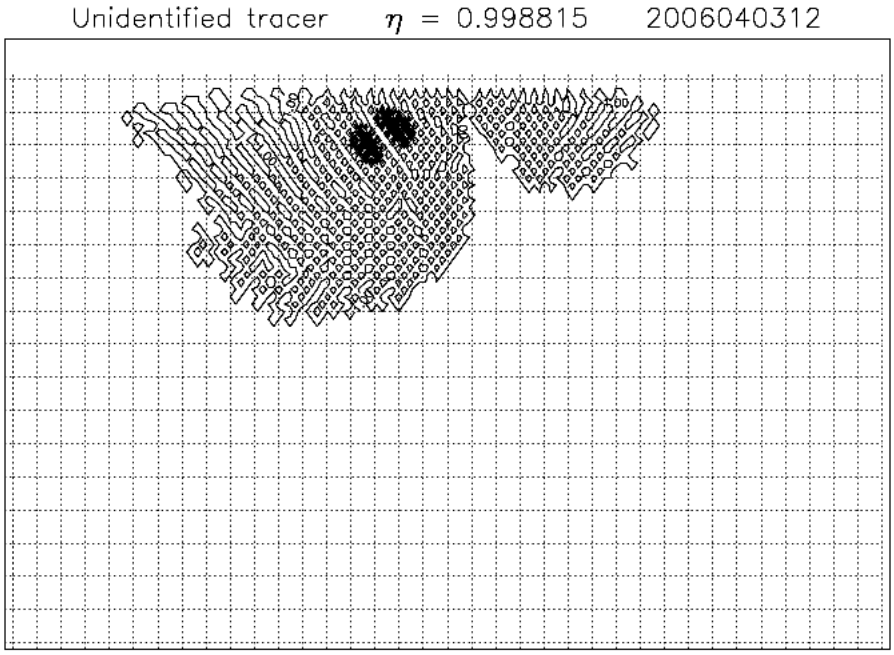

Figure 3.2: *Example of the development of oscillations downwind of the North Pole in an initially uniform tracer distribution after 2.5 days. Advection was carried out using scheme v2 with a time step of 332 seconds and at an angle of α=70. The use of a linear meridional interpolation prevents theses oscillations from amplifying and resulting in instability in the model. Region shown is for 0:180E and 0:90N.*

rest of the model runs when using scheme v2. Scheme v1 is stable for any Courant number, even with a nonlinear interpolation in the meridional direction.

3.1.2 Cosine Bell Distribution

The second set of solid body rotation experiments used a structured tracer distribution in the form of a cosine bell. The cosine bell distribution is described by the following equations:

$$q = \frac{1}{2}\left(1 + cos\frac{\pi r}{R}\right) \text{ for} r \leq R \tag{3.5}$$

$$r = acos^{-1}(sin\phi_0 sin\phi_j + cos\phi_0 cos\phi_j cos(\lambda_i - \lambda_0)) \tag{3.6}$$

where a is the radius of the earth, R is the radius at which $q = 0$ and is set at 3000km. The cosine bell is centred at (λ_0, ϕ_0) which is set to (0N,90W) and has an initial maximum amplitude of 1. A time step of 216 seconds is used, resulting in a maximum Courant number of 2.43 and 0.32 in the zonal and meridional directions respectively. The inclusion of the reduced grid resulted in a significant decrease in the distortion of the cosine bell when advected over the pole as was shown in the previous chapter (figures 2.7 and 2.8).

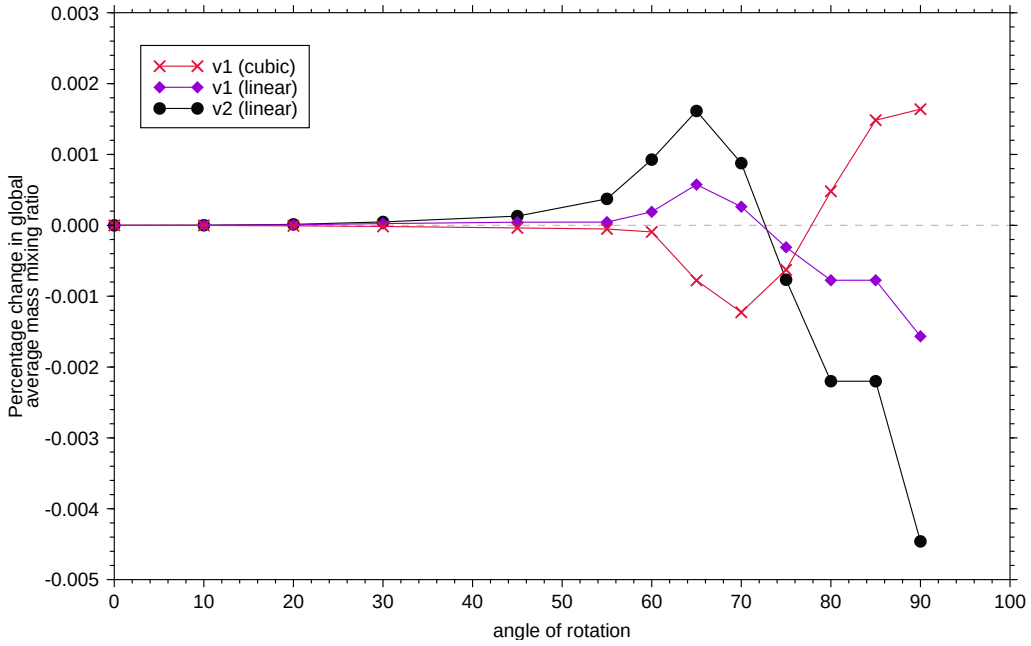

Figure 3.3: *Variation in the percentage change of global average mass mixing ratio with angle of advection to the equator, α, over one rotation. The legend identifies the scheme used and whether a cubic or linear meridional interpolation was implemented. Tracer initialised as a cosine bell of radius 3000km and advected using a time step of 216 seconds (100 steps in a 6 hour period). Maximum Courant number is 2.43 and 0.32 in the zonal and meridional directions respectively (using the reduced grid).*

Figure 3.3 shows the percentage change in global average mass mixing ratio for the cosine bell advected by solid body rotation for one complete revolution (2.5 days). The global average mass mixing ratio is calculated by using $\sum m_{ijl} q_{ijl} \Delta\lambda\Delta\mu\Delta\eta / \sum m_{ijl} \Delta\lambda\Delta\mu\Delta\eta$. Once again the results are presented for both versions of the scheme; v1 in red (cubic meridional interpolation) and purple (linear meridional interpolation), and v2 in black (linear meridional interpolation). This figure shows clearly that the mass conservation is dependent on the angle of advection, α, for all versions of the tracer advection scheme. For a purely zonal advection, $\alpha = 0$, all versions of the scheme are exactly mass conservative and no distortions are observed in the cosine bell distribution. The figure also shows that for angles α <45 degrees the level of mass conservation for all schemes over one rotation is very high.

A deviation from mass conservation is observed for scheme v2 first and at an angle of $\alpha = 65$ degrees the greatest mass gain is achieved. In comparison scheme v1 with cubic meridional interpolation initially shows a mass loss for angles greater than 60 degrees and reaches its maximum loss at $\alpha = 70$ degrees. The deviation from mass conservation for v1 can be explained by considering the fact that the cosine bell has a starting radius of 3000km, corresponding to a distance of 27 degrees on the surface of the sphere. Therefore,

this increased loss rate corresponds to when the cosine bell begins to be advected over the pole. In the case of scheme v2 this explanation still has some validity when it is taken into account that the linear interpolation causes the cosine bell to spread and become wider (as will be shown later). Therefore, advection over the pole occurs at smaller angles of rotation.

At approximately $\alpha = 72$ degrees the mass change becomes negative when using scheme v2, with the mass loss increasing and reaching a maximum of -0.0045% over one complete revolution at $\alpha = 90$. This is considerably larger than the maximum mass loss observed when using scheme v1 with cubic meridional interpolation (-0.0012%). It is also contrary to scheme v1 with cubic meridional interpolation which produces a mass gain for angles larger than $\alpha = 78$, where the largest mass gain of 0.0016% over one complete revolution is again observed for $\alpha = 90$. This is approximately the same mass gain that was observed for scheme v2 at $\alpha = 65$.

The majority of the differences between the two schemes mentioned above arise due to the different meridional interpolation. This is highlighted by the mass changes observed when using scheme v1 with a linear meridional interpolation (purple line in figure 3.3). Comparing this line to that for scheme v2 shows that the distributions of mass changes against angle of rotation are comparable. It can therefore be seen that the meridional interpolation plays a significant role in determining the sign of the mass change observed at a given angle of rotation. Overall scheme v2 produces a greater degree of mass non-conservation than scheme v1, irrespective of which meridional interpolation scheme v1 uses. The change in mass is cumulative for both versions of the tracer advection scheme. Therefore, the mass change observed after one rotation can be scaled by number of rotations to calculate the mass change that would be observed over a longer period.

The results have not been presented here, but the numerical mass change was found to scale linearly with Courant number and as such the mass change presented in figure 3.3 can be stated as a function of the Courant number. Using the maximum Courant number on the model grid, which in these experiments is C=2.43 in the zonal direction, the mass change observed over one rotation is in the range $-1.9 \times 10^{-3}\text{C\%} < x < 6.6 \times 10^{-4}\text{C\%}$ for scheme v2 with a linear meridional interpolation. Scheme v1 produces a numerical mass change in the range $-4.1 \times 10^{-4}\text{C\%} < x < 6.6 \times 10^{-4}\text{C\%}$ for a cubic meridional interpolation and $-6.2 \times 10^{-4}\text{C\%} < x < 2.5 \times 10^{-4}\text{C\%}$ for a linear meridional interpolation. The maximum Courant number is the same as for scheme v2 due to the use of the same model grid, rotation

rate and time step. Due to this scaling it can be seen that even with a maximum Courant number less than one mass non-conservation still occurs. Since a purely zonal flow results in mass conservation for all schemes, the source of non-conservation is the dimension splitting and the fact that the non-divergence of the analytical winds is not precisely obtained in the numerical solution. It is not possible to test this theory for a purely meridional flow as it does not exist due to the convergence of the grid and the condition of $V = 0$ at the poles which results in a zonal flow near the poles.

Due to the use of solid body rotation the initial cosine bell distribution should be maintained throughout the advection. However, in Section 2.4 the cosine bell was seen to develop distortions as it was advected, especially if advection is over the polar region. Using another advantage of solid body rotation, namely that after a complete rotation the tracer distribution returns to its initial position, this distortion can be considered in more detail at all angles. Figures 3.4 and 3.5 show the cosine bell at the end of one complete rotation minus the initial distribution for three angles; $\alpha = 10$, 45 and 90 degrees. In all cases the distortions observed in the cosine bell distribution are aligned with the angle of advection. It must also be noted that the schemes produce widespread weak oscillations that are not shown in the figures.

In figure 3.4 the images on the left use scheme v1 with a cubic interpolation in the meridional direction and the images on the right use scheme v1 with a linear meridional interpolation. The first point to note is that the magnitude of the distortions to the cosine bell are smaller when using a cubic interpolation in the meridional direction and so should be used when possible. When using scheme v1 with a cubic meridional interpolation and smaller values of α the tracer mass is seen to move from the very edge of the cosine bell inwards. Values at the centre of the cosine bell are also seen to decrease (i.e. dampen the peak of the distribution). At larger values of α, for example α=90 degrees as in figure 3.4(e), tracer is removed from the 'front' of the cosine bell and gained at the 'back', reflecting the distortion that is seen to occur with advection over the pole (figure 2.8).

Figure 3.4 immediately highlights the effect of the reduction in the order of interpolation in the meridional direction, with the linear interpolation creating an increased spread in the meridional direction. In particular, at smaller values of α (e.g. $\alpha = 10$ and 45 degrees) the mass is shifted to the sides of the cosine bell that are travelling in parallel to the angle of rotation. In contrast, at larger angles, for example $\alpha = 90$ degrees, the cosine

bell is stretched in the meridional direction with a mass gain at the 'front' and 'back' of the cosine bell. The damping in the cosine bell peak is also enhanced when using a linear interpolation in the meridional direction. Lastly, the mass loss observed at the edge of the cosine bell when using the cubic interpolation in the meridional direction is not observed with the linear interpolation in the meridional direction. Schemes v1 and v2, both with a linear meridional interpolation, are compared in figure 3.5. Without the difference in interpolation in the meridional direction there is a large degree of similarity between the results from the two schemes.

By considering the mass conservation after each time step, rather than after every 6 hours, the deviation from mass conservation is seen to start after the first time step (not shown). One proposed reason for this lack of mass conservation was the presence of a discontinuity in the tracer gradient when using a cosine bell, since this often proves problematic for tracer advection schemes. For this reason the same solid body rotation experiment was repeated using a Gaussian curve. In these experiments the same mass change was seen to occur, therefore demonstrating that the discontinuity in gradient when using the cosine bell is not the reason for the observed mass change. The use of a linear interpolation in the zonal direction was tested and found to have no impact on the degree of non-conservation observed when advecting the cosine bell. Unlike in the meridional direction, the higher order interpolation in the zonal direction is found to not affect the stability of scheme v2.

Experiments without the reduced grid at the poles using schemes v1 and v2 were also carried out in order to investigate the effect of the grid reduction. In the case of scheme v1 (with a cubic meridional interpolation) the grid reduction results in an increased mass change. For example, when α=90 is used with a time step of 288 seconds the reduced grid produces a mass change 6 times the magnitude of that for the full grid. However, the reduction in the distortion to the tracer distribution when advected over the pole, and the permitted increase in time step, is significant enough for the reduced grid to be used. If the interpolation in the meridional direction is linear then scheme v1 with the reduced grid produces a higher degree of mass conservation than the full grid. When using scheme v2 (with a linear meridional interpolation) then, once again, the reduced grid shows a higher level of mass conservation than the full grid. For example, when α=90 is used with a time step of 288 seconds the reduced grid resulted in a mass change that was 0.38 times that observed with the full grid at the poles.

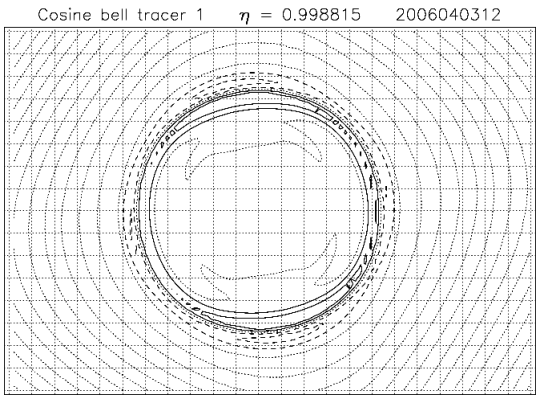

(a) α=10 (contour interval=0.001)

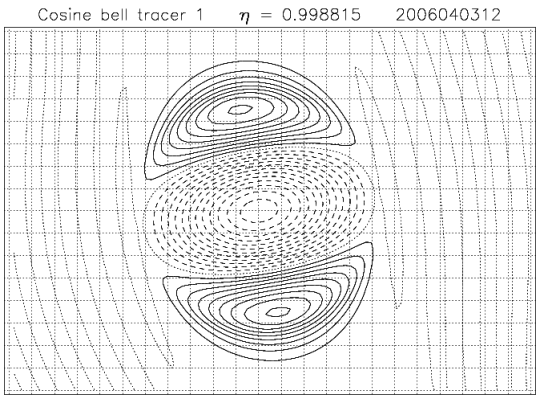

(b) α=10 (contour interval=0.01)

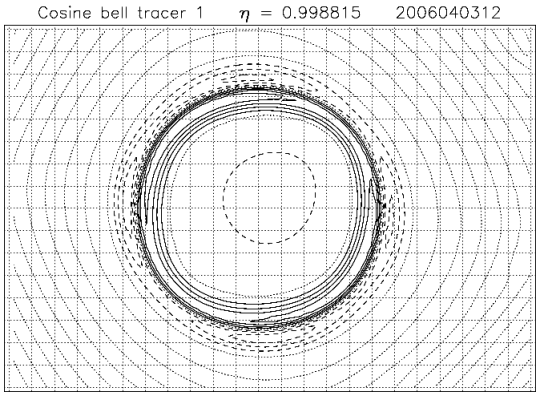

(c) α=45 (contour interval=0.001)

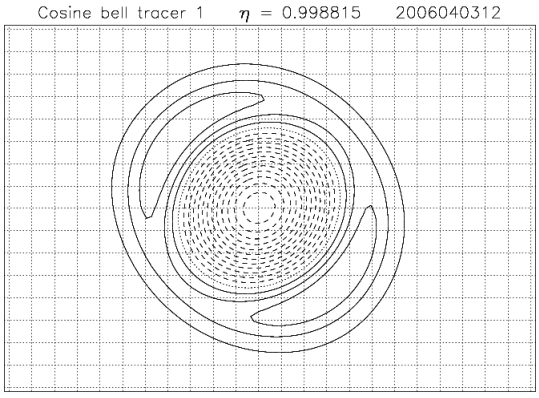

(d) α=45 (contour interval=0.03)

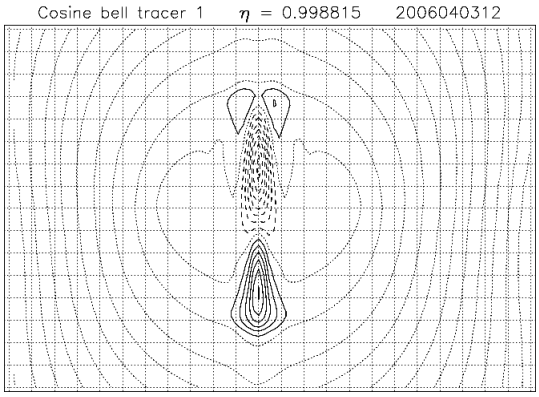

(e) α=90 (contour interval=0.01)

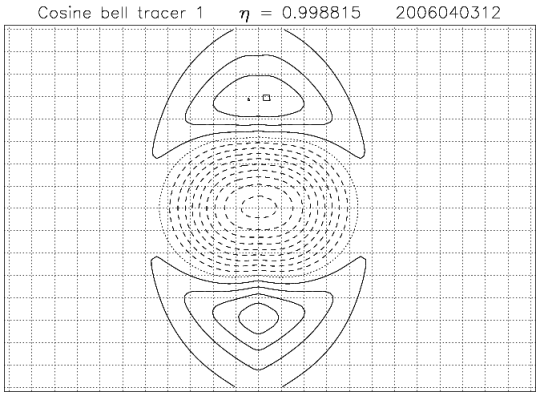

(f) α=90 (contour interval=0.05)

Figure 3.4: *Difference in the cosine bell after one complete rotation for the three cases of α=10, 45 and 90 degrees (with the corresponding flow angled towards the top right-hand corner for the first two cases and the top for the last case). Images (a), (c) and (e) use scheme v1 with a cubic meridional interpolation, whilst images (b), (d) and (f) use scheme v1 with a linear meridional interpolation. The dotted line is the zero contour, negative and positive differences are shown by the dashed and solid lines respectively.*

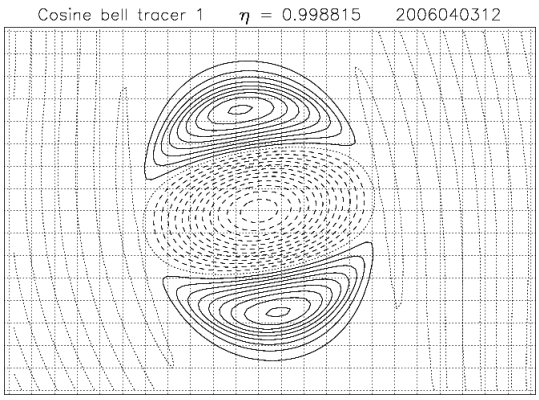

(a) α=10 (contour interval=0.01)

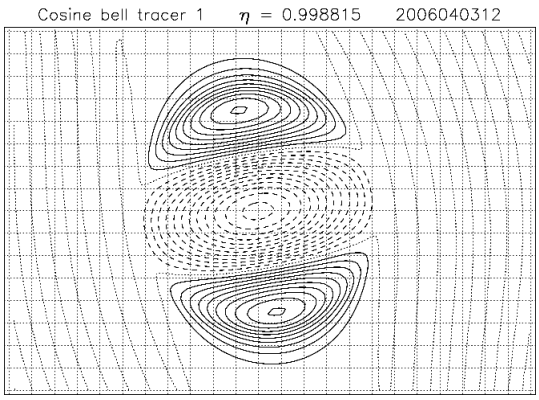

(b) α=10 (contour interval=0.01)

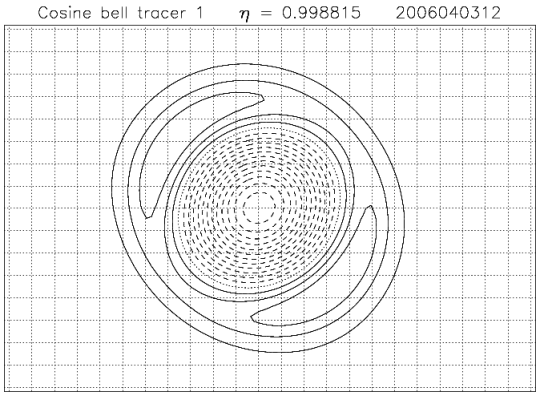

(c) α=45 (contour interval=0.03)

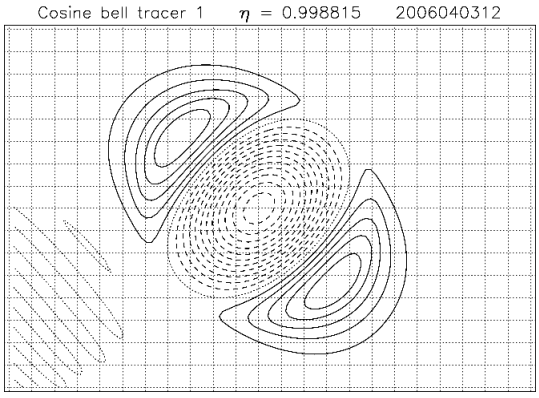

(d) α=45 (contour interval=0.03)

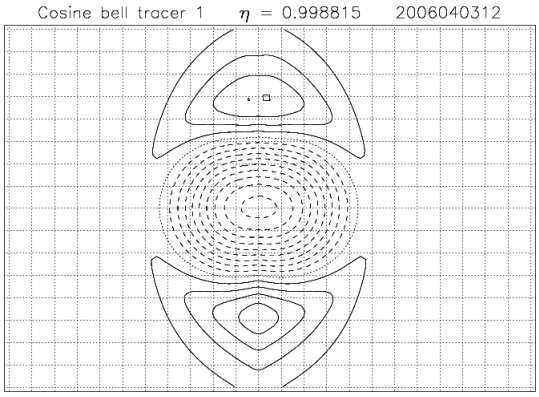

(e) α=90 (contour interval=0.05)

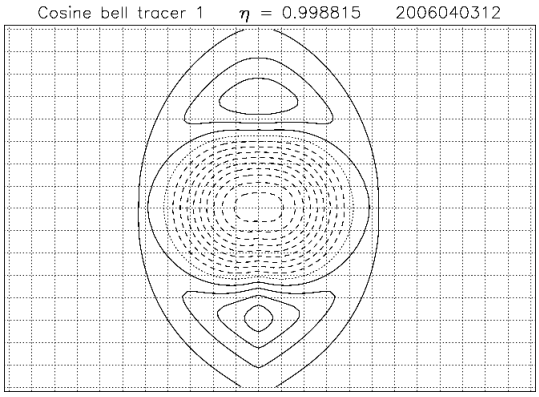

(f) α=90 (contour interval=0.05)

Figure 3.5: *Difference in the cosine bell after one complete rotation for the three cases of α=10, 45 and 90 degrees (with the corresponding flow angled towards the top right-hand corner for the first two cases and the top for the last case). Images (a), (c) and (e) use scheme v1, whilst images (b), (d) and (f) use scheme v2. Both schemes use a linear meridional interpolation. The dotted line is the zero contour, negative and positive differences are shown by the dashed and solid lines respectively.*

One final tracer advection scheme that was implemented involved making an alteration to equation (2.11). As the equation is written the updated mass field, m^+_{ijl} is used to calculate the tracer mass mixing ratio at the end of the time step, q^+_{ijl}. The alternative method implemented used the mass field that would be used at the start of the next time step, $m_{ijl}(t + \Delta t)$ to calculate q^+_{ijl}, in order to create a consistency in the model mass field between two consecutive time steps. This can be implemented due to the fact that the model does not carry an evolving mass field between time steps and as such this method effectively resets the mass field (to the prescribed distribution) before the end of the time step rather than between successive time steps. When implemented this method was found to produce mass conservation at all angles of rotation. However, the scheme was subjected to the same distortions to the cosine bell as observed when using the standard scheme v2.

3.1.3 Vertical Oscillation

The solid body rotation experiments were also repeated with the inclusion of a sinusoidal oscillation in the vertical. In these experiments the tracer distribution was moved away from the boundary to avoid the problem of a departure point outside of the domain as the invariance of $\dot{\eta}$ with vertical co-ordinate η, although consistent with zero horizontal divergence, is clearly inconsistent with $\dot{\eta} = 0$ at the boundaries η=0,1. The results from these experiments showed no appreciable difference to the global non-conservation observed for a purely horizontal advection. This supports the formulation used for the vertical advection.

3.1.4 Comparison with Other Schemes in Solid Body Rotation Experiments

Due to variations in experimental setups a direct comparison of the solid body rotation results presented above with results already published must be done with care. Many of the numerical schemes mentioned in Section 2.6 have also presented results from solid body rotation tests, predominately using a cosine bell distribution. However, details of the precise level of mass conservation are rarely given with just a general statement as to the accuracy of the advection scheme and more detail presented with regards to changes in the tracer

distribution. The schemes presented are done so in the same order as they were discussed in Section 2.6, with the semi-Lagrangian schemes considered first and the Eulerian schemes second.

Semi-Lagrangian Schemes and Solid Body Rotation

The first numerical scheme to be considered is the LMCSL (Locally Mass Conserving Semi-Lagrangian) scheme by Kaas (2008). Two solid body rotation tests are presented: rotation of a slotted cylinder and a cosine bell on a plane. Both of these tests showed a smoothing of sharp gradients, especially in the case of the rotation of a slotted cylinder, and a damping of the cosine bell peak was noted. The same features were observed in the experiments presented above. During the experiments Kaas (2008) also observed the development of negative values in the tracer field and new maxima, showing a lack of shape preservation in the numerical scheme. The changes to the tracer distributions during the rotations were seen to be dependent on the resolution used, with a higher resolution producing a numerical solution closer to the analytical one. Despite the distortions to the distributions, for which detailed diagnostics are provided in Kaas (2008), the total mass was conserved to machine precision. However, the fact that these experiments are on a plane, rather than a sphere, probably plays a significant role since problems associated with the sphere, such as grid convergence at the poles, are avoided.

Nair and Machenhauer (2002) presented the results when carrying out solid body rotation tests with the CISL (Cell Integrated Semi-Lagrangian) scheme on a sphere, which is essentially a finite-volume scheme in nature. Once again a cosine bell distribution was used, but this time with both a positive definite and monotonic version of the scheme. Two angles of rotation are presented: $\alpha = 0$ and 90 degrees. In both of these tests the monotonic version of the scheme showed a greater deviation from the analytical result, but in all experiments a distortion to the cosine bell was observed. When a purely zonal flow was carried out smaller errors were produced than for advection over the pole. Consistent with the model results presented in this thesis, the distortion in the cosine bell was seen to align with the angle of rotation. For example, in the results presented by Nair and Machenhauer (2002) the cosine bell was stretched along the direction of the flow, as was seen for $\alpha = 90$ degrees in figures 3.4 and 3.5.

Once again diagnostics on the distortion of the cosine bell are provided by Nair and Machenhauer (2002) that highlight that the majority of the error develops during advection over the poles. However, no details on the level of mass conservation are given that can be compared to the results from the numerical scheme in this thesis. Table 3 in Nair and Machenhauer (2002) presents the results for the one case where the results explicitly show that the scheme is mass conservative; the advection of a cosine bell with a strong cross polar flow. By strong cross polar flow Nair and Machenhauer (2002) refer to the fact that 72 time steps (meridional Courant number of 1.78) are needed to complete a revolution, compared to 256 time steps (meridional Courant number of 0.05). Figure 8 in Nair and Machenhauer (2002) shows that this experiment did not produce a distortion to the cosine bell as it was advected over the pole. This result is more accurate than is currently produced by the numerical scheme in this thesis and suggests that the CISL scheme has a treatment of the polar region that could be beneficial in other schemes.

The CCS (Conservative Cascade) scheme by Nair *et al.* (2002) presented results of solid body rotation similar to those in Nair and Machenhauer (2002). Once again positive definite and monotonic versions of the scheme are also considered. As was the case for the CISL scheme, the monotonic version of the CCS scheme produced the worst results in the solid body rotation using $\alpha = 90$ degrees. Specifically, the monotonic model run showed an increased distortion to the cosine bell and larger values in the error diagnostics used. Both the positive definite and standard version of the CCS scheme produced a lesser degree of distortion to the cosine bell. The most noticeable change in the cosine bell for all of the versions of the CCS scheme was at the peak of the cosine bell. When using the monotonic scheme the peak is elongated along the direction of the flow (as was seen for the CISL scheme) and the other two schemes produce some damping of the cosine bell peak, as was seen in figures 3.4 and 3.5. No values are given with regards to the mass conservation, but the distortion of the cosine bell is noted by Nair *et al.* (2002) to be worse than for the CISL scheme of Nair and Machenhauer (2002). In the case of a deformational flow test both the positive definite and monotonic CCS schemes are stated to be mass conservative. The extended CCS scheme by Nair (2004) that combined the CISL and CCS schemes produces results very similar to those observed for the CISL scheme.

The last semi-Lagrangian scheme to be mentioned is the FFSL scheme of Lin and Rood (1996). As with many of the numerical schemes considered so far, when using solid body

rotation the FFSL scheme damps the peak of the cone-shape distribution used and also smooths sharp gradients that are in the initial distribution. Even though some distortions occur, the total mass is conserved throughout the experiments. The advection of a cosine bell over the polar region shows some signs of distortion relative to the initial distribution. Using the positive definite version of the scheme again produced a more accurate result, with the monotonic version resulting in an increased distortion of the cosine bell.

Eulerian Schemes and Solid Body Rotation

As was just shown, there exist semi-Lagrangian schemes that result in mass conservation under idealised testing, which the finite volume scheme in this thesis does not always obtain. However, due to the difference in the type of scheme the mass change that was observed in the tests presented in this chapter need to be compared to other finite volume schemes. This is what will be considered now.

Li and Chang (1996) present the results from solid body rotation tests carried out using a positive-definite Eulerian scheme. In the test results presented one complete rotation was completed in 320 time steps (on a 2.8 degree grid), compared to 1000 time steps (on a 1.125 degree grid) for the results presented in this thesis. In the case where a cosine bell was advected by a purely zonal flow ($\alpha = 0$ degrees) then mass conservation was observed to computer precision, as was the case with the results presented in Section 3.2.2. During the zonal advection the peak of the distribution was seen to decrease by 2% of its original value, but some of this is attributed to the resolution of the grid used. In the results presented in this thesis the peak of the cosine bell was not observed to change when being advected by a purely zonal flow, however a slight decrease is observed for small values of α. Li and Chang (1996) also noted that the damping of the cosine bell peak varied with the angle of rotation, in agreement with what was seen in the results presented earlier.

In the case of cross polar flow, with a global maximum Courant number of 0.9, only a slight distortion was observed by Li and Chang (1996) in the cosine bell after one complete rotation. The distortion to the cosine bell as it is advected over the pole is not seen to persist away from the polar region, contrary to what was observed in the solid body rotation results presented earlier. Whether mass conservation is obtained during the cross polar experiment is dependent on the way in which the polar grid (same concept as described in Section 2.4)

is used within the scheme, namely the method used to redistribute tracer (i.e. placing the tracer values on the reduced grid back on the full grid) after the advection step. If a zeroth order redistribution method is used, as is used in the numerical scheme in this thesis and equation (23) in Li and Chang (1996), then mass conservation is obtained. If a higher order redistribution method is used (equation (19) in Li and Chang (1996)) a 0.06% mass loss over one rotation is observed. This value is an order of magnitude larger than what is observed in either version of the scheme presented in this thesis, part of which is due to the differences in time step and grid size. Li and Chang (1996) take the solid body rotation experiments one step further by including vertical motion. Even with the additional motion the scheme remained mass conservative and was able to maintain sharp gradients in the tracer distribution to a high degree.

Li and Chang (1996) also briefly present the results from other numerical schemes that show features similar to those that were observed in Section 3.2.2. For example, the third order Eulerian MPDATA (multi-dimensional, positive-definite advection transport algorithm) of Smolarkiewicz and Rasch (1991) produced a cosine bell shape similar to that observed using the scheme detailed in Chapter 2 when advecting at $\alpha = 90$. The scheme of Tremback *et al.* (1987) also produced the low level noise that covers the globe that is observed in the cosine bell experiments detailed above.

The monotonic advection algorithm by Walcek (2000) is used in a test involving a two-dimensional rotating plane with a range of tracer shapes, with a maximum Courant number of 0.5. Walcek (2000) compares the monotonic scheme to several others, amongst those are schemes documented by Prather (1986), Bott (1989) and Bott (1992). All of the schemes are stated as being globally mass conservative, but it is not uncommon for the tracer mass to be displaced throughout the domain. This displacement arises due to numerical diffusion or oscillations developing in the tracer distribution. Many of the error measures calculated are over a limited domain, therefore this displacement can cause a deviation from mass conservation in the limited area diagnostic.

After 6 rotations Walcek (2000) notes that the peaks of the tracer shapes initialised on the rotating plane have decreased by 3% to 87% of their original height, with the greatest loss occurring for the narrower shapes. When the initial distribution has more of a top hat shape (i.e. not peaked but flat) the heights of the larger shapes are maintained and the narrower shapes still experience the greatest loss (up to 87%). The same was also observed

for the cosine hill shape distributions (up to 86% loss), but an aggregation of mass around the peaks was also observed. In each of these cases the results were compared to results obtained by the method in Bott (1992), which showed less accurate results in all of the experiments. The non-monotonic schemes that were considered showed the development of oscillations around the shapes initialised on the plane and, in the case of the wider initialising shapes, the peak increased in height. The narrower initialising distributions still demonstrated a significant decrease in peak height.

The solid body rotation results presented in Section 3.2.2 have features in common with both the monotonic and non-monotonic schemes presented by Walcek (2000). The results show weak oscillations around the cosine bell that arise in the non-monotonic schemes. The cosine bell peak also decreased slightly, which is consistent with the non-monotonic schemes considered. This shows that the scheme in this thesis obtains the same general level of accuracy, with respect to maintaining the shape of a tracer distribution, as other schemes that have been developed.

Hundsdorfer and Spee (1995) consider solid body rotation acting on a cone shaped initial distribution. Section 2.6.2 presented some of the features of this scheme, such as the use of a polar cap and polar mixing. The polar cap is a homogeneous cell placed at the pole and polar mixing involves the mixing of adjacent cells after each time step. This mixing process results in zonal transport inside the polar cap and was seen to reduce the level of distortion that occurred to the tracer distribution when there is advection over the pole. However, this mixing process also causes a deviation from local mass conservation, but not global conservation. The alternative method for polar caps suggested is a deformation correction that does result in a deviation from mass conservation. For one revolution a mass change of 0.1% is reported. Also, when using a cosine bell distribution the numerical result after one revolution shows a slight distortion when compared to the analytical result. Small overshoots and undershoots are also observed in the tracer distribution.

The results from solid body rotation experiments of a cosine bell are also presented by Hubbard and Nikiforakis (2003) using a finite volume scheme at a range of horizontal resolutions. During advection over the pole ($\alpha = 90$ degrees) some distortion to the cosine bell was observed, but the amount of distortion decreased with increasing resolution. By using a decreased time step in the zonal direction, and therefore more zonal advection steps per meridional advection step, the distortions to the tracer distribution were seen

to decrease slightly. This process is an alternative to the polar grid reduction that was discussed in Section 2.4. However, Hubbard and Nikiforakis (2003) do advocate caution, as it was noted that this multi-step process in the zonal direction introduces a slight error that can eventually dominate if there is too a great a reduction in the time step in the zonal direction compared to the meridional direction. The advantage of the AMR (adaptive mesh refinement) method used in this scheme is that gradients in the tracer distribution can be well maintained. Unfortunately, Hubbard and Nikiforakis (2003) do not provide details on the level of mass conservation observed during the solid body rotation experiments.

The second-order moments method by Prather (1986) also showed mass conservation to machine precision when advecting a uniform tracer distribution, in agreement with what was presented in Section 3.2.1. When advecting a cosine bell distribution the second-order moments method produced low level numerical diffusion and absolute error. Both of these terms are an order of magnitude lower than for some of the other schemes considered by Prather (1986). Unfortunately, without specific values it is difficult to compare these results to those presented in this thesis.

3.2 Advection by Analyses

3.2.1 ERA-Interim

For this next series of experiments ERA-Interim at full resolution (T255L60, model top at 0.1hPa) from the European Centre for Medium-range Weather Forecasts (ECMWF) is used to drive the advection. ERA-Interim uses cycle 31r2 of the Integrated Forecast System (IFS) introduced in December 2006. In these experiments the zonal mean ozone distribution for April (taken from Cariolle and Teyssédre (2007)) is used to initialise a passive tracer, as shown in figure 3.6.

Figure 3.7 shows the percentage change in global average mass mixing ratio over a two month period for four model runs. The only difference between the runs is the size of the time step used. In figure 3.7 the time step size ranges from 150 seconds (144 steps) to 300 seconds (72 steps). The different runs clearly lie on top of each other at the start of the run and show a small spread of approximately 0.002% by the end of the two month period.

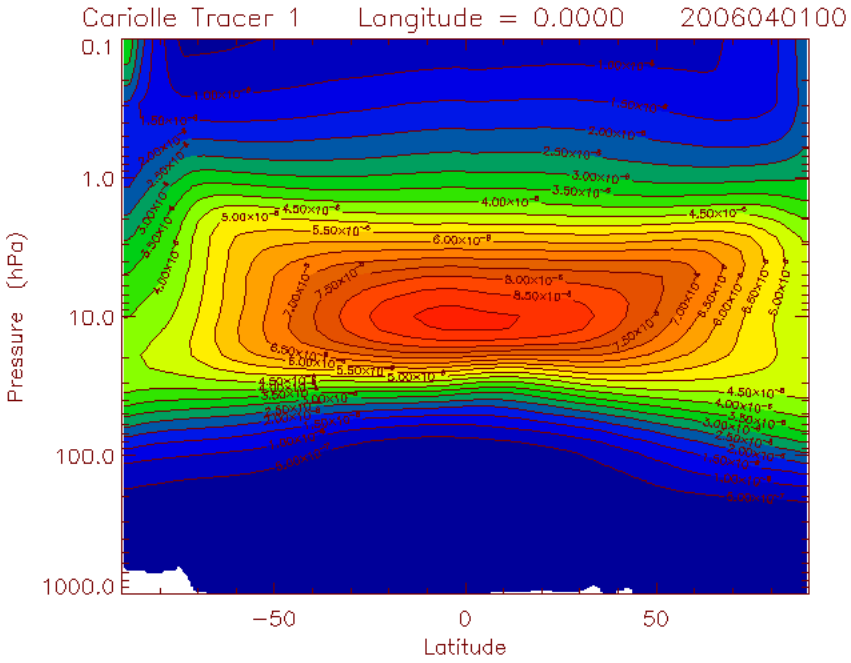

Figure 3.6: *Vertical cross section through the initialising ozone tracer field (April zonal mean). Mixing ratio is plotted with a contour interval of 0.5 ppmv.*

Therefore, in these experiments, the numerical change in global burden of the passive tracer is almost independent of the size of the time step used for the tracer advection.

Comparison of tracer advection schemes

Once again a comparison can be made between the two versions of the tracer advection scheme; v1 (tracer flux calculations as described by Gregory and West (2002)) using a cubic interpolation in the meridional direction and v2 (tracer flux calculation as in equations (2.9)-(2.11)) using a linear interpolation in the meridional direction. Figure 3.8 shows the percentage change in global average mass mixing ratio for the two different schemes, both using a time step of 150 seconds and ERA-Interim at T255. Apart from the tracer flux calculation the model runs are identical but using the flux calculation in scheme v1 results in a final numerical mass gain that is approximately 1.5 times that seen when using scheme v2.

This is more clearly seen in figure 3.9 which shows the ratio of the numerical mass change produced using the two schemes. The first month has not been plotted due to large positive and negative values that occur due to the alternation between small positive and negative percentage changes in the global average mass mixing ratio. The increasing ratio throughout

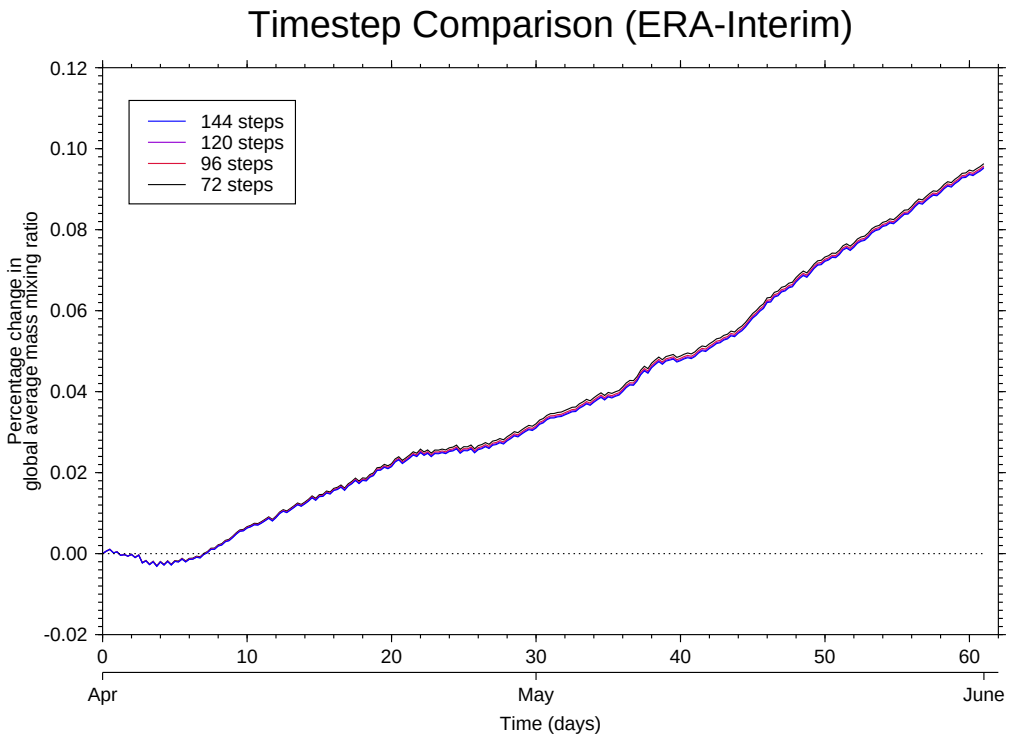

Figure 3.7: *Comparison of different time steps used in the model (scheme v2) when advecting by ERA-Interim at T255. The time step is given as the number of steps used in a 6 hour period, with the corresponding values ranging from 150 seconds (144 steps) to 300 seconds (72 steps). The observed numerical mass change is almost independent of the time step.*

May reflects the initial divergence of the two model runs before both models have an almost constant rate of mass gain that results in the ratio remaining mostly between 1.5 and 1.6. The sharp increases in the ratio coincide with periods of cross-polar transport highlighting the numerical inaccuracies of dealing with singularities in the model grid. The fact that it is a mass jump means that scheme v1 has greater difficulties with mass conservation during cross-polar flow than scheme v2.

A large proportion of the differences in the numerical mass change between the two schemes can be accounted for by the different interpolations used in the meridional direction. This can also be seen in figure 3.8 where the numerical mass change observed when using scheme v1 with a linear meridional interpolation over a two month long model run has been plotted. It can clearly be seen that with the reduction in the order of the interpolation in the meridional direction the numerical mass change of scheme v1 tracks that observed for scheme v2 much more closely, and reduces the impact of cross-polar flow on the mass conservation. However, even by the end of the two month period shown scheme v2 has a lower numerical mass gain than scheme v1. Due to the improved mass conservation

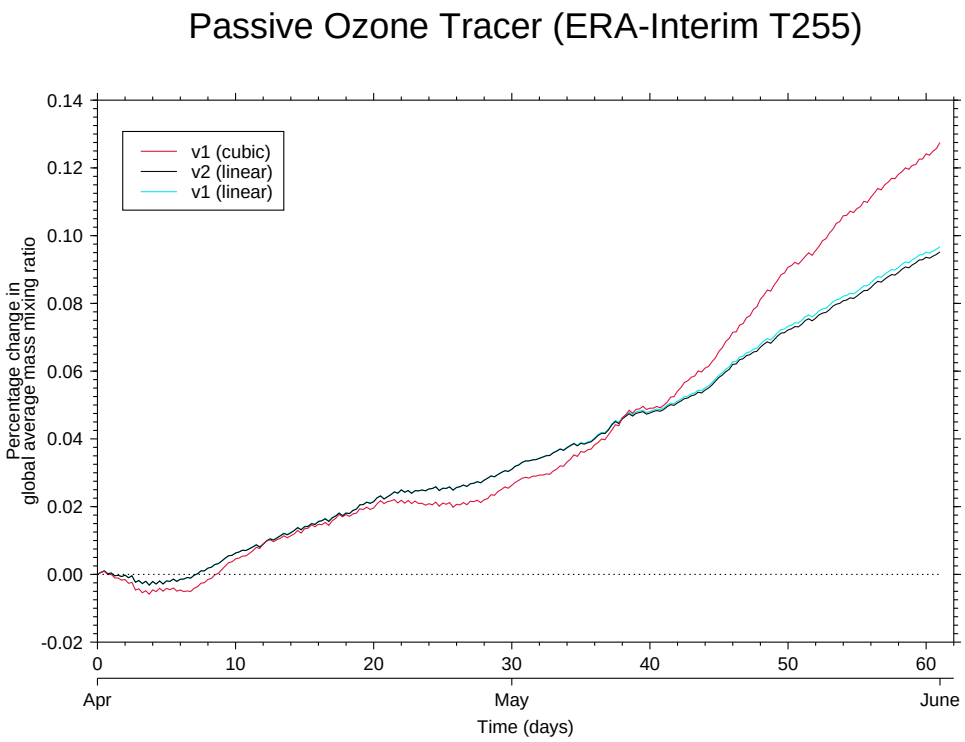

Figure 3.8: *Percentage change in global average mass mixing ratio of a passive ozone tracer using scheme v1 with a cubic and linear interpolation in the meridional direction, and scheme v2 using a linear interpolation in the meridional direction.*

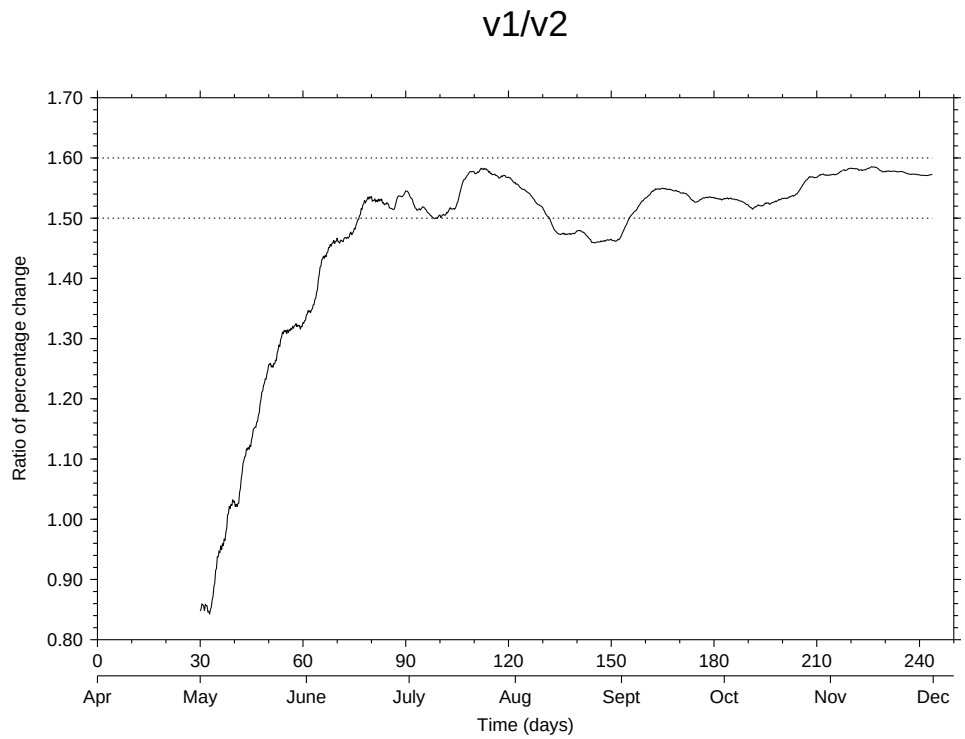

Figure 3.9: *Ratio of the percentage change in global average mass mixing ratio for schemes v1 (cubic interpolation in the meridional direction) and v2 (linear interpolation in the meridional direction) shown in figure 3.8. After three months the ratio becomes relatively constant with sharp increases in the ratio occurring during periods of cross-polar transport.*

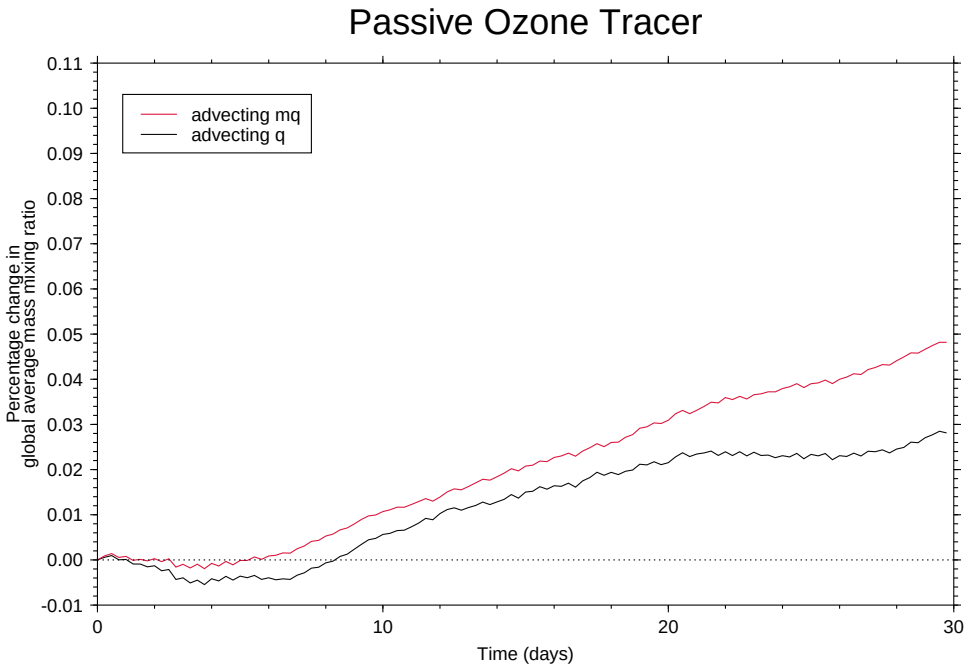

Figure 3.10: *Comparison of the percentage change in global average mass mixing ratio of a passive ozone tracer using ERA-Interim at T255 during April 2006. The black and red lines represent schemes v2 and v3 respectively, both use a linear interpolation in the meridional direction and Δt=150 seconds.*

observed when using scheme v2 this tracer advection scheme has been used for the rest of the experiments presented in this thesis.

It was also mentioned in Section 2.3 that an alternative version of scheme v2 is to use mq within the tracer flux integral (equation 2.13), rather than having the mass outside the integral as m_{up}. The integral of mq is then also used in the interpolation to the departure point in each direction. This is referred to as scheme v3. Figure 3.10 presents the results of the advection of passive ozone over April 2006 using schemes v2 and v3 with a linear interpolation in the meridional direction. It is immediately noted that scheme v3 results in a considerably larger numerical mass change than scheme v2. Therefore the advection of mq is not used in further experiments. The performance of scheme v3 may be worse because it is not consistent with the mass update in Section 2.1.2 (equations 2.5-2.7) needed to convert mq back into q before the next time step.

An additional version of the scheme also considered carrying an evolving mass field, m, internal to the model rather that resetting it at the start of each time step using the analyses (scheme v4). This follows the method of Rotman *et al.* (2001) detailed in Section 1.3.3. When this method is used in this numerical scheme the model becomes quickly unstable and so this version of the scheme was not considered further. This instability

likely arose due to the inconsistency between the model mass and that determined from the analyses at the 6 hourly intervals when the analyses are updated. In order for scheme v4 to be stable a method similar to Prather *et al.* (1987) would likely need to be used.

3.2.2 Full Spatial Resolution

Figure 3.11 shows vertical cross sections of the passive ozone tracer field at one month intervals starting from the 1st May for the case of advection by ERA-Interim at T255 using scheme v2 with a time step of 150 seconds. By June the strong vertical advection in the tropical region is clearly seen as tracer is advected into the upper stratosphere and mesosphere. The dominant meridional flow is towards the winter pole in the stratosphere and mesosphere (figure **??**) and as a result the passive tracer is advected towards the South Pole. By October the initial high in the ozone field centred in the tropics at 10 hPa has been diminished and shifted upwards, with the ozone distribution becoming overall more uniform above 30 hPa. In the troposphere the tracer distribution remains more or less the same throughout the model run.

Figure 3.8 shows the corresponding percentage change in the global average mass mixing ratio during the eight month model run for T255 (black line) of 0.8%. As shown in the Introduction, Berrisford *et al.* (2011) have carried out diagnostics of ERA-Interim and showed that the dry mass in the re-analyses has a peak to peak fluctuation of 0.04% of the long term averages. When the ERA-Interim model is allowed to run without any additional input it produces an estimated mass gain of 0.3% per year. Therefore, not all of the numerical mass gain observed in this experiment is due to the analyses and some other factors must contribute.

3.2.3 Spatial Truncation

A model run was carried out with ERA-Interim spectral data on η-levels truncated to a horizontal resolution of T159 and then transformed to wind and temperature on a linear Gaussian grid on η-levels. The model η-levels used at this resolution are the same as those used at T255. The results of this run are presented in figures 3.12 and 3.13. Figure 3.12 shows a comparison of the mass conservation for the two resolutions (T255 and T159). It

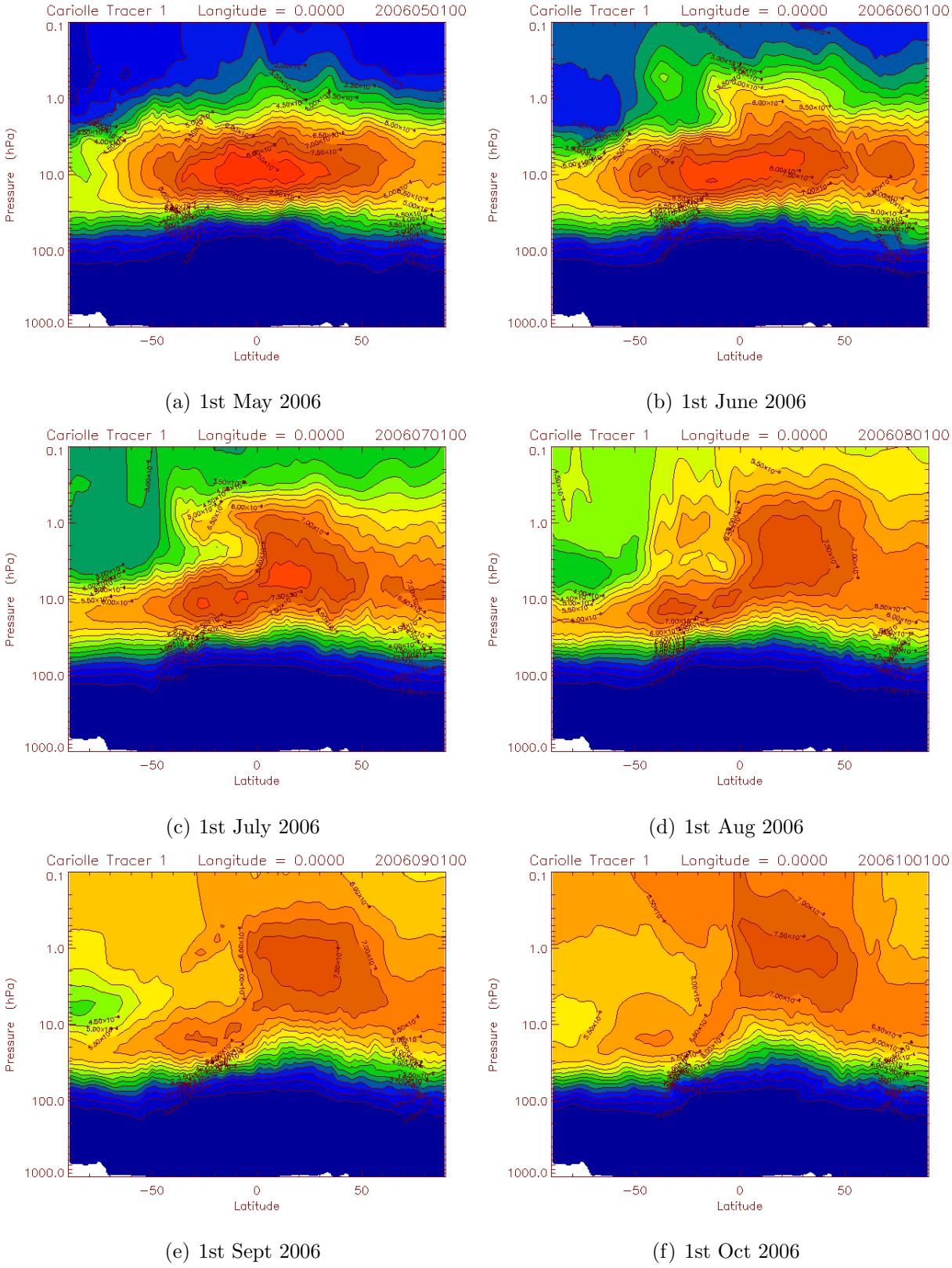

(a) 1st May 2006

(b) 1st June 2006

(c) 1st July 2006

(d) 1st Aug 2006

(e) 1st Sept 2006

(f) 1st Oct 2006

Figure 3.11: *Vertical cross sections through the passive ozone tracer field at one month intervals with advection by ERA-Interim at T255. Mixing ratio is plotted with a contour interval of 0.5 ppmv.*

is immediately seen that this lower resolution model run produces approximately 3 times the mass gain observed in the previous model run (T255). The numerical mass change observed at T159 can also be compared with a tracer transport study of the ECMWF IFS by Flemming and Huijnen (2011). When using a passive ozone tracer it was observed that at the end of a year long simulation the global burden of ozone reduces to 25% of the original global burden, i.e. a numerical mass loss of 75%. Flemming and Huijnen (2011) state that the numerical mass changes are systematic so this number can be scaled to give a numerical mass change of -50% over eight months. This is 20 times the magnitude of the observed numerical mass change at T159 in this thesis (2.4%).

A comparison of the vertical cross sections through the passive ozone tracer field at the different resolutions (figures 3.11 and 3.13) can be made and very few differences observed. The overall distribution is the same for the two model runs, with the same degree of homogeneity forming in the stratospheric tracer. What differences can be noted are due to the higher resolution model run maintaining a higher tracer concentration in the smaller features in the distribution, and hence larger gradients in the tracer field. This can be associated with a decreased averaging, due to smaller grid boxes, that allows higher tracer values to remain in the distribution for longer and less diffusion when using higher resolution analyses.

Figure 3.14 shows the percentage change in global average mass mixing ratio per day over April and May for the various experiments carried out using ERA-Interim. The minimum spatial scale of the spectral model, L, plotted against the rate of mass change produces a linear relationship. The minimum half-wavelength can be used as a proxy for horizontal resolution and is defined as $L = \pi a/N$, where a is the radius of the Earth and N is the wavenumber truncation. It can be seen that as resolution increases, and the truncation of the analyses decreases, the mass conservation improves linearly tending to 1.6E-3% numerical mass gain per day at the resolution of the analysis model (T255).

3.2.4 Source of Mass Non-Conservation

The reason for non-conservation of tracers can be linked to an inconsistency between the mass field in the model and the wind field in the analyses. Further support for this is given from two additional experiments with different initial tracer distributions. The first of these

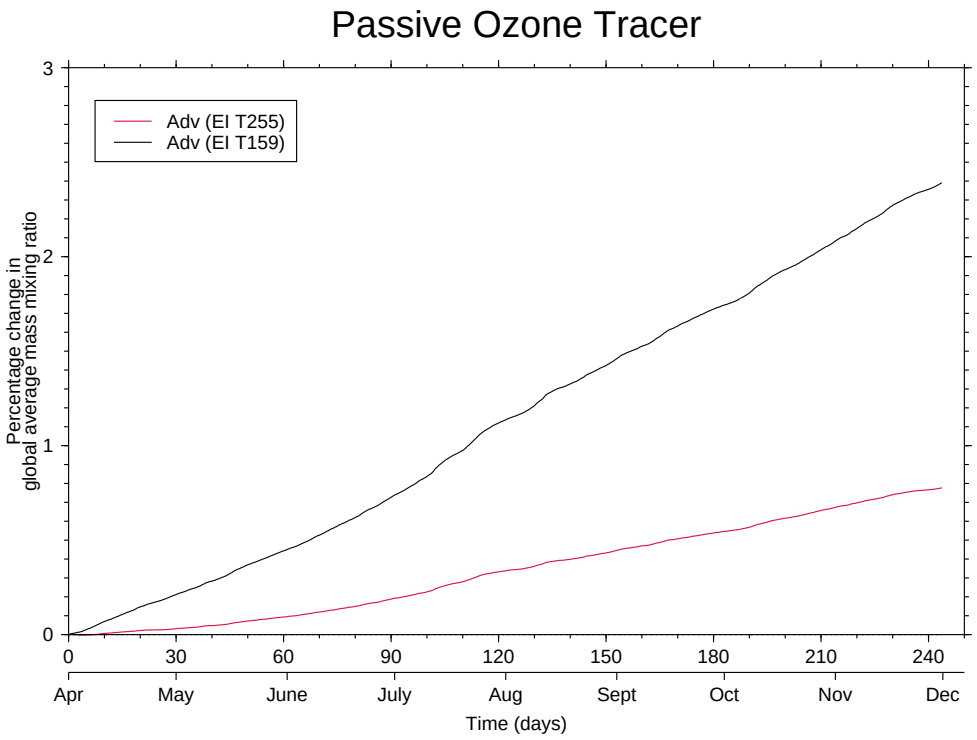

Figure 3.12: *Comparison of the percentage change in global average mass mixing ratio when using ERA-Interim at a horizontal resolution of T159 and T255. Both model runs have the same vertical resolution, use scheme v2 and Δt=150 seconds.*

experiments uses specific humidity as a passive tracer. Specific humidity is weighted to the lower troposphere, in comparison to ozone which is weighted to the mid-stratosphere. In figure 3.14 it is immediately seen that the rate of mass change for a passive specific humidity tracer is of a larger magnitude than that observed for a passive stratospheric ozone tracer. The mass conservation is worse for the tropospheric weighted tracer.

Secondly, the model was initialised with the ozone distribution, but set to zero on model levels where p >54.6hPa (referred to as "half ozone" experiments). The rates of mass change for these two tests are 1.8E-3% and 8.1E-4% per day at T159 and T255 respectively (purple stars in figure 3.14). Figure 3.15 shows the mass change during the entire 60 day period compared to those using the full ozone distribution. The results for the half ozone case are indeed better than the cases when there is tracer in the model levels closer to the surface. The significance of this occurrence can be seen through the specification of the hybrid vertical co-ordinate for the ECMWF model.

The scheme for the η vertical co-ordinate is shown explicitly in Simmons and Burridge (1981) in equations (3.2)-(3.4), but will briefly be described here. As stated in the Introduction, the pressure on each η level is calculated as $p_{l+1/2}/p_0 = A_{l+1/2} + B_{l+1/2}p_s/p_0$ where

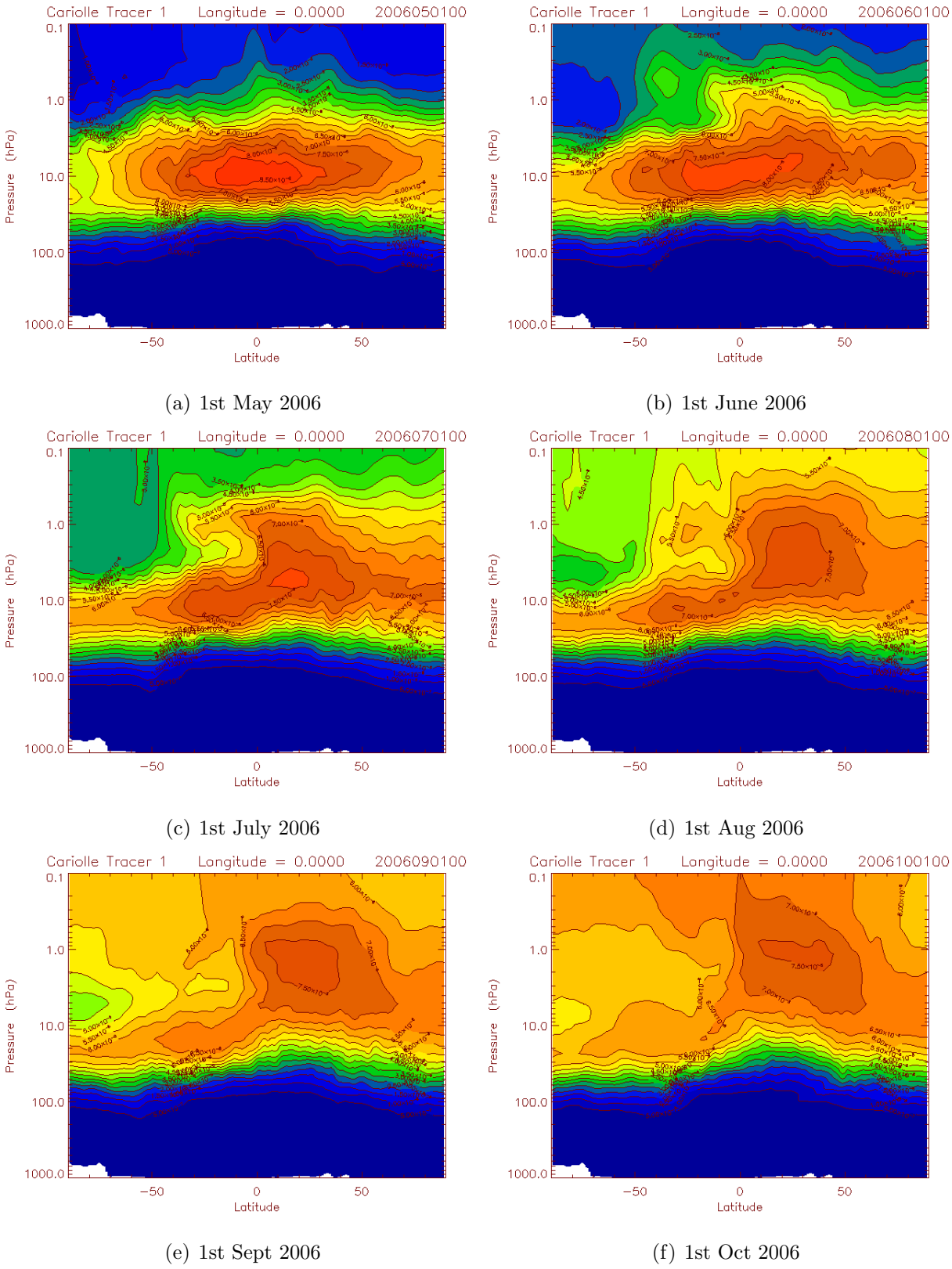

(a) 1st May 2006

(b) 1st June 2006

(c) 1st July 2006

(d) 1st Aug 2006

(e) 1st Sept 2006

(f) 1st Oct 2006

Figure 3.13: *Vertical cross sections through the passive ozone tracer field at one month intervals with advection by ERA-Interim at T159. Mixing ratio is plotted with a contour interval of 0.5 ppmv.*

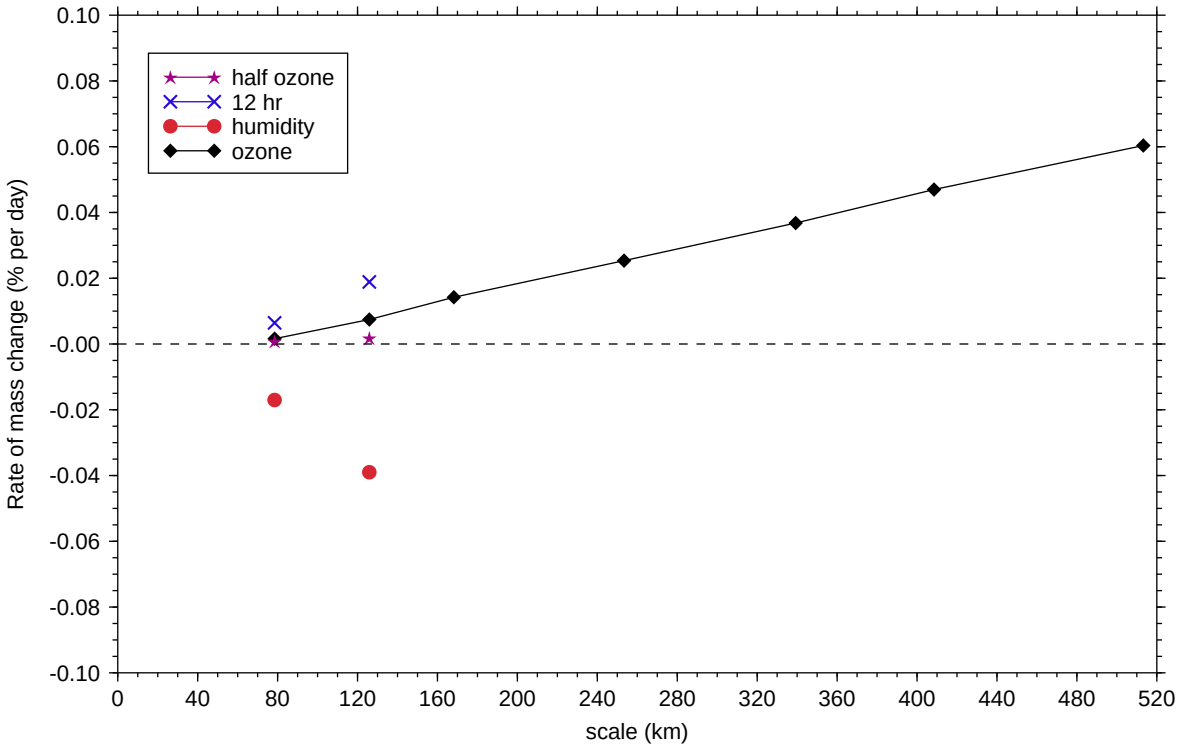

Figure 3.14: *Numerical rate of change of global average mass mixing ratio in units of percent per day during April and May against wavelength (where $L = \pi a/N$). Values are plotted only for the cases where ERA-Interim advects passive tracers using scheme v2. Unless stated otherwise the winds are updated every six hours, Δt=150 seconds and ozone is used as the passive tracer.*

A and B are coefficients, p_0 and p_s are a constant and surface pressure respectively. The higher model levels (54.6hPa and above) have $B = 0$ which removes the weighting of the surface pressure. In this case the pseudo-density is a constant ($\rho = 1/g$) and therefore the continuity equation is insensitive to temporal and spatial truncation. The half ozone tracer experiment, which is initialised with tracer only on these higher levels, shows that conservation is almost exact when pressure is the vertical co-ordinate and that there is a smaller impact of the truncation error.

Near the ground $B = 1$ and $A \approx 0$ so $\eta \simeq p/p_s$. Pseudo-density can now vary with surface pressure both in time and space. Therefore, the increase in non-conservation with increasing L arises through the truncation of surface pressure and the inconsistency between the continuity equation in the NWP (numerical weather prediction) model and the offline tracer model that this introduces. The majority of the error in the truncated p_s distribution is likely associated with the representation of orography. When using the full spatial resolution a non-conservation is still observed due to the use of analyses at 6 hour intervals and

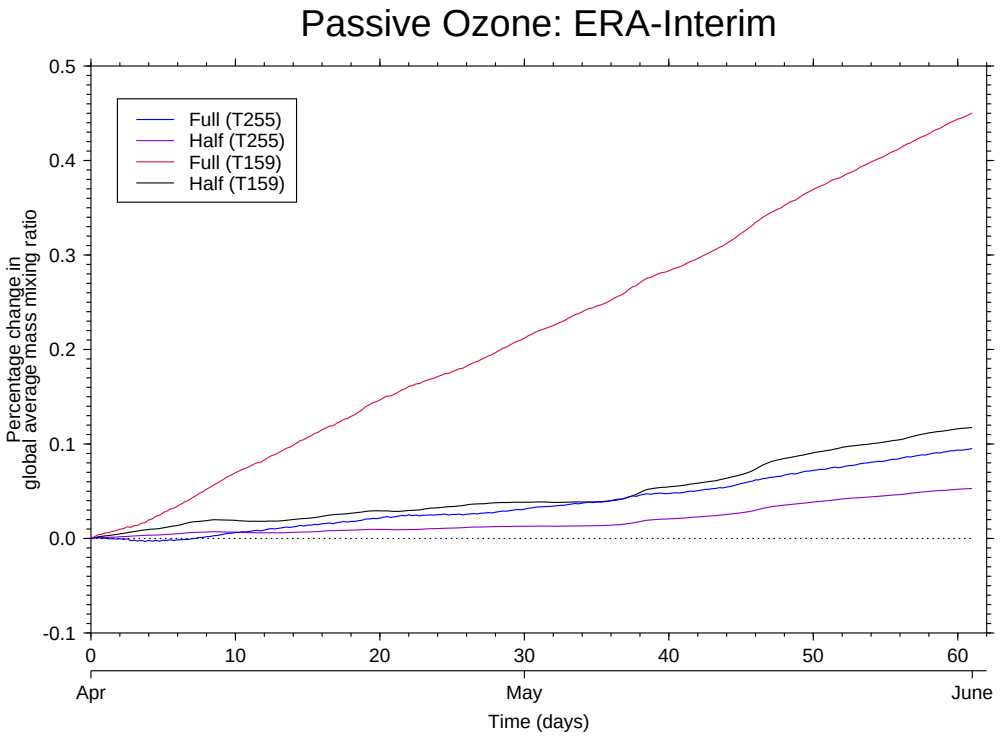

Figure 3.15: *Comparison of the percentage change in global average mass mixing ratio observed at horizontal resolutions of T159 and T255 for a passive ozone tracer initialised as the zonal mean ozone distribution (full) and set to zero on all model levels calculated using surface pressure when initialised (half).*

temporal truncation. This is because the ECMWF model uses a time step of 20 minutes, but for this work that has been changed to wind updates every 6 hours with interpolation between updates. An additional error may arise due a difference in the spatial discretisation used by the ECMWF model and the model in this thesis.

As mentioned in the Introduction, Wild and Prather (2006) varied grid resolution and studied the effects in a model run, the highest resolution in the study being T106. The most dramatic reduction in the errors (e.g. ozone emissions, ozone chemistry, ozone transport, dynamical features) was observed when increasing from the lowest resolution (T21) to the next one up (T42). The successive increases in resolution to T63 and T106 had a lower impact showing a non-linear relationship between error reduction and increasing resolution, unlike the results shown in figure 3.14. However, Wild and Prather (2006) looked specifically at ozone production, burden and lifetime rather than mass conservation. They also show that the change in resolution does not have the same effect everywhere over the globe due to other processes in the model, such as mixing. This should be kept in mind when considering the effects of truncation.

In the results presented above it can be seen that for tracers weighted towards the surface

or lower troposphere there is a numerical mass loss, whereas tracers that are weighted towards the mid-stratosphere show a numerical mass gain. This is the opposite of what is observed in the ECMWF IFS tracer transport study (Flemming and Huijnen, 2011) where a systematic mass increase is observed for tracers that have surface emissions or a maximum near the surface (such as specific humidity). Tracers that do not have surface emissions or a maximum close to the surface show a systematic mass loss (such as stratospheric ozone).

3.2.5 Temporal Truncation

The model was also run with a 12 (rather than 6) hourly wind update using ERA-Interim (blue crosses in figure 3.14) at a horizontal resolution of T159 and T255. From these tests it was clearly seen that a more frequent wind update does indeed result in improved mass conservation. By the end of the 8 month model run the 12 hourly wind update produces a percentage mass gain that is 4 and 2.6 times that produce by the 6 hourly wind update at T255 and T159 respectively.

It can also be noted that using a tracer distribution heavily weighted towards the troposphere has a larger impact on mass conservation than a halving of the wind update frequency from 6 to 12 hours. The temporal truncation error arises due to the linear interpolation between the analyses files and using instantaneous, rather than time integrated, winds. Since the time step used (150 seconds) is so much smaller than the time between the analyses this approximation is probably sufficient and the only way to improve the truncation would be to use a higher order time interpolation for the surface pressure and velocity.

This result of an improved mass conservation with an increased wind update frequency is in agreement with the work presented by Bregman *et al.* (2006). They showed that a 3 hourly wind update produced a better representation of mixing ratios and an improved age-of-air value than 6 hourly wind updates. If the model is run at the full resolution of the ERA-Interim data (T255) then the mass conservation is further improved.

Figure 3.16 shows a cross section of the passive ozone tracer field when the distribution at the end of the model run using the 12 hourly wind updates is subtracted from that using the 6 hourly wind updates. Negative differences (i.e. 12 hourly has larger tracer values) occur

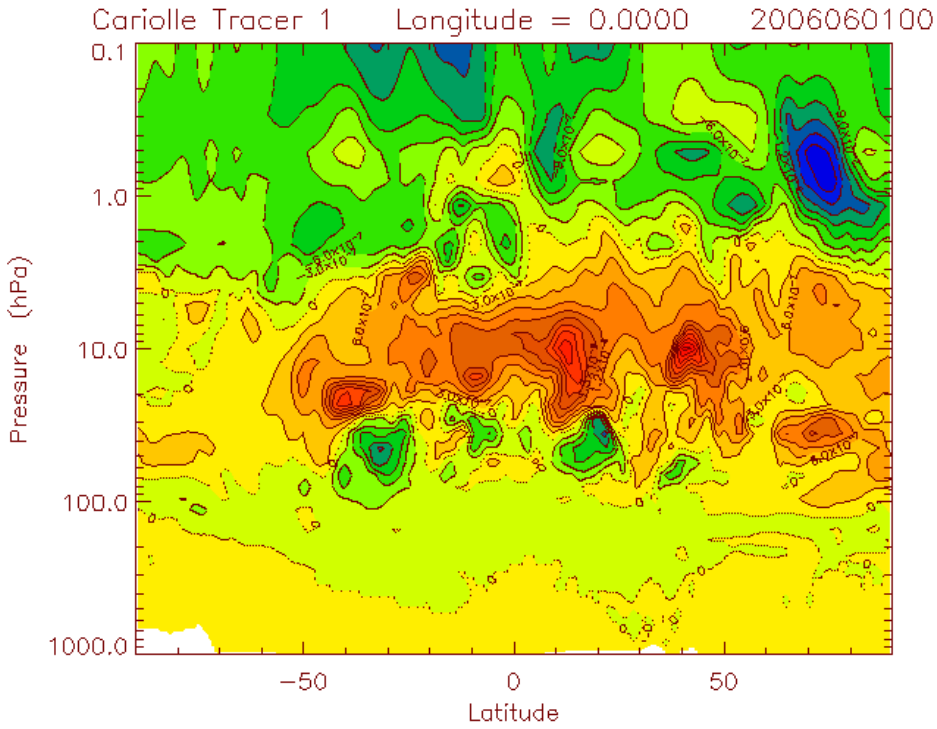

(a) T255

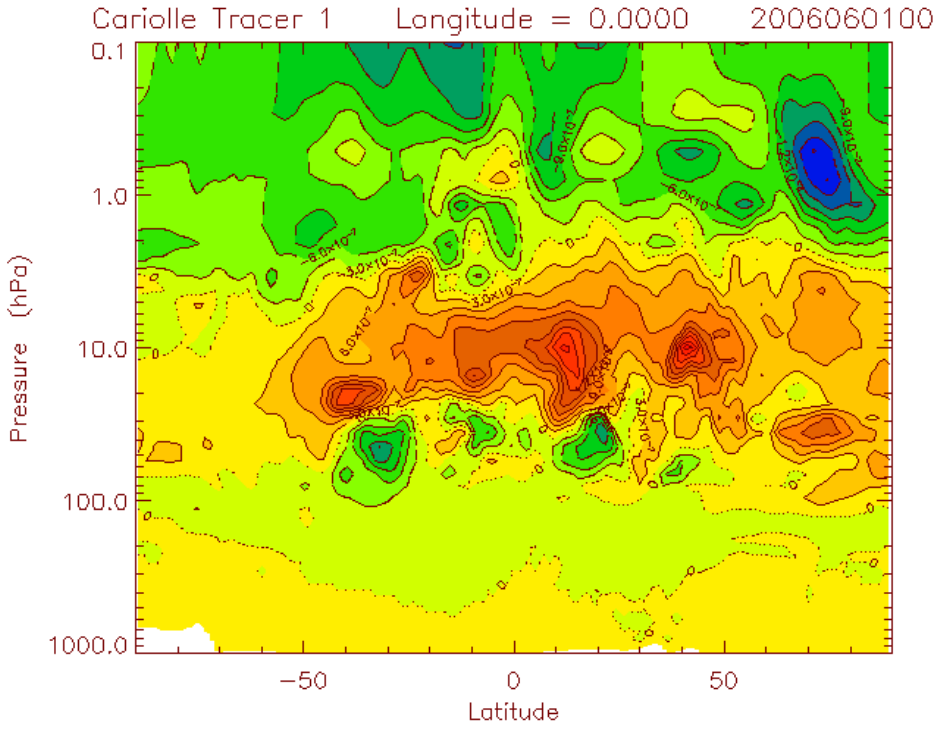

(b) T159

Figure 3.16: *Difference between the vertical cross section when the passive ozone tracer is advected by 6 hourly and 12 hourly (i.e. 6 hourly - 12 hourly) ERA-Interim analysed winds at (a) T255 and (b) T159. Difference in the mixing ratio is shown with a minimum contour of -3 ppmv and a 0.3 ppmv contour spacing. The dashed line is the zero contour.*

in the region 60-70hPa where there is an increased descent into the lower stratosphere. The positive values in the middle stratosphere are where the 12 hourly wind updates results in a greater transport of tracer out of the region and into high altitudes by the end of the model run. The longer time between analyses results in greater averaging and a less variable advection, which exaggerates the descent into the troposphere and ascent into the stratosphere. The same features are observed in the difference fields at T255 and T159. However, the higher resolution difference field shows a greater range in the difference field i.e. larger positive and negative features, and hence a slightly larger impact from the change in wind update frequency. One reason for this could be the fact that at T159 more spatial averaging is required, which will smooth out some of the differences produced due to the differing wind update frequency.

3.2.6 Operational Analyses

For one final comparison the model is run using the ECMWF operational analyses at a wind update frequency of six hours. The operational analyses have a full resolution of T799L91 with a top model level at 0.01 hPa and use cycles 30r1 (February 2006) and 31r1 (September 2006) of the IFS. The main difference between the IFS cycles used for the operational analyses and that for ERA-Interim is the increased use of satellite data in ERA-Interim. In this experiment the spectral data on η-levels is again truncated to a horizontal resolution of T159 and then transformed to wind and temperature on a linear Gaussian grid on η-levels.

Figure 3.17 shows a comparison of the percentage change in global average mass mixing ratio for both the operational analyses and ERA-Interim both truncated to T159. The mass conservation when using the operational analyses is notably worse than when ERA-Interim is used, showing a numerical mass gain that is 7 times greater. The calculated rate of mass change per day over April and May is 0.052% when the operational analyses are used. In comparison ERA-Interim at T159 produced a rate of mass change of 0.0074% per day over the same period. This increased mass gain can be attributed to the greater truncation carried out when using the operational analyses as the full resolution is T799 (compared to T255 for ERA-Interim). This is supported by Section 3.2.4 (figure 3.14) which detailed the relationship between increased truncation and increased mass non-conservation.

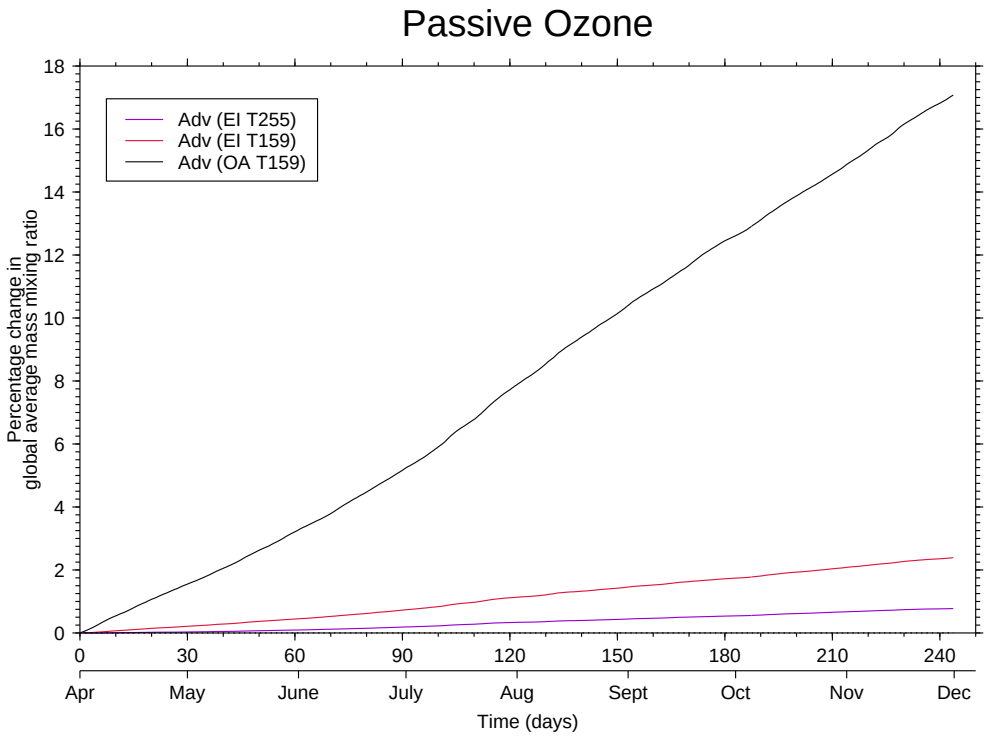

Figure 3.17: *Percentage change in global average mass mixing ratio of ozone as a passive tracer when advected using operational analyses (T159) and ERA-Interim (T255 and T159). It can clearly seen that using ERA-Interim results in a higher level of mass conservation than the operational analyses.*

Figure 3.18 shows vertical cross sections of the passive ozone tracer field that can be compared to those when ERA-Interim at T159 is used (figure 3.13). It is immediately seen that the homogeneity that develops in the tracer field in the stratosphere is more pronounced when the operational analyses are used and the small scale features are not maintained for as long. The maximum in the passive ozone field is also decreased at a much faster rate. This increased homogeneity is associated with a greater vertical diffusion, as has been noted in stratospheric tape recorder tests like those presented by Monge-Sanz *et al.* (2007) and Ploeger *et al.* (2010) (see Section 1.3.2 for details). In summary, Monge-Sanz *et al.* (2007) compared the model used to produce ERA-Interim with the ECMWF operational analyses, ERA-40 and the UK Met Office data. In both age-of-air and stratospheric tape recorder tests the ERA-Interim model produced results closer to the observations than the operational analyses. Ploeger *et al.* (2010) also noted that the operational analyses are more dispersive than ERA-Interim resulting in a faster stratospheric tape recorder due to faster upwelling at the tropical tropopause.

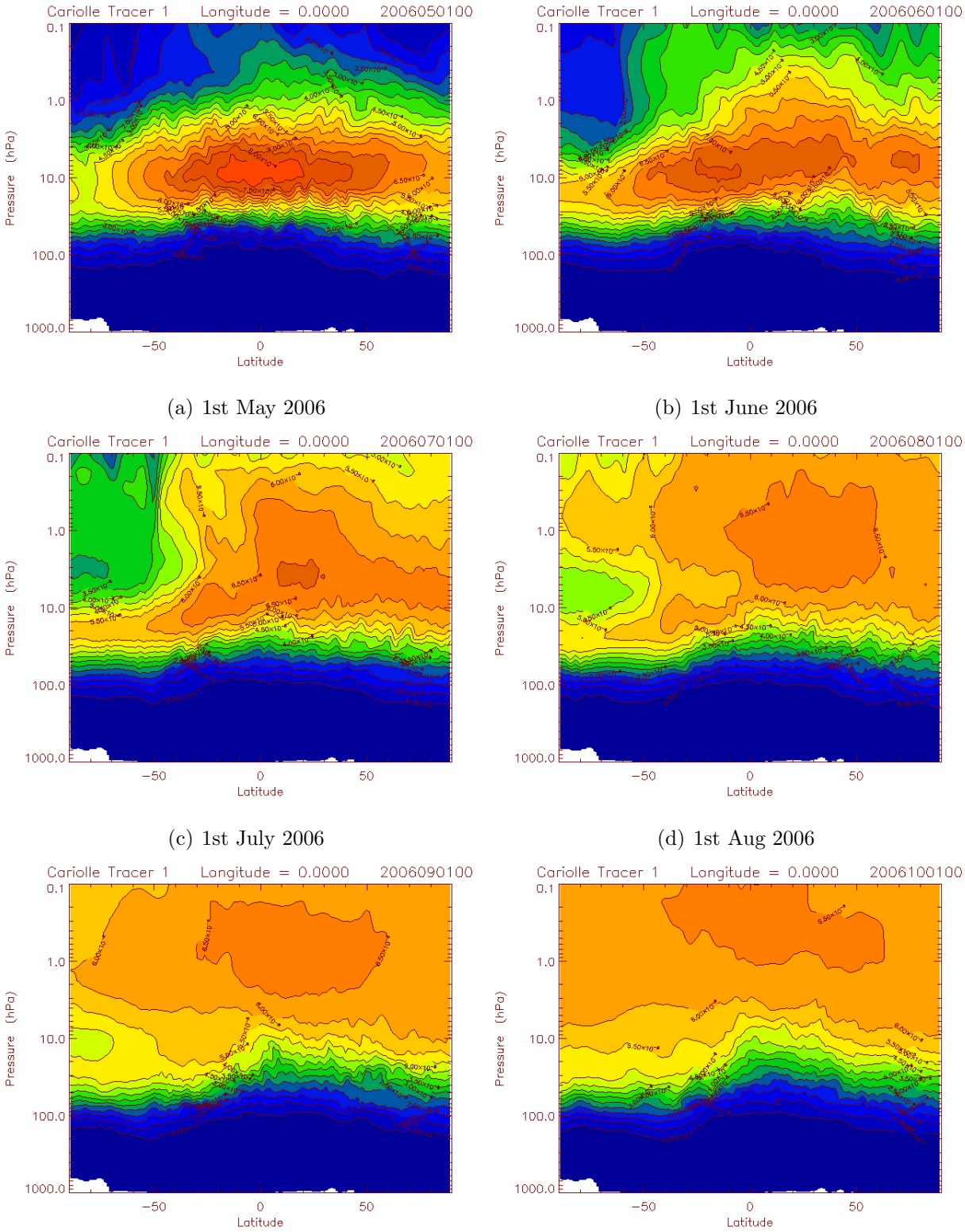

(a) 1st May 2006

(b) 1st June 2006

(c) 1st July 2006

(d) 1st Aug 2006

(e) 1st Sept 2006

(f) 1st Oct 2006

Figure 3.18: *Vertical cross sections through the passive ozone tracer field at one month intervals with advection carried out using operational analyses at T159. Mixing ratio is plotted with a contour interval of 0.5 ppmv.*

3.3 Summary

This chapter presented the results of different experiments designed to study the mass conservation of the numerical scheme presented in Chapter 2. The first set of experiments were benchmark experiments using solid body rotation acting on a uniform tracer distribution and a cosine bell. The crucial aspect of the solid body rotation tests is that the uniform density means that the analytical winds are non-divergent. The experiments were carried out using the tracer advection scheme as detailed by Gregory and West (2002) (v1) and the tracer advection scheme as presented in Chapter 2 (v2), the only difference being that the first method uses the updated tracer field and the second uses the tracer field at the start of each time step in the tracer flux calculations.

When using a uniform tracer distribution both of these methods showed mass conservation. However, when using scheme v2 fringes formed in the tracer distribution downwind of the pole (figure 3.2) and were amplified if the cubic interpolation in the meridional direction was used. A linear interpolation in the meridional direction prevented this amplification and so was used throughout the rest of the experiments with scheme v2. When using a cosine bell distribution both tracer advection schemes showed a mass change that was dependent on the angle of rotation. A mass change of $-4.1 \times 10^{-4}C < x < 6.6 \times 10^{-4}C$ percent over one rotation was observed for scheme v1 with a cubic meridional interpolation ($-6.2 \times 10^{-4}C < x < 2.5 \times 10^{-4}C$ with linear interpolation in the meridional direction), compared with $-1.9 \times 10^{-3}C < x < 6.6 \times 10^{-4}C$ percent for scheme v2 with a linear interpolation in the meridional direction (figure 3.3). In all of these values C is the maximum Courant number, in the results above this is 2.43 in the zonal direction. Both schemes showed mass conservation for a purely zonal flow, suggesting the source of non-conservation is the dimension splitting and the fact that the numerical winds do not necessarily maintain the non-divergence of the analytical winds.

Distortions were observed in the cosine bell after it had been advected, as shown for three angles in figures 3.4 and 3.5. These changes are aligned parallel to the angle of rotation, α. When using scheme v1 at smaller angles the cosine bell is distorted slightly from its circular shape and a slight damping of the peak is observed. When there is advection over the pole a dent forms in the cosine bell resulting in a shift of mass from the front to the back of the distribution. In comparison, when using scheme v2 the result of using a linear meridional

interpolation is shown as an increased damping of the cosine bell peak and the spreading of the cosine bell in the meridional direction. If both of the schemes are compared using a linear meridional interpolation then few differences can be identified.

Figure 3.8 showed that, when advection is by analyses, using scheme v2 results in a higher level of mass conservation than using scheme v1. However, this new scheme is also less stable and requires the use of a smaller time step in addition to the use of a linear meridional interpolation. Therefore, a decision has to be made between an improved mass conservation or a longer time step. Since only the 8 month period is considered here scheme v2 with a linear meridional interpolation will be used.

The parent model for ERA-Interim shows mass conservation to a degree of 0.3% change over a year (Berrisford *et al.*, 2011) which is smaller than the 0.8% mass gain observed in these experiments when using the full resolution ERA-Interim. Experiments using 12 hourly analyses, rather than 6 hourly, revealed that the temporal truncation also has an impact on the mass conservation and is a likely source for some of the discrepancy between the known mass conservation of ERA-Interim and that observed here.

Figure 3.14 summarises the rate of numerical mass change per day over a two month simulation for the various experiments carried out. Using ERA-Interim an approximately linear relationship was observed between the horizontal resolution and numerical mass gain with the full resolution (T255) having the best mass conservation. A comparison of ERA-Interim and the ECMWF operational analyses, both truncated to T159, highlights the importance of spatial truncation. Both analyses use similar cycles of the ECMWF IFS but the operational analyses have to undergo a larger spatial truncation in order to be used at T159. As a result of this the operational analyses result in a numerical mass change that is 7 times greater than that produced by ERA-Interim at the same resolution.

Experiments using an ozone passive tracer initialised above 54.6 hPa revealed that if pressure co-ordinates are used then the model is highly mass conservative. This remaining error is due to the temporal truncation, as well as due to a possible difference in the spatial discretisation between the model and the IFS used for the analyses. The reason for this increased conservation is linked to the pseudo-density, as pressure co-ordinates result in a pseudo-density that is a uniform constant. In other words the mass of each grid box cannot vary with time. If pressure co-ordinates are not used then the pseudo-density is allowed to

vary and the error introduced through the spatial and temporal truncation of the surface pressure is fed into the calculation of pressure on model η-levels.

The effects of spatial truncation have a notable implication when considering CTMs that are driven offline by either analyses or a GCM. The implication being that re-analyses have a distinct advantage over operational analyses due to the fact that the whole atmospheric system is modelled at a lower resolution that is more consistent with an affordable CTM or GCM resolution. It is advantageous, in terms of reducing the numerical non-conservation, to use analyses that are closest in resolution, without truncation, to that of the CTM/GCM being used. Using a reduced temporal truncation, i.e. more frequent wind updates, is also beneficial.

Chapter 4

Stratospheric Ozone: Photochemical Change vs. Numerical Error

Three characteristic features of the evolution of stratospheric winter ozone make it an ideal test case for analysing numerical models. Since stratospheric ozone chemistry is, to a large degree, decoupled from the troposphere the simulation does not require a well defined boundary layer or the need to include surface emissions in the model. Tracers within the polar vortex show signs of tracer contour alignment over time as the flow is dominated by the polar vortex which stirs tracers, as discussed in Section 1.1.2 and considered further in Section 6.4. Ozone chemistry in the stratosphere is also less complicated than in the troposphere and well evaluated parameterisations of ozone chemistry exist. The need to evolve many chemical species is thus avoided. In the work presented here this particular test case will be used to study global conservation and the magnitude of these errors relative to the photochemical change in global ozone burden.

4.1 Background on Stratospheric Ozone

The photochemical lifetime of ozone in the stratosphere ranges from 3 years, at an altitude of 15 km, to 2 days at 40 km above the equator (Wayne, 2000). If lifetime is defined as 1/(reaction loss rate), and not the actual lifetime in the atmosphere which is determined by chemistry and mixing, then even with a much shorter lifetime than many of the major greenhouse gases such as methane (12 years) and carbon dioxide ($\sim$100 years), stratospheric ozone plays an important role in the atmosphere. In particular ozone absorbs ultraviolet light (the majority of UV-B and all UV-C) emitted by the sun. This absorption heats the stratosphere and contributes to the distinctive temperature profile of increasing tempera-

ture with height observed in this region of the atmosphere. Therefore, the loss of ozone that occurs over the Antarctic polar region during the Southern Hemisphere spring is very significant. To a large degree the ozone loss occurs at the vortex edges as it contains the lowest temperatures and is the first place to experience the return of sunlight at the end of polar winter (see Section 1.1.2 for information on the polar vortex).

4.1.1 Ozone Photochemistry and Distribution

The distribution of ozone is strongly influenced by atmospheric flow since this transports ozone throughout the atmosphere. Cold temperatures also play a role as they are essential for heterogeneous chemistry involving polar stratospheric clouds (PSCs), which will be outlined later. Figure 4.1(a) shows the zonal mean ozone distribution in ppmv from the climatology by Fortuin and Kelder (1998). A maximum in ozone is observed in the tropical stratosphere where it is formed through photochemical reactions, specifically the Chapman cycle (Wallace and Hobbs, 2006):

$$O_2 + h\nu \rightarrow O + O \tag{4.1}$$

$$O + O + M \rightarrow O_2 + M \tag{4.2}$$

$$O + O_2 + M \rightarrow O_3 + M \tag{4.3}$$

$$O_3 + h\nu \rightarrow O_2 + O \tag{4.4}$$

$$O + O_3 \rightarrow O_2 + O_2 \tag{4.5}$$

where M is an inert third body that ensures a conservation of energy and momentum. In the atmosphere M is typically nitrogen or oxygen. These reactions cover both the destruction and creation of ozone and, if not perturbed, a balance arises between O, O_2 and O_3 given the presence of photons with sufficient energy for the photodissociation reactions. The equilibrium concentration of ozone is (e.g. Houghton (1986)):

$$[O_3] = [O_2] \left(\frac{J_2 k_2 [M]}{J_3 k_3} \right)^{\frac{1}{2}}$$

where the square brackets represent concentrations and $[M]$ represents the concentration of all molecules (primarily oxygen and nitrogen), k_2 and k_3 are the reaction rates (s^{-1}) for reactions (4.3) and (4.5) respectively. The J_2 and J_3 terms are the dissociation rates per molecule per second for reactions (4.1) and (4.4) respectively.

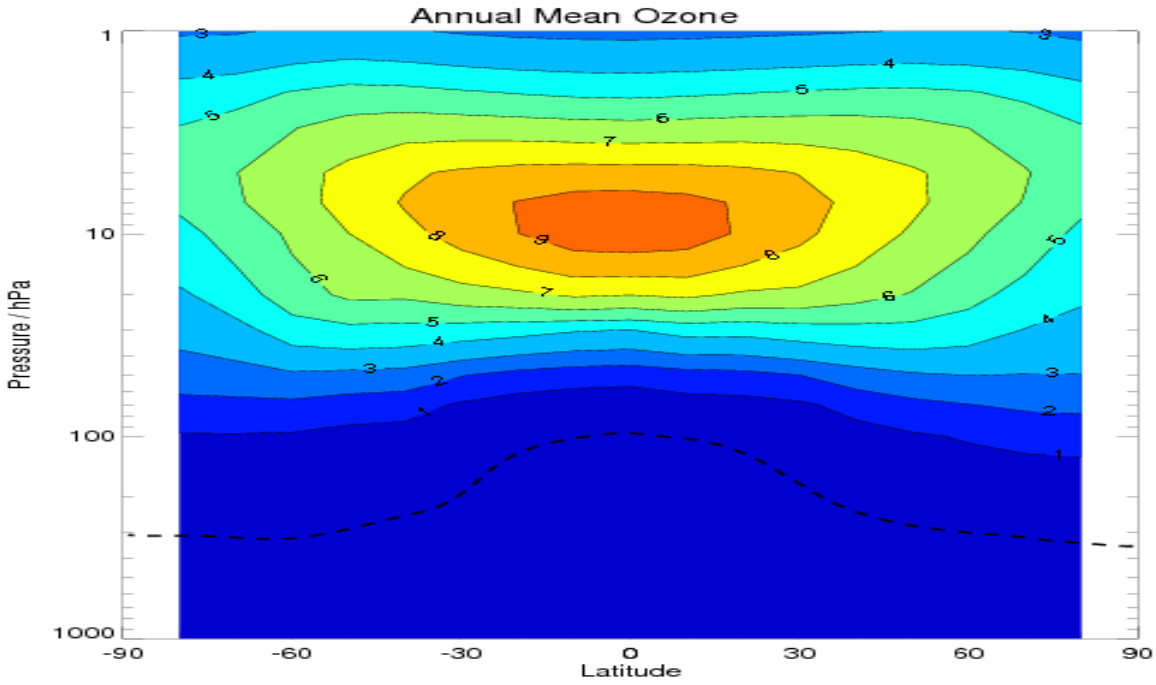

(a) Ozone

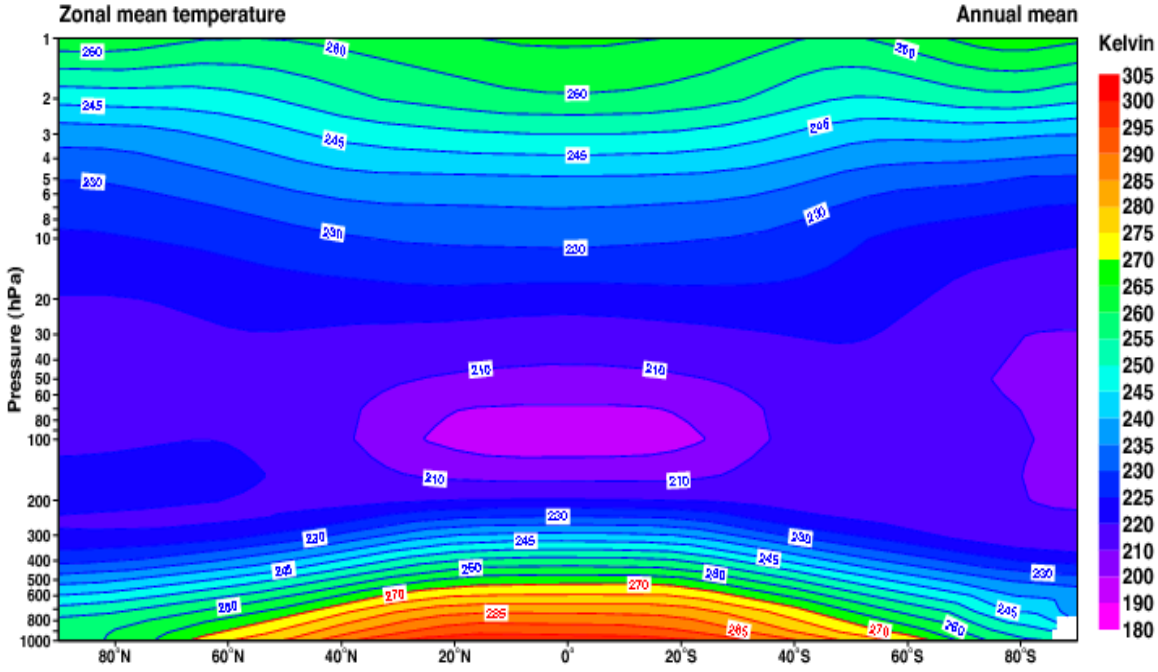

(b) Temperature

Figure 4.1: *(a)Annual zonal mean ozone distribution in ppmv from the ozone climatology by Fortuin and Kelder (1998). (b)Annual mean of the zonal mean temperature in K taken from the ERA-40 atlas.*

The amount of ozone in a column of the atmosphere can be measured in Dobson Units (DU). One DU is equivalent to a 1 mm thick layer of ozone at the surface under standard pressure and temperature of 1013 hPa and 273 K (`jwocky.gsfc.nasa.gov/dobson.html`). Alternatively, 1 DU=2.69×10^{16} ozone molecules cm^{-2}. The ozone column, S, can be calculated from the ozone mass mixing ratio, χ, via the equation

$$S = \frac{1}{g}\int_0^{p_s} \chi dp \tag{4.6}$$

where g is the acceleration due to gravity and p is pressure.

Figure 4.2 shows the annual mean distribution of the ozone column using satellite data from the Total Ozone Mapping Spectrometer (TOMS) over the period 1979-1992. Contrary to the zonal mean mixing ratio in the mid-stratosphere ($\sim$10 hPa) there is a minimum in the ozone column in the tropics and a maximum at mid-latitudes in both hemispheres. This occurs because the ozone in the troposphere and lower stratosphere dominates in the ozone column calculation due to the exponential decrease in air density with height. If a height of 50 hPa is considered in figure 4.1(a) then there is indeed more ozone at higher latitudes than in the tropics.

As stated in Section 1.1.2 the motion of ozone in the stratosphere is primarily determined by the Brewer-Dobson circulation (figure 1.3). In the Southern Hemisphere the ozone maximum at mid-latitudes is not as large as that in the Northern Hemisphere, the reason for this asymmetry being that the transport in the Northern Hemisphere winter is stronger due to increased wave driving. Iwasaki *et al.* (2009) showed that in re-analyses the general structure of the Brewer-Dobson circulation is well represented, but some of the details of the circulation are not identical in all the different re-analyses that are available. However, Iwasaki *et al.* (2009) do note that ERA-Interim contains less spatial and temporal noise due to the use of, for example, 4D-Var, improved model physics and the implementation of variational bias corrections.

It was noted above that there is a link between the ozone distribution and temperature. Figure 4.1(b) shows the annual mean of the zonal mean temperature from ERA-40. A comparison with the annual mean ozone shows that the region above the tropopause where there is a positive gradient in ozone with height corresponds with the positive gradient in temperature with height above the cold point at the tropical tropopause. The gradient in the temperature field becomes stronger as the height of the ozone maximum is approached

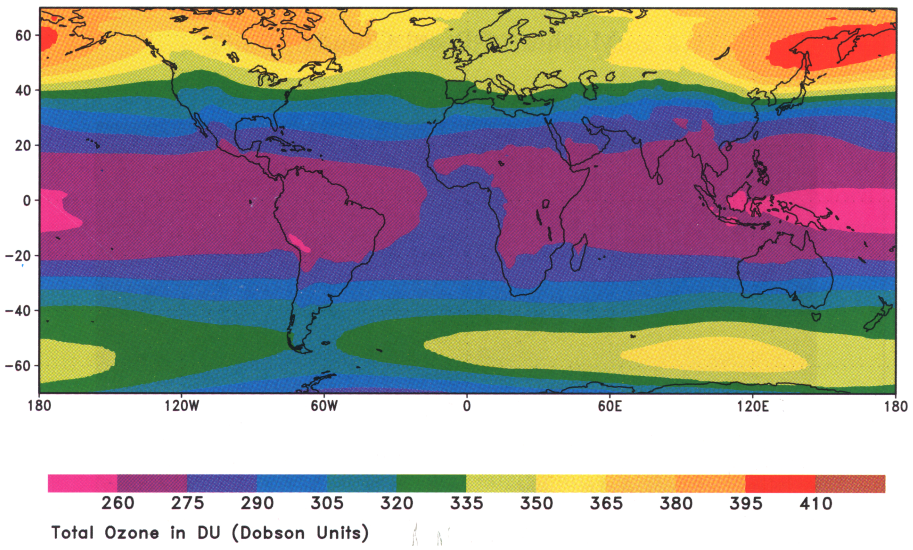

Figure 4.2: *Annual mean distribution of ozone column in DU from the 1979-1992 TOMS data. Taken from Labitzke and van Loon (1999).*

(10 hPa). When there is more ozone the temperature is warmer due to the absorption of incoming solar radiation by ozone, especially in the ultraviolet part of the spectrum, which produces a warming. The opposite is also true in that a region of lower ozone corresponds to cooler temperatures as less solar radiation is absorbed. Above 10 hPa the temperature in figure 4.1(b) continues to increase even though ozone concentration decreases due to the fact that the majority of the solar radiation is absorbed at these greater heights due to the efficiency of ozone as an absorber of solar radiation.

4.1.2 The Stratospheric Ozone Hole

The ozone hole is considered as a region where the ozone column goes below 220 DU (Wallace and Hobbs, 2006), which is lower than the annual mean in the tropics shown in figure 4.2. The earliest papers that provides details of the ozone hole was published by Farman *et al.* (1985) who considered how the release of additional chlorine in the atmosphere enhances natural ozone removal in spring. Solomon *et al.* (1986) presented further work on the ozone hole and using sonde data showed that the changes in ozone were occurring at an altitude of 10-20 km during the August-October period. It is also mentioned that the homogeneous chemistry known at the time could not fully explain the loss in ozone that was observed and that the presence of polar stratospheric clouds (PSCs) provided the ideal surfaces for heterogeneous chemistry. In the same year Crutzen and Arnold (1986) also published details about the potential role of PSCs in ozone loss.

Many of the ozone destroying chemicals that create the ozone hole have been, or are being, emitted through human activity. Of particular interest with regards to ozone are CFCs, the ozone destroying potential of which has been known a long time as can be seen in Molina and Rowland (1974). In the presence of sunlight CFCs photolyse to release chlorine (Cl) atoms which in turn react in a catalytic cycle with ozone that is described later. What is problematic is that many ozone destroying chemicals have lifetimes on the order of a half a century and so even though the emission levels have been seriously reduced (and CFCs are now prohibited) they are long-lived in the atmosphere. Figure 4.3 shows the predicted future levels of various ozone depleting substances. The figure shows that for many CFCs a decrease in concentration has only recently been observed following implementation of the Montreal Protocol (1989) and even by the end of this century total CFC removal is not predicted. Methane (CH_4) and nitrous oxide (N_2O) also play a role in ozone chemistry but the emissions of these gases are not controlled. They are primarily produced through agriculture and farming.

Photochemistry of ozone hole formation

As mentioned in Section 1.1.2 the dynamics of the Southern Hemisphere permit a considerably colder polar vortex than that in the Northern Hemisphere to form. With temperatures maintained at below -80° Celsius more PSCs, consisting mainly of frozen nitric acid, can form during the polar night. On the surface of these frozen crystals heterogeneous chemistry takes place which serves to produce chemically active chlorine. Chlorine activation describes the conversion of Cl_y (reservoir chlorine) to Cl_x (active chlorine). More specifically chlorine is converted from the form of HCl and $ClONO_2$ to HOCl and Cl_2. The reactions that occur are:

$$HCl + ClONO_2 \rightarrow Cl_2 + HNO_3 \tag{4.7}$$

$$ClONO_2 + H_2O \rightarrow HOCl + HNO_3 \tag{4.8}$$

$$HOCl + HCl \rightarrow Cl_2 + H_2O \tag{4.9}$$

$$HOBr + HCl \rightarrow BrCl + H_2O \tag{4.10}$$

The Cl and Br (bromine) radicals produced through the photolysis of Cl_2 and BrCl at the end of polar night, and the return of sunlight to the polar region, react with and destroy ozone. In the stratosphere there are many catalytic cycles that destroy odd oxygen such

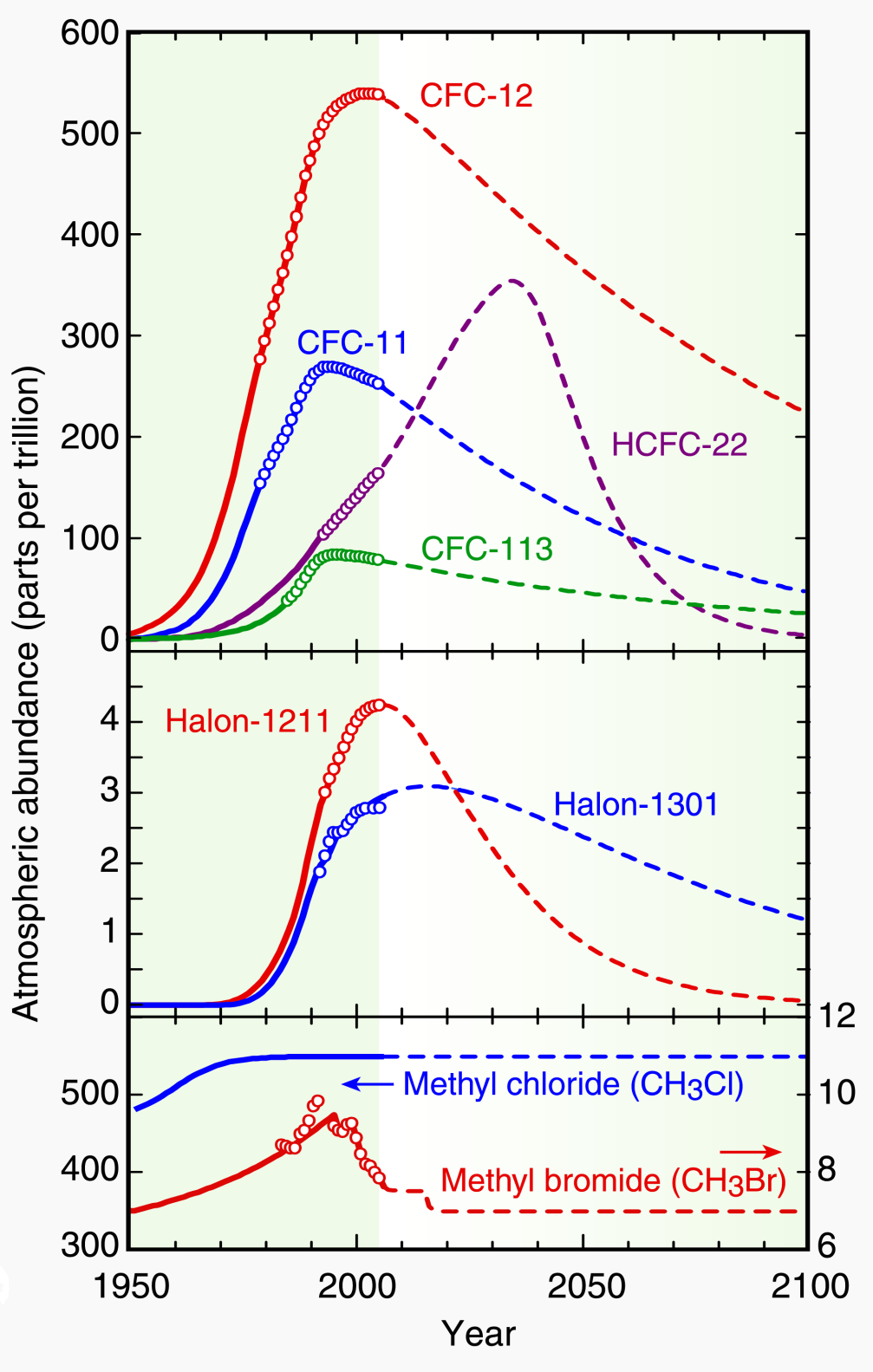

Figure 4.3: *Past and estimated future atmospheric concentrations of various halogens and CFCs from* `www.esrl.noaa.gov/csd/assessments/2002/qandas16.pdf`. *Solid lines are estimates of concentrations, circles are observations and dashed lines are future projections.*

as ozone. A catalytic cycle is one where a molecule, such as ClO, can destroy potentially thousands of ozone molecules as it is unchanged (i.e. not destroyed) during the chemical processes. Among these catalytic cycles are the Cl-ClO, NO-NO_2 and OH-HO_2 cycles. All of these catalytic cycles can be specified as follows:

$$\begin{aligned} X + O_3 &\rightarrow XO + O_2 \\ XO + O &\rightarrow X + O_2 \\ \text{Net: } O + O_3 &\rightarrow O_2 + O_2 \end{aligned}$$

where X is any of the reactive species previously stated. More details can be found in Dessler (2000). Lary (1997) also presents details on the various catalytic cycles in the stratosphere that destroy ozone, including the loss rates resulting from the various catalytic cycles and, where appropriate, their chain lengths (i.e. how many ozone molecules it can destroy). The Cl-ClO cycle is very effective at destroying ozone in the stratosphere and Lary (1997) states a chain length of greater than 10 throughout most of the stratosphere and up to 1000 in the upper stratosphere. However, this catalytic cycle will not work in the lower stratosphere, where the ozone hole forms, due to an insufficient quantity of oxygen atoms. Instead, ozone loss is driven by the ClOOCl molecule, also known as the 'ClO dimer', via reactions such as:

$$\begin{aligned} ClO + ClO + M &\rightarrow ClOOCl + M \\ ClOOCl + h\nu &\rightarrow Cl + ClO_2 \\ ClO_2 + M &\rightarrow Cl + O_2 + M \\ 2\times: \; Cl + O_3 &\rightarrow ClO + O_2 \\ \text{Net: } O_3 + O_3 &\rightarrow O_2 + O_2 + O_2 \end{aligned}$$

It is important to note that photolysis is required to produce the X species that cause ozone loss. Therefore, ozone loss does not occur during the polar night, but as it ends. Due to the progression of the terminator (the region between polar night and sunlight) ozone loss occurs at the edges of the vortex where sunlight first returns. Air that has a lower ozone concentration then moves closer to the pole as the vortex, and the terminator, moves; transport and chemistry are coupled. This coupling will be highlighted further in Chapter 6 (Section 6.4) where tracer-tracer relationships are considered using scatter plots.

The loss of ozone acts as a positive feedback within the polar vortex dynamics. In the stratosphere ozone absorbs short wave solar radiation, which in turn warms the stratosphere.

The decrease in the level of ozone means that the region remains at colder temperatures due to a reduced heating rate. The continuation of these colder temperatures in turn prolongs the conditions under which ozone can be destroyed.

The key determining factor for the absence of such pronounced ozone loss over the Arctic is simply that the temperatures are not always maintained low enough to allow the formation of the PSCs, which are a key trigger for ozone loss to occur. In years when temperatures are low enough then ozone loss has been observed, as presented in Bregman *et al.* (1997), Hoppel *et al.* (2002) and Chipperfield *et al.* (2005). It is often observed that there is a significant loss of ozone in the Arctic, but due to the dynamical resupply of ozone to the region no, or small, ozone holes form.

Ozone Hole Collapse

With the collapse of the polar vortex in October (in the Southern Hemisphere) the ozone depleted air is no longer contained over the polar region and is stirred with air from the mid-latitudes, eventually mixing. Also, around the outside of the polar vortex a region of high ozone concentration forms. This is likely to be a combination of photolytic ozone production and transport of ozone into the region from above due to the Brewer-Dobson circulation. When the polar vortex collapses the ozone depleted air can mix with the region of higher ozone concentration. Transport of ozone depleted air on the break up of the polar vortex into the mid-latitudes in the Northern Hemisphere was presented in Piani *et al.* (2002). At heights greater than 450 K an increased transport of the ozone depleted air to lower latitudes was observed, while ozone at lower levels is confined more poleward. By the end of December the ozone hole is no longer present in the Southern Hemisphere, i.e. the minimum ozone column has a value above 220 DU (figure 4.5).

In summary the ozone hole forms over the Antarctic due to colder temperatures and fewer Rossby waves resulting in a more stable polar vortex with a stronger circulation than over the Arctic. A more stable vortex means that it has a longer duration and as a result isolates the air within it for longer. The isolation, low temperatures, and associated photolysis of active chlorine and catalytic reactions on PSCs with the return of sunlight at the start of spring results in large scale ozone loss within the polar vortex.

4.2 Ozone Parameterisation

Stratospheric ozone chemistry is complex and in chemical transport models (CTMs) the mechanisms are usually reduced. Examples of these chemistry models are TOMCAT, SLIMCAT (Chipperfield (1999) and Chipperfield (2006)) and MOZART (Brasseur *et al.*, 1998). The SLIMCAT and TOMCAT models advect 43 chemical species and have 86 chemical and 29 photolytic reactions. This is very similar to MOZART which advects 50 chemical species and has 112 chemical and 28 photolytic reactions. An alternative approach is to parameterise the chemistry using a scheme such as that in Cariolle and Teyssédre (2007).

The parameterisation chosen to be used here is a simple linear ozone parameterisation that represents the stratospheric ozone photochemistry. The parameterisation is shown in equation (4.11) and was published in this form in Cariolle and Teyssédre (2007), which is an improved version of the one originally published by Cariolle and Déqué (1986). The parameterisation was developed as a way to retain the key features of the ozone chemistry without the inherent complexity of using a full chemistry scheme. The equation is obtained in this form by taking the ozone continuity equation and expanding it using a Taylor series. Only the terms up to the first order for the local ozone mixing ratio, temperature and ozone column values are retained. All terms in the angular brackets are the zonal monthly mean values taken from the 2D photochemical model MOBIDIC (see `www.astr.ucl.ac.be/index.php?page=MoBidiC%40Description` for details). The coefficients are contained in a two dimensional array that depends only on latitude and pressure.

$$\frac{Dr}{Dt} = \langle P - L \rangle + \left\langle \frac{\partial (P-L)}{\partial r} \right\rangle (r - \langle r \rangle) + \left\langle \frac{\partial \, (P-L)}{\partial T} \right\rangle (T - \langle T \rangle) + \left\langle \frac{\partial (P-L)}{\partial S} \right\rangle (S - \langle S \rangle) - R_{het} r \tag{4.11}$$

P and L are the gas phase photochemical production and loss of ozone respectively. The first term on the right-hand side represents the monthly zonal average net production at a point. Term two is the change in ozone volume mixing ratio, r, associated with a deviation from the mean, $\langle r \rangle$. Next is the term that represents the change associated with the temperature deviations and the fourth term is the radiation term, so called since the column ozone, S (in units of molecules cm^{-2}), above a point determines the amount of solar radiation that reaches that location and hence the level of photochemistry that can occur.

The final term is the heterogeneous chemistry term and represents the chemistry that will

cause the formation of the ozone hole. This term has two conditions that represent the requirements that both PSCs and sunlight are required for this chemistry to take place. Firstly, the temperature must be below 195 K and, secondly, the solar zenith angle must have an angle less than 87 degrees (i.e. above the horizon). Both of these conditions at latitudes greater than 45 degrees will result in the activation of this heterogeneous chemistry term. R_{het} then varies depending on pressure and latitude, but is zero in the tropics. The values of the coefficient are dependent on the concentration of chlorine in the atmosphere with the simple equation:

$$R_{het} = \frac{1}{\tau_0}\left(\frac{[Cl_x]}{2ppbv}\right)^2 \tag{4.12}$$

where τ_0 is the destruction timescale of ozone and has a value of 8 days and [Cl_x] is the concentration of chlorine. This allows the value of R_{het} to be recalculated for any year being modelled. The 2 ppbv on the denominator ensures that a chlorine concentration of 2 ppbv will result in an ozone loss rate of 8 days. The calculation of R_{het} has included the assumption that all of the required processes (i.e. PSC formation, chlorine activation, etc.) occur simultaneously and stop as soon as the temperature or sunlight condition is no longer met. The R_{het} term for September is shown in figure 4.4(e). The pressure and latitude dependence is easily seen, as is the zero value in the tropics due to conditions for heterogeneous chemistry never being met in this region. The asymmetrical nature of the loss is also clearly seen with an enhancement in the winter hemisphere where conditions are more favourable for the chemistry to occur.

The linear ozone parameterisation shown in equation (4.11) is implemented after the advection at each time step using a mixed explicit-implicit scheme that is stable and second-order in mixing ratio. Any terms that are not dependent on the ozone mixing ratio, r, are treated explicitly. The first stage of this discretisation is:

$$\begin{aligned}\frac{r^{n+1}-r^n}{\Delta t} &= \frac{1}{2}\left[\left(\left\langle\frac{\partial(P-L)}{\partial r}\right\rangle^{n+1} - R_{het}^{n+1}\right)r^{n+1} + \left(\left\langle\frac{\partial(P-L)}{\partial r}\right\rangle^{n} - R_{het}^{n}\right)r^{n}\right] \\ &\quad +\beta^n - \left\langle\frac{\partial(P-L)}{\partial r}\right\rangle^n \langle r\rangle^n \end{aligned} \tag{4.13}$$

$$\beta^n = \langle P-L\rangle^n + \left\langle\frac{\partial(P-L)}{\partial T}^n\right\rangle (T-\langle T\rangle)^n + \left\langle\frac{\partial(P-L)}{\partial S}\right\rangle^n (S-\langle S\rangle)^n$$

where n refers to values at time t and $n+1$ are the values at $t+\Delta t$. Rearranging so that the equation can be solved for r^{n+1} produces equation (4.14) which is the scheme as applied

in the model:

$$r^{n+1}\left(1-\frac{\Delta t}{2}\left(\left\langle\frac{\partial(P-L)}{\partial r}\right\rangle^{n+1}-R_{het}^{n+1}\right)\right)=\Delta t\beta^{n}-\Delta t\left\langle\frac{\partial(P-L)}{\partial r}\right\rangle^{n}\langle r\rangle^{n}$$
$$+r^{n}\left(1+\frac{\Delta t}{2}\left(\left\langle\frac{\partial(P-L)}{\partial r}\right\rangle^{n}-R_{het}^{n}\right)\right) \quad (4.14)$$

In order to use the parameterisation a bilinear interpolation was used in order to transfer the coefficients from the latitude-pressure grid provided with the scheme onto the tracer model grid. The coefficients are not interpolated in time, but simply updated at the start of each month. The temperature, T, is interpolated linearly in time between the analyses records, which are every six hours.

The coefficients for the month of September, after the bilinear interpolation has been carried out, are shown in figure 4.4. The temperature, radiation and photochemical production terms have been weighted by the monthly global mean tracer mixing ratio, r_0, so that the coefficients are given in the form of rates (s^{-1}). r_0 is the weighted, taking into account both altitude and latitude, global average $\langle r\rangle$. Since this is the same at all latitude and height points any structure seen in the images in figure 4.4 is due to the coefficients. Note that the various rates range in size by several orders of magnitude, with the heterogeneous chemistry being the smallest and the temperature dependent rate the largest. However, since temperature perturbations are fractionally small relative to $\langle T\rangle$ this does not mean that the temperature term dominates in equation (4.11). Even though figure 4.4 shows R_{het} values in the lower troposphere conditions are not met for them to be used. One final point to note is that all of the coefficients produce smooth distributions, apart from $\langle P-L\rangle/r_0$. This likely arises due to the fact that the other coefficients are concerned with the change in $(P-L)$ and so produce smoother distributions, whereas $\langle P-L\rangle$ is determined through the effects of chemistry and transport, neither of which act uniformally over extensive regions.

The rate coefficients of equation (4.11) can be determined, and of particular interest is $\langle\partial(P-L)/\partial r\rangle$, the photochemical relaxation rate. If all other terms in the parameterisation are constant then this is the rate at which the ozone distribution is driven back towards the prescribed 2D state, $\langle r\rangle$. Table 4.1 shows the maximum, minimum and mean of this rate, and the other four rates, over the entire 12 months. The difference in signs for the coefficients shows the dominance of some terms in creating ozone and others in destroying ozone. There is also a large range in the orders of magnitude amongst the terms showing the variability throughout the year of the various terms.

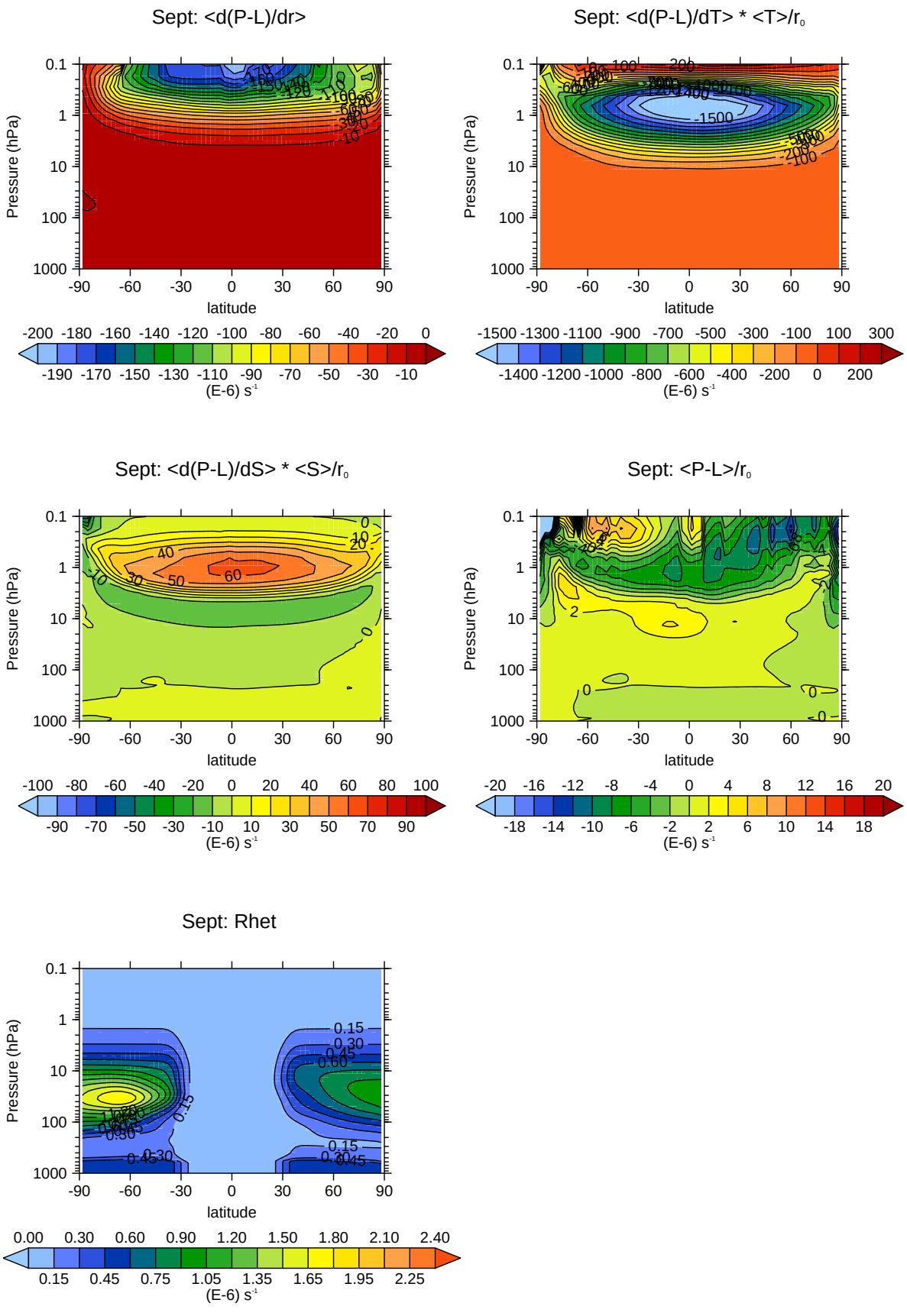

Figure 4.4: *Zonal mean rates from the coefficients in equation (4.11) for the month of September interpolated onto the model grid. r_0 is the monthly mean ozone mixing ratio for September calculated using $\langle r \rangle$. Note the change in scales.*

Timescale	Max	Min	Mean
$\left\langle \frac{\partial(P-L)}{\partial r} \right\rangle$	1.67E-8	-2.47E-4	-1.33E-5
$\left\langle \frac{\partial(P-L)}{\partial T} \right\rangle \frac{\langle T \rangle}{r_0}$	3.96E-4	-1.98E-3	-9.74E-5
$\left\langle \frac{\partial(P-L)}{\partial S} \right\rangle \frac{\langle S \rangle}{r_0}$	8.36E-5	-1.03E-4	1.78E-6
$\frac{\langle P-L \rangle}{r_0}$	2.90E-5	-1.28E-4	-2.77E-6
R_{het}	2.31E-6	0	3.21E-7

Table 4.1: *Max, min and mean of the five rates used in the ozone parameterisation (4.11) over all months. All values have units of s^{-1}. The reciprocal of these values provides the respective timescales.*

There are already known errors within the ozone parameterisation and, as such, some of the errors observed in the model runs to be presented can be put into context using literature that has already been published. In particular these deficiencies are presented in Cariolle and Teyssédre (2007) as well as an analysis presented in Geer *et al.* (2007), referred to as C07 and G07 respectively hereafter.

In G07 several ozone chemistry schemes are analysed and compared. For the most part G07 focuses on the ozone parameterisation presented in Cariolle and Déqué (1986), referred to as v1.0, and briefly mentions some results when using the update version of the parameterisation from C07. This is due to the fact that the later version of the parameterisation, referred to as v2.x (where x can be various numbers due to the continual alterations to the scheme), was only made available near the end of their study.

The known problems in the parameterisation with regards to the ozone background and Northern Hemisphere will briefly be detailed now. The Southern Hemisphere will be considered during the analysis of the results presented in the following section in order to highlight the deficiencies of the parameterisation in the model output.

Annual Mean Ozone Distribution

C07 present results when the ozone parameterisation was used in the Modélisation de la Chimie Atmosphérique Grande Echelle (MOCAGE), a multi-scale chemistry and transport model developed by Météo-France. The advection scheme is semi-Lagrangian and not

globally conservative. Analyses from the ECMWF were used to drive the advection at a resolution of T42 and the model has a one year spin up time. All of the main features of the ozone column distribution seen in TOMS are reproduced. These features are the equatorial minimum, spring maximum over high northern latitudes, mid-latitude ozone belt maxima in the southern mid-latitudes and the ozone hole, as seen in figure 4.2.

In C07 the main features of the zonal mean ozone distribution are reproduced by the parameterisation with the ozone maximum in the tropics located in the correct place. C07 found that the ozone parameterisation was able to reproduce ozone variability over the polar regions, such as the formation of the ozone hole. The mean ozone distribution has the largest differences from HALOE (Halogen Occultation Experiment) at the tropopause and from the climatology of Fortuin and Langematz (1994) (+40%) in the troposphere. Since a representation of the mean ozone distribution is required, the differences from the climatology could be considered to be of greater significance than the differences from HALOE. At low and mid-latitudes the differences are below 15% when in the altitude range 15-40 km.

Northern Hemisphere

In the study of the ozone parameterisation presented in C07 for the Northern Hemisphere mid and high latitudes the main features of the seasonal variation are produced, but the scheme overestimates the polar ozone in the Spring and Autumn by 60-80 DU. The results obtained from the model used in this thesis do not show the same overestimate in the Northern Hemisphere, and obtain similar column ozone values as shown in OMI (Ozone Monitoring Instrument) satellite data, except regions of low ozone column are absent. This is probably due to the heterogeneous chemistry term not being activated.

In C07 it was noted that there was an overestimation of ozone in the UTLS (upper troposphere lower stratosphere) region in particular. Two possible reasons for this are put forward in C07: not allowing enough ozone depletion in the parameterisation or excessive transport from the mid-latitudes by the ECMWF analyses. The use of the cold tracer (see Section 4.2.1) in the parameterisation was seen to improve, but not remove, the overestimation. The conclusion reached was that this was associated with an excessive meridional circulation in the analyses as it was not observed in MOBIDIC. In the seasonal evolution

at low latitudes there is a tendency to underestimate the column minima and the timing of the annual minimum is a month early.

In a newer parameterisation by Monge-Sanz *et al.* (2010) the incorporation of the heterogeneous chemistry into the other coefficients, rather than as a separate R_{het} term, produces more accurate results. This new formulation no longer has the temperature and solar zenith angle dependence for the heterogeneous chemistry and as such more chemistry can occur. In comparison to the parameterisation by C07 used in the ECMWF model, this new parameterisation produced an additional loss of 30 DU at northern high latitudes.

4.2.1 Cold Tracers

The scheme presented in C07 also has the option to include a cold tracer. A cold tracer is used to record the temperature history of the air parcel and therefore more accurately determine the degree of chlorine activation. Without a cold tracer the formation of active chlorine and the destruction of ozone is one instantaneous process when both conditions for R_{het} are met at the same time. Times when the temperature is cold enough for chlorine to activate but there is no sunlight to destroy ozone are not considered, but the active chlorine still exists. The cold tracer allows a more accurate quantification of the amount of active chlorine by keeping a record of the active chlorine that is created in the absence of sunlight.

G07 considered scheme v1.0 when the cold tracer is included and it was seen to remove the excess production of ozone by increasing the amount of heterogeneous chemistry that can take place. C07 also noted that the improved representation of the heterogeneous chemistry by using a cold tracer resulted in a deeper ozone hole and a later ozone hole recovery, resulting in better agreement with observations. As mentioned above, an alternative to a cold tracer is to use a scheme that incorporates heterogeneous chemistry more fully into the parameterisation, such as that developed by Monge-Sanz *et al.* (2010). This scheme shows the improvements in stratospheric ozone modelling that are obtained with the use of a cold tracer, but without the need for an additional complex tracer.

Many of the problems noted above in regards to ozone values that are too high in comparison to the observations will be seen to arise in the results presented below. However, since the aim of this work is a quantitative comparison of mass changes it is not essential for the

ozone tracer to be completely in agreement with the observations. The simple formation of the ozone hole is sufficient at this point.

4.3 Observations of the Ozone Hole

A year was chosen in which to see whether the model could produce an ozone hole in the Southern Hemisphere. Any recent year could have been used since they all have recorded observations and measurements that could be used for the comparison with the model. However, it would probably be best to avoid the 2002 ozone hole since this was an anomalous year due to the fact that this is the only Southern Hemisphere ozone hole split known to date. The 2006 ozone hole was chosen because it is the year that cycle 31r2, used for ERA-Interim, of the ECMWF IFS was made operational.

Figure 4.5 shows some ozone hole data over the 1979-2005 period taken from the TOMS/OMI (Total Ozone Mapping Spectrometer/Ozone Monitoring Instrument) dataset. The top image is the minimum column ozone value in the Southern Hemisphere and the bottom image is the evolution of the ozone hole area. The rapid growth in the ozone hole area is representative of the progression of the polar night terminator. The ozone hole area undergoes a slower rate of change when polar night has completely ended over the South Pole. The rapid growth in area coincides with a rapid decrease in the minimum ozone column value. This is also consistent with the end of polar night, with lower minimum values obtained as sunlight reaches the colder regions closer to the pole. In 2006 the ozone hole was one of the deepest on record and it also had the latest recovery (c.f. grey shading which shows the range from 1979-2005).

Figure 4.6 shows TOMS/OMI satellite data of the ozone hole on October 15th 2006, and will be used to compare with model results. The figure highlights the size and depth of the ozone hole on this one day by plotting the ozone column from the South Pole to 15S. A comparison with figure 4.5 reveals that this date is just after the maximum depth of the ozone hole has been reached in this particular year.

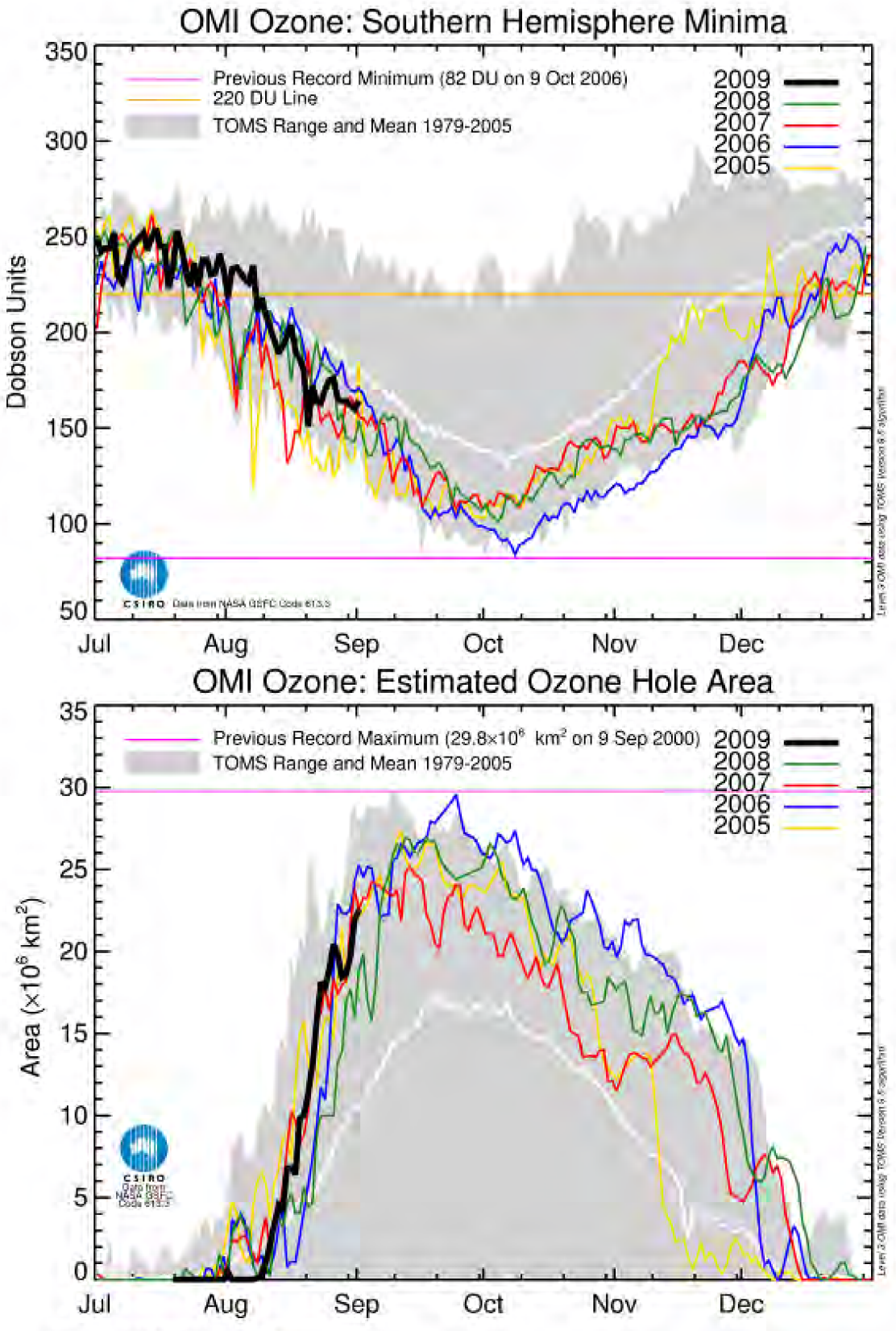

Figure 4.5: *The evolution of the ozone hole in terms of minimum column ozone in the Southern Hemisphere and ozone hole area. Data taken from TOMS/OMI. (www.environment.gov.au/atmosphere/ozone/publications/pubs/ozone-reports04sept09.pdf)*

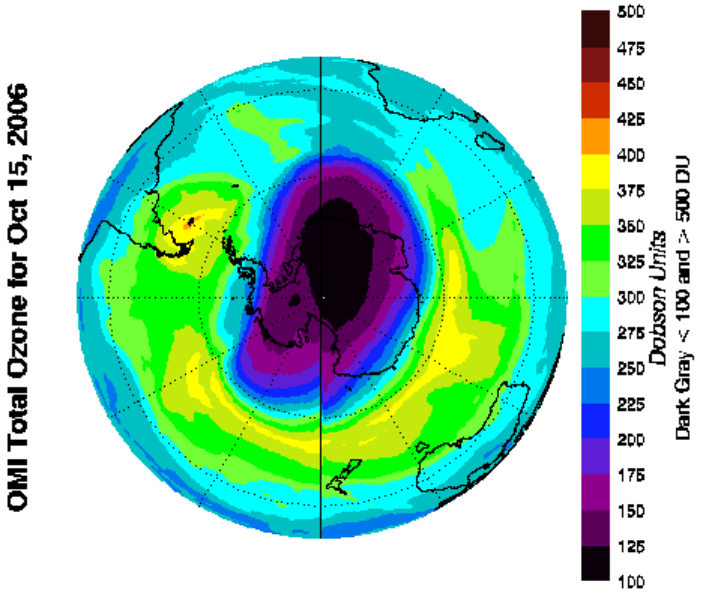

Figure 4.6: *Satellite data of the ozone hole on the 15th October 2006 from TOMS/OMI, showing both the area coverage and depth of the ozone hole using column ozone in Dobson Units (DU) (*`http://jwocky.gsfc.nasa.gov/ozone/ozone_v8.html`*). Rotated to make a comparison with figure 4.7.*

4.4 Advection by ERA-Interim

The first model run uses ERA-Interim at full resolution (T255L60) with a time step of 150 seconds. Photochemistry (equation 4.11) is included in order to create a chemically active ozone tracer. The model was initialised using the climatological zonal average ozone distribution from the C07 scheme, coefficient $\langle r \rangle$, and the model run covers the period April 1st 2006 to December 1st 2006. This gives the model four months to build up the ozone level over the south pole before the ozone loss is triggered by the return of sunlight at the start of the Southern Hemisphere spring.

Figure 4.7(b) shows the ozone column over the Southern Hemisphere which can be compared with the TOMS/OMI satellite data in figure 4.6. The extent of the ozone is comparable between the observations and the model and the gradients in the ozone column that represent the edge of the vortex, and hence ozone hole, are in approximately the same places. The shape and position of the ozone hole are primarily determined by the vortex and therefore by the re-analyses used in the model. The ozone column goes down to values of 150-175 DU, approximately 50 DU larger than in the observations, but the ring of high ozone column (375-400 DU) around the ozone hole is in the same DU range as the observations. C07 also show that in the Southern Hemisphere there are noticeable differences between their

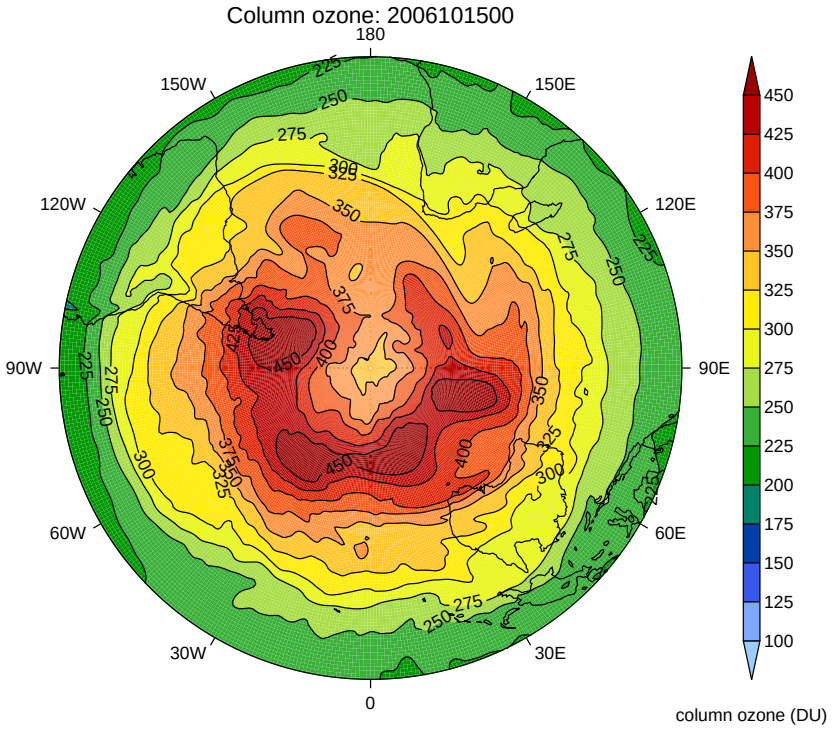

(a) Passive ozone

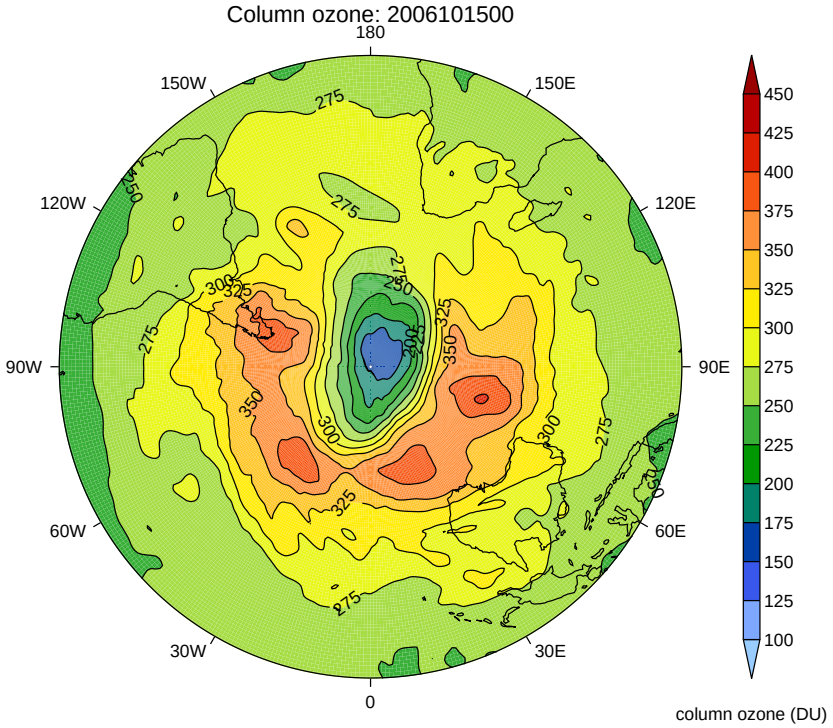

(b) Active ozone

Figure 4.7: *Ozone column on 15th October 2006 when using the (a) passive ozone tracer and (b) active ozone tracer advected by ERA-Interim at T255. Stereographic projection extends to the equator.*

model ozone column and TOMS. In the mid-latitudes the ozone column is underestimated by 20-40 DU throughout the year. This shows that some of the differences between the model results presented here and the observations are partially due to the representation of ozone photochemistry by equation (4.11).

The effect of the chemistry on the ozone column is easily seen by comparing figures 4.7(a) and 4.7(b). Since the main features of the distribution are determined through advection they can be seen in both the passive and active ozone images. The ozone chemistry acts to reduce the column ozone throughout the hemisphere, except in the tropics. This is most evident closer to the polar region where the chemistry counteracts the increase in ozone caused by the Brewer-Dobson circulation advecting ozone from the tropics to higher latitudes.

Cross sections through the tracer field from May to October are shown in figure 4.8 (with the image for April being the initialising field shown in figure 3.6). These can be compared with those for the passive tracer shown in figure 3.11. Due to the inclusion of the ozone chemistry parameterisation the model now maintains a distinct ozone maximum in the tropics and the overall shape of the distribution remains similar throughout the model run. Also, the ozone hole can be seen to form over the South Pole in the images for August to October. The ozone hole is initially seen in August as an intrusion of lower tracer values upwards in the region between 50-60S at around 40 hPa. This becomes more pronounced with time and spreads poleward with the progression of the polar night. As it spreads poleward this ozone loss is seen to reach heights of 10 hPa and has been circled in the cross section on 1st October (figure 3.11e). This is consistent with the vertical structure of the ozone hole as shown in van Peet *et al.* (2009), and appears to be a consequence of the temperature structure in the region preventing cold enough temperatures for the ozone loss from occurring at higher altitudes.

Figure 4.9 shows the percentage change in the global average mass mixing ratio of ozone when undergoing advection and chemistry. The purple line shows the resulting mass change when using ERA-Interim at T255. The dark green line shows the mass change for passive ozone at the same resolution and shows a change in global burden that is considerably smaller in magnitude than that caused by photochemistry. The reasons for the non-conservation of the passive ozone tracer were explained in Section 3.3. Between April and November the active ozone tracer shows a decrease in global average mass mixing ratio

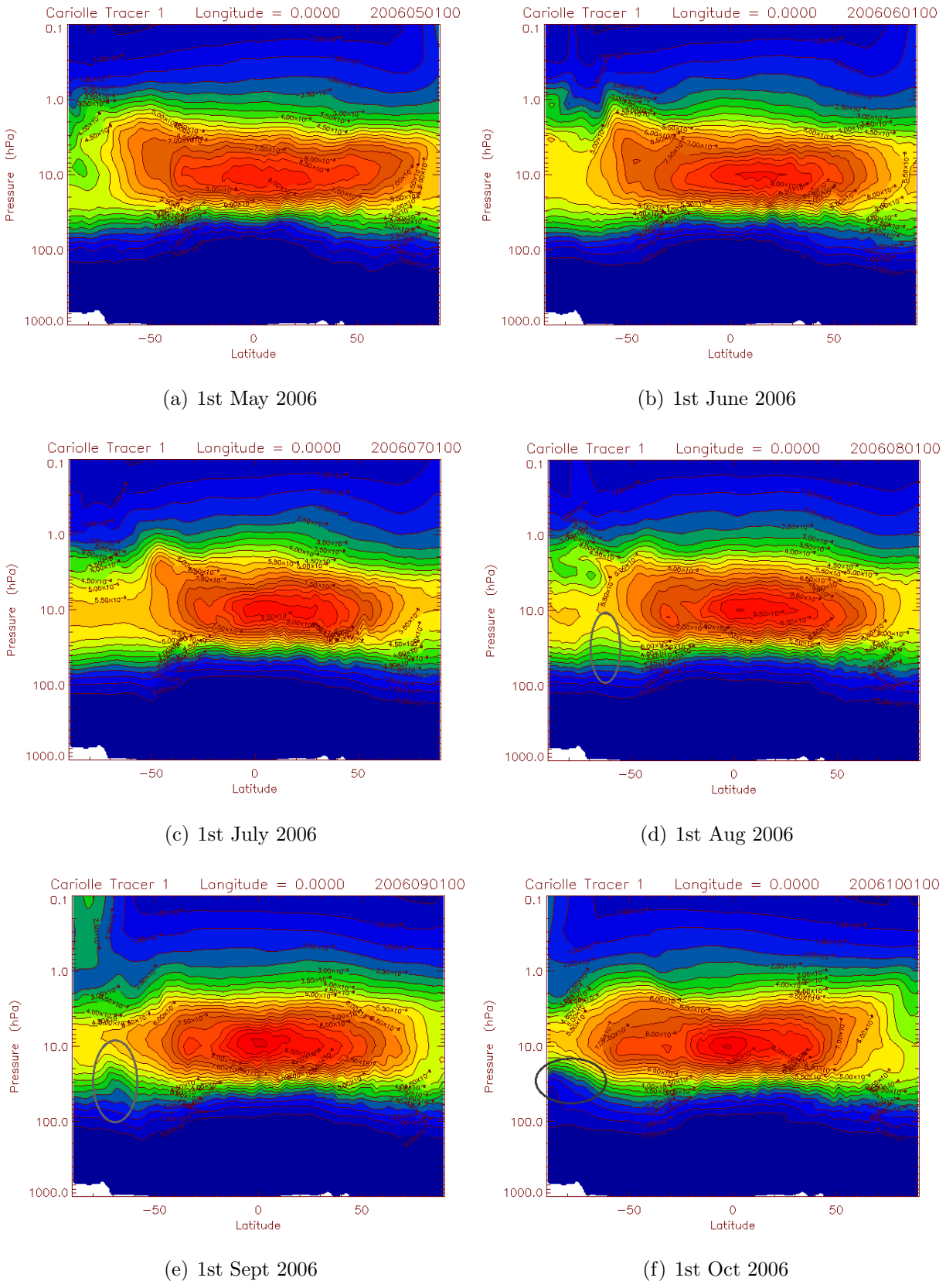

(a) 1st May 2006

(b) 1st June 2006

(c) 1st July 2006

(d) 1st Aug 2006

(e) 1st Sept 2006

(f) 1st Oct 2006

Figure 4.8: *Vertical cross sections through the active ozone tracer field at one month intervals with advection carried out using ERA-Interim at T255. Mixing ratio is plotted with a contour interval of 0.5 ppmv. In the last three images the ozone hole near the South Pole has been circled.*

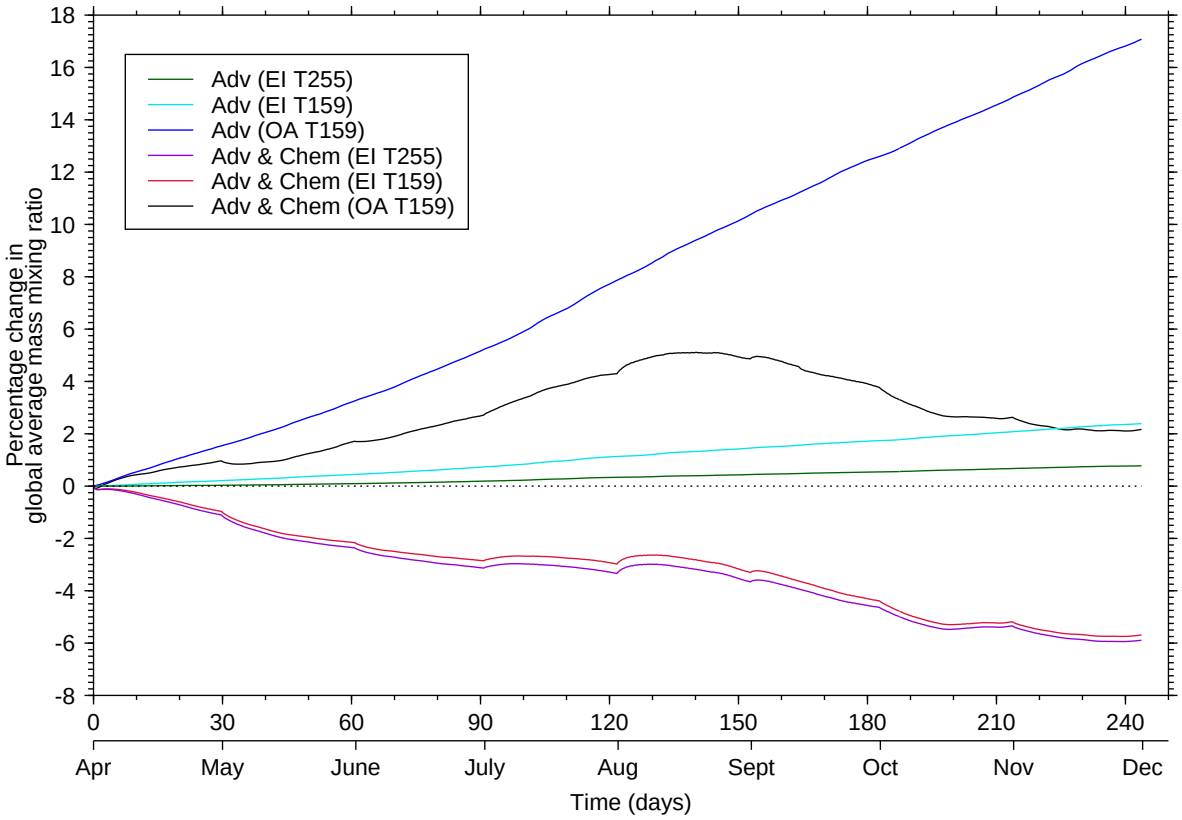

Figure 4.9: *Percentage change in global average mass mixing ratio of ozone as a passive and chemically active tracer when advected using operational analyses and ERA-Interim. It can clearly be seen that using ERA-Interim results in a higher level of mass conservation than the operational analyses.*

of approximately 6%. This can be compared to figure 4.10 which shows the global average ozone column calculated over two different decades (Wayne, 2000). The decrease from April to November was observed to be approximately 10-12 DU (3.5%) and is of comparable magnitude with that produced by the model.

One feature in figure 4.9 to note is the slight jumps in the change in global burden that occur at the start of every month. These occur due to a step change in the monthly coefficients used in equation (4.11). This is the method used in C07 and G07, although it is clearly artificial. If the aim was to have a completely accurate scheme then an interpolation between monthly coefficients could be carried out that would gradually change the coefficients and remove the discontinuities.

A typical measure of ozone hole depth is the minimum ozone column value poleward of 30S (`www.temis.nl/protocols/o3hole/`). In this work this will be increased to 70S, as shown in figure 4.11, due to the use of the passive tracer and the desire to calculate the lowest column value in the polar region. Comparing the OMI time series of minimum ozone value (figure 4.5) with that from the model it can be seen that at the start of July the model has

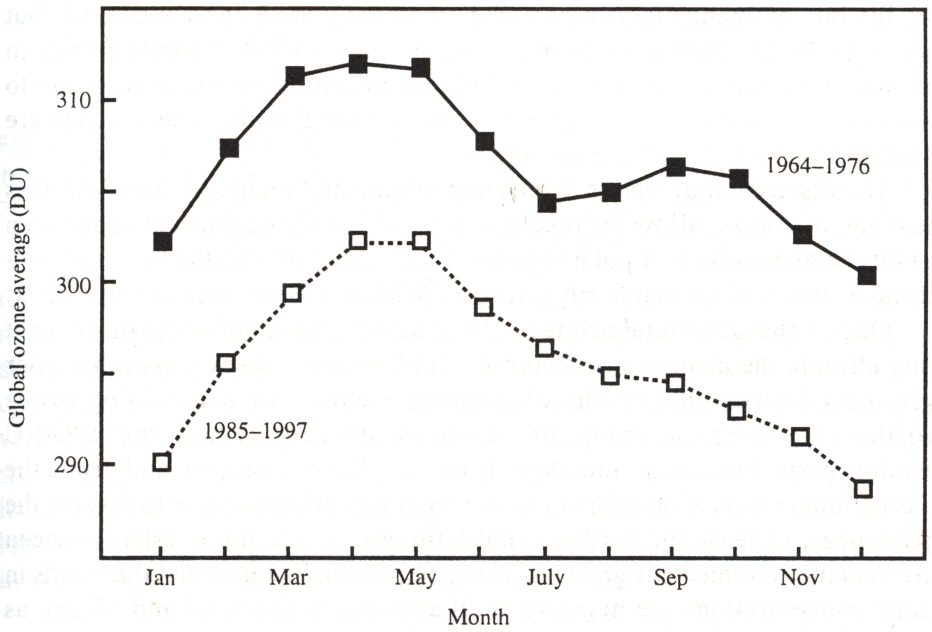

Figure 4.10: *Global average ozone concentration during two periods, figure 4.38 from Wayne (2000).*

a higher minimum column ozone value than was actually observed. As a result the timing error in ozone hole formation and development between the observations and the model is the consequence of a magnitude error as the model has a constant offset of approximately 45±15 DU. The largest difference is observed at the time of greatest mass loss (140 DU compared to 80 DU in the observations) with the difference being smallest at the start of July and December, this suggests that the observations detect a sharper rate of ozone loss and recovery than is produced by the photochemistry in the model. The model column minimum is also larger than that observed by C07, which at high latitudes was in the range 100-120 DU in late September, in good agreement with the observations in figure 4.5.

The ozone column minima in the model occur in early-mid October and again near the end of October. The first minimum coincides with that observed and shown in figure 4.5, with the second minimum showing that the ozone hole recovery in the model is slightly delayed. Figure 4.11 also shows the minimum column for the passive ozone tracer (green line) continually increases reflecting the effect of mixing reducing the contrast in the passive ozone field (as in figure 1.1).

C07 also found that the ozone hole recovery (i.e. column ozone values above 200 DU) occurred approximately two weeks early every year. This is in agreement with the model results shown in figure 4.11 where the ozone hole can be seen to potentially recover 10-14 days early if the general upwards trend in column ozone minimum is continued. As

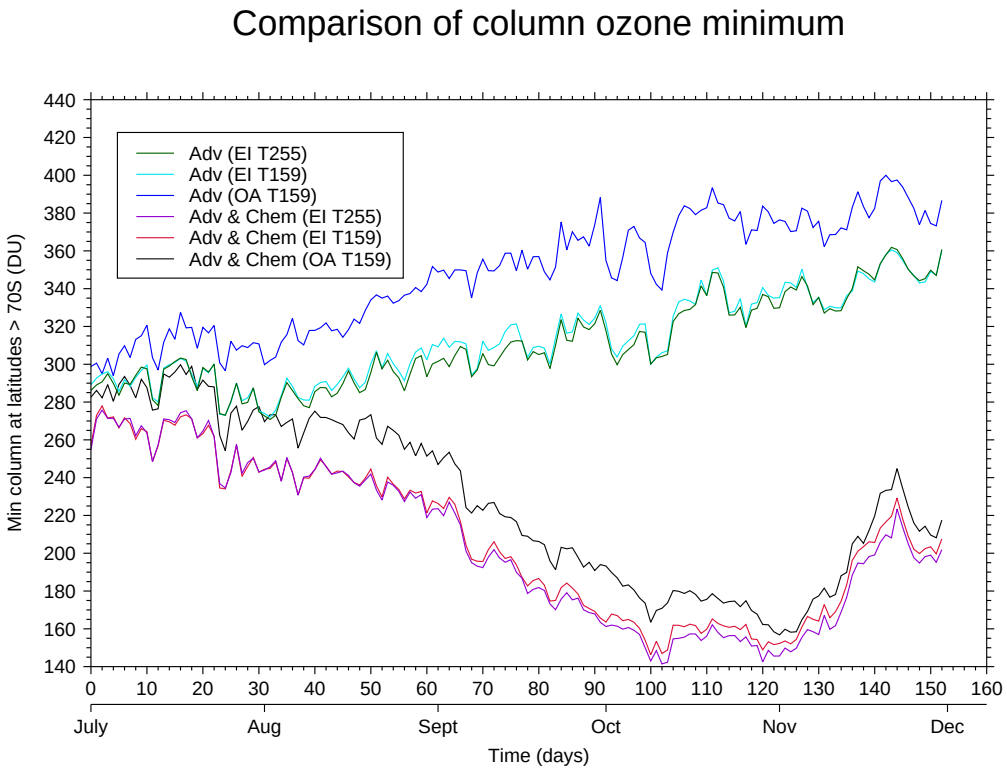

Figure 4.11: *Time series of the minimum ozone column value (DU) south of 70S when the ozone tracer is advected by the operational analyses at T159 compared to ERA-Interim at T159 and T255.*

mentioned above this early recovery is due to the fact that there are higher ozone column values throughout the ozone hole evolution.

4.4.1 Heterogeneous Chemistry Excluded

In this model run ERA-Interim at T255 is again used to drive the advection, but this time no heterogeneous chemistry is included (i.e. $R_{het} = 0$) in the evolution of ozone. As previously stated, it is already known that heterogeneous chemistry plays an important role in the formation of the ozone hole, but this model run makes it possible to determine just how significant the heterogeneous chemistry term is in equation (4.11). Figure 4.12 shows the monthly cross sections through the ozone field that have been previously presented for the passive ozone experiment in Chapter 3 (figure 3.11) and the model run above with heterogeneous chemistry included (figure 4.8).

As was the case when the heterogeneous chemistry is included, the ozone distribution maintains a well defined ozone maximum in the tropics due to the photochemical production and loss of ozone. Directly comparing figure 4.8 with figure 4.12 shows that the heterogeneous

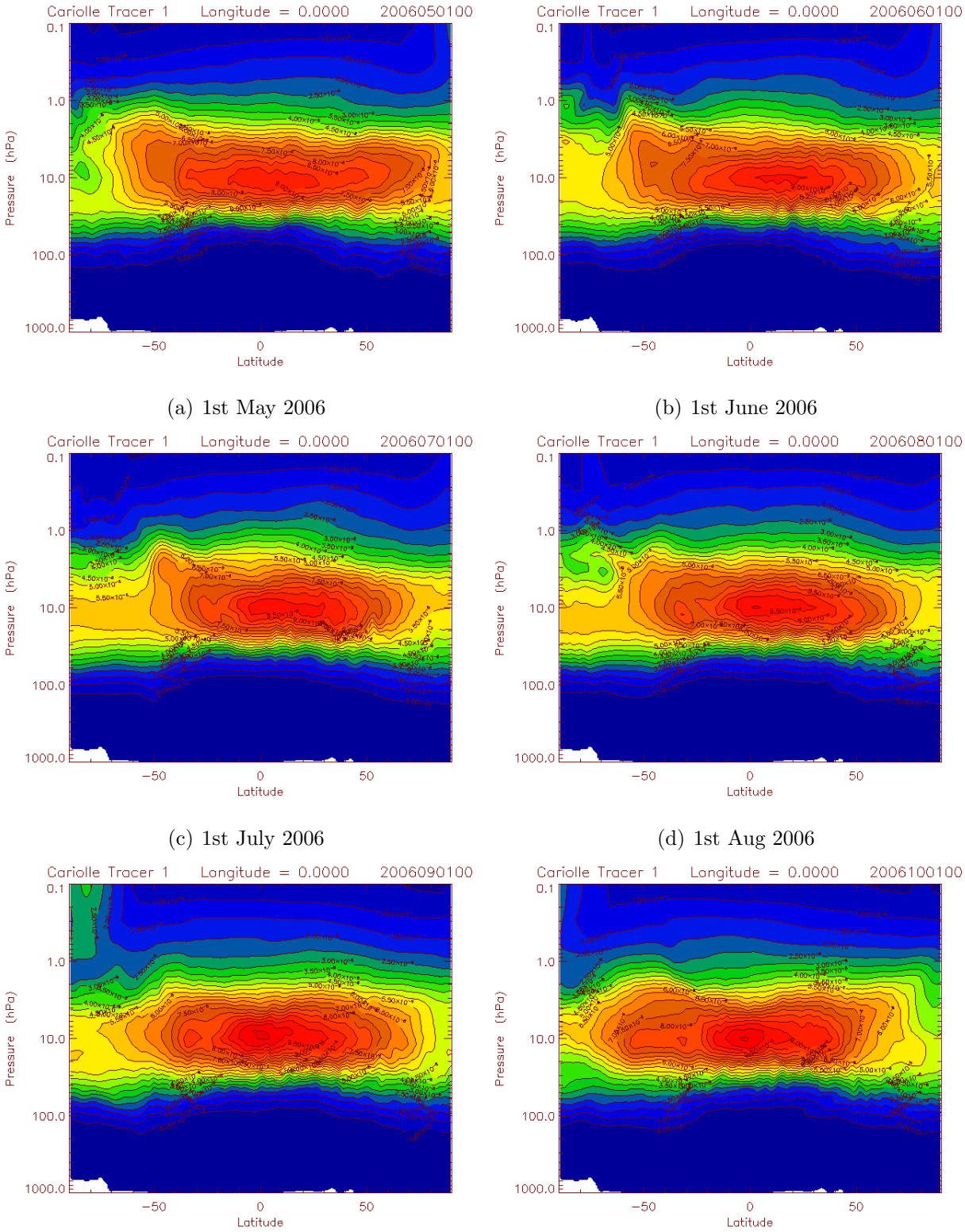

(a) 1st May 2006

(b) 1st June 2006

(c) 1st July 2006

(d) 1st Aug 2006

(e) 1st Sept 2006

(f) 1st Oct 2006

Figure 4.12: *Vertical cross sections through the active ozone tracer field with heterogeneous chemistry excluded at one month intervals, and advection carried out using ERA-Interim at T255. Mixing ratio is plotted with a contour interval of 0.5 ppmv.*

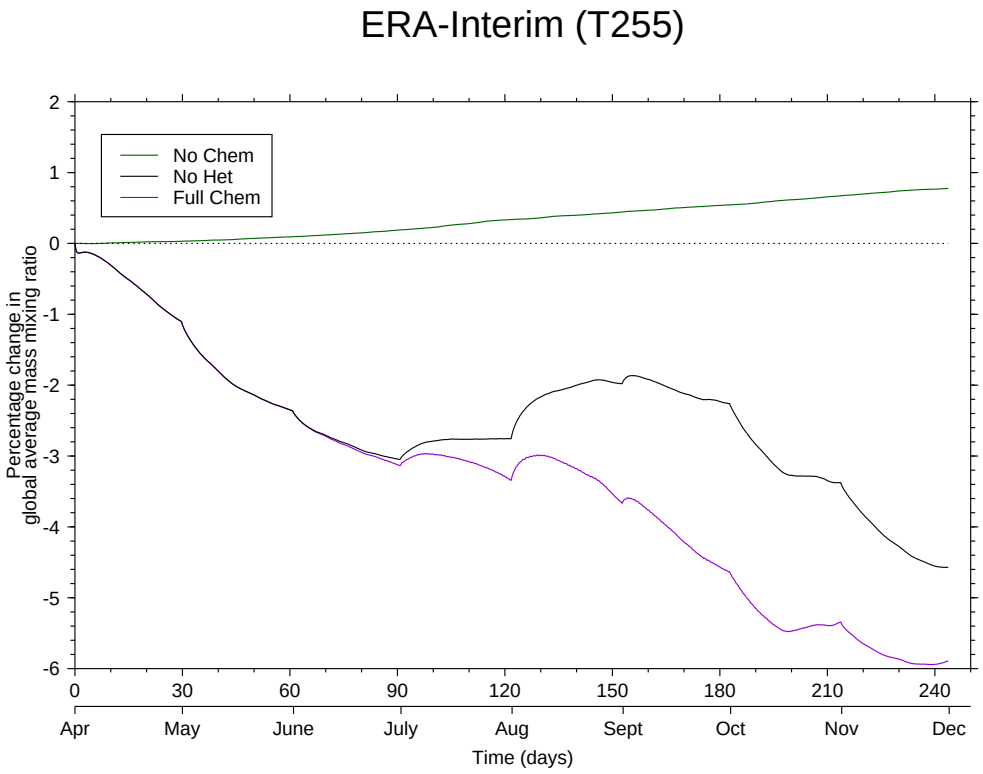

Figure 4.13: *Percentage change in global average mass mixing ratio of ozone advected using ERA-Interim at T255. The three experiments are for passive ozone (no chem), chemically active ozone (full chem) and when heterogeneous chemistry is excluded (no het).*

chemistry does not have a noticeable impact until August. This difference is noticeable at higher latitudes in the Southern Hemisphere in the region of 10-20 hPa. The fact that this region is different is expected since this is region where sunlight will first begin to return to the higher latitudes after polar night and the temperatures will also be cold enough for heterogeneous chemistry. At the start of September the absence of heterogeneous chemistry becomes increasingly noticeable as the previously seen intrusion of lower ozone values to higher altitudes at the edge of the polar vortex is not present. This is enhanced by the start of October when the ozone hole is conspicuously absent, showing how dependent the ozone hole formation is on the heterogeneous chemistry.

Figure 4.13 compares the percentage change in the global average mass mixing ratio for the three different model runs: full chemistry, heterogeneous chemistry excluded and no chemistry. When there is no chemistry (i.e. passive ozone tracer) a numerical mass gain of 0.8% is observed and when there is full chemistry then a mass loss of 6% is produced. If the heterogeneous chemistry is excluded then the resulting mass change lies between these two. This is expected since the absence of the heterogeneous chemistry will reduce the amount of ozone that is destroyed, but the remaining terms in equation (4.11) still produce

a change in global ozone that is able to counter the numerical mass gain and produce an overall loss of 4.5%. Figure 4.13 also clearly shows that the heterogeneous chemistry does not impact the global average mass mixing ratio until the middle of June.

The ozone column over the Southern Hemisphere is shown in figure 4.14 (c.f. figure 4.7(b)). The distinct similarities between the two images are obvious with the differences concentrated at the higher latitudes. In the band of higher ozone column outside the polar vortex the ozone column is 25 DU higher than when heterogeneous chemistry is included. Within the polar vortex the largest differences are observed with a minimum column of 225 DU compared to 150 DU on this particular day. The small differences observed in the comparison of the cross sections are seen to have a noticeable impact on the ozone column. This is due to the fact that the ozone that is not removed is located in the lower stratosphere and will therefore have a larger weighting in the ozone column calculation due to there being more mass here than higher up in the stratosphere.

The effect on the minimum ozone column is quantified in figure 4.15 which shows the minimum ozone column poleward of 70S. The heterogeneous chemistry begins to have a noticeable effect after 10th July. As in the case of the global average mass mixing ratio, the minimum ozone column when heterogeneous chemistry is excluded lies between the model run of no chemistry and full chemistry. At the time of the deepest ozone hole, when a minimum ozone column of 140 DU is seen (when the heterogeneous chemistry is included), the model run with heterogeneous chemistry excluded is only able to reach approximately 212 DU. This means that a very weak ozone hole does form, as the definition of the ozone hole is when the ozone column goes below 220 DU, but the heterogeneous chemistry accounts for over 80 DU of additional ozone loss over the South Pole. Near the end of the eight month model period the run with the full chemistry and that with heterogeneous chemistry excluded begin to converge again as the heterogeneous chemistry no longer has such a dominant role in the evolution of global ozone burden.

C07 also presented results from a model run where the heterogeneous chemistry is excluded. The results showed a resulting ozone column in the range 280-320 DU through June to September. This is larger than the results presented above which have an ozone column below 280 DU from July to December. This difference could be due to the different advection schemes, resolutions, and also different sets of coefficients in equation (4.11) as C07 uses v2.1 and the work presented in this thesis uses v2.9. C07 also found that the exclu-

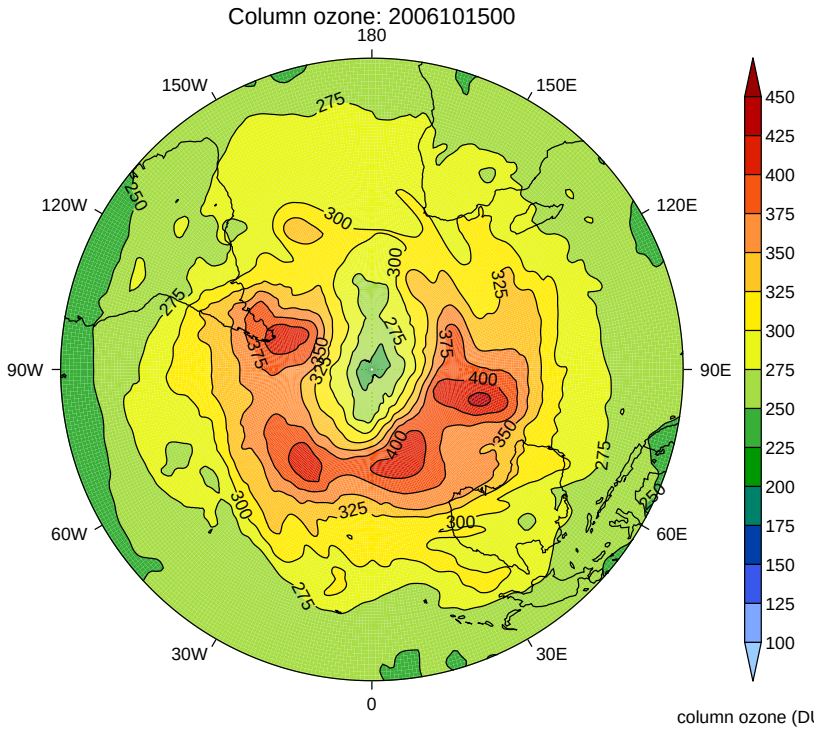

Figure 4.14: *Ozone column on the 15th October 2006 when heterogeneous chemistry is excluded and advection is by ERA-Interim at T255. Stereographic projection extends to the equator.*

sion of the heterogeneous term resulted in an ozone column maximum in the mid-latitudes that is approximately 40 DU higher than when heterogeneous chemistry is included. This is a larger difference than is observed in the results above which only shows a 25 DU difference with the lower value once again likely due to the other terms in equation (4.11) utilising improved coefficients.

Overall the heterogeneous chemistry has a noticeable effect on many aspects of the ozone distribution: cross sections, ozone column distributions, global mass mixing ratio and minimum ozone column at high latitudes in the Southern Hemisphere.

4.4.2 Spatial Truncation of Analyses and Tracer Model

The advection and chemistry experiment was repeated with ERA-Interim spectrally truncated to T159 before transforming the data onto the associated linear Gaussian grid ($\Delta\lambda$=$\Delta\phi$ ≈1.125 degrees) and a time step of 150 seconds. The percentage change in global average mass mixing ratio (red line in figure 4.9) shows a global mass loss that is 95.8% of the 6% global mass loss observed at T255 (purple line) by the end of the eight month model run.

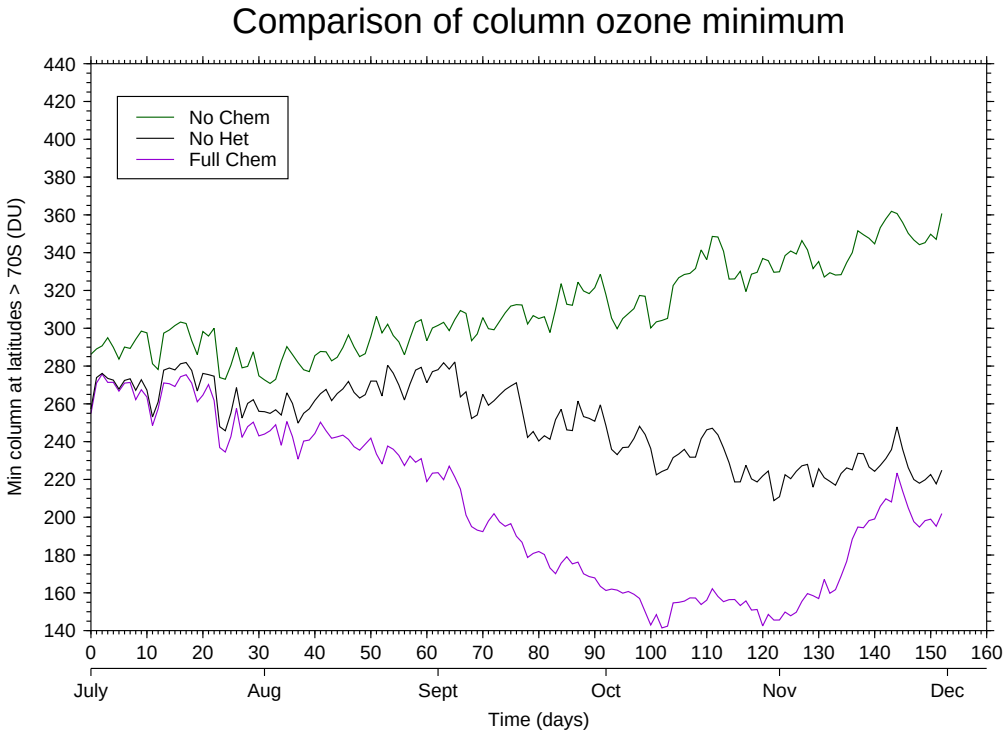

Figure 4.15: *Time series of the minimum ozone column value (DU) south of 70S when the ozone tracer is advected by ERA-Interim at T255 with heterogeneous chemistry included (full chem), excluded (no het) and as a passive tracer (no chem).*

Considering that the passive ozone tracer run at T159 results in a numerical mass gain (light blue line) that is approximately 2.8 times that at T255 (green line) means that the chemistry has compensated for a larger mass gain in order to produce similar results for the active tracer. The minimum column ozone can also be compared and is shown in figure 4.11. The difference between the use of ERA-Interim at T255 and T159 is small for both the passive (green and light blue lines) and chemically active (purple and red lines) ozone tracer. The reasons for the additional global mass gain were explored in the previous chapter, Section 3.3.4. When looking at cross-sections through the ozone distribution the differences are not noticeable. If not for the global diagnostics of the average mass mixing ratio and its variation with time the two model runs would look almost identical.

4.5 Advection by Operational Analyses

ECMWF operational analyses truncated to T159 were also used to drive the advection of the active ozone tracer with a time step of 150 seconds in order to compare the effects of differing analyses. The details of the operational analyses are given in the passive ozone

experiments in Section 3.3.6. The global average mass mixing ratio is compared to those for the ERA-Interim runs in figure 4.9. The significant fact to note about the active ozone tracer run using the operational analyses (black line) is that the overall mass change at the end of the model run is positive, showing a mass gain. This is contrary to what is expected of the global burden of ozone during this time of year (4.10). The reason for this failure to show a mass loss can be linked to the passive ozone tracer run (dark blue line) which shows a 17% global mass gain over the model run. The ozone chemistry is then unable to compensate for this severe numerical mass gain.

Figure 4.16 shows the ozone column over the Southern Hemisphere for the passive and active ozone tracer when advecting by the operational analyses at T159. The impact of the chemistry is immediately noticeable, as are the similarities between the two images, with the main features determined by the analyses. Comparing this figure with that for ERA-Interim (figure 4.7) shows that the operational analyses and ERA-Interim produce the same overall distribution of ozone in agreement with the observations in figure 4.6. However, the higher global burden of ozone when using the operational analyses is clearly seen in the passive ozone tracer image. The high ozone ring around the south pole is more pronounced and the area covered by column ozone values of 450 DU and greater dominates a larger fraction of the hemisphere than in the ERA-Interim model runs.

The active ozone column in figure 4.16(b) also shows higher column ozone values, with the ozone hole having the lowest column ozone values in the range of 175-200 DU. In the belt of high ozone around the outside of the polar vortex the peak ozone column values are in the range of 425-450 DU. The column minimum and maximum are both greater than those seen for the ERA-Interim model run reflecting the reduced global loss of ozone when using the operational analyses.

The difference between the operational analyses model run and those using ERA-Interim is also reflected in the column ozone minimum in figure 4.11. Both the passive (dark blue line) and active (black line) ozone tracer runs using the operational analyses show higher ozone column minima than those using ERA-Interim. At the start of July the difference is small and then increases with time for the passive tracer and decreases with time for the active tracer as the ozone hole chemistry dominates. The difference for the active ozone tracer means that the ozone hole forms over a week later when using the operational analyses. However, considering the significant differences in the global average mass mixing ratio

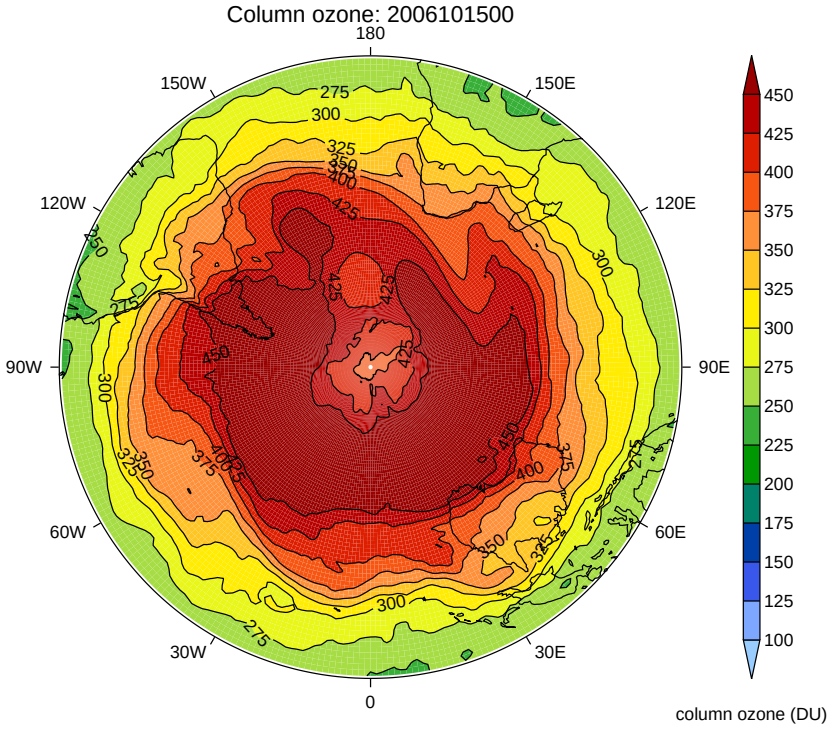

(a) Passive ozone

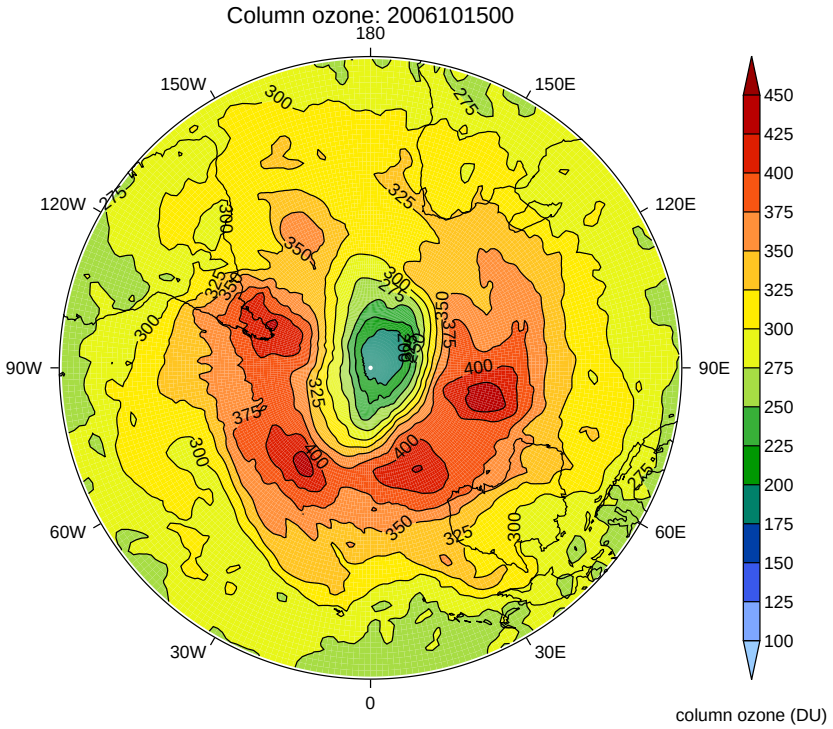

(b) Active ozone

Figure 4.16: *Ozone column on the 15th October 2006 when using the (a) passive ozone tracer and (b) active ozone tracer advected by the operational analyses at T159. Stereographic projection extends to the equator.*

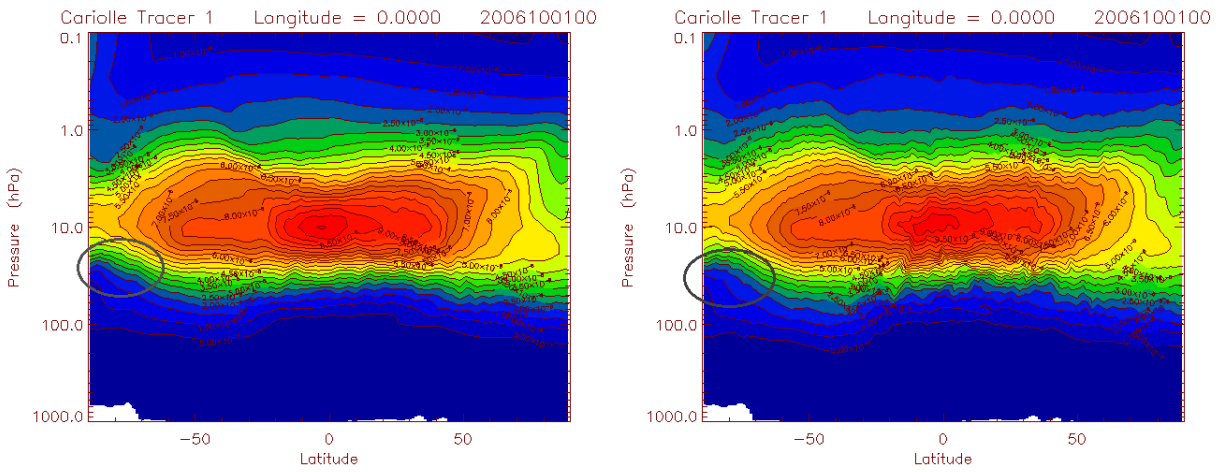

(a) ERA-Interim (b) Operational Analyses

Figure 4.17: *Vertical cross sections through the active ozone tracer field on the 1st October 2006 with advection carried out using (a) ERA-Interim truncated to T159 and (b) Operational analyses truncated to T159. The mixing ratio is plotted with a contour interval of 0.5 ppmv. The ozone hole over the South Pole has been circled.*

during this period the differences in the column ozone minimum are relatively small. This shows that if evaluating a model using a localised diagnostic, such as the depth of the ozone hole, the model can appear accurate, whereas looking at a global diagnostic, such as the mass conservation, reveals inaccuracies within the model.

Finally, a cross section through the ozone tracer field on the 1st October when advected by the operational analyses truncated to T159 is shown in figure 4.17 and compared to the corresponding image when using ERA-Interim. This can also be compared with figure 4.8(f), which is the equivalent for ERA-Interim at T255. These images show that the maximum in the tropics is larger when using the operational analyses but that overall they are very similar. The initial development of the ozone hole in August and September is not as pronounced in the cross sections when using the operational analyses (not shown). However, by October the ozone hole is clearly seen and has been circled in the operational analyses image. The ozone hole is almost identical to that seen when using ERA-Interim, showing that this small scale feature can still be produced by the ozone chemistry. One difference between the two cross sections is that the operational analyses are seen to produce contours of ozone mass mixing ratio that are less smooth than those seen when using ERA-Interim. The most likely source of this is the increased level of truncation that is required to obtain the analyses at T159. This in turn results in a poorer consistency between the analysed winds and the tracer advection in the model.

4.6 Summary

A linear ozone parameterisation by Cariolle and Teyssédre (2007) was incorporated into the model to produce an active ozone tracer which was then advected by ERA-Interim and the operational analyses from the ECMWF for the April-December period of 2006. Figure 4.9 clearly sums up the mass conservation aspect of these experiments. As shown in Chapter 3, when ERA-Interim is used to drive the advection an increased spatial truncation results in an increased deviation from mass conservation in the passive ozone tracer runs. The increased numerical mass change when using the operational analyses was also shown and explained. When using ERA-Interim the active ozone tracer shows a realistic change in the global burden of ozone (loss of 6%) which is similar whether a resolution of T255 or T159 is used. The ozone photochemistry was able to compensate for the numerical mass gain observed when using ERA-Interim. The consequences of the large numerical mass gain when using the operational analyses is reflected in the chemically active ozone tracer by the fact that the model is not able to produce a global mass loss of ozone.

When looking at the ozone distribution the main features are reproduced in all three (operational analyses, ERA-Interim at T159 and T255) model simulations. The differences that arise between the T255 and the two T159 model runs can mostly be linked to the change in the horizontal resolution, such as fewer smaller scale features due to increased averaging. When using the operational analyses the contours of ozone mixing ratio are also seen to be less uniform, possibly as a consequence of the increased truncation and hence a poorer consistency between the analysed winds and the model tracer advection. The mid-latitude ozone maximum around the polar vortex is larger when using the operational analyses, likely due to the previously mentioned inability of the photochemistry to compensate for the numerical mass gain. The ozone column is generally larger in the simulations using the operational analyses. This also affects the onset time of the ozone hole when using the operational analyses, which is a few days later than that when ERA-Interim is used.

By looking at the minimum column ozone poleward of 70S (figure 4.11) it can be seen that the change in analyses used for the advection has a smaller impact on the depth of the ozone hole than on the global burden. The effects of spatial truncation are also not observed in a local diagnostic, such as the ozone hole minimum. Due to this fact it is only when using a global diagnostic, such as the change in global burden, that the accuracy of a numerical

scheme can be quantified. However, the column minimum in figure 4.11 does show that chemistry does not necessarily compensate for a numerical mass gain, as seen when using the operational analyses truncated to T159. When carrying out multi-year model runs this can have a significant impact.

An example of this is the Stratospheric Processes and their Role in Climate (SPARC) Chemistry-Climate Model Validation Activity (CCMVal) project for CCMs, which has carried out an in depth comparison study of a range of diagnostics in a large number of CCMs. The full CCMVal report (Eyring *et al.*, 2010) has chapters on radiation, dynamics, transport, natural variability and more (the report can be found at `www.atmosp.physics.utoronto.ca/SPARC`). A full list of the diagnostics used in the study can be found at `www.pa.op.dlr.de/CCMVal/CCMVal_EvaluationTable.html`. What is of note from the many diagnostics considered is that none investigate the mass conservation within the various CCMs, which from the results presented above can be seen to have a notable impact.

Austin *et al.* (2010) presented some work from the CCMVal project, specifically that regarding a diagnostic of the ozone hole minimum over the Antarctic. The models produced a range of 150 DU (50-200 DU, with the result in this thesis being 140 DU) for this local diagnostic, which shows how much these models can differ with regards to a small scale feature. Given what has been shown here with respect to how a local diagnostic does not provide an accurate measure of the absolute error (e.g. global conservation) in a numerical model means that this range of values for a local diagnostic could signify potentially large inaccuracies for global conservation in some of these CCMs.

Chapter 5

Sarychev Peak 2009

Chapters 3 and 4 have examined the global burden of tracers, using passive tracers to quantify model error associated with advection as well as its relative magnitude compared with chemical changes using stratospheric ozone as the illustration. This chapter examines the ability of this offline model to simulate the transport and decay of a tracer away from a source and studies the impacts of stirring and mixing which cannot be seen in global measures. The test case chosen is the volcanic eruption of Sarychev Peak that occurred in 2009. This specific eruption was chosen due to the benefit of being able to obtain global data from IASI (Infrared Atmospheric Sounding Interferometer) over the period of the eruption. Specifically IASI measured the sulphur dioxide emitted by the volcano in terms of a column total with a footprint of 12 km in diameter.

5.1 Sarychev Peak Eruption

Sarychev Peak is a volcano located on the north-west end of Matua Island in the Kuril Islands in the north-west Pacific, as shown in figure 5.1. It is one of the most active volcanoes in the island chain with a peak at an elevation of 1496 metres and a 250 metres wide crater. Eruptions of the volcano have been recorded as far back as the 1760's. A recent eruption of Sarychev Peak was recorded in 2009.

The volcano erupted overnight on the 11-12th June 2009 with the most energetic eruptions continuing until the 17th June. Continued ash emissions were observed up to the 18th June. During this initial energetic period ash clouds were detected as high up as 16 km, with some estimates giving a value of 21 km. Intense gas emissions were detected from the hot deposits on Sarychev Peak up to the 20th July, with gas and steam plumes seen daily during the first week of July. The plumes observed during this week reached altitudes of

up to 3 km. Gas and steam plumes were still observed up to the end of July, however, at times they were described as being "diffuse" in nature and therefore the model does not necessarily need to be extended to cover this period of weak emissions. According to the Smithsonian Global Volcanism Project (`www.volcano.si.edu`) an estimated minimum volume of 0.4 km^3 of material (volcanic glass, ash, gases, etc.) was ejected from the volcano.

5.2 IASI Satellite Measurements

The IASI instrument is located on the European Meteorological Operational (MetOp-A) sun-synchronous satellite launched on the 19th October 2006. The satellite has an orbit at a 98.7 degree inclination to the equator (polar orbiting) and is located at an altitude of approximately 817 km. It takes 101 minutes for the satellite to complete one orbit and has a repeat cycle of 29 days, equating to 412 orbits.

IASI operates in the infrared, specifically wavelengths ranging from 15.5-3.62 μm (or a spectral range of 645-2760 cm^{-1}). It has a spectral resolution of 0.3-0.5 cm^{-1}. A wide range of gases are detected by IASI. These include many long and medium lived species such as carbon dioxide, nitrous oxide, CFCs, water vapour, ozone, carbon monoxide, methane and nitrous oxide. Shorter lived species such as sulphur dioxide and trace gases released during forest fires (methanol, formic acid, ethylene) are only detected close to sources or during a specific event, such as a volcanic eruption in the case of sulphur dioxide. Due to operating in the infrared, IASI can only detect the gases when the measurements are made in a cloud free environment. For more information on IASI see `www.latmos.ipsl.fr/index.php/fr/tact/themes-de-recherche/iasi`, or alternatively Clerbaux *et al.* (2009).

During the period of the Sarychev Peak eruption IASI was able to take measurements of sulphur dioxide (SO_2) over the Northern Hemisphere. The levels of SO_2 were interpolated by the IASI team onto the longitude-latitude grid of the Unified Model for the UK Met Office as a column value for each grid box in DU (Dobson Units). Each grid box measures 1.875 degrees longitude by 1.25 degrees latitude. The satellite data was provided by Jim Haywood at 12 hour intervals between the 12th June and mid-July and is the same data as used in Haywood *et al.* (2010). IASI data has been used to track volcanic plumes previously, one such example is the eruption at Jebel at Tair in 2007, presented by Clarisse *et al.* (2008).

Figure 5.1: *Top: Map showing the Kuril Islands to the east of Russia and north of Japan (`www.russiamap.org/mpa.php?map=physical-ng`). Matua Island is located in the centre of the red circle. Bottom: Matua Island with Sarychev Peak labelled in the north-west of the island (`earthobservatory.nasa.gov/NaturalHazards/view.php?id=44283`).*

Another example is shown in Karagulian *et al.* (2010) using the Kasatochi volcanic eruption in 2008.

5.3 Model Runs

The model was initialised so that the tracer was released at a constant rate in a single column of constant tracer, q, ranging from 350 hPa - 95 hPa. This range covers the upper troposphere to lower stratosphere (UTLS) region, consistent with observations of the ash cloud stated by the Smithsonian Global Volcanism Project. The tracer release period was the 12th-17th June in order to encompass the period of most intense emissions. The amount of tracer to be released was calculated using the estimated volume of erupted material (0.4 km^3) converted to kilograms using the density of volcanic glass (2400 kgm^{-3} from `volcanoes.usgs.gov/ash/properties.html`) as the average density of the erupted material. This is easily converted to a uniform release rate over the five day tracer release period by dividing by the emission period. Many features of the model initialisation (constant release in a specified height range over the UTLS) are in agreement with Haywood *et al.* (2010). ERA-Interim at full spatial resolution (T255), with wind updates every 6 hours, was used to drive the model.

Three different model runs were carried out. The first was a control run where the passive tracer was advected by the standard advection scheme. In the second run monotonicity was enforced and in the final model run the positive definite option was used. In order to make the model output and IASI data comparable the model output needed to be scaled. This scaling was required because the mass released in the model was representative of the total mass released by the volcano, whereas IASI only measured the amount of SO_2 that was released. This scaling factor was determined by calculating the area weighted global column total of tracer for both the IASI data and the output from the control run in the Northern Hemisphere. The ratio of these two numbers was taken at the first available data point after the model finished emitting tracer (0600 hours, 17th July). This date was chosen as the point to calculate the scaling factor because it coincides with the end of the most violent eruptions and therefore maximum loading of tracer in the atmosphere. The ratio was calculated as 753, one over this number is used to scale the model output.

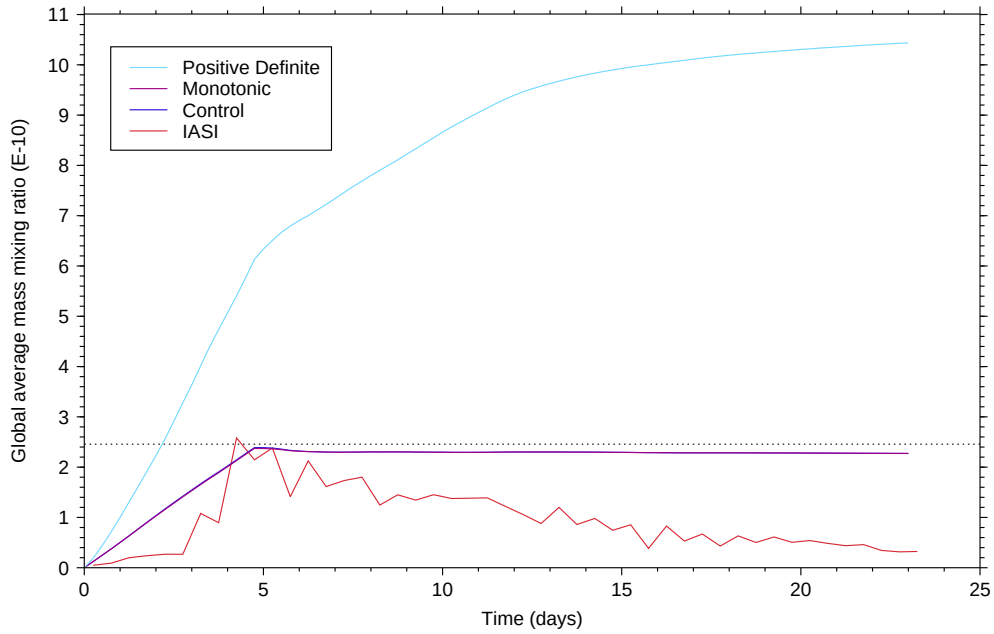

Figure 5.2: *Time series of global average mass mixing ratio (tracer global mass/atmospheric mass) for the control, monotonic and positive definite runs (multiplied by a factor of 1/753). The dashed line represents the global mass that is set to be released in the model. The red line is the time series derived from the IASI data.*

5.3.1 Control Run

The model was initialised as above and run until the end of the 5th July. Figure 5.2 shows the global average mass mixing ratio (tracer global mass/atmospheric mass) over the course of the model run for the IASI data (red) compared to the model runs. The control run (dark blue) can be seen to have a linear increase in global average mass mixing ratio during the 5 day tracer release period, as expected from a constant release rate. The black dotted line represents the total tracer set to be released in the model. The control run can be seen to approach this value and then level off slightly below it. Numerical diffusion would not cause this since it would not affect the global amount. The source of this decrease has not been identified specifically.

The global evolution of tracer burden from the model run will not match that from IASI due to the fact that the model is using a passive tracer and no lifetime for the tracer has been enforced. The fact that the model is approximately mass conservative over this three week period is a very positive result given the slow change in global burden demonstrated for the passive ozone tracer in Chapter 3 (approximately 0.02% and 0.07% for T255 and T159

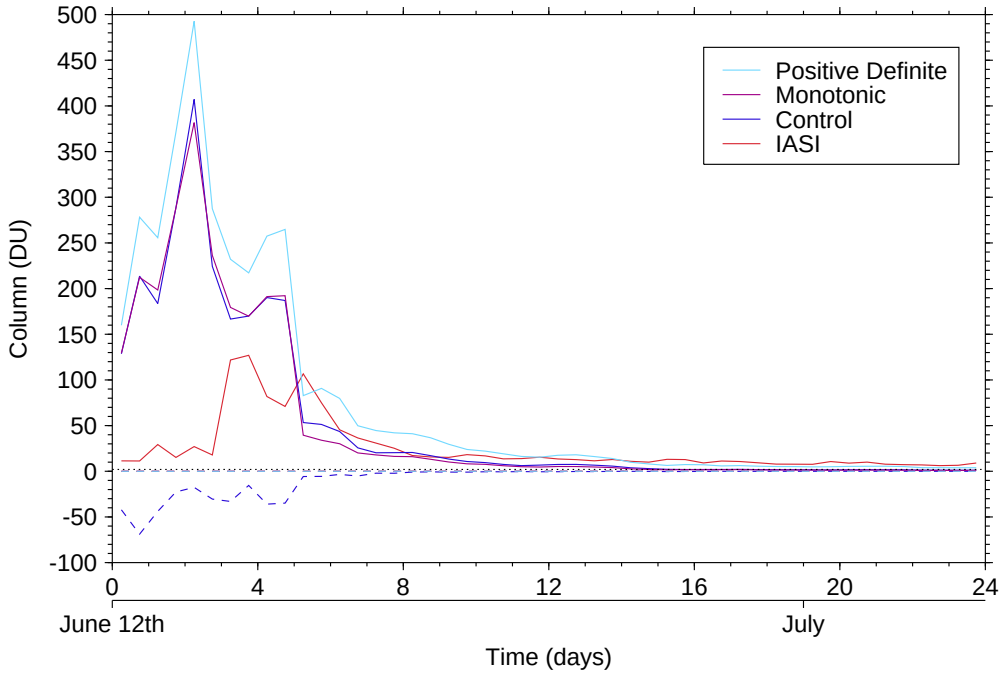

Figure 5.3: *Maximum (solid) and minimum (dashed) column SO_2 values for the three model runs: control, monotonic and positive definite (all scaled by 1/753) plotted with the IASI maximum and minimum. Note that the minimum column values for the positive definite and monotonic runs, as well as the IASI data, are plotted on top of each other and are approximately zero.*

respectively over ten days). In comparison, a volcanic plume experiment carried out during the Monitoring Atmospheric Climate and Composition (MACC) project showed a mass gain of 20-80% over a ten day period (depending on the monotonic and mass fixing options used) when using the IFS from the ECMWF. This result was documented by Flemming and Huijnen (2011) as an IFS tracer transport study.

Figure 5.3 shows the maximum (solid lines) and minimum (dashed lines) column SO_2 for the IASI data and the model runs. During the first two days of the model run there is a greater release in the model than in the IASI observations. However, the second peak in the tracer maximum in the control run is a lot closer to that seen with IASI. After the release period the tracer maximum is seen to rapidly decrease as the tracer is mixed and becomes more uniform. By the end of the model run the control maximum is close to zero as the tracer becomes evenly distributed. In contrast, the IASI data remains at around 10 DU. This is possibly due to IASI detecting the continued emissions from Sarychev Peak as well as the natural background level of SO_2 due to combustion of fossil fuels and other volcanoes and wild fires. Figure 5.3 also shows that at the start of the control run the model produces minima that approach -40 DU. After seven days these negative column values are no longer

evident. However, these negative column values are clearly unphysical, and are associated with fringes flanking the sharp peak in the tracer field associated with the column source (not shown).

The distribution of the natural logarithm of the tracer column on the 17th June at 0600 hours is shown in figure 5.4. The white areas represent zero and negative tracer values. Comparing the IASI data (5.4a) and the control run (5.4b) shows that the model advects tracer to the correct places, however the absolute values of column SO_2 are different. There are several possible reasons for the differences in the tracer distributions. The key difference is the rate of decay assumed in the model, which will be addressed later. With respect to IASI there are other limitations such as tracer being obscured by clouds and the polar orbit of the Met-Op satellite means that the region close to the pole is not necessarily covered by the satellite. Lastly, the higher levels of tracer released in the model compared to IASI could have resulted in larger tracer features from the earlier released material. Many of the small differences can be tracked back to an over simplified tracer release in the model.

Figure 5.5 shows a comparison between the control run and the IASI data over a longer period. The dates shown are the 18th June, 25th June and 2nd July. Throughout this period the limitations of IASI must be kept in mind, primarily the inability to detect the tracer plume through cloud and the detection limit of the instrument. At the first time shown the volcanic plume is situated in approximately the same place in both the IASI data and the model. Specifically, the high column features over Canada and the east of Russia are well represented, but in the model the tracer column has slightly lower values. In the model low column values are observed along the coast of Alaska that are not present in the IASI data. On the 25th June the volcanic plume is less coherent but the majority of the tracer over Alaska and Canada is well represented by the model. Not all features shown by the IASI data are reproduced by the model, such as a filament over the North Pacific. However, the model shows tracer over the Atlantic and a distinct filament near to the North Pole that are only partially seen by IASI. There is a continued trend of higher column values in IASI than in the model and low column values are now seen to wrap around the model hemisphere. At the final time shown many of the distinct features detected by IASI are reproduced in the model, albeit more weakly. Once again there are features produced by the model, such as a distinct feature to the north of Greenland, that IASI does not observe. The model has produced a more uniform low level column over most of the hemisphere

between 30N-90N, which is expected due to the action of numerical mixing and the absence of any tracer removal processes in the model.

5.3.2 Monotonic Model Run

The model run was repeated using the monotonic version of the advection scheme (see Section 2.1.3 for details). When looking at the global average mass mixing ratio in figure 5.2 there is very little difference between the results for the monotonic (purple) and the previous control run (dark blue). The monotonic run shows values slightly lower than that seen for the control due to the fact that the monotonicity suppresses the formation of spurious extrema. This is also seen in figure 5.3 where the column maximum in the monotonic run (purple) tends to have lower values than the control run (dark blue). As the model run progresses the control and monotonic runs produce almost identical results in both the global average mass mixing ratio and column maximum. This suggests that after the first ten days there are no longer spurious maxima or minima in the model that the monotonicity in the scheme is suppressing. The most noticeable difference is the removal of the negative values of column tracer as seen in figure 5.3 where the minimum in the monotonic run tracks the zero line.

Figure 5.4(c) shows the natural logarithm of the tracer column for the monotonic run. Many of the features seen in the control run are once again observed here. A comparison of the actual column values shows that the monotonic run has slightly larger tracer columns over some areas than the control. This is due to the differences previously stated between the two model runs, namely the reduction of negative values which are not then mixed into, and reduce, the positive column values. A large reduction in the area of white in the figure is also obvious. This is again due to the development of smaller negative tracer values around the point source than are seen in the control run. The increase in area covered by the low tracer values is compensated for by the decrease in the maxima so that the global average mass mixing ratio is comparable to that seen in the control run.

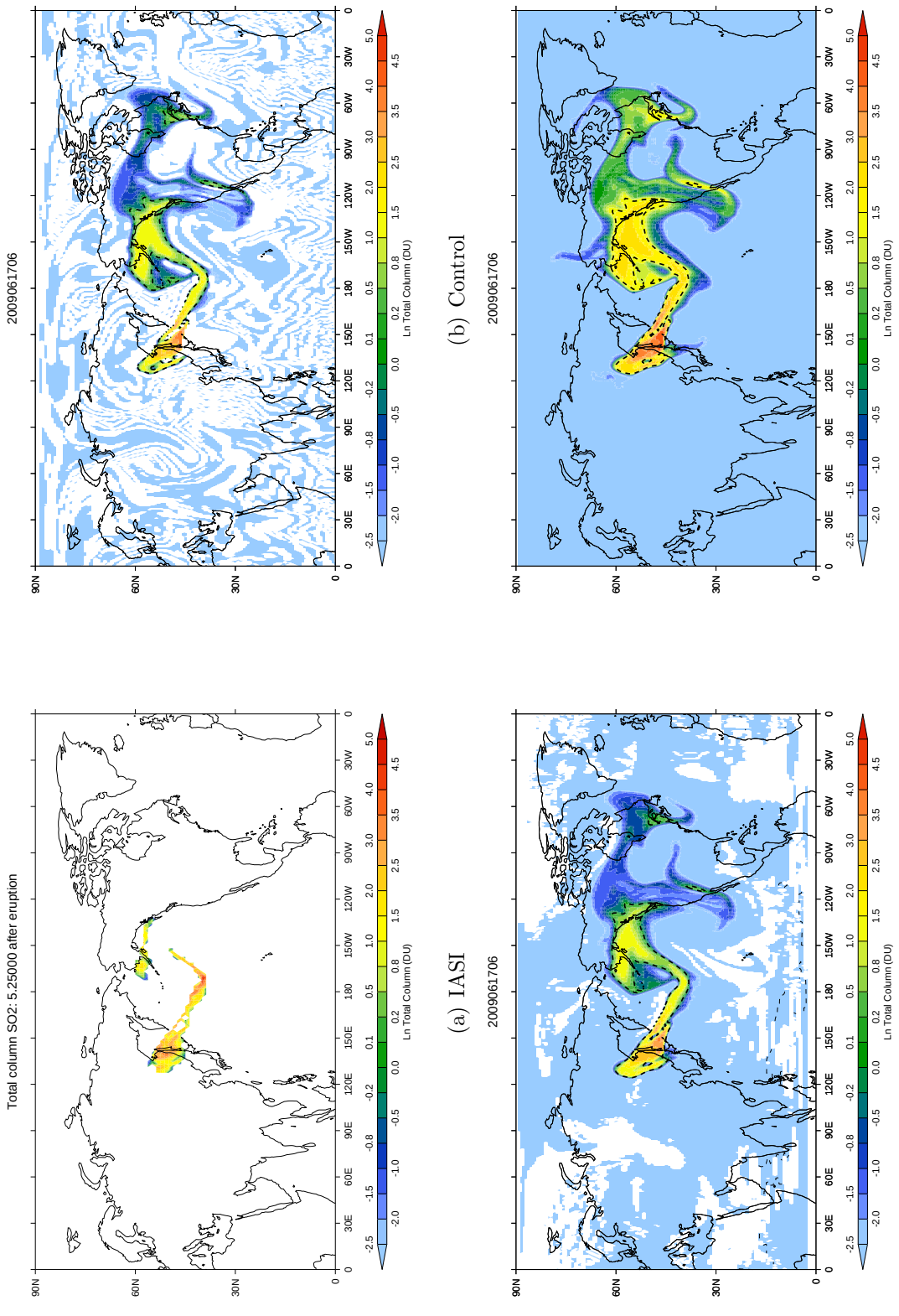

(a) IASI (b) Control (c) Monotonic (d) Positive Definite

Figure 5.4: *Visual comparison of the natural log of column SO_2 5.25 days after the model initialisation. White areas represent areas of zero or negative tracer values and the dashed line is the 97th percentile of the tracer column. All three model runs have been scaled by the factor of 1/753.*

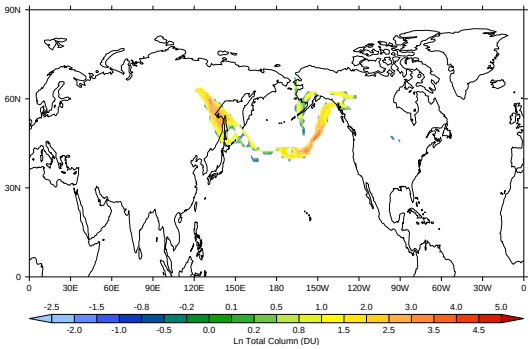

(a) IASI: 18th June

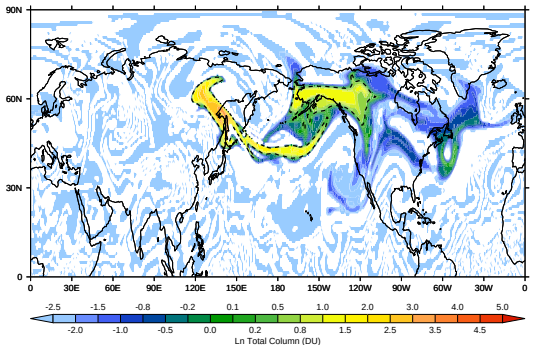

(b) Model: 18th June

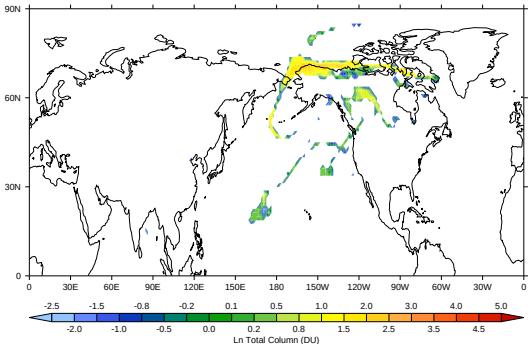

(c) IASI: 25th June

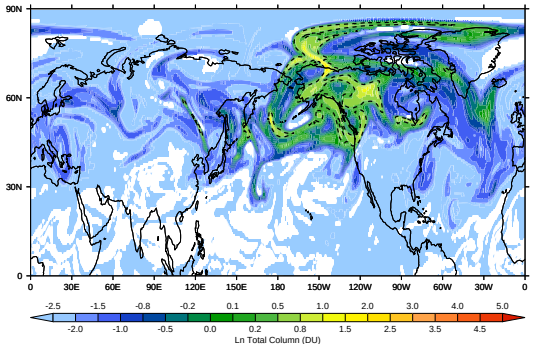

(d) Model: 25th June

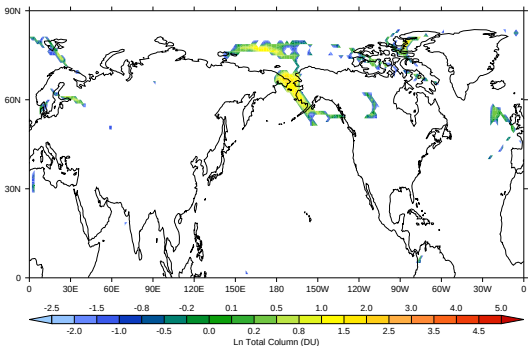

(e) IASI: 2nd July

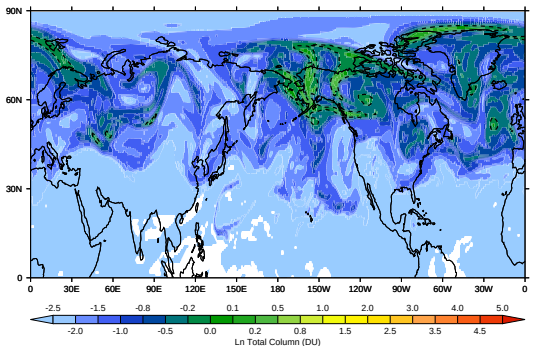

(f) Model: 2nd July

Figure 5.5: *Comparison of IASI SO_2 column and model (control run) SO_2 column at three times. Once again the model SO_2 column is scaled by the factor 1/753.*

5.3.3 Positive Definite Model Run

The final model run included the positive definite option (and not the monotonic option). Enforcing this means that all negative values in the tracer field are simply set to zero (i.e. $q = 0$ for $q < 0$) after every tracer advection step. Due to this a mass gain would be expected in the global average mass mixing ratio. Figure 5.2 shows that this is indeed true, with the positive definite model run obtaining a global average mass mixing ratio over three times that seen for the other two model runs. Due to this fact it is definitely advantageous not to use this simple positive definite scheme if possible when using a point source. This is due to the fact that the presence of a sharp spike in the tracer field results in the creation of troughs surrounding it which can be negative, therefore creating a mass gain when they are reset to zero. As would be expected this also results in the largest column maxima, as shown in figure 5.3 (light blue line). This model run also levels off to a higher column value than the other two model runs due to the increased tracer amount, as well as taking longer for the model to reach this constant value. As would be expected with the positive definite case, the minimum tracer column remains at approximately zero.

Using figure 5.4(d) the tracer distribution can be compared to the other model runs. Immediately the result of the increased tracer is seen in the removal of all zero and negative tracer values. The regions of tracer also located in the other figures have increased in magnitude. The maximum around the source has increased by 50-60%, and this region has also increased in area. Over much of the region the tracer column has noticeably increased due to the numerical mass gain.

5.4 Including Tracer Loss

In order to more realistically model a volcanic plume a decay rate was included in the model. For these model runs the monotonic scheme was used and the tracer release period was shortened to cover a 2.5 day period from noon on the 14th June to the 17th June. This was done due to the fact that from the IASI data (red line) plotted in figure 5.2 it can be seen that the majority of SO_2 is actually released during this shorter period. In order to compensate for a reduction in tracer release period a corresponding doubling in the tracer release rate was implemented.

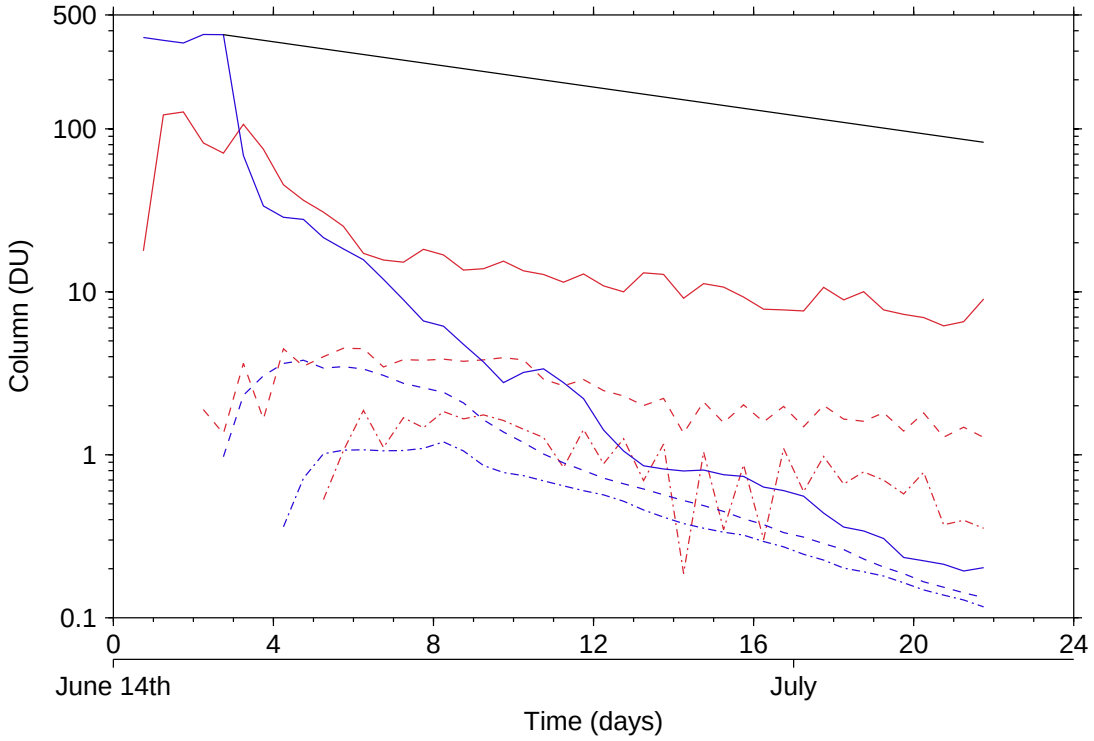

Figure 5.6: *Output from the monotonic model run with a relaxation rate of 12.5 days. Plotted on this figure are the maximum tracer column (solid blue), the 99th percentile (dashed blue) and the 97th percentile (dot-dashed blue). The corresponding values for the IASI data are in red. A decay rate of 12.5 days would produce a line with a gradient equal to that of the solid black line.*

The relaxation rate calculated from the rate of decay of the 99th percentile of the SO_2 column in the IASI data is 12.5 days. The 99th percentile of the global tracer was chosen because it picks out the tracer values that remain above the detection limit of IASI for the longest and therefore provides the most reliable decay rate. On the 17th June approximately 2% of the grid points have column values that are non-zero and above the detection limit of IASI. The maximum was not used since this is most affected by tracer release and there is a distinctive rapid decay early in the data. If this 12.5 day decay rate is used in the monotonic model then figure 5.6 is produced. The maximum, 99th and 97th percentiles of the tracer column distribution are shown for the model (blue) and the IASI data (red). From figure 5.4 it was shown that the 97th percentile of the model data marks the edges of the younger filaments and contains the majority of the tracer. For this reason smaller percentiles are not considered as the small and zero column values begin to dominate. The straight solid black line in figure 5.6 represents an exponential decay rate of 12.5 days. The model decays at a faster rate due to mixing in the model. But what is this mixing rate? In order to determine this the relationship between imposed decay rates (representing a

chemical loss of tracer) and the numerical mixing rate has to be determined, i.e. are the rates additive or is the relationship more complicated? The following work first looks at answering this question.

5.5 Ideal Decay of a Filament

This section aims to pick apart the contribution of diffusion and decay using tracer histograms since only the column amounts are observed in the volcano experiment. In order to do this a basic 2D model was set up to carry out diffusion as well as an exponential decay (equation 5.1) acting on an idealised filament cross-section. This is shown as the red line in figure 5.7 where there is a peak in the concentration in the centre of the filament, decay either side and a well defined filament edge. Using this well defined shape allows the effects of decay and diffusion on the filament to be clearly seen. This distribution also produces an almost rectangular histogram allowing any distortion to be observed quickly.

The diffusion and exponential decay is defined mathematically as:

$$\frac{\partial N(x,t)}{\partial t} = D\frac{\partial^2}{\partial x^2}N(x,t) - \lambda N(x,t) \tag{5.1}$$

D is the diffusion coefficient, λ is the decay rate and $N(x,t)$ is the mixing ratio. For these experiments the diffusion coefficient and decay rate were set as $D = 1.5$ m^{2}s^{-1} and $\lambda = 25$ s^{-1} in order for both processes to be easily seen over a short model run. In order to ensure stability the time step is calculated using the relationship $\Delta t < \Delta x^2/4D$, which gives $\Delta t = 0.0001$ s with $\Delta x = 0.025$ m. The diffusion was implemented using a forward-in-time centred-in-space scheme and the exponential decay using a simple explicit scheme.

Figure 5.7 shows the wave undergoing exponential decay only and figure 5.8 shows the corresponding figure for only diffusion acting. Finally, figure 5.9 is when both diffusion and exponential decay are included. In the case of only exponential decay the resulting histogram would be expected to maintain the same shape and propagate towards lower values with time (figure 5.10). When diffusion acts on the filament an extension of the histogram to lower values is expected due to the tails that form in the distribution in figure 5.8. Figure 5.11 shows this immediately as well as a distinctive peak at the higher value end of the histogram. When the two processes occur at the same time the resultant histograms in figure 5.12 show the distinctive features that arise due to diffusion and disguise the

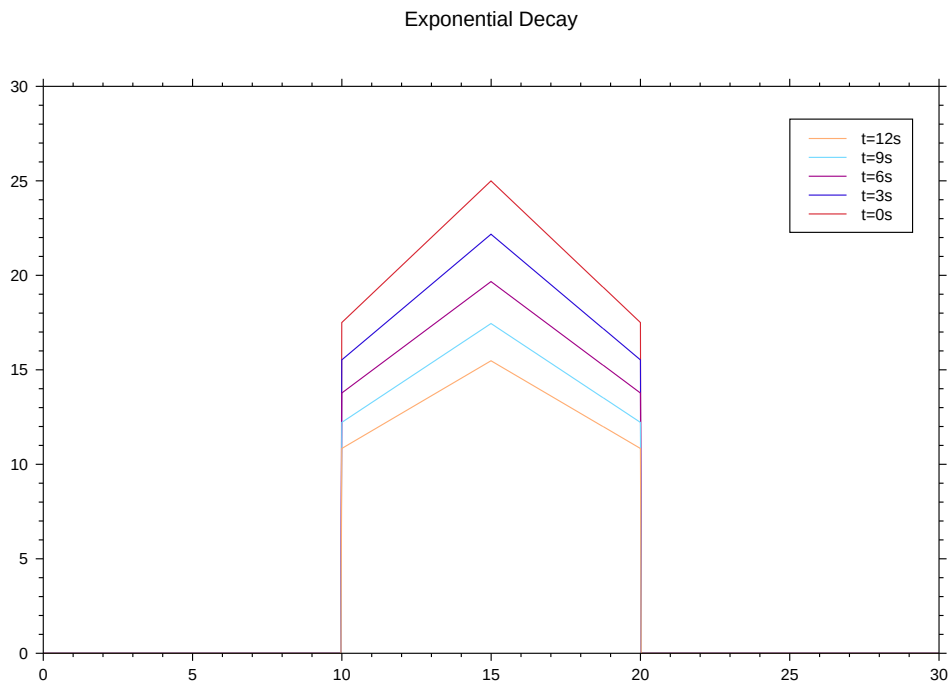

Figure 5.7: *Shape of curve (initial in red) undergoing exponential decay only 3, 6, 9 and 12 seconds after initialisation.*

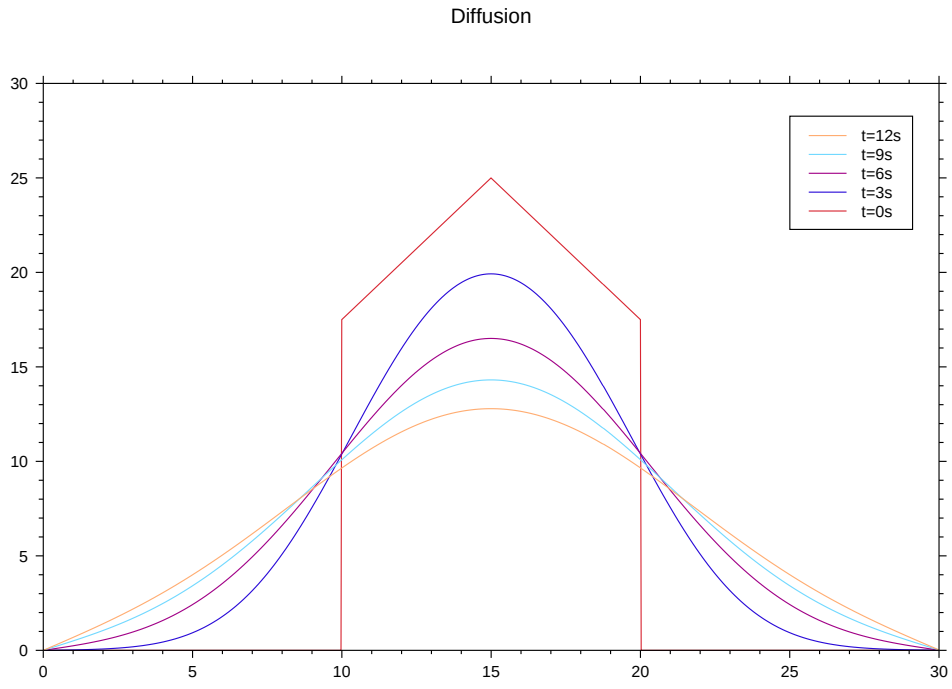

Figure 5.8: *Shape of curve (initial in red) undergoing diffusion only 3, 6, 9 and 12 seconds after initialisation.*

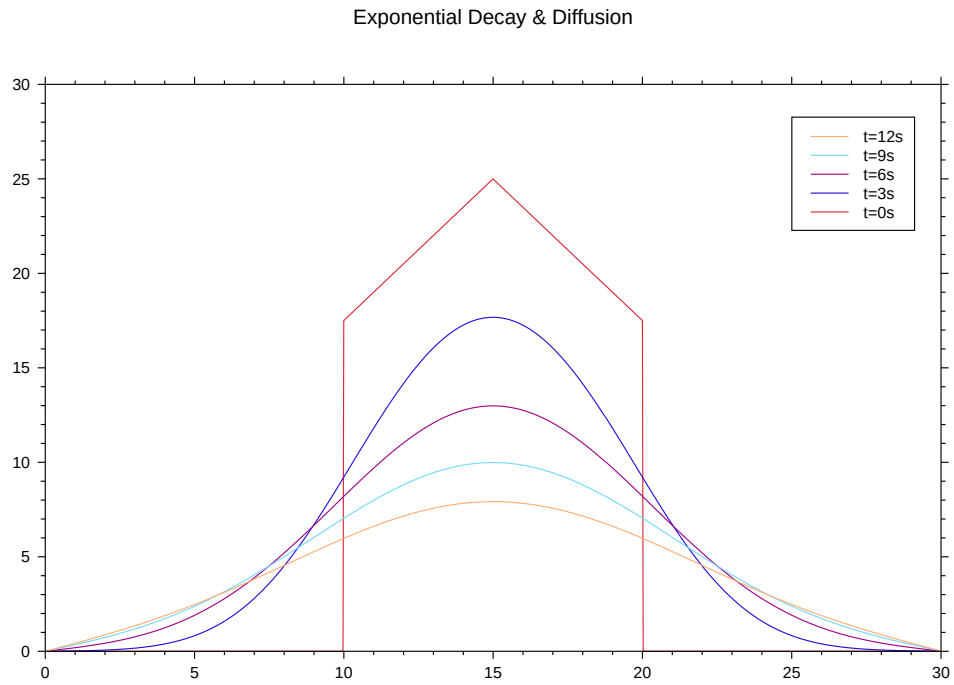

Figure 5.9: *Shape of curve (initial in red) undergoing exponential decay and diffusion 3, 6, 9 and 12 seconds after initialisation.*

effects of the exponential decay, except for the faster shift to smaller values over time when compared to figure 5.11.

Some work has been carried out on the use of tracer histograms, or in the case of Hu and Pierrehumbert (2001) probability distribution functions (PDFs) of the tracer concentration. From looking at the advection-diffusion equation Hu and Pierrehumbert (2001) studied two cases: zonal mixing and meridional mixing. In the case of zonal mixing an equation to derive the time evolution of the PDF, as well as another to derive the shape of the PDF were developed. The initially peaked PDF develops a Gaussian core, which corresponds to the homogeneous part of the tracer field, and exponential tails. The shape of the tails on the PDF depends on the type and duration of the flow. A change in resolution was found to have no effect on the PDF shape, but a reduction in the standard deviation was observed. In the meridional mixing case mixing barriers develop that prevent mixing between the tropics and extra-tropics, and the polar vortex and mid-latitudes. Due to this the resulting PDF has more than one peak, with one peak at the centre of each mixing zone. Over time the developing homogeneity within each mixing zone creates a Gaussian core and exponential tails around each PDF peak, as in the zonal mixing case. Slower mixing produces broader Gaussian PDFs as the homogenisation is slower, and very weak mixing also creates broader/fatter tails in the PDF distribution.

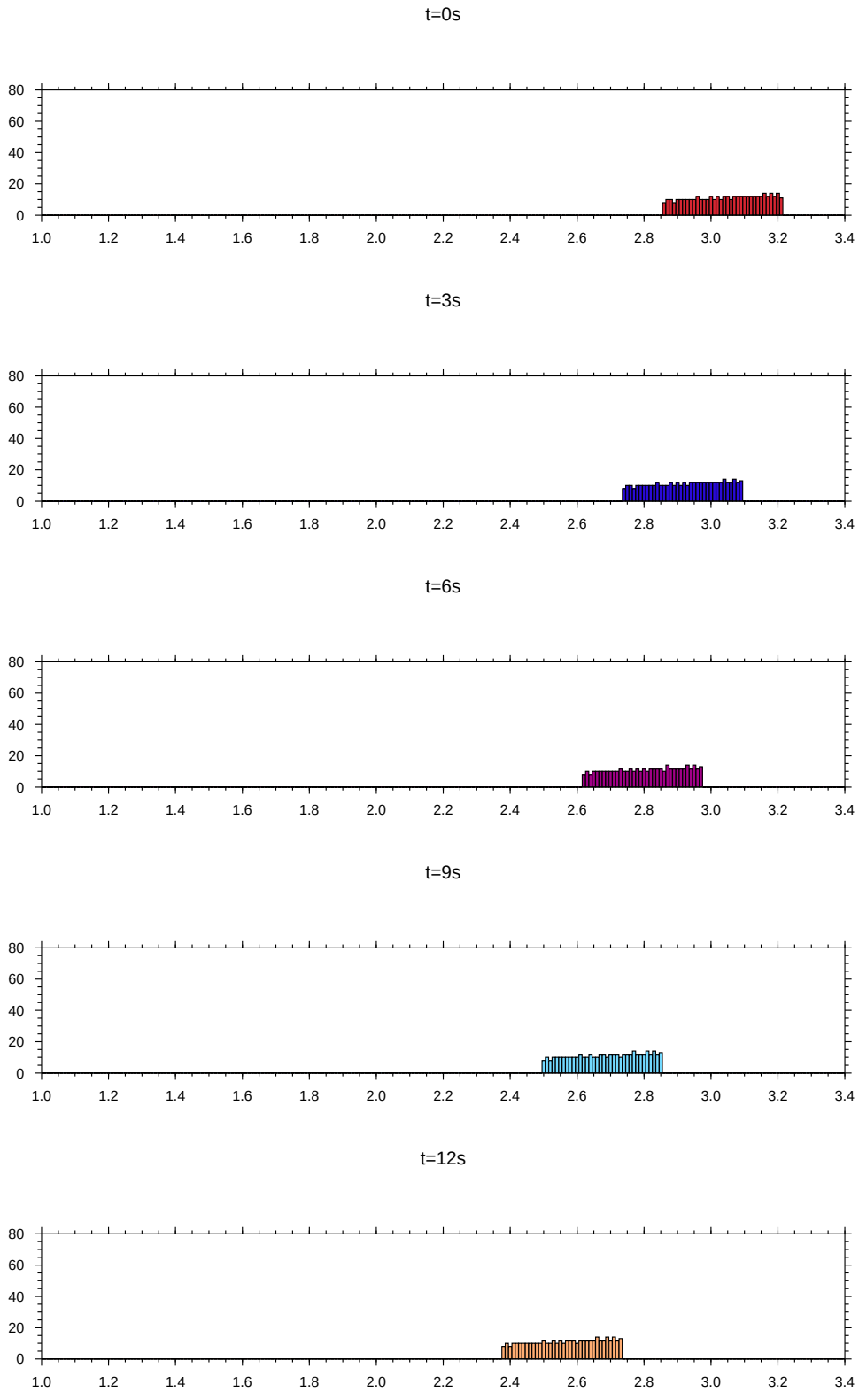

Figure 5.10: *Histogram of ln(y) of the curve shown in figure 5.7 for exponential decay only. Ln(y) is used in order to produce a box like shape at t=0. Bins are equally sized in ln(y).*

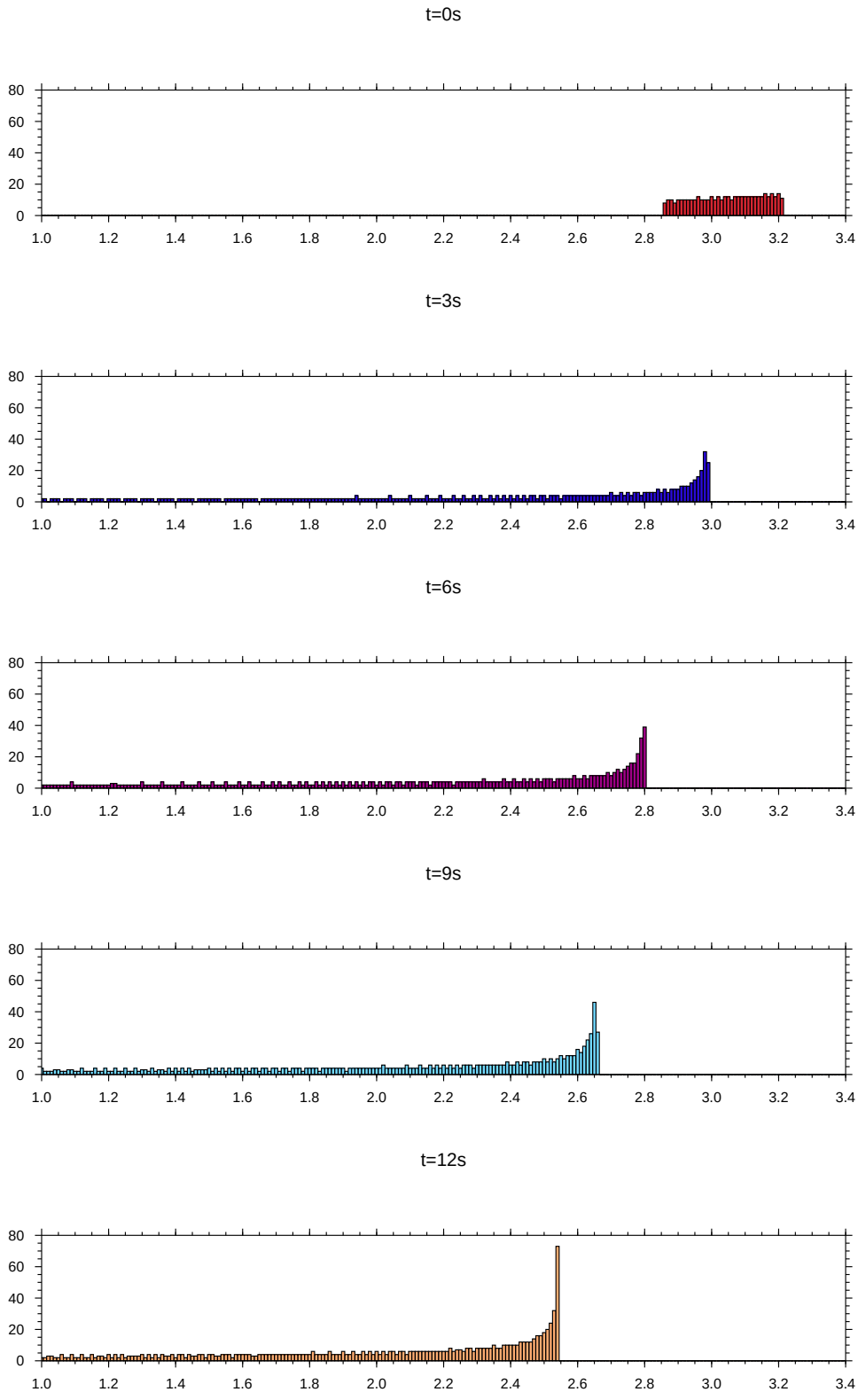

Figure 5.11: *Histogram of ln(y) of the curve shown in figure 5.8 for diffusion only. Ln(y) is used in order to produce a box like shape at t=0. Bins are equally sized in ln(y).*

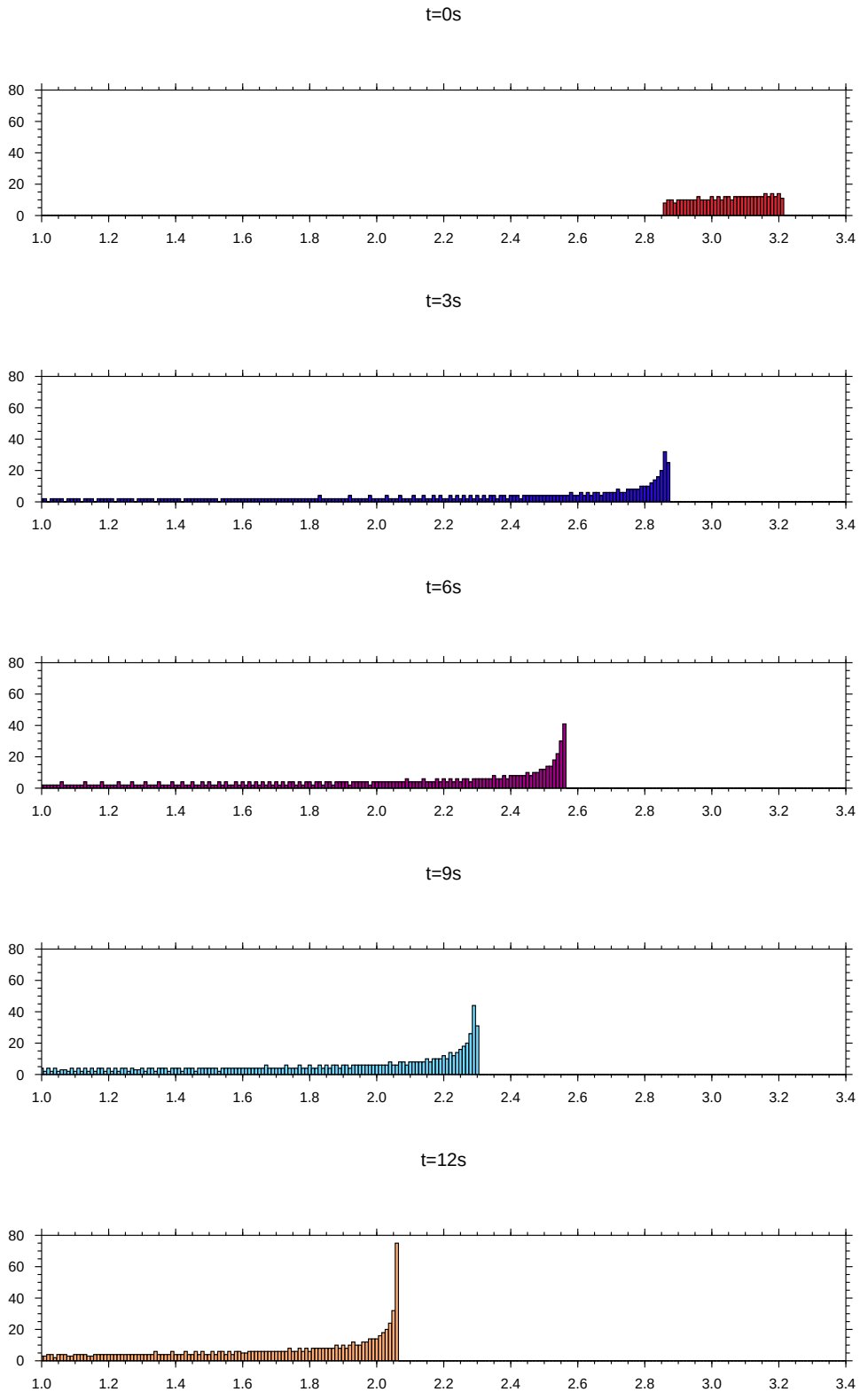

Figure 5.12: *Histogram of ln(y) of the curve shown in figure 5.9 for exponential decay and diffusion. Ln(y) is used in order to produce a box like shape at t=0. Bins are equally sized in ln(y).*

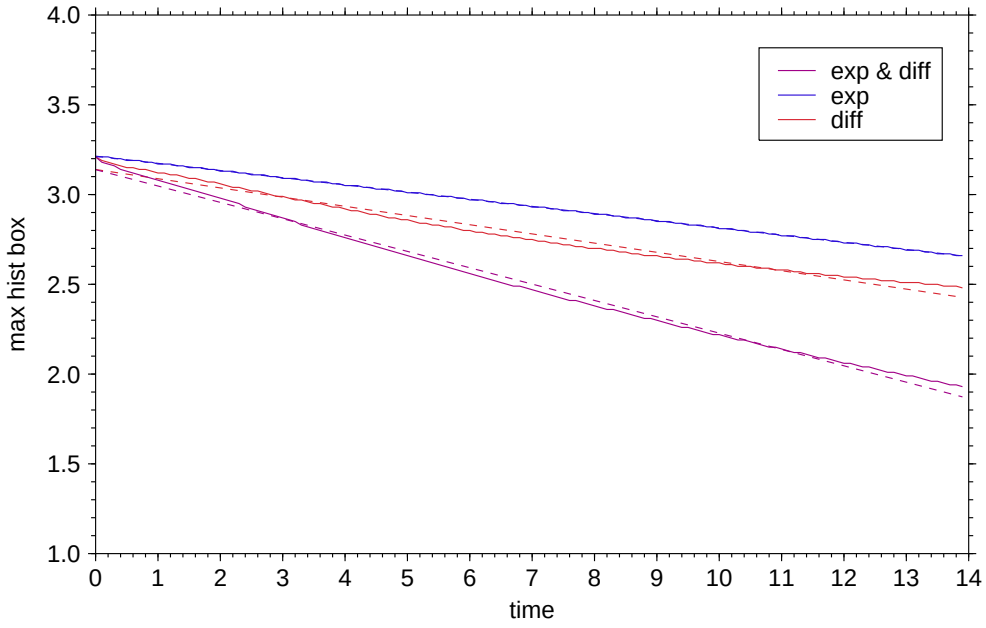

Figure 5.13: *Decay rate of the maximum for diffusion only, exponential decay only, and diffusion and exponential decay. The solid lines represent the data and the dashed lines are the lines of best fit. The gradients of the diffusion only and exponential decay only lines (i.e. the decay rates) are additive within the bounds of the errors to provide that of the diffusion and exponential decay case.*

However, these idealised tests and the derived equations cannot be applied to this simple experiment. The precise nature of the relationship between the two individual decay rates (diffusion and exponential decay), which is of interest here, is not revealed by the work presented in Hu and Pierrehumbert (2001). In order to determine this relationship the well defined edge at the upper end of the histogram, representing the centre of the filament, was utilised. The maximum histogram box that had a non-zero value was plotted against time for all three of the experiments in order to produce figure 5.13. The curve seen in the lines for the diffusion only and exponential decay and diffusion cases arises due to the non-linearity of the decay of the curve peak when there is diffusion acting (figure 5.8).

The gradients and errors for the three lines in figure 5.13 are shown in table 5.1. The gradients were then converted into the decay rates by taking 1/gradient and the corresponding errors also calculated by using the error in the line of best fit. It can be seen immediately that the values of the exponential decay and diffusion gradients add together to provide the gradient of the joint experiment within the limit of the errors. The same is also true for the decay rates if the relationship is considered as shown in equation (5.2) (since τ=1/gradient). Since this equation takes into account the two dominant processes that act in the atmosphere. Therefore, this relationship can now be used in the model

Experiment	Gradient	Error	Tau	Error
Diffusion	-0.0512	6.0E-4	19.5	±0.2
Exponential decay	-0.0400	6.0E-5	25.0	±0.04
Diffusion and Exponential decay	-0.0910	6.0E-4	11.0	±0.07

Table 5.1: *Gradients and associated errors of the maximum determined from the histograms for the three different experiments shown in figure 5.13. These values were then converted into the decay rate τ=1/gradient and the corresponding errors.*

where, instead of τ_{diff} and τ_{exp}, it is τ_{mix} (mixing timescale) and τ_{rel} (relaxation timescale) respectively.

$$\frac{1}{\tau_{tot}} = \frac{1}{\tau_{diff}} + \frac{1}{\tau_{exp}} \tag{5.2}$$

Prather and Jaffe (1990) investigate the action of strain and diffusion on a tracer filament. They found that strain dominates at larger scales and diffusion at smaller scales. Where there is a sharp gradient in a tracer field the effects of the two processes can cancel as diffusion will weaken the gradient and strain will sharpen it. This continues until a threshold is reached whereby the diffusion will dominate as the filament becomes so thin that it is finally mixed into the atmosphere. Due to this Prather and Jaffe (1990) state that the behaviour of the distribution at the boundaries is non-linear since diffusion is a non-linear process, as shown in figure 5.8. Therefore, the linear equation stated above is applicable for the centre of the filament and the maximum of the distribution. In the case of the volcano tracer, as shown in figure 5.4, the 97th percentile of the tracer column contains the majority of the tracer and so this and higher percentiles are used. The same two processes of diffusion (mixing) and exponential decay (chemistry) act on the sulphur dioxide tracer and so can be separated in the same way with the different percentiles providing a range of values.

5.5.1 Numerical Mixing Rate

Now that it has been determined that the different rates are additive the total rate of decay in the model needs to be determined as the first step in calculating the numerical mixing rate of the model. The total decay timescale, τ_{tot}, is the timescale of decay that occurs when a relaxation timescale of τ_{rel} is imposed on the tracer. Due to the fact that

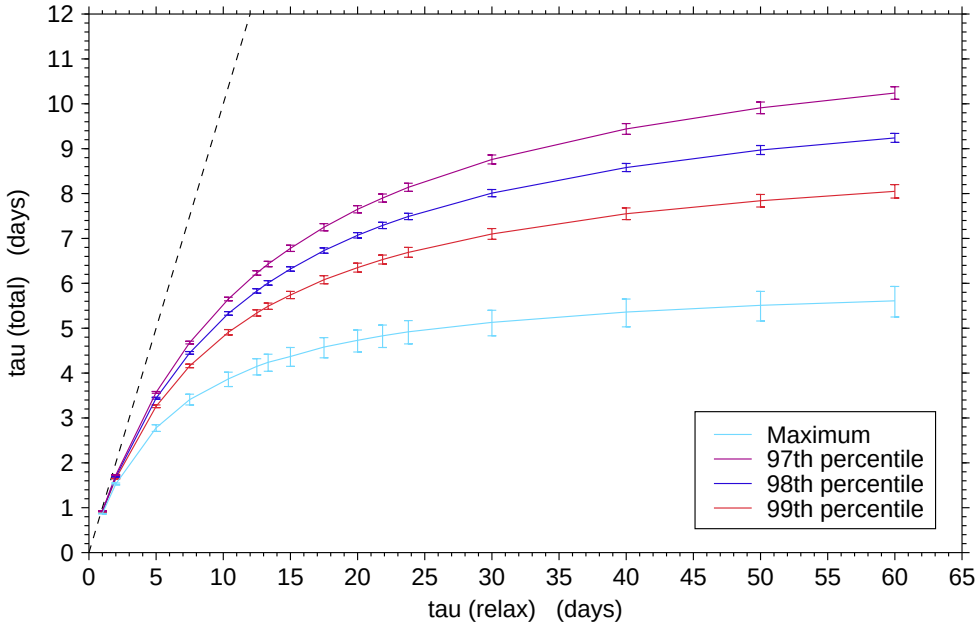

Figure 5.14: *Imposed relaxation timescale (τ_{rel}) plotted against effective decay timescale (τ_{tot}) for the maximum column, 97th, 98th and 99th percentiles at T255. τ_{rel} is set to a specific value in the model and τ_{tot} is what is observed in the model output, both in units of days. Dashed line is the 1:1 line.*

τ_{tot} may be dependent on the percentile from which it is being calculated it was calculated for the maximum tracer column as well as the 99th, 98th and 97th percentiles. The decay timescales were calculated from the 24th June (10 days after model initialisation) to the end of the model run so that only the period where the decay rate had become uniform was considered. However, for some of the faster relaxation timescales the lower percentiles decay to very low values and the period over which the decay rate can be calculated was reduced. The resulting data is shown in figure 5.14 with errors at each data point.

Figure 5.14 shows that the choice of percentile does indeed affect the value of τ_{tot} that is calculated. However, if the maximum column (light blue line) is not considered the remaining three percentiles are very close to each other. It is also expected that the maximum column may exhibit a different behaviour due to it containing the most extreme values that tend to decay more rapidly. It can also be seen that when τ_{rel} is low then $\tau_{tot} \approx \tau_{rel}$. This arises because at these faster relaxation rates the mixing does not have sufficient time to act on the tracer and deviate τ_{tot} from τ_{rel}.

Figure 5.15 shows $1/\tau_{rel}$ against $1/\tau_{tot}$. The first important point to note is that a straight line is produced showing that the mixing rate is constant for any imposed relaxation rate, as desired. Once again it is clearly seen that the line calculated from the maximum column

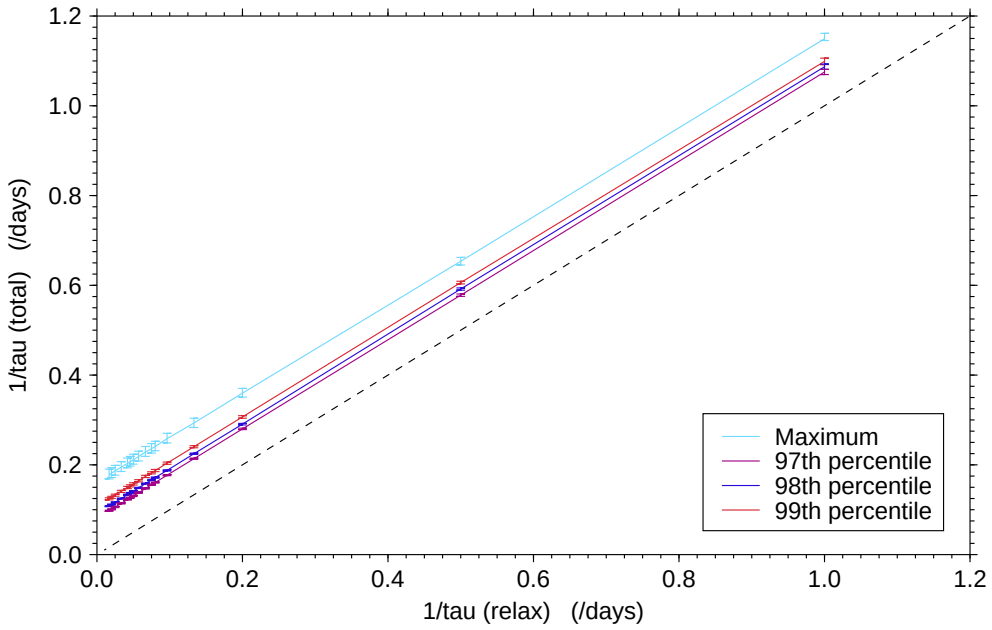

Figure 5.15: *The previous figure re-plotted in terms of rates ($1/\tau$). The y-intercept is the value of $1/\tau_{num}$. Dashed line is the 1:1 line.*

(light blue line) is noticeably different from the other three. From equation (5.3) it is known that the y-intercept is $1/\tau_{num}$, the rate of numerical diffusion or mixing rate.

$$\frac{1}{\tau_{tot}} = \frac{1}{\tau_{num}} + \frac{1}{\tau_{rel}} \tag{5.3}$$

The values of τ_{num} are presented in table 5.2 along with the error in each value. If the numerical mixing timescale calculated from the maximum is once again not considered then the numerical mixing timescale is between 9.3-12.3 days.

Percentile	τ_{num} (days)	Error (days)
97	12.33	±7E-3
98	10.90	±0.02
99	9.26	±0.02
max	6.17	±9E-3

Table 5.2: *Estimates of τ_{num} at T255 calculated from the respective y-intercepts.*

Percentile	τ_{num} (days)	Error (days)
97	13.37	±0.05
98	12.35	±4.9E-3
99	11.32	±6.2E-5
max	8.33	±0.01

Table 5.3: *Estimates of τ_{num} at T159 calculated from the respective y-intercepts.*

Spatial Truncation

The previous experiments were repeated at a truncated horizontal resolution of T159. No other alterations were made to the model set-up. The reduced horizontal resolution had only a minor effect on the column distribution of the tracer. Figure 5.16 shows a comparison for the $\tau_{rel} = 12.5$ days case 0.25 and 7.25 days after the tracer release period (2.75 and 9.75 days after model initialisation). The same general structure of the tracer plume is observed at both resolutions. However, the higher resolution allows for smaller scale features to exist and a larger range of tracer column values. This can be seen by comparing figures 5.16(a) and (c), for T255 and T159 respectively. The increased tracer column range arises due to the smaller grid boxes resulting in slower numerical mixing of the tracer field. This allows the higher resolution model to maintain higher tracer column values, as can be seen a week later in figures 5.16(b) and (d) for T255 and T159 respectively.

As for the previous T255 case the numerical mixing rate was calculated for the various percentiles of the tracer column. The same overall shape is observed as in figure 5.14 and the method for calculating τ_{mix} shown previously is repeated. The values of τ_{num} are presented in table 5.3 along with the error in each value. Excluding the numerical mixing rate calculated from the maximum, at T159 the numerical mixing timescale is between 11.3-13.4 days (compared to 9.3-12.3 days at T255). The numerical mixing timescale varies with horizontal resolution due to a difference in the column values represented by the percentiles used in the calculations. Referring back to figure 5.6, which shows some of the percentiles at T255, if the same percentiles for T159 were overplotted they would be smaller column values and from the calculations shown it is already known that higher tracer column values experience a faster numerical mixing (table 5.2). Therefore, the numerical mixing timescale at T255 is shorter than at T159.

5.6 Mixing Rate Inferred from IASI Data

Now that the numerical mixing rate has been calculated there needs to be something to which it can be compared. In this case it will be the IASI data. Since IASI is measuring SO_2 in the real atmosphere, the rate of decay observed in the data will be as a result of the

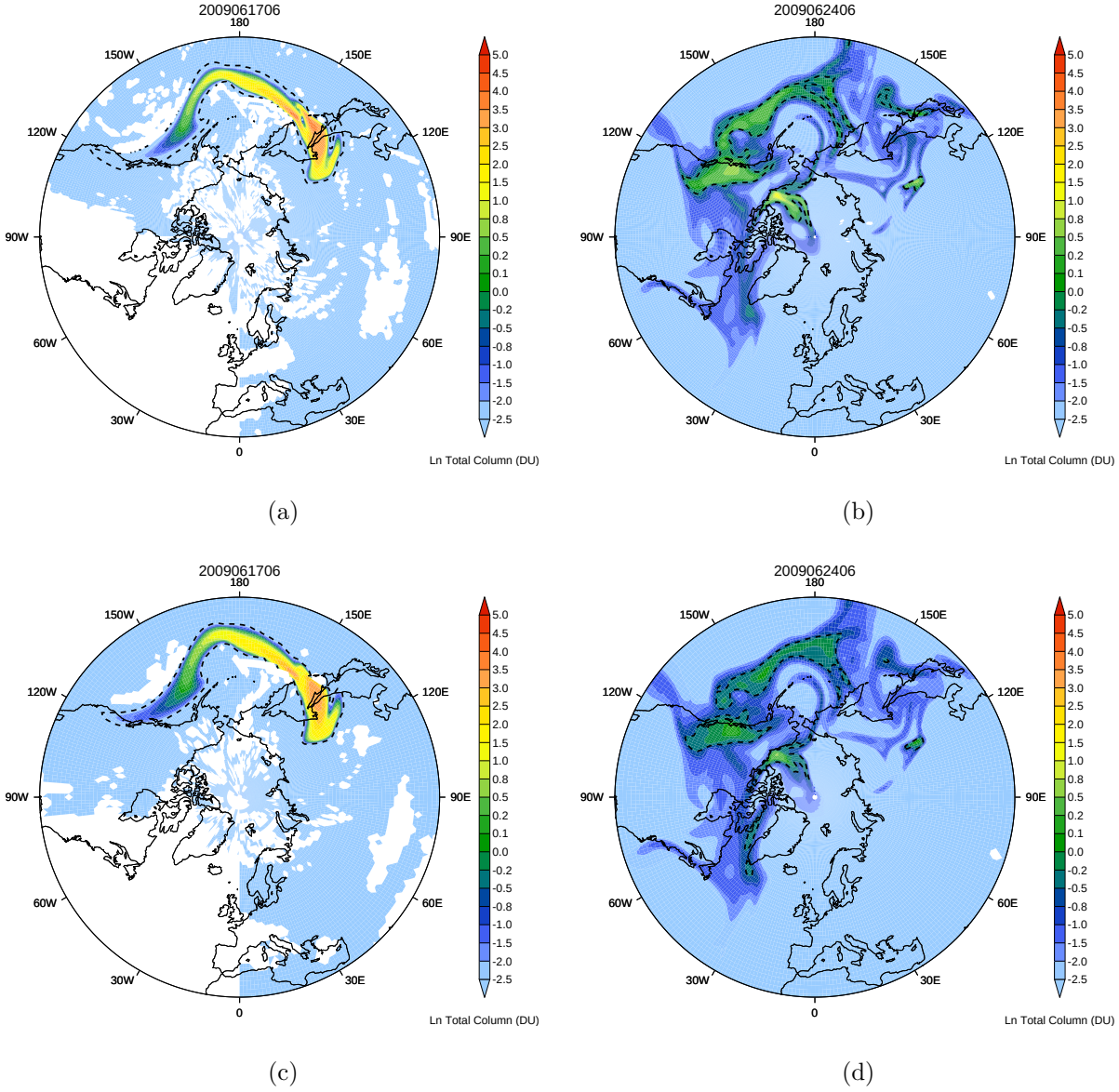

Figure 5.16: *Comparison of model output using $\tau_{rel} = 12.5$ days for (a) and (c) 2.75 days after model initialisation at T255 and T159 respectively. (b) and (d) 9.75 days after model initialisation at T255 and T159 respectively. The dashed line represents the 97th percentile of the distribution.*

chemical loss and mixing. In this case equation (5.2) becomes:

$$\frac{1}{\tau_{obs}} = \frac{1}{\tau_{mix}} + \frac{1}{\tau_{chem}} \tag{5.4}$$

The easiest term to determine is the τ_{obs} (equivalent to the previous τ_{tot}) since this is obtained directly from the IASI data. The calculation of τ_{chem}, which is equivalent to the previous τ_{rel}, is more complicated and will be dealt with secondly.

Total Decay Rate

As with the model output, different percentiles were considered in the calculation of the rate of decay in the IASI data. In this case the 98th, 98.5th, 99th and 99.5th percentiles along with the column maximum are considered. In the case of the IASI data there is a lower limit to the percentile that can be effectively used in the decay rate calculation. This limitation arises from the fact that the majority of the data points maintain a value of zero, indicating values below the detection limit. At most the percentage of non-zero data points is approximately 8%, and this is only achieved at a handful of times. This means that the lowest percentile that could possibly be used would be the 92nd percentile, but a consistent time series of non-zero values would not be available. By increasing the minimum possible percentile to the 98th the non-zero values will be obtained consistently from the 18th June.

Figure 5.17 shows the maximum and four percentiles of the tracer column that are used to calculate the decay rate of the IASI data. The gradients and the equivalent τ_{obs} for each, along with errors, are shown in table 5.4. If the decay timescale from the maximum is once again excluded due to a different behaviour then τ_{obs} is in the range 11.3-15.3 days.

Haywood *et al.* (2010) briefly discuss the mixing rate as diagnosed from IASI and the Hadley Centre Global Environment Model version 2 (HadGEM2) used in their work. The main focus of the presented work was on the radiative impacts of the volcanic plume, but the e-folding time of SO_2 over the Northern Hemisphere is briefly mentioned. For IASI this is stated as being 10-11 days, but due to the detection limit of IASI this was increased to a range of 20-22 days. The doubling of the e-folding time to account for the detection limit was determined through experiments using HadGEM2 which suggested that the detection limit of 0.3 DU for IASI reduced the e-folding time by 50%. However, other limitations to the IASI data, such as the hindrance of cloud cover, are not taken into account. And,

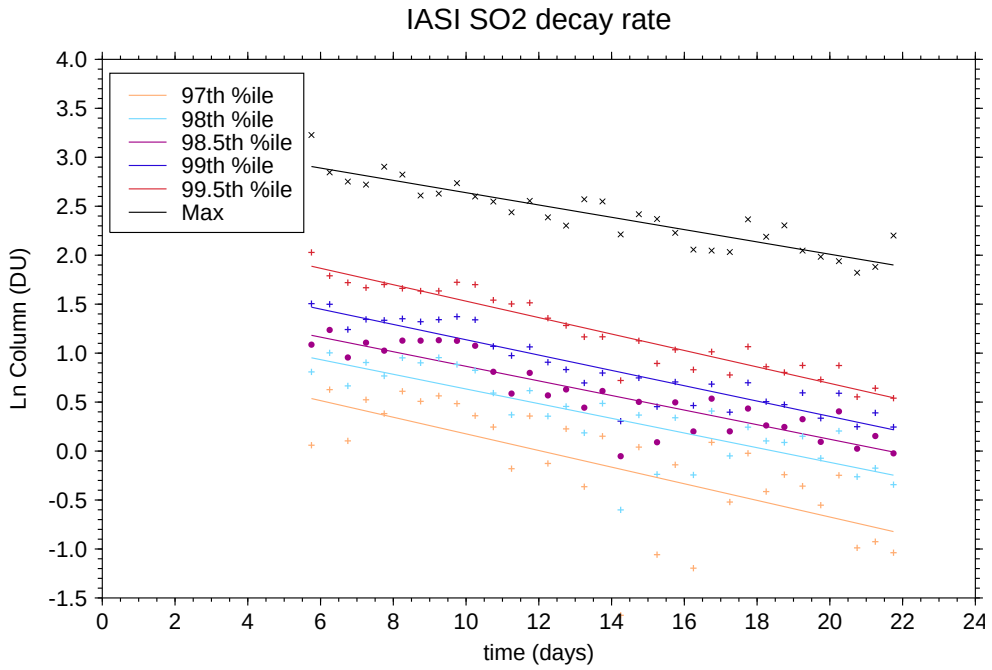

Figure 5.17: *The maximum and percentiles of ln(column) from the IASI data from 1800 hours on the 19th June onwards. Data is represented by the crosses and the solid lines are the lines of best fit.*

Percentile	Gradient	Error	τ_{obs}	Error	
98	-0.07	9.3E-3	13.35	-1.48	+1.90
98.5	-0.07	6.8E-3	13.42	-1.13	+1.36
99	-0.08	5.7E-3	12.78	-0.87	+1.01
99.5	-0.08	4.8E-3	11.91	-0.65	+0.73
max	-0.06	5.1E-3	15.91	-1.19	+ 1.40

Table 5.4: *SO_2 column decay timescale in days as calculated from percentiles of the IASI data.*

more importantly, this method does not account for numerical mixing and dispersion effects within HadGEM2 and will make this doubling of the e-folding time inaccurate and most likely result in an e-folding time that is too long.

Chemical Decay Rate

The τ_{chem} term is concerned with the loss rate of SO_2 through chemistry. The dominant reaction with SO_2 in the atmosphere is its reaction with the hydroxyl radical as shown in reaction (5.5). The reaction rate for this process varies throughout the atmosphere and is dependent on several factors: concentration of OH, temperature and pressure. In this reaction M is a molecule needed in order to conserve momentum and energy. For this work

it will be considered to be molecular nitrogen, N_2, since it makes up 78% of the atmosphere.

$$OH + SO_2 + M \longrightarrow HOSO_2 + M \tag{5.5}$$

The IUPAC (International Union of Pure and Applied Chemistry) has various equations to determine the reaction rate which varies depending on whether the reaction is being carried out at high or low pressure, as well as the temperature range at which it is occurring. Cross sections of the model run show the tracer to be within the 500 hPa-75 hPa pressure range. Taking this as low pressure the relevant reaction rate equation from IUPAC is equation (5.6) (taken from `www.iupac-kinetic.ch.cam.ac.uk/datasheets/xhtml/SOx15_HO_SO2_M.xhtml_mathml.xml` and obtained from laboratory based experiments).

$$k = 4.5\text{x}10^{-31} \left(\frac{T}{300}\right)^{(-3.9\pm1)} [N_2] \tag{5.6}$$

where k is in units of $\text{cm}^3\text{molecule}^{-1}\text{s}^{-1}$, where $[N_2]$ is in units of molecules cm^{-3} and is pressure dependent. Square brackets denote a concentration. This equation is valid for low pressures and temperatures in the range 200 K$\leq$T$\leq$300 K. In order to calculate a rate in s^{-1}, k has to be multiplied by the concentration of OH in units of molecules cm^{-3}. In these calculations the values of [OH] used were taken from Wang and Jacob (1998) which shows a zonally-averaged annual mean distribution.

An alternative reaction rate that has been stated in DeMore *et al.* (1997) and Jones *et al.* (2001), similar to that used by IUPAC, is:

$$k = 3.3\text{x}10^{-31} N_{air} \left(\frac{T}{300}\right)^{-3.3} \tag{5.7}$$

where the units are the same as for equation (5.6).

In comparison, Somnitz (2004) provides yet another equation to calculate k. Choosing the one derived for a pressure of 300 hPa, in the centre of the pressure range of interest, the equation for k is:

$$k = 1.29\text{x}10^{-12} \left(\frac{T}{300}\right)^{-3.92} exp\left(\frac{-443}{T}\right) \tag{5.8}$$

where once again k is in units of $\text{cm}^3\text{molecule}^{-1}\text{s}^{-1}$, and multiplying by [OH] in molecule cm^{-3} will give a rate in s^{-1}. Equation (5.8) produces lower values than the equation recommended by IUPAC. Somnitz suggests that this difference arises due to the use of a different scheme in the calculation of the reaction rates. This particularly refers to the

Pressure	Temperature	[OH] molecule/cm^3	k cm^{3}molecule^{-1}s^{-1}	k[OH] s^{-1}	τ_{chem} days
75 hPa	220 K	5x10^5	5.42x10^{-13}	2.71x10^{-7}	42.7
500 hPa	256 K	7.5x10^5	4.26x10^{-13}	3.19x10^{-7}	36.3

Table 5.5: *Reaction rates for $SO_2 + OH$*

work of Wine *et al.* (1984) whose results are used as the basis for equation (5.6). IUPAC used this work due to the fact that it also reproduced the results of Paraskevopoulos *et al.* (1983), Leu (1982) and Lee *et al.* (1990). Somnitz (2004) also compares the results to Leu (1982) and Lee *et al.* (1990) which both provide reaction rates that are larger than, but in a similar range to, those presented in the paper.

Equation (5.8) was chosen to be used over equation (5.6) due to the fact that it appears to be a more updated version of that presently recommended by IUPAC. The results are presented in table 5.5, with a value corresponding to the top and bottom of the pressure range in which the tracer plume is primarily located. A key point to make note of is that there exists a range of equations to calculate the reaction rate, k, which differ due to varying methods used to calculate them.

Using τ_{chem} along with τ_{obs} in equation (5.4) provides a range within which the rate of mixing occurs in the atmosphere as determined from the IASI data. Using combinations of the maximum and minimum values for τ_{obs} and τ_{chem}, then τ_{mix} is calculated as being 15.3-26.1 days.

5.7 Comparison of Mixing Rates

From the model a numerical mixing timescale of 12.35 ($\pm$1.05) days has been calculated (at T255), compared to 20.7 ($\pm$5.4) days from the IASI data. One reason for the difference between the two values could be due to the calculation of τ_{chem} (which would alter the mixing rate determined from IASI). To calculate this term several assumptions have been made. Firstly, all reactions apart from the reaction with OH have not been considered. Whilst it is true that this is the dominant reaction, other reactions do occur, especially within clouds or regions of high humidity. This reaction is outlined in reactions (5.9) and

(5.10). There is also the production of sulphuric acid from SO_2 in the presence of liquid water.

$$SO_2 + H_2O \rightleftharpoons H^+ + HSO_3^- \quad (5.9)$$

$$HSO_3^- \rightleftharpoons H^+ + SO_3^{2-} \quad (5.10)$$

Reversible chemical reactions that can produce SO_2 have also not been taken into account. This additional loss of SO_2 would result in a greater chemical loss rate (larger τ_{chem}). In order to obtain the same value of τ_{obs} this means that the mixing rate would decrease (smaller τ_{mix}).

There are also several limitations with using the IASI data. Firstly, the previously mentioned detection limit of IASI means that the data may indicate a faster decay rate than actually occurs due to the column dropping below the detectable value. SO_2 column not detected due to the presence of cloud will also have a similar effect. The other limitation is that Sarychev Peak continued to emit gases for a considerable amount of time after the initial eruptive period, with observations noting gas emissions into July. This continued emission will replace SO_2 that has already undergone chemical reactions and therefore a slower loss rate will be determined. Since these effects oppose each other they will cancel partially, but to what extent is not known.

One other unknown is in the chemical mixing rate where the concentration of OH varies depending on season as well as other chemical process that are occurring. In volcanic plumes it is not uncommon for all of the OH to be removed due to the large quantity of chemical processes occurring (von Glasow, 2010). This would decrease the rate of SO_2 loss due to chemistry. However, there can be elevated concentrations of OH relative to the surrounding unpolluted atmosphere which would increase the rate of chemical loss of gases such as SO_2. These facts will make the chemical loss rate of SO_2 highly variable. Never-the-less, any shorter chemical timescale (smaller τ_{chem}) would imply a smaller mixing rate (hence longer timescale) in order to be consistent with the observed total loss.

A comparison can also be made with existing diffusivity rates and mixing timescales in literature. The mixing timescales calculated from the model are slightly faster than what is currently assumed to be the mixing rate in the true atmosphere. Arnold *et al.* (2007) presents a mixing rate determined from data obtained during the International Consortium for Atmospheric Research on Transport and Transformation (ICARTT) experiments.

From the data they calculated a joint hydrocarbon loss (via reaction with OH) and mixing rate of 0.1 day^{-1}, which is faster than calculated in the work here. One reason for this difference is that the work presented by Arnold *et al.* (2007) focuses on the lower troposphere whereas this work considers the UTLS region. Therefore the difference would be expected as the upper troposphere experiences less convection, and hence mixing, than the lower troposphere. Balluch and Haynes (1997) presented a vertical diffusivity for the lower stratosphere of 0.014 m^{2}s^{-1}. This is in agreement with values presented in Legras *et al.* (2005) who measured a vertical diffusivity of 0.01 m^{2}s^{-1} in the lower stratosphere vortex and 0.1 m^{2}s^{-1} in the lower stratosphere surf zone. Legras *et al.* (2005) also state that the vertical diffusivity rates that have been calculated and published range from 5-0.001 m^{2}s^{-1}. The large range arises due to the differing methods used to determine the vertical diffusivity and the different regions of the atmosphere considered.

In order to compare these diffusivity rates with the model the mixing timescale, τ_{num}, needs to be converted into a diffusivity. In order to do this the equation determined from ICARTT Lagrangian experiments that considered a layer of polluted air in between two less polluted layers will be used. From this work it was determined that (Cain, 2009):

$$\frac{1}{\tau_{num}} = \frac{2\kappa}{H^2} \tag{5.11}$$

where κ is the diffusivity (m^{2}s^{-1}) and H (m) is the depth of the layer being considered since the vertical mixing dominates horizontal mixing (Haynes and Anglade, 1997).

A depth range of 20-2000 m would cover all of the features in the tracer field, but as any diffusivity would be dominated by smaller features in the tracer field then an estimate of 200 m is not unreasonable. If the mixing timescales previously stated are used then both T255 and T159 give an approximate diffusivity of 0.02 m^{2}s^{-1}. One reason for the difference between this diffusivity and that published by Legras *et al.* (2005) and Balluch and Haynes (1997) is that the mixing rate calculated for the model is an average mixing rate that takes into account all of the length scales in the tracer distribution. If the largest length scale is considered then the model diffusivity increases by a factor of 100. Even so, the model diffusivity is still within the range of diffusivities that have been calculated as presented by Legras *et al.* (2005).

5.8 Summary

Initial testing with the numerical scheme shows that if possible it is best not to use a simple positive definite scheme due to a significant mass gain (there are more complex and accurate positive definite schemes available). In this case the mass input into the model was more than tripled. The monotonic option resulted in a much better mass conservation, only creating a slight mass gain compared to the control run, but removing some of the extrema that were produced in the control run. The mass non-conservation observed in the control and monotonic runs was -2.65% and -2.29% respectively. This is worse than the 0.02% mass gain over ten days observed when using a stratospheric ozone tracer and ERA-Interim at T255. However, Chapter 3 also showed that tracers that are weighted towards the lower model levels, such as this volcano experiment, show a greater mass change. The model run shows a much better mass conservation than the volcano experiment presented in the IFS study (Flemming and Huijnen, 2011) which shows a 10% mass gain over ten days for the best case scenario.

The inclusion of a relaxation timescale in the model revealed an additional source of tracer decay, leading to the deduction of a numerical mixing timescale, τ_{num}. From carrying out work with diffusion and exponential decay acting on an ideal filament it was found that decay rates were additive. Using this fact allowed for τ_{num} to be calculated and was found to be 10.8 ($\pm$1.5) days at T255 and 12.35 ($\pm$1.05) days at T159. A comparison of the tracer column distribution at the two different horizontal resolutions shows the differences that would be expected due to the use of a coarser model grid. Specifically, a tendency towards a larger range of tracer values at higher resolutions due to the decreased level of averaging that arises with the use of smaller grid boxes.

Using the rate of decay of the IASI data and the chemical reaction rate of OH+SO_2 a τ_{mix} of 20.7 ($\pm$5.4) days was calculated for the atmosphere. This mixing timescale is slower than that calculated in the model partly due to the assumptions made during the calculation of τ_{chem}. It must also be noted that the mixing timescale from IASI may be slightly slower than the true mixing timescale due to the fact that that IASI can only detect tracer in clear, or cloud free, air (figure 5.5) in the upper troposphere where there is reduced convection. Some of the differences between the two values of mixing timescale could arise from the fact that there are a lot of uncertainties with the calculation of τ_{chem}. Also, limitations in

IASI will feed into the calculation of τ_{mix}. Without a precise quantification of these factors it is difficult to say how accurate the mixing timescale of 3 weeks calculated from the IASI data is.

Converting the mixing timescale into a diffusivity rate for the model obtained a mid-range value of 0.02 m^2s^{-1}. The literature on diffusivity rates gives a value of 0.01 m^2s^{-1} in the lower stratosphere outside of the surf zone. The difference in the values can be associated with the fact that the model mixing timescale implicitly takes into account all length scales thereby providing an average diffusivity, whereas the diffusivity from the literature will be for a more specific length scale. The model diffusivity also takes into account the upper troposphere and is not restricted to the lower stratosphere where the diffusivity of 0.01 m^2s^{-1} was calculated. Even though the model diffusivity is larger it is within the range of diffusivities that have been published. As such the numerical mixing timescale within the model can be seen as a realistic value.

Chapter 6

Feasibility of a Tracer-Relative CTM

Up to this point the work in this thesis has focused on the conservation properties of a global three dimensional tracer advection model. The next step is to take the output from this three dimensional model and use it to investigate the concept of a background state, specifically, whether a tracer-relative CTM of the chemical background state is feasible. Some details on the concept of a background state were described in the Introduction. The chemical background state can be loosely defined as the slowly varying state of the atmosphere to which perturbations, such as gas emissions, then occur.

It is sometimes useful to define a background state in atmospheric chemistry. In air quality studies, the deviation from some norm or background is required to define pollution and identify the effects of recent emissions. Another example of when a background state is used is in trajectory photochemical models when there is mixing between the trajectory and some nominal background state defined in the model. Neither of these examples provide a precisely defined background state. Is it possible to define a background state in a meaningful way?

As mentioned in the Introduction (Sections 1.1.3 and 1.1.4) some long-lived gases that are emitted remain in the atmosphere for years and contribute to the background state composition. This is a slow process because it takes time for the emitted gases to cease being a perturbation and instead be incorporated into the background state of the atmosphere. This is highlighted by the work of Prather (1994) and Wild and Prather (2000) on the existence of global chemical eigenmodes in the atmosphere, as also presented in Section 1.1.4. This work showed that the primary mode in the troposphere has an estimated lifetime of 14.2 years and therefore perturbations can exist for this length of time before being incorporated into the background state. However, Chapter 5 showed that the mixing timescale in the atmosphere for a point source of tracer is in the range of 10-20 days and so

an actual pulse release of passive tracer would be indistinguishable from the atmospheric background within a month. Mixing on larger scales, such as interhemispheric mixing and stratosphere-troposphere mixing, can have a much longer mixing timescale. The problem is that the background state is rarely defined precisely. The aim of the work presented here is to investigate the feasibility of defining a background state that evolves on timescales greater than 10 days as a result of mixing and photochemistry.

6.1 Theory

The tracer-relative CTM is based one particular property of the evolving atmosphere; the alignment of contours of long-lived tracers. A characteristic of chaotic advection is that, assuming that mixing and chemistry occurs on slower timescales than the decorrelation timescale of the tracer trajectories, contours of long-lived tracers align over time. Therefore, if the distribution of one tracer is known it is conceivable that the distribution of other tracers can be determined if the scaling factor between the respective tracers can be calculated.

The alignment of tracer contours can be shown using the 3D model by initialising two different tracer distributions, advecting them over the same period and then comparing the outputs (e.g. figure 4.7). This will reveal that both distributions will reflect the same key features and an alignment of contours implies a compact relationship on a scatter plot, as mentioned in Section 1.1.3. Many concentrations of the shorter-lived chemical species are dependent on the concentrations of the long-lived chemical species in the air mass. One good example of this is the concentration of OH which is strongly dependent on gases such as H_2O and O_3. This results in the short-lived tracers also aligning even though they are chemically active on much shorter timescales than the advection.

Nakamura (1996) underlines the basic theory behind the use of equivalent latitude and 'equivalent length' in order to describe mixing and the evolution of a tracer, q. The equivalent length is in essence the length of a contour and contains information on the change in area (and hence mass) contained by that contour. The two cases of potential vorticity (PV) and a generic chemical tracer are considered by Nakamura (1996). There are several other published papers that further develop the theory outlined by Nakamura (1996). Among

these are Bühler and Haynes (1999) who investigate fluxes in PV-θ co-ordinates, Thuburn and Lagneau (1999) and Methven (2003). This theory, along with that of the background state, will be presented in detail in this section.

Thuburn and Lagneau (1999) explain the disadvantages of using a Eulerian mean method. Firstly, the Eulerian mean can change via adiabatic as well as non-conservative processes (such as friction, diabatic heating, irreversible PV mixing), and it can be difficult to isolate these slow processes. Also the gradients in PV, especially around the polar regions, can be smeared out during Eulerian zonal averaging. These disadvantages are reduced with the use of a co-ordinate based on mass contained within contours, such as that used by Nakamura (1996) for a non-divergent 2D flow.

6.1.1 Single Layer Flow on the Sphere

The concept of a background state is first presented for a simple fluid layer. To begin with a reference tracer, q, and the associated rate of change in mixing ratio, S, will be defined as:

$$\frac{Dq}{Dt} = S \tag{6.1}$$

The continuity equations for column mass and tracer amount are:

$$h_t + \nabla.(\underline{u}h) = H \tag{6.2}$$

$$(hq)_t + \nabla.(\underline{u}hq) = hS + qH \tag{6.3}$$

where H is the mass source in the layer and h is the fluid depth. The above equations are also outlined in Thuburn and Lagneau (1999) where some of the following steps are shown.

Next define the volume (or alternatively mass with density set to unity) of reference tracer, q, that is within a contour, Q.

$$M(Q) = \frac{1}{2\pi} \iint\limits_{q \geq Q} h a^2 d\lambda d\mu \tag{6.4}$$

where the corresponding area, $A(Q)$, is:

$$A(Q) = \frac{1}{2\pi} \iint\limits_{q \geq Q} a^2 d\lambda d\mu \tag{6.5}$$

and λ is longitude and μ is the sine of the latitude. This definition of mass is identical to equation (15) in Thuburn and Lagneau (1999).

The change of $M(Q)$ with time is of interest. Differentiating equation (6.4) with respect to time gives:

$$\frac{\partial M}{\partial t} = -\frac{1}{2\pi} \oint\limits_{q=Q} h\underline{u}_c.\underline{n}dl + \frac{1}{2\pi} \iint\limits_{q \geq Q} \frac{\partial}{\partial t} h a^2 d\lambda d\mu$$

Using equation (6.2) this becomes:

$$\frac{\partial M}{\partial t} = \frac{1}{2\pi} \oint\limits_{q=Q} h(\underline{u} - \underline{u}_c).\underline{n}dl + \frac{1}{2\pi} \iint\limits_{q \geq Q} H a^2 d\lambda d\mu \tag{6.6}$$

$$\underline{u}_c = -\frac{\partial q}{\partial t} \frac{\underline{n}}{|\nabla q|} \tag{6.7}$$

$$\underline{n} = \frac{\nabla q}{|\nabla q|} \tag{6.8}$$

where a is the radius of the planet, $\underline{u}_c$ is the velocity of the contour and $\underline{n}$ is the inward pointing normal (towards higher values of q). Equations (16) and (17) in Thuburn and Lagneau (1999) combine to produce equation (6.6), and equation (18) supports the definition of $\underline{u}_c$ presented above. The notation used by Thuburn and Lagneau (1999) defines the first term on the right-hand side of equation (6.6) as $V(Q)$, which is the net mass flux across a contour, Q. Methven (2003) also interprets $-V(Q)$ as the rate of change of the sine of equivalent latitude for the contour, Q.

If the equations for $\underline{u}_c$, $\underline{n}$ and $\underline{u}$ detailed above are used along with equations (6.2)-(6.3), the $h(\underline{u} - \underline{u}_c).\underline{n}$ term can be written as:

$$\begin{aligned} h(\underline{u} - \underline{u}_c).\underline{n} &= \frac{h\underline{u}.\nabla q}{|\nabla q|} + h\frac{\partial q}{\partial t}\frac{1}{|\nabla q|} \\ &= \frac{1}{|\nabla q|}\left[h\left(\underline{u}.\nabla q + \frac{\partial q}{\partial t}\right)\right] \\ &= \frac{1}{|\nabla q|} hS \end{aligned} \tag{6.9}$$

Substituting this into equation (6.6) gives:

$$\frac{\partial M}{\partial t} = \frac{1}{2\pi} \oint\limits_{q=Q} \frac{hS}{|\nabla q|} dl + \frac{1}{2\pi} \iint\limits_{q \geq Q} H a^2 d\lambda d\mu \tag{6.10}$$

This is also stated as equation (19) in Thuburn and Lagneau (1999). After this point Thuburn and Lagneau (1999) and the work presented here deviate as Thuburn and Lagneau

(1999) are dealing with the dynamical shallow water equations, whereas this work is concerned with ozone and its photochemical evolution.

The novel stage for this work is to then define a second (active or passive) tracer, r. Once again the mass of this tracer contained within a reference tracer contour Q is defined as:

$$B(Q) = \frac{1}{2\pi} \iint\limits_{q \geq Q} hra^2 d\lambda d\mu \tag{6.11}$$

The rate of change of $B(Q)$ at a fixed location in tracer co-ordinates, $Q = q_0$, is similar to that for $M(Q)$ (equation 6.6).

$$\left.\frac{\partial B}{\partial t}\right|_Q = \frac{1}{2\pi} \iint\limits_{q \geq Q} \frac{\partial}{\partial t}(hr) a^2 \lambda d\mu - \frac{1}{2\pi} \oint\limits_{q=Q} hr \underline{u}_c . \underline{n} dl \tag{6.12}$$

Using the conservation law

$$\frac{\partial}{\partial t}(hr) + \nabla . (\underline{u} hr) = hR + rH \tag{6.13}$$

where

$$R = \frac{Dr}{Dt} \tag{6.14}$$

Substituting equation (6.13) into the definition of $\partial B/\partial t$ in equation (6.12) gives:

$$\left.\frac{\partial B}{\partial t}\right|_Q = \frac{1}{2\pi} \iint\limits_{q \geq Q} (hR + rH) a^2 d\lambda d\mu + \frac{1}{2\pi} \oint\limits_{q=Q} hr(\underline{u} - \underline{u}_c) . \underline{n} dl \tag{6.15}$$

Following through the method used to produce equation (6.9) again and using the definitions for $\underline{u_c}$ and $\underline{n}$ given previously provides:

$$\left.\frac{\partial B}{\partial t}\right|_Q = \frac{1}{2\pi} \iint\limits_{q \geq Q} (hR + rH) a^2 d\lambda d\mu + \frac{1}{2\pi} \oint\limits_{q=Q} \frac{rhS}{\mid \nabla q \mid} dl \tag{6.16}$$

Up to this point the equations have been kept general. The first approximation is introduced in the next step which is to define the background mixing ratio, r_0:

$$\begin{aligned} r_0 &= \left.\frac{\partial B}{\partial Q}\right|_\theta \Big/ \left.\frac{\partial M}{\partial Q}\right|_\theta \\ &= \frac{\partial B}{\partial M} \end{aligned} \tag{6.17}$$

Taking equation (6.16) and using the condition $r = r_0(Q, \theta)$ is constant around the contour $q = Q$, as well as equation (6.10) means that $\partial B/\partial t$ can be defined as the mass rate of change at a location, $q_0 = Q$, in tracer co-ordinates:

$$\begin{aligned} \left.\frac{\partial B}{\partial t}\right|_Q &= r_0 \frac{\partial M}{\partial t} - \frac{r_0}{2\pi} \iint\limits_{q \geq Q} H a^2 d\lambda d\mu \\ &+ \frac{1}{2\pi} \iint\limits_{q \geq Q} r H a^2 d\lambda d\mu + \frac{1}{2\pi} \iint\limits_{q \geq Q} h R a^2 d\lambda d\mu \end{aligned} \tag{6.18}$$

If H, R, $q(\lambda, \mu, t)$ and $h(\lambda, \mu, t)$ are known then the equation can be integrated forward in time to solve for $r_0(Q, \theta)$.

Special Case: PV in the shallow water equations

Thuburn and Lagneau (1999) considered shallow water PV:

$$q = \frac{\zeta}{h}$$

If this is used then the PV conservation equation will contain a friction, $\underline{X}$, term such that:

$$(hq)_t + \nabla.(\underline{u} hq) = -\nabla.(\underline{k} \times \underline{X})$$

and

$$h \frac{Dq}{Dt} = -qH - \nabla.(\underline{k} \times \underline{X})$$

Using these means that equation (6.10) becomes:

$$\frac{\partial M}{\partial t} = -\frac{1}{2\pi} \oint\limits_{q=Q} \frac{Hq + \nabla.(\underline{k} \times \underline{X})}{|\nabla q|} dl + \frac{1}{2\pi} \iint\limits_{q \geq Q} H a^2 d\lambda d\mu$$

One of the first points made by Bühler and Haynes (1999) is that between any two PV contours within two isentropic surfaces mass is conserved under the condition that there are no diabatic or frictional processes. Methven (2003) shows (using the non-divergent quasi-geostrophic case) how this can be transformed into an equation for the evolution of the background PV, $q_0(\mu)$. Note that in this case μ is the equivalent latitude.

The circulation around a contour, Q, can also be defined using the absolute velocity, $\underline{u}_{abs}$,

(which includes planetary rotation) such that:

$$\begin{aligned} C(Q) &= \frac{1}{2\pi} \oint_{q=Q} \underline{u}_{abs}.dl \\ &= \frac{1}{2\pi} \iint_{q \geq Q} hqa^2 d\lambda d\mu \end{aligned} \tag{6.19}$$

Thuburn and Lagneau (1999) were the first to show that $A(q_0)$ and $C(q_0)$ can be used to obtain $q_0(\mu, t)$:

$$Q\frac{\partial M}{\partial Q} = \frac{\partial C}{\partial Q} \tag{6.20}$$

Which is, in essence, the same as equation (6.17). Bühler and Haynes (1999) also calculate the circulation around a contour as stated in equation (6.19). This equation is then used in order to determine mass fluxes (both horizontal and vertical) across the contour, Q, rather than the mass contained within the contour.

6.1.2 Isentropic Co-ordinate Equations on the Sphere

Now that the method has been shown, the generalisation to 3D isentropic co-ordinates will be made and note that throughout the following work the hydrostatic approximation is used. This method only varies slightly from that already detailed. The first stage is to define a pseudo-density:

$$\sigma = -\frac{1}{g}\frac{dp}{d\theta} \tag{6.21}$$

where p is pressure and g is the acceleration due to gravity. The pseudo-density in turn defines a mass element:

$$m = \sigma \delta x \delta y \delta \theta \tag{6.22}$$

where θ is the potential temperature and is used as the vertical co-ordinate.

Via conservation it is known that

$$\frac{\partial \sigma}{\partial t} + \nabla.(\sigma \underline{u}) = 0 \tag{6.23}$$

where, in isentropic co-ordinates,

$$\underline{u} = (u, v, \dot{\theta}) \tag{6.24}$$

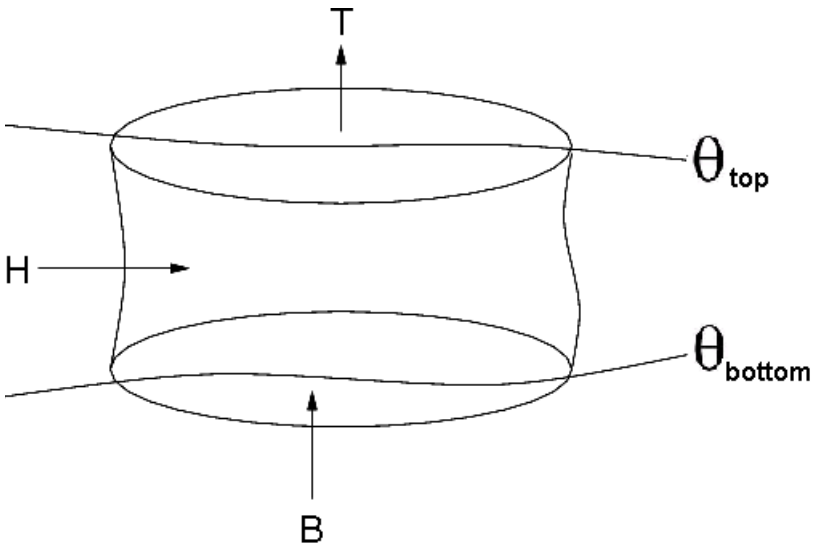

Figure 6.1: *Schematic of the control volume used. The top and bottom are defined by potential temperature surfaces and the sides by a reference tracer concentration, Q. The arrows represent the lateral and diabatic mass fluxes that then need to be considered.*

where u and v are the velocity components on θ-surfaces and $\dot{\theta}$ is the heating rate.

For a reference tracer, q, with a source, S, the continuity equation becomes:

$$\frac{\partial}{\partial t}(\sigma q) + \nabla.(\sigma q \underline{u}) = \sigma S \tag{6.25}$$

$$\frac{Dq}{Dt} = S \tag{6.26}$$

As before define the mass of reference tracer within the reference tracer contour $q = Q$ on an isentropic layer,

$$M(Q) = \frac{1}{2\pi} \iiint_{q \geq Q} \sigma a^2 d\lambda d\mu d\theta \tag{6.27}$$

The time evolution of M within a control volume $[\theta,\theta + \delta\theta]$ for $q \geq Q$, such as that shown in figure 6.1, is determined by the increase in volume for a fixed density plus the increase in density for a fixed volume. This can be written as

$$\frac{\partial M}{\partial t} = \frac{1}{2\pi} \int\!\!\oint_{q=Q} -\sigma \underline{u}_c.\underline{n} dl d\theta + \frac{1}{2\pi} \iiint_{q \geq Q} \frac{\partial \sigma}{\partial t} a^2 d\lambda d\mu d\theta \tag{6.28}$$

The first term on the right-hand side includes the motion of the lateral boundaries of the control volume.

The three $\underline{n}$ vectors (side, bottom and top of control volume) are defined as:

$$\underline{n} = \frac{\nabla_H q}{\mid \nabla_H q \mid} \tag{6.29}$$

$$\underline{n}_b = \frac{\nabla \theta}{\mid \nabla \theta \mid} \tag{6.30}$$

$$\underline{n}_t = \frac{\nabla \theta}{\mid \nabla \theta \mid} \tag{6.31}$$

Substituting equation (6.23) into equation (6.28) gives:

$$\begin{aligned}
\frac{\partial M}{\partial t} &= \frac{1}{2\pi} \oint\!\!\!\!\!\!\int_{q=Q} -\sigma \underline{u}_c . \underline{n} dl d\theta - \frac{1}{2\pi} \iiint_{q \geq Q} \nabla . (\sigma \underline{u}) a^2 d\lambda d\mu d\theta \\
&= \frac{1}{2\pi} \oint\!\!\!\!\!\!\int_{q=Q} -\sigma \underline{u}_c . \underline{n} dl d\theta - \frac{1}{2\pi} \iint_{dV} \sigma \underline{u} . d\underline{S} \\
&= \frac{1}{2\pi} \oint\!\!\!\!\!\!\int_{q=Q} -\sigma \underline{u}_c . \underline{n} dl d\theta + \frac{1}{2\pi} \oint\!\!\!\!\!\!\int_{q=Q} \sigma \underline{u} . \underline{n} dl d\theta \\
&\quad -\frac{1}{2\pi} \iint_{q \geq Q} ([\sigma \dot{\theta}]_t - [\sigma \dot{\theta}]_b) a^2 d\lambda d\mu
\end{aligned} \tag{6.32}$$

where the first two integrals on the right-hand side represents the change in volume due to the mass flux across the contour $q = Q$, for example that in figure 6.1. The inward normal across the contour $q = Q$ (points towards higher q) is represented by $\underline{n}$ and dl is a distance element along the contour.

If the first two terms on the right-hand side are combined then:

$$\frac{\partial M}{\partial t} = \frac{1}{2\pi} \oint\!\!\!\!\!\!\int_{q=Q} \sigma (\underline{u} - \underline{u}_c) . \underline{n} dl d\theta - \frac{1}{2\pi} \iint_{q \geq Q} [\sigma \dot{\theta}]_b^t a^2 d\lambda d\mu \tag{6.33}$$

The equations previously defined for $\underline{u_c}$ and $\underline{n}$ are once again used for the lateral boundary. Therefore, expanding out the bracket in the first integral on the right-hand side, as in equation (6.9) and using the definition of S previously given (equation 6.25), produces:

$$(\underline{u} - \underline{u}_c) . \underline{n} = \frac{1}{\mid \nabla_H q \mid} \left(S - \dot{\theta} \frac{\partial q}{\partial \theta} \right) \tag{6.34}$$

Substitute this back into the equation for $\partial M / \partial t$ to get:

$$\frac{\partial M}{\partial t} = \frac{1}{2\pi} \oint\!\!\!\!\!\!\int_{q=Q} \frac{\sigma}{\mid \nabla_H q \mid} \left(S - \dot{\theta} \frac{\partial q}{\partial \theta} \right) dl d\theta - \frac{1}{2\pi} \iint_{q \geq Q} [\sigma \dot{\theta}]_b^t a^2 d\lambda d\mu \tag{6.35}$$

The first term on the right-hand side is the mass flux into the volume across the q contours forming the lateral boundary. The second term then describes the mass flux into the volume across θ surfaces forming the top and bottom boundaries.

The novel step then arises from the definition of a second (active or passive) tracer, r, and the mass within a reference tracer contour, Q:

$$B(Q) = \frac{1}{2\pi} \iiint\limits_{q \geq Q} \sigma r a^2 d\lambda d\mu d\theta \tag{6.36}$$

and for continuity

$$\frac{\partial \sigma r}{\partial t} + \nabla.(\sigma r \underline{u}) = \sigma R \tag{6.37}$$

where R is the material derivative of r that represents sources and sinks.

Using the same control volume as that for M and using equation (6.37) the evolution of B with time is:

$$\begin{aligned} \frac{\partial B}{\partial t} &= \frac{1}{2\pi} \oint\limits_{q=Q} \int -r\sigma \underline{u}_c.\underline{n} dl d\theta + \frac{1}{2\pi} \iiint\limits_{q \geq Q} \frac{\partial(\sigma r)}{\partial t} a^2 d\lambda d\mu d\theta \\ &= \frac{1}{2\pi} \oint\limits_{q=Q} \int -r\sigma \underline{u}_c.\underline{n} dl d\theta + \frac{1}{2\pi} \iiint [-\nabla.(\sigma r \underline{u}) + \sigma R] a^2 d\lambda d\mu d\theta \end{aligned} \tag{6.38}$$

The right-hand side of the equation is similar to that for M, but with an additional term in the form of R. If Gauss' Theorem and the steps in equations (6.29)-(6.33) used then

$$\begin{aligned} \frac{\partial B}{\partial t} &= \frac{1}{2\pi} \oint\limits_{q=Q} \int r\sigma(\underline{u} - \underline{u}_c).\underline{n} dl d\theta - \frac{1}{2\pi} \iint\limits_{q \geq Q} [r\sigma\dot{\theta}]_b^t a^2 d\lambda d\mu \\ &\quad + \frac{1}{2\pi} \iiint\limits_{q \geq Q} \sigma R a^2 d\lambda d\mu d\theta \end{aligned} \tag{6.39}$$

The last term on the right-hand side is the only additional term when compared to the equivalent equation for M (equation 6.33).

It is at this point that the background mixing ratio, r_0, is defined. The key assumption in this definition is that contours of r and q are parallel,

$$r = r_0(q_0, \theta, t) \tag{6.40}$$

where r_0 is a relationship between M and B. This relationship is determined by considering a shell defined by $[\theta,\theta + \delta\theta]$ and $[Q,Q + \delta Q]$. Therefore, r_0 can be defined as:

$$r_0 = \frac{\text{mass of tracer in shell}}{\text{mass of shell}} = \left(\frac{\partial B}{\partial Q}\right) \Big/ \left(\frac{\partial M}{\partial Q}\right) \tag{6.41}$$

The next stage uses the background mixing ratio (6.40) to approximate the lateral flux in equation (6.39) to produce:

$$\begin{aligned}\frac{\partial B}{\partial t} &\simeq \frac{1}{2\pi}\int r_0(Q) \oint_{q=Q} \sigma(\underline{u}-\underline{u}_c).\underline{n} dl d\theta \\ &\quad -\frac{1}{2\pi}\iint_{q\geq Q}\left[r\sigma\dot{\theta}\right]_b^t a^2 d\lambda d\mu + \frac{1}{2\pi}\iiint_{q\geq Q}\sigma R a^2 d\lambda d\mu d\theta \end{aligned} \tag{6.42}$$

Equation (6.40) is then used again in order to approximate the diabatic mass flux:

$$\begin{aligned}\frac{\partial B}{\partial t} &\simeq r_0\frac{\partial M}{\partial t} - \frac{1}{2\pi}\iint_{q\geq Q}[(r_0(q)-r_0(Q))\sigma\dot{\theta}]_b^t a^2 d\lambda d\mu \\ &\quad +\frac{1}{2\pi}\iiint_{q\geq Q}\sigma R a^2 d\lambda d\mu d\theta \end{aligned} \tag{6.43}$$

A further level of approximation on the diabatic mass flux, and an alternative to equation (6.43), is to assume that $r \simeq r_0(Q)$ over the whole volume or $r - r_0$ is uncorrelated with $\sigma\dot{\theta}$:

$$\iint_{q\geq Q}\left[r\sigma\dot{\theta}\right]_b^t a^2 d\lambda d\mu \simeq r_0(Q)\iint_{q\geq Q}\left[\sigma\dot{\theta}\right]_b^t a^2 d\lambda d\mu \tag{6.44}$$

So that equation (6.43) reduces to:

$$\frac{\partial B}{\partial t} \simeq r_0\frac{\partial M}{\partial t} + \frac{1}{2\pi}\iiint_{q\geq Q}\sigma R a^2 d\lambda d\mu d\theta \tag{6.45}$$

Note that the 3D distribution of r is not needed, just R, S, $q(\lambda,\mu,\theta,t)$ and $\sigma(\lambda,\mu,\theta,t)$.

In summary, the two equations that will be taken from here are:

$$\frac{\partial M(Q,\theta,t)}{\partial t} = \frac{1}{2\pi}\int\oint_{q=Q}\frac{\sigma}{\mid\nabla_H q\mid}\left(S-\dot{\theta}\frac{\partial q}{\partial\theta}\right)dl d\theta - \frac{1}{2\pi}\iint_{q\geq Q}[\sigma\dot{\theta}]_b^t a^2 d\lambda d\mu$$

and

$$\begin{aligned}\frac{\partial B(Q,\theta,t)}{\partial t} &\simeq r_0\frac{\partial M(Q,\theta,t)}{\partial t} - \frac{1}{2\pi}\iint_{q\geq Q}[(r_0(q)-r_0(Q))\sigma\dot{\theta}]_b^t a^2 d\lambda d\mu \\ &\quad +\frac{1}{2\pi}\iiint_{q\geq Q}\sigma R a^2 d\lambda d\mu d\theta \end{aligned}$$

where:

σ - is the pseudo-density

M - is the atmospheric mass within a reference tracer contour, $q = Q$, in an isentropic layer.

Visually, it is the mass contained within the volume in figure 6.1. In all of the following work PV is used as the reference tracer

B - is the mass of chemically active tracer contained within a reference tracer contour $q = Q$

r_0 - is the background state

λ - is the longitude

μ - is the sine of the latitude

θ - is the potential temperature

R - is the chemistry or source/sink term for the active tracer, r

a - is the radius of the planet

g - is the acceleration due to gravity.

The first equation relates the rate of change in mass of the control volume (figure 6.1) to the horizontal mass flux across reference tracer contours and the diabatic mass flux divergence across the bounding isentropic surfaces. The second equation relates the rate of change of a tracer in the control volume to the rate of change in total mass, a term related to the correlation between the tracer and heating and lastly a term representing the material source/sink of the tracer.

6.2 Pseudo-height and Lait PV

In the following figures the vertical axis is plotted as a pseudo-height relative to 380 K at the tropics. The 0 km line indicates the location of the 380 K isentrope in the tropics and then heights are calculated using the equation:

$$z = \frac{H}{\kappa} ln \left(\frac{\theta}{\theta_0} \right) \tag{6.46}$$

where:

- $\kappa = R/C_p = 2/7$
- $H = 6.5$ km, is the pressure scale height
- $\theta_0 = 380$ K reference potential temperature

Pseudo-height, z, is derived assuming an isothermal profile (a good approximation for the lower stratosphere) and using the definition of potential temperature $\theta = T(p/p_0)^{-\kappa}$. Three

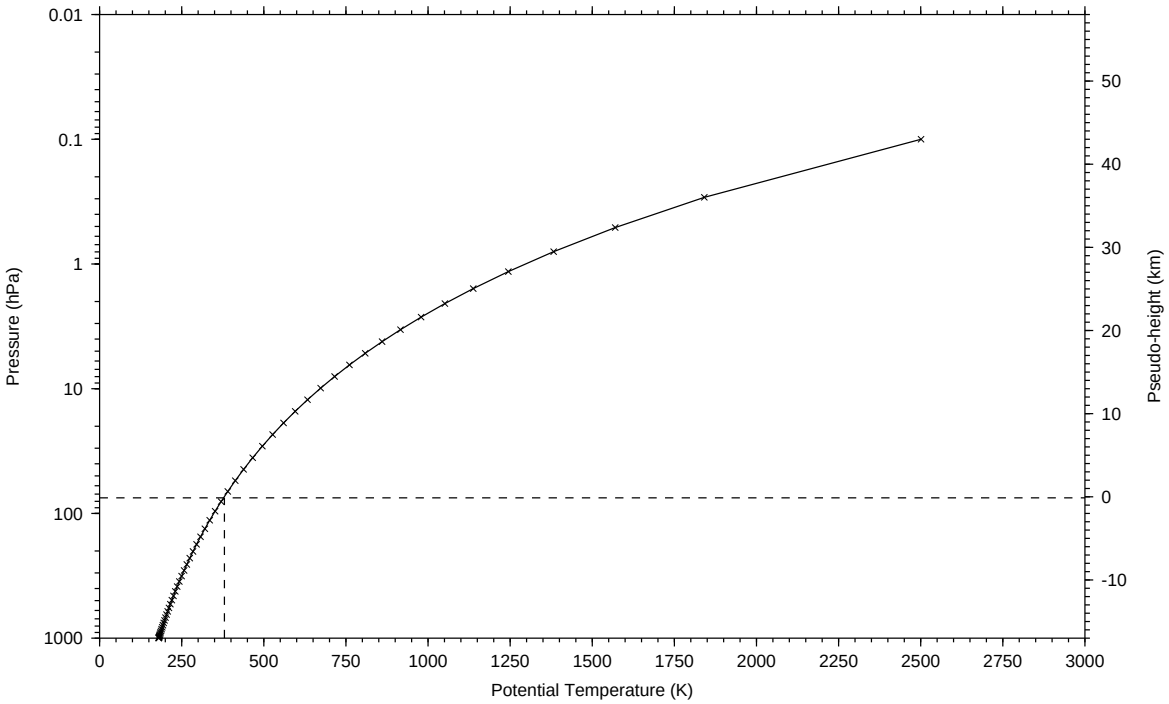

Figure 6.2: *Plot showing the relationship between the various vertical co-ordinates: pressure (hPa), potential temperature (K) and pseudo-height (km). The dashed lines represent the 380 K reference height. Crosses mark the model levels.*

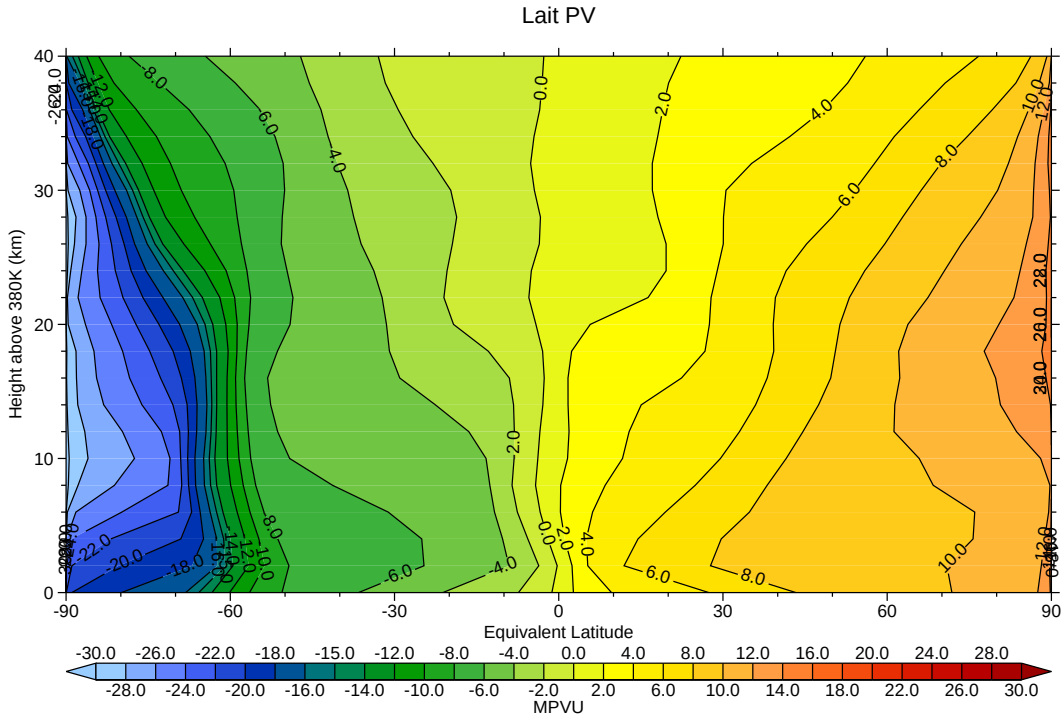

Figure 6.3: *September mean distribution of stratospheric Lait PV in modified PV units (MPVU) plotted in pseudo-height-equivalent latitude (ϕ_e) co-ordinates. ϕ_e is obtained from the area within PV contours.*

vertical co-ordinates, pressure (hPa), potential temperature (K) and pseudo-height (km), have all been plotted against each other in figure 6.2 in order to provide a clear reference for the pseudo-height in the following figures. The dashed line represents the 380 K potential temperature reference height (θ_0) used in the above calculation of the pseudo-height.

The other property that needs to be briefly discussed is a modified version of PV otherwise known as Lait PV. Lait (1994) published this form of PV as a way to reduce the strong vertical gradient observed in Ertel PV, and is once again derived assuming an isothermal profile and an exponential decrease in pressure. Lait PV is defined as:

$$P_{Lait} = P_{Ertel} \left(\frac{\theta}{\theta_0} \right)^{-\frac{9}{2}} \tag{6.47}$$

where P_{Ertel} is the Ertel PV and θ_0 has the same value as in equation (6.46).

The September mean of the stratospheric Lait PV is shown in figure 6.3 plotted in co-ordinates of pseudo-height and equivalent latitude (z,ϕ_e). The concept of equivalent latitude was presented in the Introduction (Section 1.1.2). The region of particular interest for the following work is the Southern Hemisphere as the Brewer-Dobson circulation has yet to shift the direction of dominant flow into the Northern Hemisphere (due to the change in season). The ozone hole is also present over the South Pole at this time of year and is a noticeable feature in some of the following work.

6.3 Evolution of the Background State

This next section looks specifically at the evolution of the background state composition (defined by equation 6.41) when using PV as the reference tracer. Both M and B are calculated as a sum whereby the grid box is included in the sum if $q \geq Q$. (Note that because q is located at the centre of the grid box the grid box is included in the summation only if the centre of the box is contained within the contour Q.) Figure 6.4 shows the evolution of the background state throughout the month of September 2006. The plots on the left of each figure are the background state for the passive ozone tracer and those on the right are for the chemically active ozone tracer. Both tracers were initialised as the April ozone climatology from Cariolle and Teyssédre (2007) and advected with ERA-Interim at T255.

In the background state for both the passive and active tracers the circulation and chemistry are reflected. As such both of the evolving background states strongly resemble the cross-sections shown in figures 3.11 and 4.8 for the passive and active ozone tracers respectively. In the passive ozone tracer background state images the ascent in the tropics and descent over the Southern Hemisphere pole is shown by the tropical values in the lower stratosphere decreasing over time as the high values are advected upwards. The increase in values in the 20-30 km range over the South Pole highlights the downward motion of the circulation. The ozone hole is located at a pseudo-height of approximately 10 km and has been circled in the last image. The ozone maximum is also maintained by photochemistry (as was shown in Section 4.1.1) in the tropical region at a pseudo-height of 20 km. The key point from this is that the background state is able to represent the slow evolution of the tracer field and highlight the non-conservative processes (such as photochemistry).

6.4 Parallel Contour Approximation

In the Introduction (Section 1.1.3) the use of tracer-tracer correlations was presented as a method to identify regions of mixing and chemistry. Tracer-tracer correlations are also exceedingly useful here to determine the validity of one of the main assumptions made at the start of this work that the contours of different long-lived tracers will align over time as long as advection is the dominant process in determining the tracer distribution. This assumption can be tested by using tracer-tracer scatter plots as a compact relationship between the two tracers will represent an alignment of tracer contours. During this investigation it can be determined whether there is a more compact tracer-tracer relationship when using a PV-θ or a latitude-η co-ordinate system. For the work in this chapter the two tracers used are Lait (or Modified) PV (reference tracer, q) and ozone (active/passive tracer, r), and as such these two tracers are used in the scatter plots presented below. All of the scatter plots shown are for the 15th September as this is the middle of the month that will be considered for the rest of this chapter.

The first comparison to be made is between Lait PV and active ozone on a model η-surface and on the nearest potential temperature surface in figures 6.5(a) and 6.5(b) respectively. The scatter plot for the model level that is at approximately 30 hPa shows a large spread in the Southern Hemisphere. When both the ozone and Lait PV are interpolated on to poten-

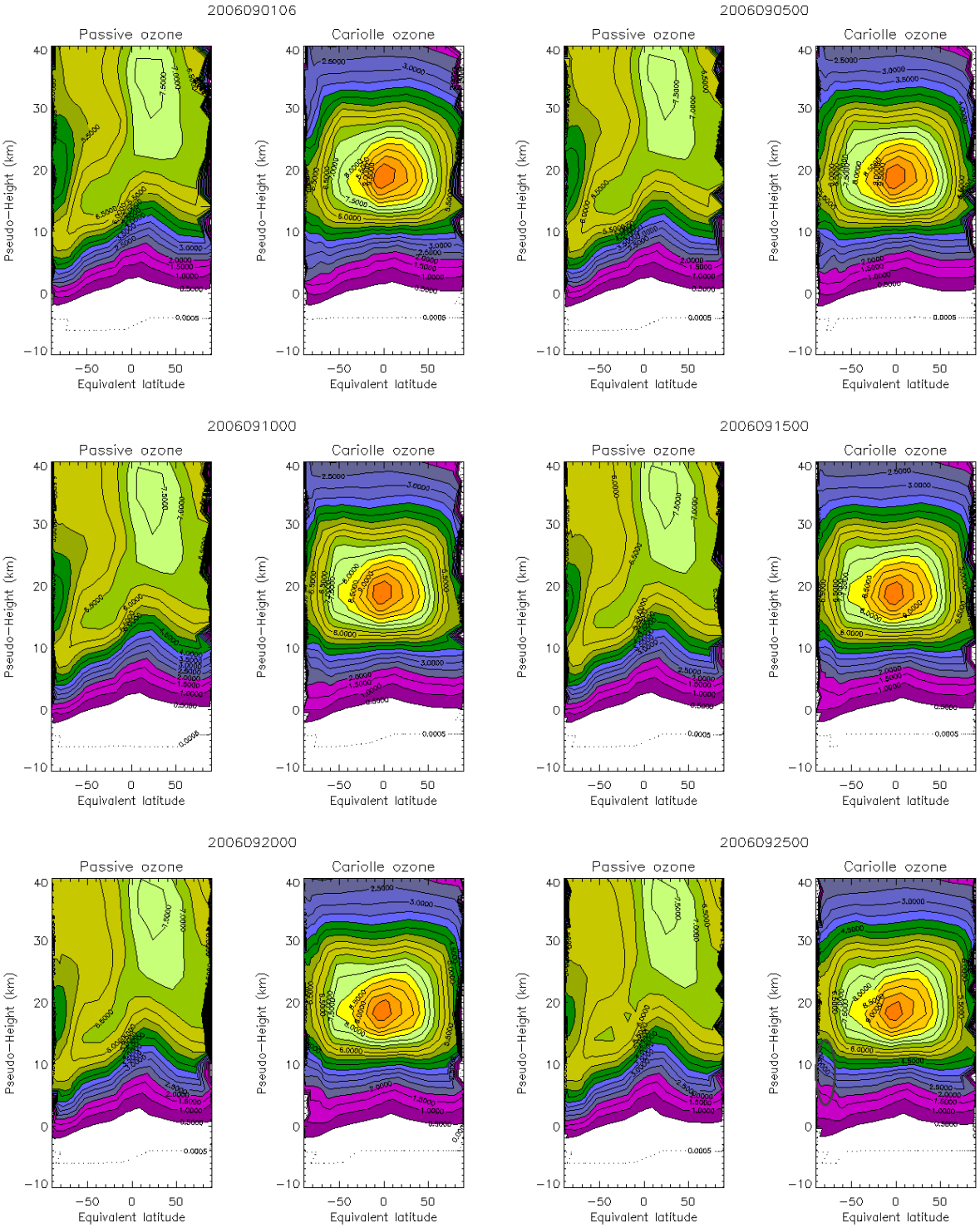

Figure 6.4: *Background state (ppmv) for a passive and active ozone tracer throughout the month of September. A contour interval of 0.5 ppmv is used. The circle in the last image highlights the region of the ozone hole. The pseudo-height can be considered as the distance above the 380 K isentropic surface in km.*

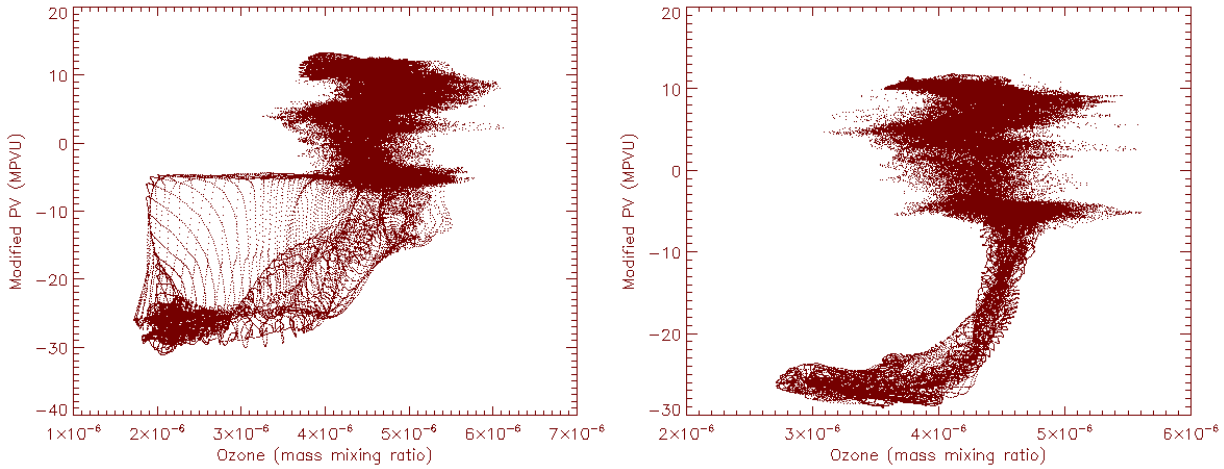

(a) 28.9 hPa pressure level

(b) 590 K potential temperature surface

Figure 6.5: *Comparison of the relationship between active ozone contours and Lait PV contours on (a) a model η-level at 28.9 hPa and (b) 590 K potential temperature surface. A more compact distribution means that the parallel contour approximation is valid. This supports the use of potential temperature, rather than pressure as the vertical co-ordinate.*

tial temperature surfaces the resulting scatter plot, figure 6.5(b), shows a considerably more compact relationship, and tracer contours are more closely aligned. In particular the spread of ozone values in the Southern Hemisphere has reduced considerably. This arises due to the transport in the stratosphere having a predominately adiabatic component (Plumb, 2007), resulting in an alignment of tracers on each isentropic surface. Since a single pressure level will intersect a range of isentropic surfaces the resulting scatter plot is more diffuse. As such the use of a potential temperature co-ordinate in the vertical is definitely beneficial for this work. Sparling *et al.* (1997) also state that potential temperature co-ordinate is of particular advantage when considering vertical motion as the effects of vertical displacement, and general movement, of the isentropic surfaces is removed. In the stratosphere this is useful as diabatic motion is slow relative to the adiabatic motion and thus the vertical motion calculated is not artificially enhanced by the natural movement of the isentropic surfaces. In particular, fast gravity waves are just undulations in the isentropic surface.

Figure 6.6 compares the use of latitude and PV as the second co-ordinate used in the background state. The figure also compares the relationship between Lait PV and active ozone and Lait PV and passive ozone. In all cases the horizontal surface considered is the 590 K isentropic surface. If the active ozone tracer is considered first, the most notable feature of the scatter plot using latitude (figure 6.6(a)) is the broad region that covers the region from 50S to 80N. When Lait PV is used instead (figure 6.6(b)) this broad

region becomes less dominant and the compact relationship in the Southern Hemisphere more noticeable. This tropical feature arises because in this region there is the strongest deviation from parallel contours due to the significant amount of ozone photochemistry. By using Lait PV the emphasis on this region is reduced due to the small range of Lait PV values (figure 6.3). This in turn emphasises the contour alignment between PV and ozone in the Southern Hemisphere polar vortex and the surrounding surf zone. The scatter plot supports the choice of PV as the second co-ordinate.

Now that the choice of co-ordinate system has been supported, the last comparison to be made is between the active and passive ozone tracer. Due to the fact that the chemistry does not act uniformly around an ozone contour an increased spread in the scatter plot is expected when using the active ozone tracer. Figure 6.6 shows that this is indeed the case by comparing figure 6.6(b) using active ozone and figure 6.6(d) using passive ozone. In the active ozone scatter plot there is a highly variable region in the tropics and the entire Northern (summer) Hemisphere that highlights the strong chemistry maintaining the ozone distribution. This in turn reveals that stirring by the flow is much weaker in the summer hemisphere and it takes longer for tracer contours to align.

In the Southern Hemisphere the chemistry does not have as large an impact (at this time) and the advection is allowed to have an increased effect on the ozone distribution. However, by comparing with the passive ozone scatter plot it can be seen that the curved shape in the Southern Hemisphere (-8 to -24 MPVU) is a consequence of the chemistry acting to decrease the amount of ozone and maintain a more structured distribution. An increased spread in ozone values is also a result of the chemistry. The range in active ozone close to the South Pole is representative of the polar vortex and the processes behind it will be considered later. In the Northern Hemisphere the effect of including chemistry is significant as the passive ozone tracer image shows a very strong alignment of contours that is difficult to see when using the active ozone tracer.

Strong correlations between the passive tracer and PV (figure 6.6d) are a direct result of transport and mixing. The Brewer-Dobson circulation as represented in figure 6.7 can help to explain the origin of some of the features in the scatter plots. The distinct ozone minimum in the scatter plot at 20N is associated with the northern flank of the tropical upwelling region. The reason for the ozone minimum being shifted into the Northern Hemisphere is due to the fact that the tropical upwelling is known to migrate into the summer

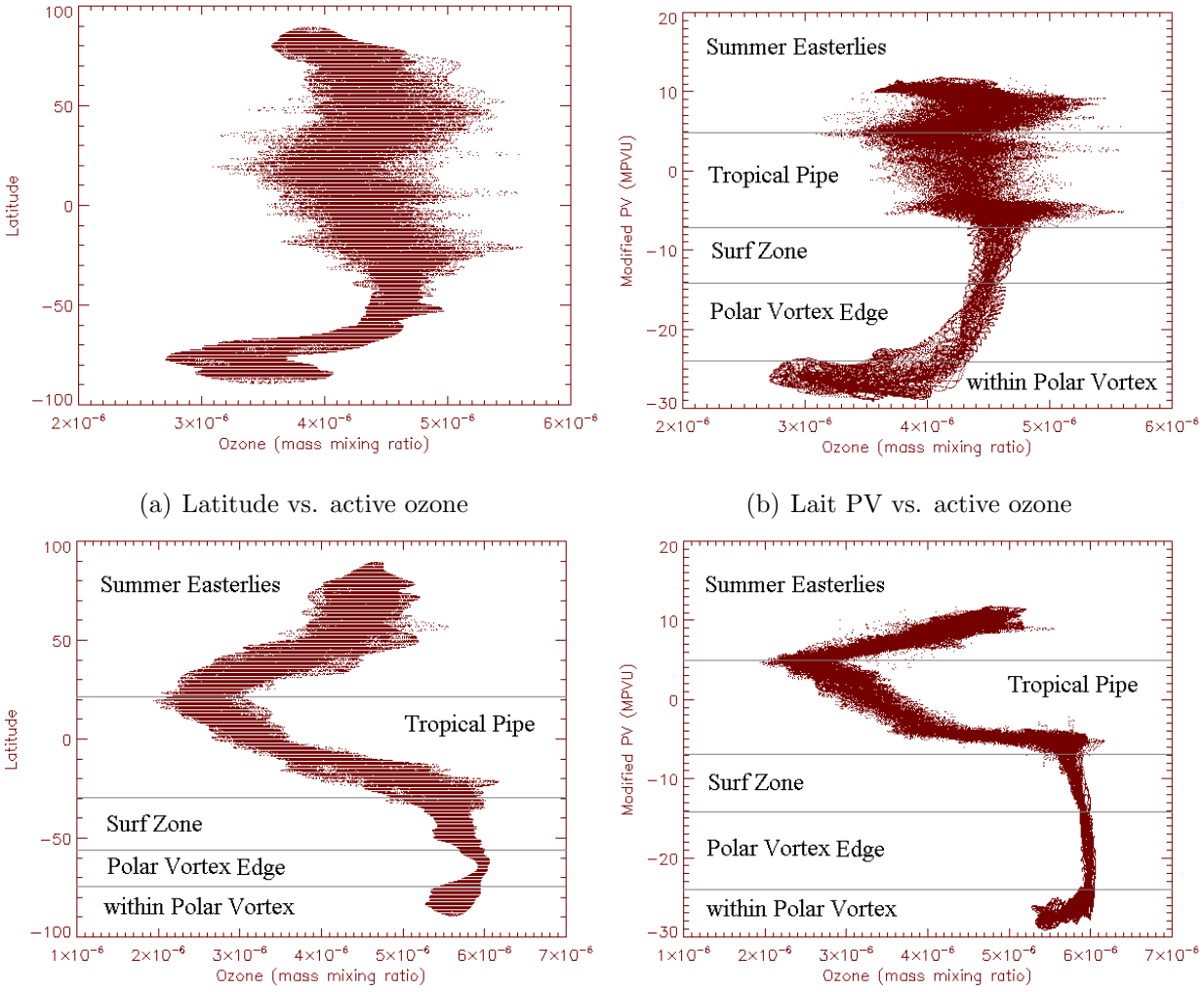

(a) Latitude vs. active ozone

(b) Lait PV vs. active ozone

(c) Latitude vs. passive ozone

(d) Lait PV vs. passive ozone

Figure 6.6: *Comparison of the relationship between contours of active ozone tracer against (a) latitude and (b) Lait PV, which is a proxy for equivalent latitude. As well as a comparison of the relationship between contours of passive ozone tracer against (a) latitude and (b) Lait PV. In all cases ozone has been interpolated onto the 590 K potential temperature surface. The use of Lait PV reduces the emphasis of the tropical region in the scatter plot and allows the compact relationship in the Southern Hemisphere to dominate, thereby supporting the use of Lait PV in the co-ordinate system. Due to the absence of photochemistry the passive ozone tracer demonstrates a more compact relationship as the distribution is determined purely by advection, resulting in a strong contour alignment.*

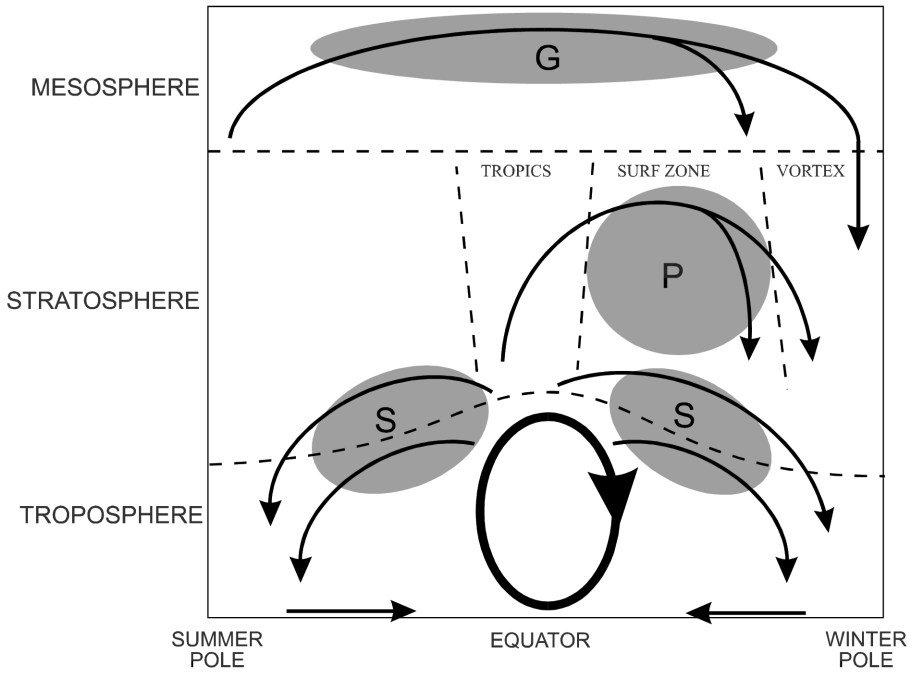

Figure 6.7: *A schematic of the residual mean circulation in the stratosphere taken from Plumb (2002). The dark ellipse in the troposphere represents the Hadley circulation. The shaded ellipses represent regions of synoptic (S), planetary (P) and gravity (G) wave breaking which drive branches of the stratospheric and mesospheric circulation.*

hemisphere (Plumb, 2002). The ascent associated with the Brewer-Dobson circulation is also biased towards the summer hemisphere. The gradient in the relationship arises due to the combination of weak mixing, that does not produce homogeneity in the passive tracer distribution on isentropic surfaces, and the diabatic transport of low ozone values from below.

The Southern (winter) Hemisphere shows two distinct features: the surf zone and the polar vortex. The dominant feature is the nearly constant ozone mixing ratio which signifies the mixing and homogenisation of tracers across the surf zone. The transition from the tropical region to the surf zone is seen as a sharp gradient at approximately 30S in figure 6.6(c) which signifies the subtropical mixing barrier. Strong local mixing within the surf zone is required to create this compact tracer-tracer relationship (Plumb, 2007). Figure 6.7 also shows that planetary-scale wave breaking occurs in this region which is the dominant driver of the strong mixing in the surf zone.

Figure 6.6(c) shows a change in the tracer-tracer relationship at the southern edge of the surf zone. This marks another mixing barrier, this time it is the polar vortex edge and is marked in figure 6.7 as the dashed line separating the surf zone and the vortex. When using

the active ozone tracer this region is highlighted in the scatter plot by a linear decrease in ozone mixing ratio between the almost constant values in the surf zone and the wide range in the polar vortex. The PV gradient is very tight across the vortex edge, with PV decreasing from -14 MPVU to -24 MPVU over a small latitude range, as seen in figure 6.6d. The range of ozone values that arise within the vortex is due, as stated by Plumb (2002), not just to the descent within the vortex, but also the weak mixing. The range cannot be attributed just to descent because the surf zone also experiences a broad region of descent which is a feature of the Brewer-Dobson circulation. Plumb (2002) also mentions that the air within the polar vortex descends at a faster rate than in the surf zone due to the fact that the strong horizontal mixing within the surf zone causes the air to descend at the mean rate of descent across the broad region. No air parcels remain at the higher latitudes within the surf zone, where the localised descent is stronger, for long.

In the Northern (summer) Hemisphere the mixing is weaker than in the Southern (winter) Hemisphere (Plumb, 2007). As a result a broader range of ozone values is maintained and a gradient in the scatter plot is produced. In general few features will be observed in the Northern Hemisphere due to the dominance of the tropical region stated previously. The sharp change in gradient on the northward flank of the tropical pipe at approximately 20N is due to the presence of a subtropical mixing barrier (i.e. dashed line to the left of the tropics in figure 6.7). This barrier is maintained through diabatic processes (Plumb, 2002) and only allows weak mixing between the tropical region and the rest of the Northern Hemisphere. Detailed theory on the barrier is presented by Neu and Plumb (1999) as part of the leaky pipe model. It is considered as a leaky pipe as the subtropical barrier in each hemisphere allows weak mixing in both directions, meaning that the different regions are not completely isolated and, as a result, weakens the tracer gradient between them.

As mentioned above, due to weak diabatic processes in the stratosphere tracers tend to be advected adiabatically along isentropic surfaces, which impacts the tracer-tracer scatter plots. Namely a strong isentropic mixing means that tracer distributions become more uniform across portions of isentropic surfaces (Plumb, 2007) and different tracer-tracer relationships develop on the different potential temperature surfaces (Morgenstern *et al.* (2002) and Waugh *et al.* (1997)). This strong dependence on potential temperature is reflected in the fact that if the scatter plots presented above are produced on a different isentropic surface there is a distinct difference in the shape of the relationship between Lait

PV and both the active and passive ozone tracer.

6.5 Mass, Heating and Tracer Budgets

The mass and tracer equations ((6.35) and (6.39) respectively) will now be analysed by application to September 2006. Throughout the following work the subscript system of (k, m) as an abbreviation for the co-ordinate system (Q_k, θ_m). Also, the model grid is regular in pseudo-height (Δz=2 km) and in Lait PV contours (ΔQ=2 MPVU). The mass evolution in equation (6.35) will be considered first as it deals solely with the reference tracer and is required for the evolution of the active or passive tracer. Equation (6.35) can be integrated from $\theta_{m-1/2}$ to $\theta_{m+1/2}$ and abbreviated to:

$$\frac{\partial M_{k,m}}{\partial t} = V_{M_{k,m}} - (D_{k,m+1/2} - D_{k,m-1/2}) + \epsilon_{M_{k,m}} \tag{6.48}$$

$$D_{k,m+1/2} = \frac{1}{2\pi} \iint\limits_{q \geq Q} \left[\sigma\dot{\theta}\right]_{m+1/2} a^2 d\lambda d\mu \tag{6.49}$$

where $M_{k,m}$ is the mass contained within an isentropic layer (θ_m) integrated within the contour $q \geq Q_{k,m}$. D is the diabatic mass flux across the interfaces between isentropic layers, and V_M is the adiabatic mass flux across reference tracer contours (figure 6.1). These two together describe the Brewer-Dobson circulation, which will be discussed in more detail later. The final term, ϵ_M is the error in the equation. Since the V_M term on the right-hand side of equation (6.48) is not explicitly calculated there is no way to separate the error, ϵ_M, from V_M.

There are two possible approximations with respect to the evolution of the second tracer (equation 6.39) that can be made in the diabatic heating term. The first option is to use the full tracer field rather than the background state inside the diabatic tracer flux calculation. In which case equation (6.42) can be written as:

$$\begin{aligned}\frac{\partial B_{k,m}}{\partial t} = {} & r_{0_{k,m}} \frac{\partial M_{k,m}}{\partial t} + r_{0_{k,m}} \left(D_{k,m+1/2} - D_{k,m-1/2}\right) \\ & - E_{k,m+1/2} + E_{k,m-1/2} + R_{k,m} + \epsilon_{a_{k,m}}\end{aligned} \tag{6.50}$$

$$E_{k,m+1/2} = \frac{1}{2\pi} \iint\limits_{q \geq Q} \left[r\sigma\dot{\theta}\right]_{m+1/2} a^2 d\lambda d\mu \tag{6.51}$$

Equation (6.48) has been substituted in to represent the V_M term. The $R_{k,m}$ is representative of the last integral on the right-hand side of equation (6.43) that represents the sources and sinks (e.g. chemistry) of the tracer. The budget error is represented by ϵ_a, where the a denotes that this is the error for the first approximation (using E).

The second option is to use the background state within the diabatic tracer flux integral as in equation (6.43):

$$\begin{aligned}\frac{\partial B_{k,m}}{\partial t} &= r_{0_{k,m}}\frac{\partial M_{k,m}}{\partial t} + r_{0_{k,m}}\left(D_{k,m+1/2} - D_{k,m-1/2}\right) \\ &\quad -F_{k,m+1/2} + F_{k,m-1/2} + R_{k,m} + \epsilon_{b_{k,m}} \end{aligned} \tag{6.52}$$

$$F_{k,m+1/2} = \frac{1}{2\pi}\iint\limits_{q\geq Q}\left[r_0(q)\sigma\dot{\theta}\right]_{m+1/2} a^2 d\lambda d\mu \tag{6.53}$$

The same notation is used in these equations as for the previous approximation, but this time the subscript b represents the error for this second approximation (using F). If $r_0(q) \sim r_0(Q)$ in equation (6.53) then $F_{k,m+1/2} \sim r_0(Q)D_{k,m+1/2}$ and the ΔD and ΔF terms would cancel in equation (6.52). This is the next level of approximation that was previously discussed in equation (6.44). The magnitudes of the different residual errors are quantified in the next section. All of the heating rates needed for the diabatic fluxes (D, E and F) are calculated using ERA-Interim. It must also be noted that the majority of the coding required for these calculations was completed by John Methven.

6.6 Monthly Mean Mass Evolution and Errors

6.6.1 Thermal Tides and Time Filtering

Due to the rotation of the planet there is a strong thermal tide that arises in the atmosphere due to the solar heating. The two main components of this are the diurnal and semi-diurnal components (Andrews *et al.*, 1987). The semi-diurnal component of the tide is stronger than the diurnal component and arises due to the absorption of solar radiation, especially UV radiation by ozone. The largest absorption of UV radiation is near the stratopause, the heating signal then propagates down through the atmosphere and can be observed in the surface pressure, therefore effecting all levels of the atmosphere.

Since this semi-diurnal heating is a strong feature in the diabatic fluxes (D, E and F) there is also a strong signal in the tendencies of both M and B. The diurnal cycle makes the time series over the month noisy, and as such it is difficult to see any trends. In order to remove this diurnal signal from the time series a simple time filter was applied over each day by implementing;

$$M^n = \frac{1}{4}\left(M^{n-1} + M^n + M^{n+1} + M^{n+2}\right) \tag{6.54}$$

where M is the quantity that is being filtered and n is the current analysis time point (at 6 hour intervals). Obviously this method means that the first and last two time points cannot be included in the time series, but if the series is long enough a loss of these points will not have a significant impact.

6.6.2 Diabatic Circulation

The mean behaviour over September will be considered first, and the mass budget in particular. The global mean values integrated in the vertical over September for the three terms in equation (6.48) are shown in table 6.1 along with the root mean square error values. The important point to note is that for the mean values it can be seen that the dominant term in determining the net change in the mass field is the $V_M + \epsilon_M$ term. However, if the root mean square value is determined then all of the terms are of the same order of magnitude and so all three terms are important. The mean value for $\partial M/\partial t$ can be compared to the September mean value of M which is 0.019 kg over the entire domain (i.e. for all (k, m)). Therefore, over the month M does not vary significantly over the domain.

Note that all of the terms in the above equations are in units of mass relative to the total atmospheric mass per day. In order to convert to units of kg then all values would need to be multiplied by $4\pi a^2 p_0/g$, where a is the radius of the Earth, p_0 is a factor of 1×10^5 Pa and g is the acceleration due to gravity. The only exception is r_0 which is a mixing ratio in units of ppbv. As mentioned previously, the mass stated is relative to the total atmospheric mass and therefore these numbers are not expected to be comparable with the true atmospheric mass, but give a general idea as to the average value over the domain.

In order to allow a comparison with atmospheric mass, as determined by Berrisford *et al.* (2011) for example (Section 1.3.1), the mean atmospheric mass over September has also been

	Mean	rms
$\frac{\partial M}{\partial t}$	1.4E-6	3.6E-4
$V_M + \epsilon_M$	1.4E-6	9.7E-4
$D_{m+1/2} - D_{m-1/2}$	-3.2E-9	8.2E-4
global mass	5.20×10^{18} kg	

Table 6.1: *Mean and root mean square values over the entire domain (i.e. for all (k, m)) for September of the three terms in equation (6.48). The $V_M + \epsilon_M$ represents the combined isentropic mass flux and error, and $D_{k,m+1/2} - D_{k,m-1/2}$ is the diabatic mass flux. All terms have units of kg day^{-1} divided by M_{atm} unless otherwise stated.*

included in table 6.1. The atmospheric mass of 5.20×10^{18} kg calculated from the reference tracer that contains all of the mass, $M_{1,\theta}$ (multiplying by the factor $M_{atm} = 4\pi a^2 p_0/g$), is comparable to that determined by Berrisford *et al.* (2011) using ERA-Interim (5.11×10^{18} kg). One final point that needs to be made is that it is unknown how large the error term, ϵ_M, is as it would be computationally expensive to calculate the contour integral for V_M. This raises uncertainties in how accurate equation (6.48) is.

$V_{M_{k,m}}$ represents the mass flux across a contour, $q = Q_k$, in an isentropic layer, θ_m in units of kg day^{-1}. The mass flux per unit depth of the layer is then $V_M/\Delta z$ (kgm^{-1}day^{-1}). The $D_{k,m}$ term is the diabatic mass flux across the entire surface, $\theta = \theta_m$, where $q \geq Q_k$. The portion of the diabatic mass flux crossing $\theta = \theta_m$ per unit length in the vicinity of $\phi_e(Q_k)$ is $(D_{k+1/2,m} - D_{k-1/2}, m)/a\Delta\phi_e$, where ϕ_e is equivalent latitude. This also has units of kgm^{-1}day^{-1}. If the mean of both of these terms over September is plotted, figure 6.8 is produced. Since September is close to the equinox, i.e. the mid-point between summer and winter, the stratospheric circulation is in the process of shifting from a dominant flow into the winter Southern Hemisphere to dominant flow into the winter Northern Hemisphere.

In figure 6.8 the horizontal component is $\sim10^3$ times larger than the vertical component. This is partly due to the normalisation that has been used since $a\Delta\phi_e \gg \Delta z$, and the domain size in the horizontal ($\pi a \sim 20000$ km) is considerably larger than in the vertical (40 km) so that a ratio of these two shows that there is a factor of $\sim$500 difference. It would be expected for this to be reflected in the difference between the components.

In the horizontal component a negative value shows motion towards the South Pole and

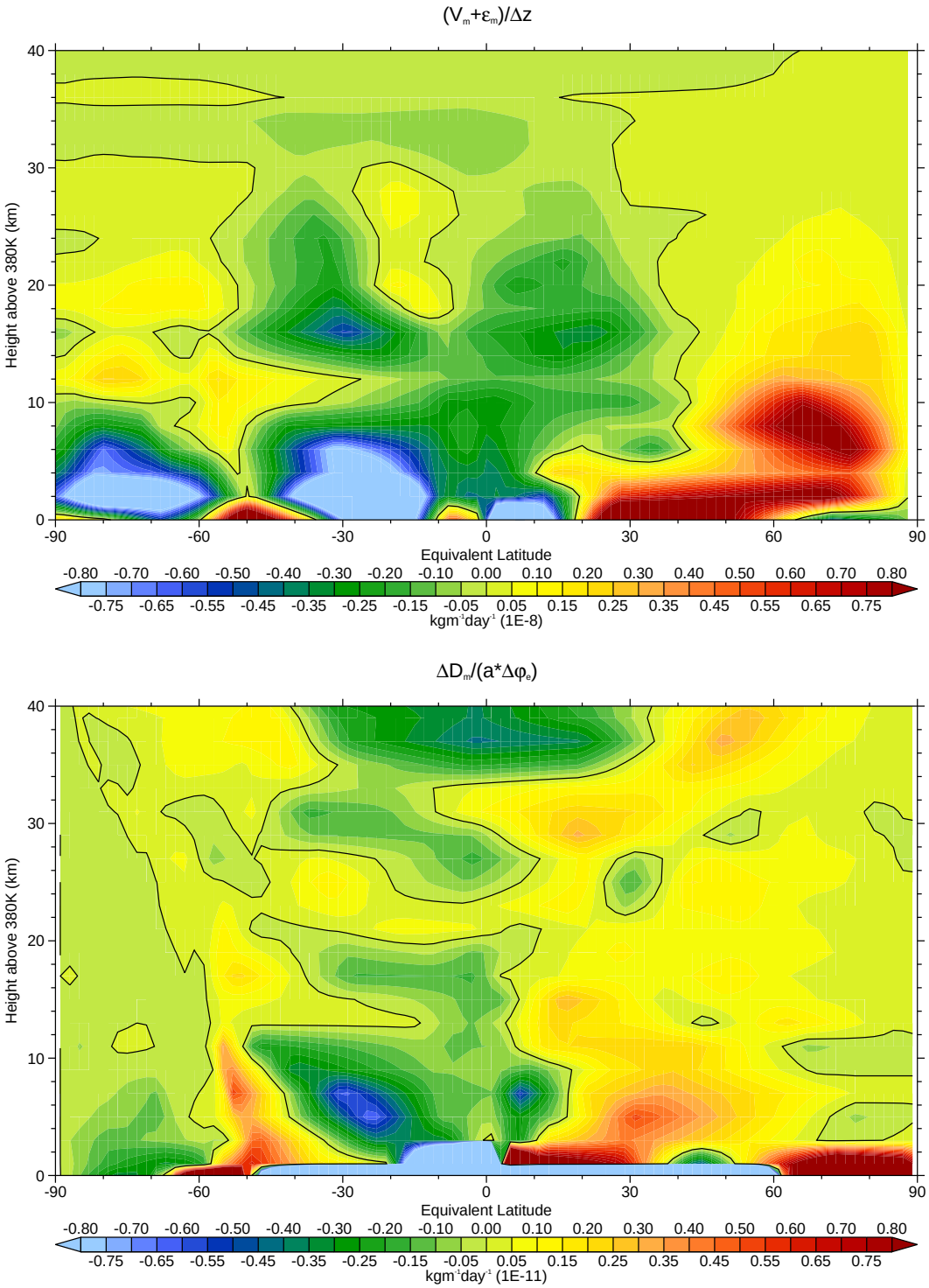

Figure 6.8: *September mean of the horizontal (top) and vertical (bottom) motion above 380 K as determined from equation (6.48). Note that in the vertical* $\Delta D_m = D_{k+1/2,m} - D_{k-1/2,m}$ *to obtain a meridional gradient. Both are in units of* $kgm^{-1}day^{-1}$ *divided by* M_{atm}*. The black line is the zero contour.*

positive values are towards the North Pole. The maximum in the horizontal flux at an equivalent latitude of -55 degrees (in the region 6-14 km) corresponds with the region of equatorward wave breaking, more on which will be considered in the next section. In order to fully understand the circulation both the horizontal and vertical components need to be considered together. In a broad band over the tropical region the dominant motion is descending flow towards the South Pole. In the mid-latitudes in both hemispheres the air is ascending and flowing towards the North Pole. At high latitudes and over the polar region in both hemispheres the air again descends with a northward horizontal component. As a result of the combined flow $\partial M/\partial t$ is not zero locally.

Many of the features described are reflected in the schematic of the Brewer-Dobson circulation shown in figure 6.7, namely the strong ascent in the summer (Northern) hemisphere and the broad descent in the winter (Southern) hemisphere. The poleward motion in the lower stratosphere in both hemispheres is also reflected in figure 6.8 as is the southward motion at the top of the stratosphere. The fact that there is ascent and northward motion in the Southern Hemisphere in figure 6.8 reflects the fact that the equinox is approaching and the Brewer-Dobson circulation is changing the direction of flow as the Northern Hemisphere enters winter and the Southern Hemisphere enters summer.

Overall, the flow diagnosed from $V_M + \epsilon_M$ and $D_{k+1/2} - D_{k-1/2}$ still shows the ascent in the summer (Northern) hemisphere and descent in the winter (Southern) hemisphere. If the model run was extended then the motion for this time of year would begin to develop a distribution closer to that observed in figure 6.9 (Kållberg *et al.*, 2005), which shows the stratospheric flow as diagnosed from ERA-40 over the three month period September-November over many SON seasons. The symmetry between the hemispheres is clearly shown as the direction of the Brewer-Dobson circulation reverses.

6.6.3 Error in the Tracer Budget

The terms used in the calculation of $\partial B/\partial t$ will be considered next. Table 6.2 shows the root mean square values over the entire domain (i.e. for all (k, m)) for all of the terms in equations (6.50) and (6.52) averaged over September. The first point to be made is that the diabatic mass fluxes are among the smallest terms in the budget and therefore have the smallest influence on the tracer evolution. When using the full tracer field, r,

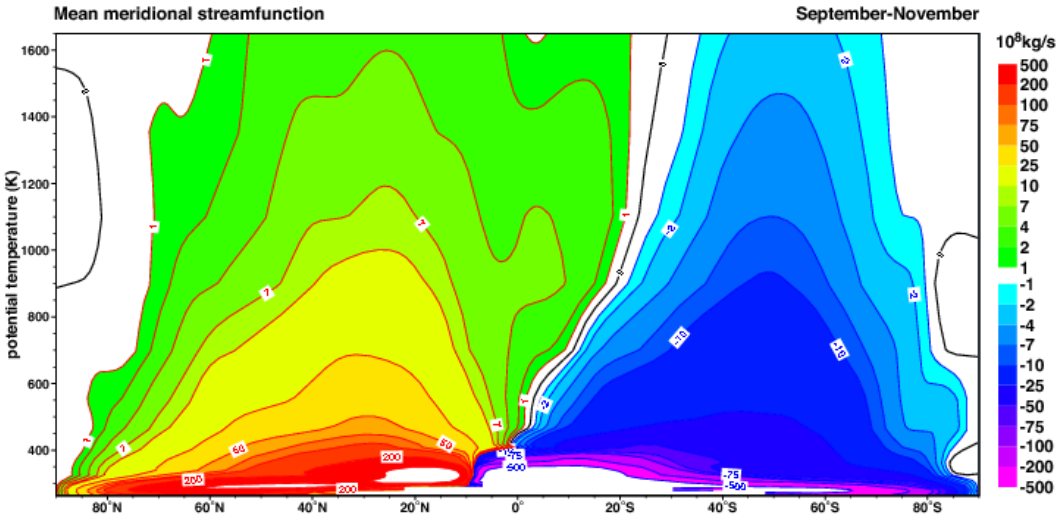

Figure 6.9: *ERA-40 atlas: mean meridional streamfunction ($[\bar{\sigma}\bar{v}]$) for September-November. Positive values represent a counter-clockwise flow.*

in the heating calculation (i.e. equation 6.51) the resulting root mean square error of the diabatic mass flux is approximately 7 times smaller than when the background state is used (equation 6.53). However, the resulting root mean square error values of the errors, ϵ_a and ϵ_b respectively, are very similar and comparable with the time averaged $\partial B/\partial t$. This suggests that on a global scale the differences introduced by using either equation (6.50) or (6.52) are not of the same sign, and that at some places there is a reduced error and others an increased error when the calculation method is changed.

6.7 Time Varying Mass Fluxes Across PV Contours

When all of the terms in the evolution of the mass (equation 6.35) are plotted as a time series for a point in (q, θ) space (i.e. a contour) then distinct peaks are observed throughout the month. Figure 6.10 shows an example of this at a pseudo-height of 10 km and a Lait PV contour of -20 MPVU. Clearly, $\partial M/\partial t$ is much greater in magnitude than the diabatic mass flux divergence. Therefore, the budget can only be balanced by mass fluxes across Lait PV contours. Using figure 6.3 shows that this particular Lait PV contour is near the edge of the polar vortex. In order to understand these peaks more fully the $V_M + \epsilon_M$ term was considered at a range of vertical locations along two different Lait PV contours; -20 MPVU and -8 MPVU. These are shown in figure 6.11, from which it can be seen that there is not a strong correlation in the vertical if the PV value is constant. Figure 6.3 shows that keeping a constant PV value is almost the same as remaining at a fixed equivalent latitude.

	Passive	Active
$\frac{\partial B}{\partial t}$	2.0E-1	5.4E-2
r_0	2670	2546
$r_0 \frac{\partial M}{\partial t}$	3.6E-2	3.0E-2
$r_0(D_{m+1/2} - D_{m-1/2})$	4.9E-2	3.4E-2
$E_{m+1/2} - E_{m-1/2}$	5.5E-3	3.7E-3
$F_{m+1/2} - F_{m-1/2}$	4.0E-2	2.5E-2
ϵ_a	2.1E-1	6.1E-2
ϵ_b	2.1E-1	5.9E-2
R	0	2.8E-2

Table 6.2: *Root mean square values over the entire domain (i.e. for all (k, m)) for September of the terms used in calculating $\partial B/\partial t$. ϵ_a and ϵ_b are the corresponding errors for when ΔE and ΔF are used in the equation. All terms are in units of kg day^{-1} divided by M_{atm}, except r_0 which is a mixing ratio in units of ppbv.*

Due to the variability in the time series with height a comparison was also carried out whereby the height remained constant and different Lait PV contours considered, as shown in figure 6.12. If the -4 MPVU line is excluded then it can immediately be seen that the remaining lines are highly correlated at both 12 km and 16 km. This suggests that whatever behaviour is creating the peaks in the distribution is constrained more by the vertical level than the PV contour. It can also be seen that the time series for 16 km shows a smaller range of values than at 12 km.

The peaks in the distribution can actually be seen to coincide with periods of wave breaking and it is already known that wave breaking results in a mass flux. Nakamura (2004), for example, calculated mass and tracer fluxes that arise when both equatorward and poleward wave breaking occurs. Figure 6.13 shows the Lait PV distribution on the 703 K isentropic surface (z=14 km) at four times that coincide with peaks in the time series of $V_M + \epsilon_M$ in figure 6.12(a). Note that in the time series $t = 0$ corresponds to the 1st September. In the first two images of the Lait PV distribution (figure 6.13) a filament of Lait PV is seen to extend from the edge of the polar vortex equatorward. During these two times the time series for 12 km shows distinct peaks. These wave breaking events are observed in the range of Lait PV contours due to the origin of the filaments being the edge of the polar vortex

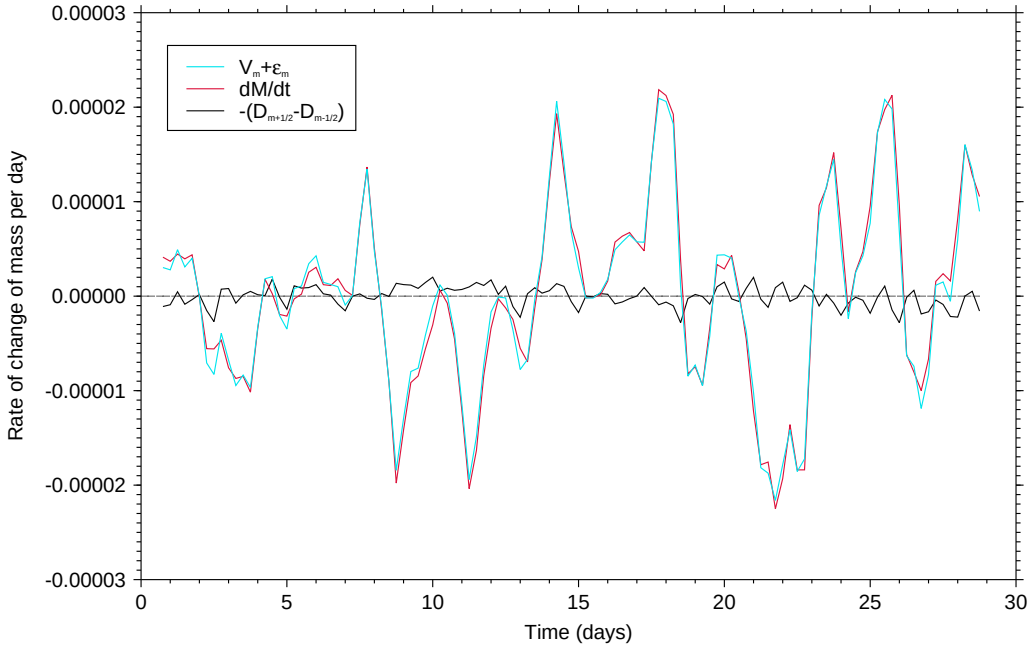

Figure 6.10: *The three terms in the mass budget (equation 6.48) for a point in (q, θ) space throughout September. The point chosen is at a pseudo-height of 10 km and a Lait PV value of -20 MPVU. All three terms are in units of kg day^{-1} divided by M_{atm} and have been diurnally averaged. The dashed line represents zero.*

where there is a sharp gradient in PV and Lait PV values <-20 MPVU.

The next Lait PV distribution to be mentioned is on the 22nd September when no filamentation or wave breaking away from the polar vortex is observed and the distribution is overall more zonal than the other times. The time series at 12 km in figure 6.12(a) also shows that there is no peak in mass for this time, therefore supporting the theory that the peaks represent mass change due to wave breaking. Up to this point the time series for z=16 km has not been considered (figure 6.12(b)). If the time series is looked at it can be seen that the peaks associated with wave breaking at 12 km are not seen in this figure. The two exceptions are the 8th September where the peak is observed but is delayed relative to 12 km, suggesting that the wave breaking does not occur at all heights simultaneously. Also, on the 22nd September there is a peak in this distribution that is absent in the figure for 12 km. This suggests that there may have been a smaller scale, localised wave breaking event.

Both of the time series in figure 6.12 show negative features as well as the positive features considered up to this point. These negative features occur after a period of poleward wave breaking. The strongest negative gradients coincide with periods when there is a filamentation of higher (i.e. less negative) PV values towards the pole that wrap around the

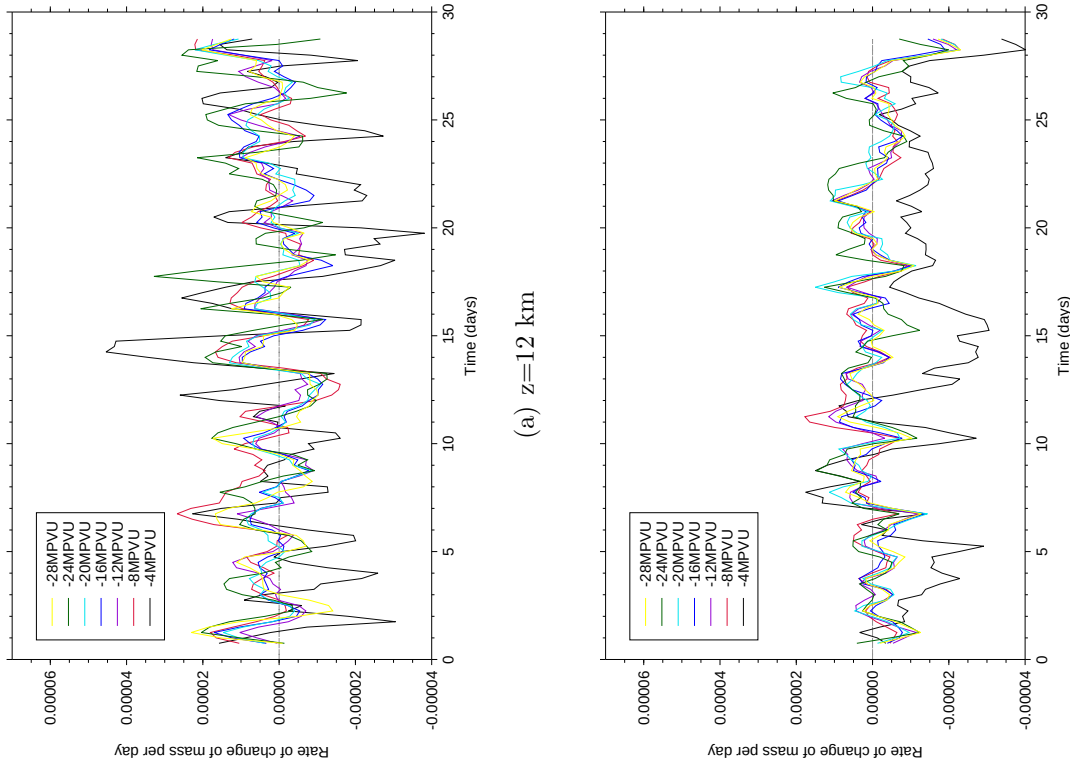

(a) z=12 km (b) z=16 km

Figure 6.12: *$V_M + \epsilon_M$ term of mass budget for two different pseudo-heights (12 km and 16 km) at a range of Lait PV contours. All time series have been diurnally averaged.*

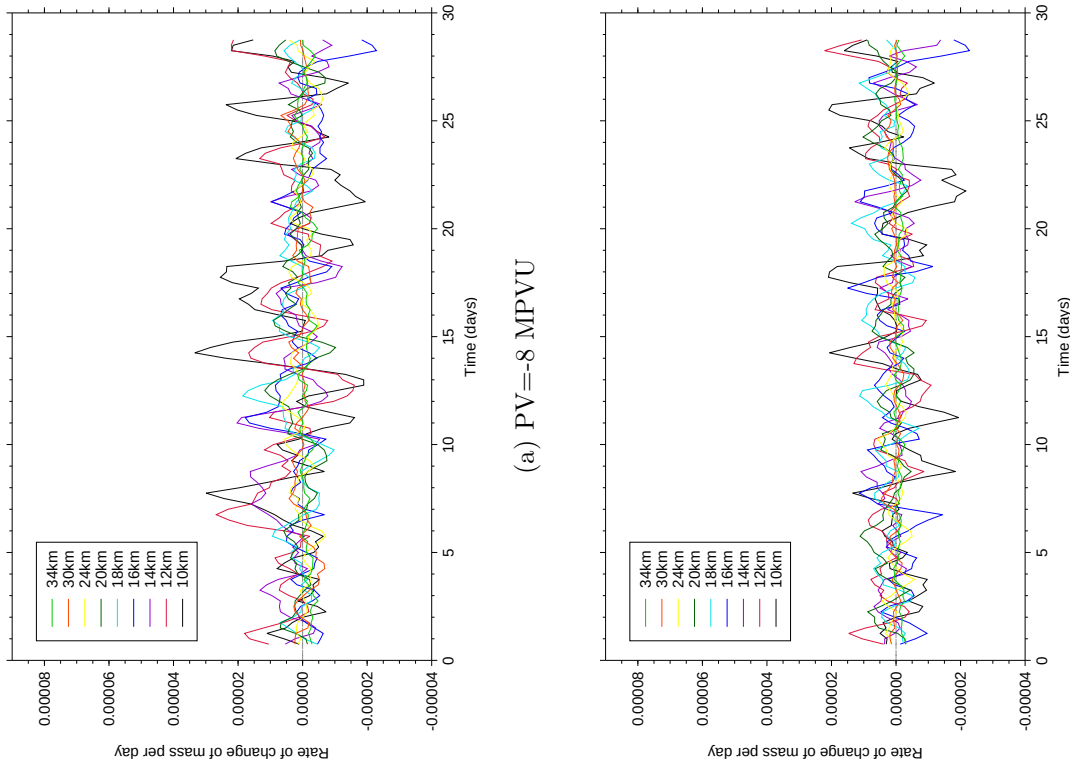

(a) PV=-8 MPVU (b) PV=-20 MPVU

Figure 6.11: *$V_M + \epsilon_M$ term of mass budget for two different locations in Lait PV (-8 MPVU and -20 MPVU) at various pseudo-heights. All time series have been diurnally averaged.*

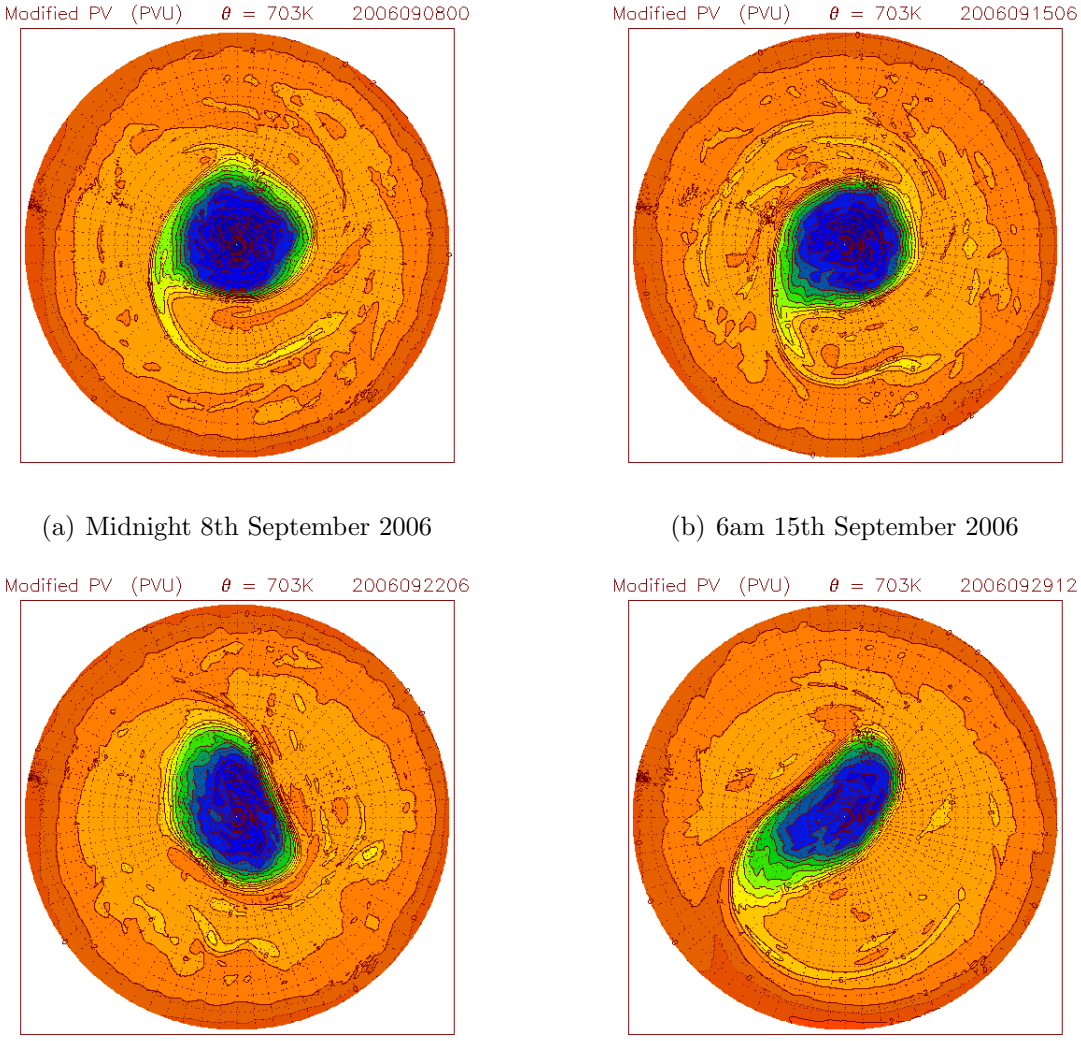

(a) Midnight 8th September 2006

(b) 6am 15th September 2006

(c) 6am 22nd September 2006

(d) Noon 29th September 2006

Figure 6.13: *Lait PV distribution on the 703 K (14 km pseudo-height) isentropic surface for four times corresponding to peaks in the $V_M + \epsilon_M$ time series. Contours are at every 2 MPVU, and the -20 MPVU contour is the transition from green to blue. The dotted contour is the zero contour.*

polar vortex. One consistent feature between the two different heights is that the -4 MPVU line has a distinctly different behaviour to the others, especially at the higher altitude. This is likely associated with the fact that this Lait PV contour does not experience the same filamentation and wave breaking as the others as it is considerably further equatorward, as shown in figure 6.3 as well as figure 6.13.

The other feature to consider is the reduced range in rates of change of mass shown at 16 km. This is linked to the mean isentropic mass flux shown in figure 6.8(a). From this figure it can be seen that the isentropic mass flux at 12 km is away from the pole. At 16 km the equatorward mass flux is weaker, and at some locationss is reversed so that the flow is poleward. However, it must be remembered that the mass fluxes shown here are all

cross-Lait PV contour fluxes and involve non-conservative processes. They are not to do directly with advection by the winds which affect all tracers equally.

6.8 Tracer Budgets at a Point in (q,θ) Space

The evolution of mass ($\partial M/\partial t$) is the only equation that has been considered so far. As shown in figure 6.10 the evolution of the mass field is primarily determined by the $V_M + \epsilon_M$ term in equation (6.48). However, using this equation it is not possible to estimate the error, ϵ_M, and to determine how accurate the approximations are. Specifically whether the parallel contour approximation and the approximation of the background state as stated in equation (6.40) are accurate.

The overall aim of this work is to use a tracer-relative CTM to represent the evolution of active tracers. To this end the contribution of terms in the tracer-relative mass budget, including approximations to the diabatic mass fluxes, need to be considered. The same location used in figure 6.10 will be used here, i.e. a pseudo-height of 10 km (28.9 hPa) and a Lait PV value of -20 MPVU, in the consideration of $\partial B/\partial t$.

6.8.1 First Approximation of the Diabatic Mass Flux: E

The first method to be considered uses equation (6.50) for the calculation of $\partial B/\partial t$. This method uses the full tracer field, r, when calculating the diabatic mass flux. The resulting time series for all of the terms during September are shown in figure 6.14. The sharp peaks seen in the time series are again associated with periods of wave breaking.

A comparison of the time series for the passive (6.14a) and active (6.14b) tracer shows that at any instant, in both cases, the strongest term in determining the evolution of B is often $r_0\partial M/\partial t$. The two terms associated with the heating field, $r_0\Delta D$ and ΔE, can be seen to be almost equal and opposite throughout the month. The other significant term is the error, ϵ_a, which accounts for the majority of the difference between $\partial B/\partial t$ and $r_0\partial M/\partial t$.

Table 6.3 shows the root mean square error values for each of the terms over the month for both the passive and active ozone tracers at a psuedo-height of 10 km and a Lait PV

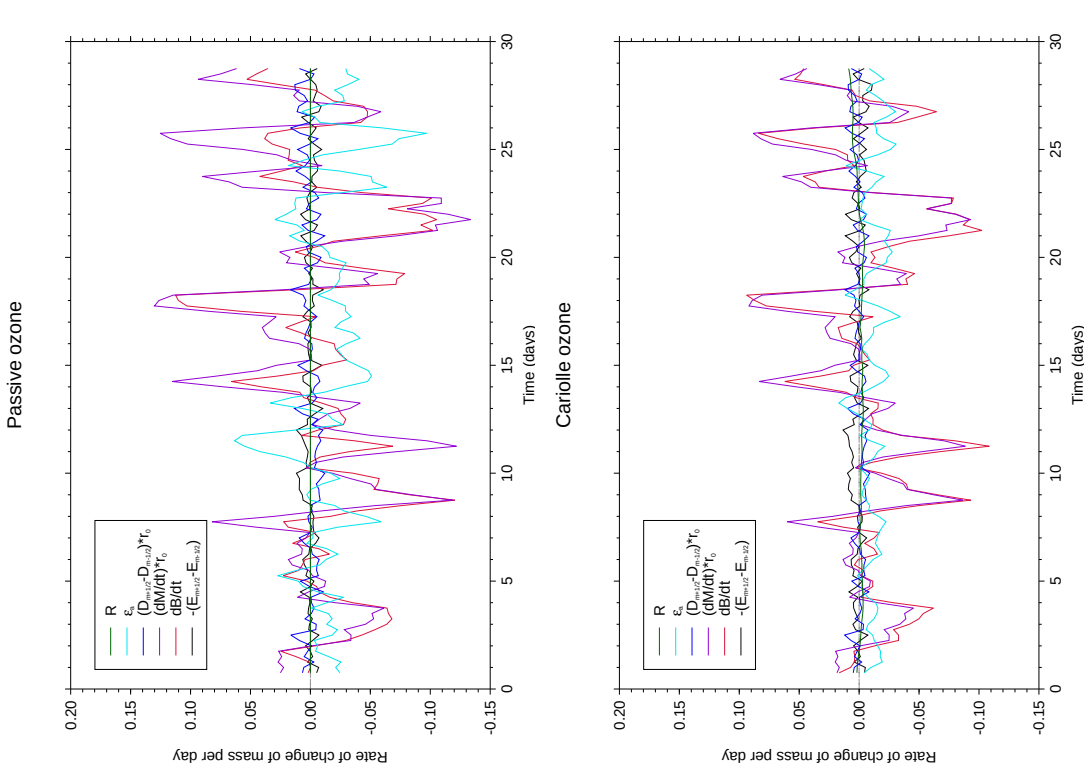

Figure 6.14: *Time series over September for all of the terms in equation (6.50) (using the full field, r) for a point at z=10 km and Q=-20 MPVU. Both the passive and active ozone tracers are shown. All time series have been diurnally averaged.*

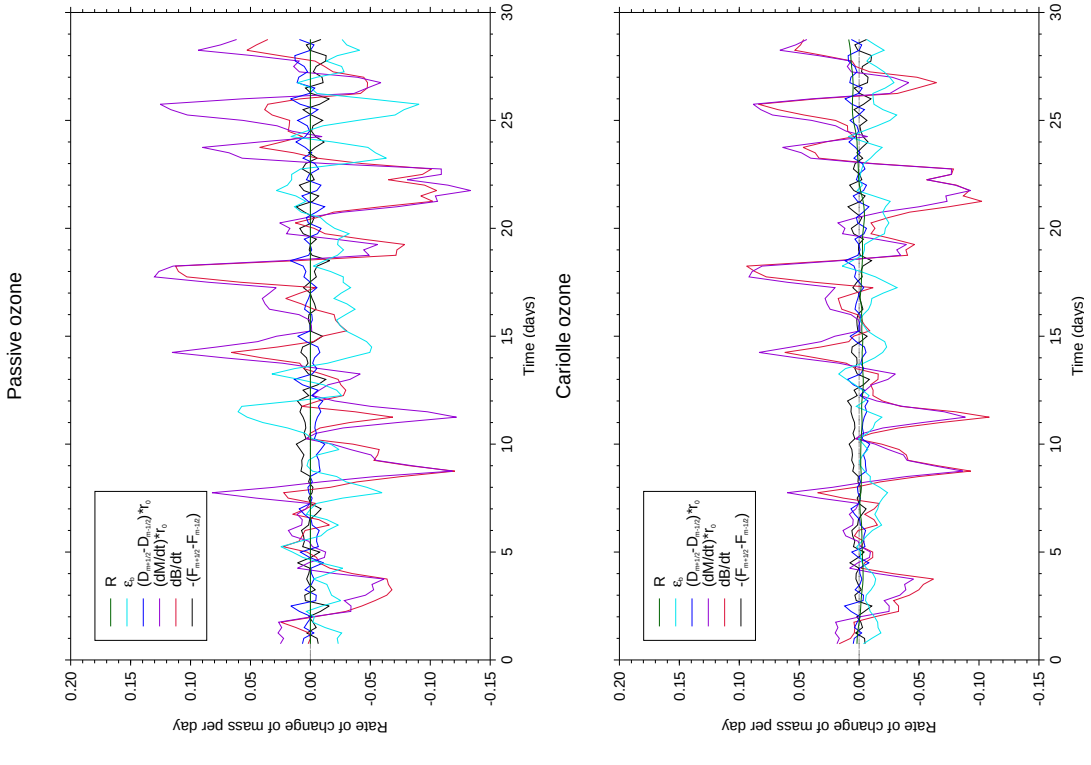

Figure 6.15: *Time series over September for all of the terms in equation (6.52) (using the assumption that $r = r_0$) for a point at z=10 km and Q=-20 MPVU. Both the passive and active ozone tracers are shown. All time series have been diurnally averaged.*

	Passive	Active
$\frac{\partial B}{\partial t}$	4.6E-2	4.2E-2
r_0	5970	4290
$r_0 \frac{\partial M}{\partial t}$	5.8E-2	4.1E-2
$r_0(D_{m+1/2} - D_{m-1/2})$	6.4E-3	4.6E-3
$E_{m+1/2} - E_{m-1/2}$	4.7E-3	5.2E-3
$F_{m+1/2} - F_{m-1/2}$	6.3E-3	4.6E-3
ϵ_a	3.0E-2	1.5E-2
ϵ_b	2.9E-2	1.4E-2
R	0	3.2E-3

Table 6.3: *Root mean square values for September for the terms in equations (6.50) and (6.52) for a point located at a pseudo-height of 10 km and a Lait PV contour of -20 MPVU. All terms are in units of kg day^{-1} divided by M_{atm}, except r_0 which is a mixing ratio in units of ppbv.*

contour of -20 MPVU. The first point to note is that the dominant terms in the evolution of $\partial B/\partial t$ are $r_0 \partial M/\partial t$ and the error, ϵ_a. However, all of the terms in table 6.3 only differ by a factor of 10. This is also reflected in the global root mean square error in table 6.2, showing the importance of all terms in the evolution of B and the large bias introduced in $\partial B/\partial t$ by the error. In figure 6.14, the error, ϵ_a, is seen to be noticeably smaller for the active ozone tracer than the passive ozone tracer, which is also reflected in the root mean square error both at this location and that for the entire domain (table 6.2).

The last point to take note of from table 6.3 is that the root mean square values for the diabatic mass flux terms ($r_0 \Delta D$ and ΔE) are of the same order of magnitude and appear to cancel in the time series. In order to investigate this further the difference between the two terms was taken and plotted as a time series in figure 6.16 for both the active and passive ozone tracer (blue and red lines respectively). It can immediately be seen that for both the passive and active ozone tracers the two heating terms produce a residual that is noticeably different from zero. This is especially true for the passive ozone tracer, where a larger range in the residual is observed. If the absolute values are taken the mean residual value over the month can be calculated and is shown in table 6.4. From this it can be shown that neither ozone tracer has an residual that is consistently larger than the other throughout the month. The final significant point about the residual between the two terms is that it highlights the errors that arise when using the approximated form of the diabatic

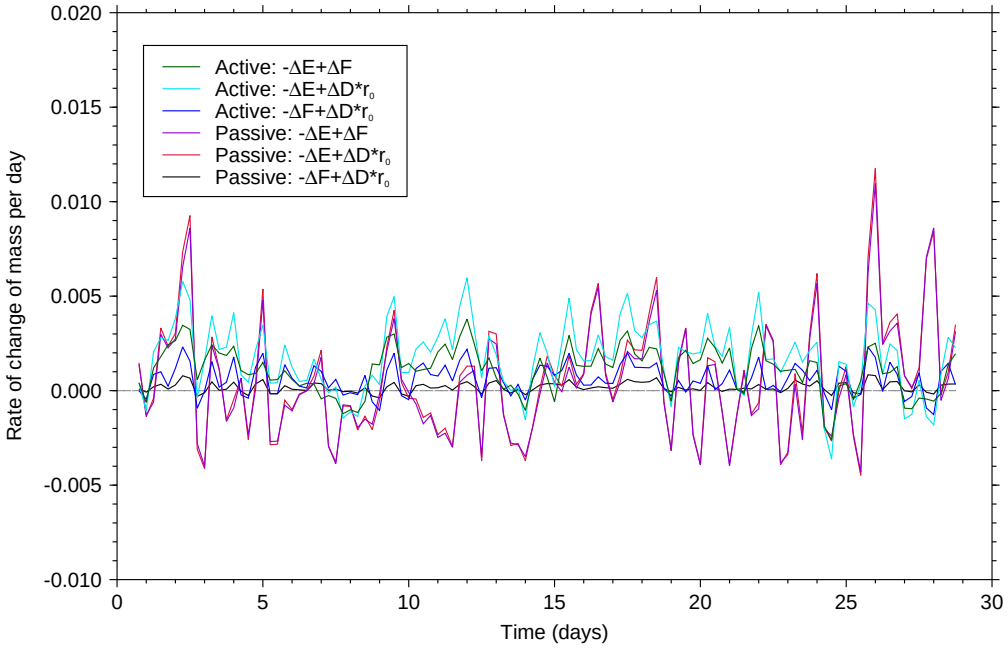

Figure 6.16: *Time series for September of the resultant of the heating terms in equations (6.50) and (6.52) for a point located at a pseudo-height of 10 km and a Lait PV contour of -20 MPVU. Both the passive and active ozone tracers are shown.*

mass flux, $r_0 \Delta D$. The approximations being that the full tracer field can be replaced by the background state in equation (6.40), which in turn can be taken outside of the integral. Ideally the residual with ΔE, which contains no approximations, would be negligible and hence show that the approximations do not introduce errors into the calculations.

6.8.2 Second Approximation of the Diabatic Mass Flux: F

The results presented above can be compared to the case when equation (6.52) is used in the calculation of $\partial B/\partial t$. This method makes the approximation that the background state can be defined as stated in equation (6.40) and is used in the integral with the heating in

	Passive	Active
$-\Delta E + r_0 \Delta D$	2.4E-3	2.1E-3
$-\Delta F + r_0 \Delta D$	2.5E-4	8.2E-4
$-\Delta E + \Delta F$	2.3E-3	1.4E-3

Table 6.4: *Mean of the absolute values of the time series shown in figure 6.16, in units of kg day^{-1} divided by M_{atm}.*

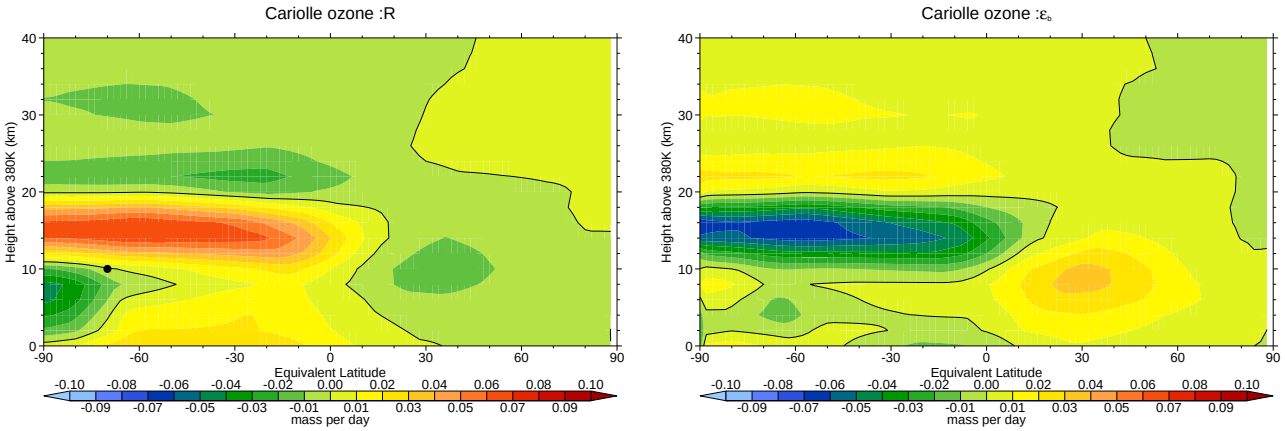

Figure 6.17: *Contour plot of the September mean chemistry (R) and error using approximation F (ϵ_b) for the active ozone tracer. ϵ_a has the same structure as ϵ_b. The dot on the left figure corresponds to the point used in this section (z=10 km and Q=-20 MPVU).*

place of the full tracer field, r. The time series for all the terms for both the passive and active ozone tracers are shown in figure 6.15. There is a high degree of similarity between the resulting time series that use this approximation and those that use equation (6.51). The differences become more noticeable when looking at the monthly root mean square error values in table 6.3. The resulting error (ϵ_b) is also slightly smaller than the previous error ϵ_a for both the active and passive ozone tracers.

There is also a significant difference when the residual between the heating terms is calculated and shown as a time series (figure 6.16). The difference with the previous method is immediately seen by fact that the residual for both the passive and active ozone tracers (black and purple lines respectively) are considerably closer to zero and have a smaller range. When the mean of the absolute values of the time series is taken the resulting value is an order of magnitude smaller than when equation (6.51) is used (table 6.4). The assumption made in equation (6.44) that $r_0(Q)$ can be taken outside of the diabatic mass flux is the only difference between the $r_0\Delta D$ and ΔF terms. In essence this is assuming that the heating field also aligns with the background state. The fact that this resulted in a small residual signifies that the majority of the difference between $r_0\Delta D$ and ΔE arises from the parallel contour approximation that the 3D tracer field can be replaced by the background state, r_0. This is supported by the fact that the difference between ΔE and ΔF (table 6.4) is of the same order of magnitude as the difference between $r_0\Delta D$ and ΔE.

The point (Q_k,θ_m) used to present the mass and tracer budgets in Sections 6.7 and 6.8 corresponds to a location where the ozone photochemistry is approximately zero. Figure 6.17

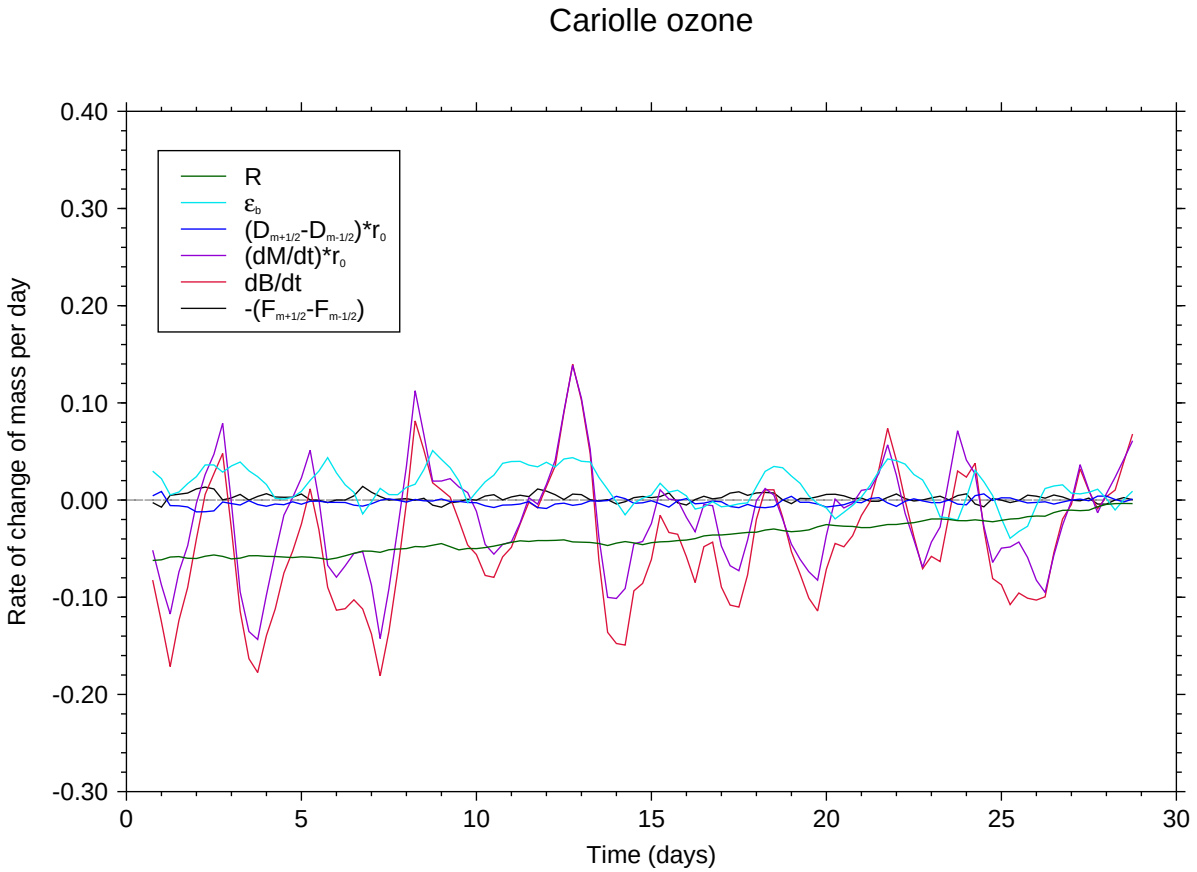

Figure 6.18: *Time series over September for all of the terms in equation (6.52) for a point at z =8 km and Q =-26 MPVU. Only the active ozone tracer is shown. All time series have been diurnally averaged.*

shows the September mean ozone photochemistry on the left, where the circle corresponds to the point z=10 km and Q=-20 MPVU used in the above work. If an alternative point is considered, such as z=8 km and Q=-26 MPVU so that the point is located within the region of ozone loss, then the resulting time series is shown in figure 6.18. It can immediately be seen that there is a large negative chemistry term acting due to the formation of the ozone hole. The other time series to note is that for the error, ϵ_b, which is smaller in magnitude than R when the chemical loss is most active.

Comparing figure 6.18 with the time series for active ozone in figure 6.15 reveals a notable point. In figure 6.15 ϵ_b has a maximum magnitude twice that of ϵ_b in figure 6.18. In these same two locations R is approximately zero at the first location and significantly larger at the second. This suggests a relationship between the chemistry and the error and is shown in figure 6.17. It can be seen that the region of largest positive (negative) R coincides with the region of largest negative (positive) error. This is due to the fact that the increased level of chemistry will reduce the validity of the parallel contour approximation.

6.9 Summary

A range of areas were covered in this chapter. Primarily the theory behind the background state was discussed in detail and the derivation of the mass and tracer evolution was shown. The various approximations that can be made with regards to defining the background state (equation 6.40) and assuming that the background state and heating field also align means that there are two possible ways in which the evolution of the tracer can be calculated, as shown in equations (6.50) and (6.52).

A key assumption in this work is that the contours of long-lived tracers will align in the atmosphere due to advection being the dominant process acting on the tracer distribution. Using the ozone and Lait PV tracers this is indeed shown to be true as the resulting tracer-tracer scatter plots show a compact relationship that reflects an alignment of tracer contours. Inevitably the passive ozone tracer has a more compact relationship with the Lait PV distribution due to the absence of chemistry which acts non-uniformly around a contour. By comparing these relationships on model η-levels and potential temperature surfaces, as well as using latitude instead of Lait PV, the use of the PV-θ co-ordinate system is supported as it provides the most compact relationships in the scatter plots.

When the evolution of mass as defined in equation (6.48) is calculated several properties of the stratosphere can be determined. Firstly the two terms determining the evolution of mass are in essence the horizontal and vertical components of the stratospheric circulation. All of the key features of the circulation are represented, along with the initial signs of the Brewer-Dobson circulation changing direction due to the fact that September is approaching the equinox. The mass tendency ($\partial M/\partial t$) is dominated by the lateral mass flux across the tracer contours, V_M. As such the time series of $\partial M/\partial t$ can also be used to identify periods of wave breaking at the edge of the polar vortex in the Southern Hemisphere due to peaks in the time series of V_M arising from filamentation and mixing. Unfortunately, the error in the calculation cannot easily be separated from the isentropic mass flux, V_M, as an explicit calculation of V_M would involve integration around PV contours. It is therefore presently unknown how large the error is relative to the other terms. Errors could arise from the tracer model (that is currently used to calculate B and R), analyses (both of which were investigated in Chapters 3 and 4 and found to be relatively small), or the numerical integration used to obtain the terms in equation (6.35).

The evolution of the second tracer ($\partial B/\partial t$) is primarily determined by the mass evolution, which in turn has been shown to be dominated by the lateral mass flux, and as such the wave breaking can also be seen in this time series. The different approximations used in the calculation, i.e. equation (6.51) or (6.53), has only a small impact on the error that arises in the calculation. Determining which method is the best is also not a simple problem as the error observed at a point is dependent on the sign of various errors and varies from point to point and in time. Over the month of September the use of equation (6.51) produced a smaller mean error. This is not completely unexpected as this method uses the full tracer field, r, in the calculation rather than the background state, r_0.

By calculating the residual between the various diabatic mass flux terms ($r_0\Delta D$, ΔE and ΔF) it was clearly shown that the use of the background state (equation 6.40), rather than the full tracer field, in both the lateral and diabatic mass fluxes introduces the larger error. The further assumption made with regards to the diabatic mass flux (equation 6.44) is of considerably less importance. Given that this is the case it enables the use of the simplest equation (6.45) as the error is not significantly worse than the more complex calculation for $\partial B/\partial t$ (equation 6.43).

The resulting implication of this work is that it is possible to evolve r_0 without the need to reference a fully 3D state, r. By using the relationship $r = r_0(q(\lambda, \mu, t), \theta)$ (equation 6.40) a 3D tracer distribution could be determined by using the parallel contour approximation. This in turn can be used to calculate the photochemistry (in this case via the linear ozone parameterisation of Cariolle and Teyssédre (2007), equation 4.11), R.

Although the fluctuations in the tracer budgets associated with the wave breaking are large and the instantaneous, point-wise budget residuals are sometimes larger in magnitude than the diabatic mass flux divergence, the tracers are well aligned. The residual error in the tracer evolution is also clearly smaller for the active ozone tracer than the passive ozone tracer. The difference between the diabatic mass flux terms accounts for only a fraction of the total error. The systematic error in this method of modelling the evolution of a tracer field is unknown at this stage. In other words, a tracer-relative CTM may be capable of simulating the distribution in figure 6.4 through the integration of equation (6.45) combined with the relation in equation (6.41).

Chapter 7

Conclusions and Future Work

The scientific questions addressed by this thesis were stated in Section 1.4. In summary, the first aim of the thesis was to quantify the mass non-conservation produced in a new global tracer advection model when driven offline by a prescribed wind field and by analyses. An additional consideration is how the observed mass non-conservation varied with the analyses used and what the ramifications of the numerical mass gain are for long-lived tracers.

The second question considered the properties of the model on a smaller scale. In particular the ability of the advection scheme to produce small scale features and filamentation in a tracer field when advected away from a point source, in this case a volcano. An important factor in the modelling of these smaller scale features is the numerical mixing rate in the model and whether it is a reasonable representation of the true atmosphere.

The last stage of this thesis required using the output from the numerical model to investigate the concept of a tracer-relative chemical transport model (CTM). In particular, the thesis aimed to answer the question of whether a tracer-relative CTM is feasible and the ability of the equivalent latitude-theta co-ordinate system to encode three dimensional tracer distributions. The following sections aim to address each of these areas and answer the questions posed at the start of this thesis.

7.1 Mass Conservation in a Global Advection Model

7.1.1 Mass Conservation Advecting with Prescribed Wind Fields

In version 1 (v1) of the tracer advection scheme the tracer flux is a function of the updated tracer field such that $F(q)$, $G(q^*)$ and $H(q^{**})$, where q^* denotes the tracer after the effects of

the zonal flux divergence in $F(q)$ and q^{**} denotes the tracer after the fluxes in the meridional direction, $G(q^*)$. This follows the method of Gregory and West (2002). However, in order to make the tracer advection consistent with the mass advection an alternative method (v2) is presented whereby the tracer flux is a function of the tracer field at the start of the time step irrespective of which direction is being considered, i.e. $F(q)$, $G(q)$ and $H(q)$. Both versions of the tracer advection scheme ensure that mass and tracer remain uniform, if uniform at the initial time, and if the flow is non-divergent, and approximate the solution when there is a divergent flow. It was shown that the atmospheric density must not be updated within the mass flux terms for each dimension in turn since this results in mass lumping.

When the numerical model is driven by a prescribed wind field, in this case solid body rotation, there are several properties of the scheme that need to be noted. Firstly, as shown analytically, when a uniform tracer field is advected by a uniform wind field then both versions of the advection scheme demonstrate mass conservation. However, scheme v2 produces oscillations in the tracer field downwind of the polar region unless a sufficiently small time step is used. When the full cubic interpolation in the meridional direction is used then these oscillations grow and the scheme develops instabilities. They do not grow when using the linear interpolation in the meridional direction.

A second set of experiments using solid body rotation acting on a cosine bell tracer distribution shows exact mass conservation when the scheme was driven by a purely zonal flow. Mass non-conservation was observed to be dependent on the angle of rotation, with a noticeable deviation occurring when advection at angles greater than 45 degrees is used. The largest magnitude mass change after one rotation for schemes v1 and v2 is 6.6×10^{-4}C% and 1.4×10^{-3}C% respectively, where C is the maximum Courant number. For a prescribed wind field a higher degree of mass conservation is obtained when using scheme v1. The non-conservation is linked to the dimension splitting and the fact that the analytical non-divergence of the winds is not exactly met by the numerical solution.

One similarity between the two tracer advection schemes is that the mass change observed at the end of one complete rotation is scalable, so that the mass change observed after x rotations is simply x times the mass change after one rotation. The numerical mass change is also dependent on the time step, with a smaller time step producing a smaller numerical mass change. The cosine bell is also distorted during the advection process irrespective of

the version of the scheme used, with the changes in the cosine bell distribution aligning with the angle of rotation. The effect of the linear interpolation in the meridional direction is especially noticeable as it creates a spreading in the meridional direction. Scheme v1 produced a lower level of distortion to the tracer distribution due to the use of a cubic interpolation in the meridional direction which results in instability in scheme v2.

7.1.2 Mass Conservation Advecting with Analysed Wind Fields

The next set of work focused on answering question 1 posed in the Introduction (Section 1.4). This involved using an analysed wind field to drive the advection and including a stratospheric ozone photochemistry parameterisation. A comparison between the photochemical and numerical changes in global ozone burden could then be made. This is of importance as there are many offline CTMs that investigate the evolution of chemically active tracers that impact long term atmospheric composition and climate, in which errors in global burden can have important feedbacks (e.g. methane and climate change).

ERA-Interim at full horizontal resolution (T255L60) was used to drive the model offline and the passive tracer was initialised as the zonal mean ozone climatology for April from Cariolle and Teyssédre (2007). It has already been shown by Berrisford *et al.* (2011) that ERA-Interim model, if no observations are assimilated, results in an atmospheric mass gain of 0.3% over a year. However, in the tracer model the observed numerical global tracer mass change is 0.8% over eight months when using scheme v2. When scheme v1 is used the resulting tracer mass change is approximately 1.5 times larger. From these results the decision was made to use the tracer advection scheme with the better mass conservation (v2) for the experiments, even though it was conditionally stable, limiting the time step.

The mass non-conservation is dominated by the difference between the change in grid box mass with time implied by the offline model and the change occurring in the analyses (i.e. the evolution of surface pressure). If tracer is initialised only where pressure is used as a vertical co-ordinate the mass non-conservation is much smaller due to a constant grid box mass. This is more marked when combined with spatial truncation of the analyses. The continuity problem results in a linear dependence of the global non-conservation on spatial resolution and time interval between analyses. The best mass conservation is obtained at the highest spatial resolution with the most frequent update of analyses.

In order to observe the effects of different analyses on the model the ECMWF operational analyses were also used. The operational analyses of the year under consideration and ERA-Interim use very similar cycles of the integrated forecast system (IFS). When the operational analyses are used to drive the model a much larger numerical mass gain is observed. This arises due to the fact that the operational analyses at full resolution are T799L91, and therefore undergo a greater spatial truncation than ERA-Interim to reach a horizontal resolution of T159. The resulting numerical mass change is 7 times larger than when ERA-Interim at T159 is used.

The implication of this result is that ideally analyses need to be produced at a comparable resolution to that used in an affordable global circulation model (GCM) or CTM. Therefore, using re-analyses to drive a model is currently the better option as they are produced at a lower resolution than operational analyses where a higher degree of spatial truncation would be required. Temporal truncation also has an impact, for example using ERA-Interim (T255) with a 12 hourly update produces a numerical rate of change in global burden that is 4 times that using 6 hourly updates. As a result the more frequently the analyses can be updated the better.

The importance of the numerical violation of global conservation was tested in a relevant problem where chemistry and dynamics are coupled: the stratospheric ozone hole problem. A linear ozone photochemistry parameterisation developed by Cariolle and Teyssédre (2007) was included and the net photochemistry changes were used to put the numerical changes into context. The relative magnitudes of numerical and chemical mass changes are particularly significant due to the wide use of CTMs and the importance of chemical systems on climate (as shown in the CCMVal project) where the mass evolution can have significant influence. One such example is the global burden of methane and its radiative impacts. The three model runs of operational analyses at T159, ERA-Interim at T255 and T159 were considered again with the chemically active ozone tracer.

In both of the ERA-Interim model runs the resulting evolution of the global burden of ozone tracks that presented by Wayne (2000) in the true atmosphere. By the end of the eight month long model runs the percentage changes in global average mass mixing ratio (-6% at T255) differed from each other by only 0.25% of the initial global burden. However, the numerical mass change observed when using the operational analyses with the passive ozone tracer is so large that the chemistry is not able to compensate for it. The resulting

global burden increases over time, contrary to observations. Therefore, an unrealistic cycle in the global burden of ozone is observed when the numerical change in global burden is significantly larger in magnitude than that arising due to chemistry.

The minimum ozone column between 70-90S was also calculated since it is frequently used to quantify the depth of the ozone hole (`www.temis.nl/protocols/o3hole2/`). In this diagnostic both of the ERA-Interim model runs produced almost identical results despite the noticeable difference in the global average mass mixing ratio. However, the more important feature arises when the same diagnostic is considered for the operational analyses model run. When compared to the ERA-Interim results there is a difference on the order of 10-20 DU, which is small considering the significant difference in the global average mass mixing ratio. This reveals just how misleading the use of local diagnostics in the assessment of numerical models can be, as all three of these models showed a realistic ozone hole minimum. In the case of ERA-Interim at T255 the ozone hole minimum differed from the observations by 45±15 DU. The models used in the CCMVal project produced ozone hole minima ranging from 50 DU to 200 DU (Austin *et al.*, 2010). The value of 140 DU determined from the experiments using scheme v2 fits well within this range.

The important point to note from these results is that the use of a local diagnostic is insufficient to determine the accuracy of a numerical scheme, it is only when the global diagnostics, such as global burden, are considered that accurate numerical schemes are identified. This fact is of importance in multi-model studies such as CCMVal where considerably more attention is given to local diagnostics. Ideally, a combination of global and local diagnostics need to be considered.

7.2 Investigating Numerical Mixing using a Volcano Source

So far the focus has been on the global conservation properties of the model. The second question addressed in this thesis concerns the material conservation following air masses and the influence of mixing on the tracer distribution and concentration. The aim is to estimate the rate of mixing implicit in the numerical advection method and its magnitude relative to mixing in the atmosphere. The test case presented was the volcanic eruption of

Sarychev Peak in 2009. This example was chosen due to the existence of IASI satellite data of column sulphur dioxide over the duration of the eruption (gridded dataset provided by Jim Haywood as shown in Haywood *et al.* (2010)).

In these model runs the unrealistic nature of a simple positive definite scheme (v2P) that merely sets $q = 0$ where $q < 0$, is highlighted as it results in 3 times the amount of mass input from the source by the end of the model run. However, the advantages of a monotonic scheme (v2M) are highlighted due to the fact that the large negative tracer features that naturally develop around a strong point source in a numerical model are considerably reduced. In terms of the global average mass mixing ratio the monotonic version of the scheme remained as accurate as the standard version (v2). Both schemes v2 and v2M show a greater degree of mass conservation than results published in a tracer transport study by Flemming and Huijnen (2011) of the ECMWF IFS, where mass non-conservation was $\sim$5 times greater for a point source.

During the period considered the model is able to reproduce the regions of filamentation and other small scale features observed in the IASI data. Through work published by Haywood *et al.* (2010) a qualitative comparison can also be made between the model and HadGEM2 (Hadley Centre Global Environment Model version 2). From this comparison it can be noted that the model produces more noise in the tracer field in the form of very low column tracer values than HadGEM2, but does reproduce some features of the tracer distribution that are not present in HadGEM2. The majority of the differences between the model and IASI tracer distributions arise due to the limitations of the IASI data as well as the simplified emissions scenario used in the model. The most notable limitations for the IASI data being that the instrument is unable to take measurements when there is cloud cover and also has a detection limit of 0.3 DU, preventing the detection of the weakest features in the tracer column. In terms of the emission scenario used in the model, the assumption of a constant release rate throughout a constant depth is over simplified, and by starting the emission release a couple of days after the eruption started at least two features in the tracer field are not reproduced by the model. This highlights the importance of an accurate and realistic emissions scenario.

However, following the main eruption period the comparison with IASI was sufficiently good to determine the numerical mixing rate within the model (question 2). When adding an exponential decay to the volcano tracer with a timescale τ_{rel}, the observed rate of tracer

decay (τ_{tot}) is noted to be different, with the difference occurring as a result of the numerical mixing (τ_{num}). Using the idealised decay of a filament the two decay rates were found to be additive ($1/\tau_{tot} = 1/\tau_{rel} + 1/\tau_{num}$), thereby allowing the determination of the numerical mixing timescale by varying τ_{rel} and fitting the results for τ_{tot}. In order to provide an error on the mixing timescale a range of percentiles of the tracer column were used in the estimation of τ_{tot}. The lowest percentile used was 97% as this encompassed the majority of the filaments in the tracer distribution (the majority of the globe does not contain tracer).

The numerical mixing timescale was calculated as 10.8±1.5 days and 12.35±1.0 days at a respective horizontal resolution of T255 and T159. This can be compared to a value of 20.7±5.4 days that was calculated from the IASI data using a similar method that required the calculation of the chemical loss rate of sulphur dioxide in the atmosphere. An additional method of comparison is to transform the mixing timescale from the model into a diffusivity rate which can then be compared to other values that have been published. The diffusivity rate inferred from the mixing timescales for the model (using equation 5.11) is 0.02 m^2s^{-1}, which is twice as large as the diffusivity rate published by Legras *et al.* (2005) for the lower stratosphere outside of the surf zone. This fact, along with the comparison with the IASI data, indicates that the model is too diffusive in the region of the atmosphere being considered.

7.3 Feasibility of a Tracer-Relative CTM of the Chemical Background State

The final stage of this thesis answers question 3 posed in Section 1.4 and investigated the feasibility of a tracer-relative CTM that would rely on the alignment of chemical tracer fields by time dependent advection. The first stage involved the derivation of a new definition and theory for the evolution of reference tracer mass and the active/passive tracer. The model was then implemented using the output from the 3D tracer advection model and the results previously presented for the ozone tracers. Throughout the derivation of the equations used there are several important assumptions that are made. One of these being the parallel contour approximation which arises due to the fact that for long-lived tracers in the atmosphere the tracer contours will align as the dominant mode of transport is through

advection.

The parallel contour approximation is a key assumption in the development of the tracer-relative CTM. The use of this approximation was supported through tracer-tracer scatter plots which, even though some spread was observed, show a compact relationship. Using tracer-tracer scatter plots with both active and passive ozone shows that even with the chemistry a compact relationship between ozone and PV tracers is maintained, as required for this work. As would be expected the most compact relationship was produced when there is slow acting, or no, chemistry. Problems arise when chemistry is included due to the fact that chemistry does not act uniformly around a tracer contour and so causes a deviation from the parallel contour approximation. Tracer-tracer scatter plots proved to be particularly useful as they not only show that the parallel contour approximation for long-lived tracers is valid, but also supported the choice of a mixing ratio-potential temperature co-ordinate system, $C(q, \theta, t)$.

With respect to the diabatic mass flux integral (equation 6.51) in the equations for the evolution of the reference tracer (equation 6.35) and the ozone tracer (equation 6.43) there are several approximations that can be made. When no assumptions are made in the diabatic mass flux integral then the full tracer field, r, is used. The first assumption made is that r can be replaced by the background state, r_0, in the diabatic mass flux integral. The final approximation assumes that $r_0(Q)$ is not correlated with the heating field and can be taken outside of the integral for the diabatic mass flux. By taking the difference between the various versions of the diabatic mass flux integral it can be seen that the use of r_0 in place of r has a large impact on the tracer evolution. From this it can also be assumed that this approximation also has a notable impact on the calculated lateral mass flux. The subsequent assumption with regards to the diabatic mass flux introduces only a tenth of the error (table 6.4) created by the previous assumption. This work shows that $r = r_0(q, \theta, t)$ (equation 6.40) can potentially be used as the basis of a tracer-relative CTM.

7.4 Future Work: Development of a Tracer-Relative CTM

The work presented in Chapter 6 showed that a tracer-relative CTM that uses $C(q, \theta, t)$ rather than $C(x, y, \theta, t)$ is feasible. It is possible to assume that the background state, r_0 can replace the full tracer field, r and that the heating field ($\dot{\theta}$) can be considered as function of r_0 and θ only. The error introduced by this heating field assumption is small compared with the parallel contour approximation. The error that does arise from the parallel contour approximation is the dominant source of the error and can be estimated from the mass and tracer budgets. Without solving the tracer-relative system numerically it is not possible to determine whether the systematic errors will accumulate over time or not.

Equation (6.45) is the basic equation for the tracer-relative CTM. This is used in conjunction with equation (6.41) to define the background state and equation (6.40) as the functional relation between the two tracers (representative of the parallel contour approximation), r and q. The steps that would then make up the model are as follows:

- Obtain the initial background state, r_0 (figure 6.4), and q_0
- Calculate reference tracer, q, and its mass evolution (dM/dt) from the analyses
- It is then possible to calculate the tracer evolution (dB/dt) from equation (6.45) given the chemical reactions contributing to R
- Time step the equation forward to update B
- Use equation (6.41) to obtain the new background state, r_0

A key point that needs to be noted is that the full tracer distribution, $r = r_0(q, \theta)$, may be needed in order to calculate the photochemistry occurring to sufficient accuracy. Once again taking stratospheric ozone and the parameterisation of Cariolle and Teyssédre (2007), equation (4.11), as an example then it can be seen that photochemistry occurring along a contour of constant ozone mixing ratio is not uniform. This arises due to reaction dependent properties, such as temperature or sunlight, not being constant around an ozone contour.

Other factors that will need to be considered is how the tracer-relative CTM would work with a tropospheric tracer. The troposphere will prove problematic due to the fact that the isentropic surfaces intersect the ground and can form isolated regions such as subtropical highs. Consideration will also need to be given to sources of tracers, for instance a point source of tracer (e.g. volcanic emissions) for which the parallel contour approximation will not be valid. The tracer distribution would need to evolve before the model, in its current form, would be able to represent it.

Bibliography

Allen, D. and Nakamura, N. (2003). Tracer Equivalent Latitude: A Diagnostic Tool for Isentropic Transport Studies. *J. Atmos. Sci.*, **60**, 287–304.

Andrews, D., Holton, J., and Leovy, C. (1987). *Middle atmosphere dynamics*. Academic Press.

Arnold, S., Methven, J., Evans, M., Chipperfield, M., Lewis, A., Hopkins, J., McQuaid, J., Watson, N., Purvis, R., Lee, J., Atlas, E., Blake, D., and Rappenglück (2007). Statistical inference of OH concentrations and air mass dilution rates from successive observations of nonmethane hydrocarbons in single air masses. *J. Geophys. Res.*, **112**, D10S40, doi:10.1029/2006JD007594.

Austin, J., Struthers, H., Scinocca, J., Plummer, D., Akiyoshi, H., Baumgaertner, A., Bekki, S., Bodeker, G., Braesicke, P., Brühl, C., Butchart, N., Chipperfield, M., Cugnet, D., Dameris, M., Dhomse, S., Frith, S., Garny, H., Gettelman, A., Hardiman, S., Jöckel, P., Kinnison, D., Kubin, A., Lamarque, J., *et al.* (2010). Chemistry-climate model simulations of spring Antarctic ozone. *J. Geophys. Res.*, **115**, doi:10.1029/2009JD013577.

Balluch, M. and Haynes, P. (1997). Quantification of lower stratospheric mixing processes using aircraft data. *J. Geophys. Res.*, **102**, 23,487–23,504.

Batchelor, G. (1967). *An introduction to fluid dynamics*. Cambridge University Press.

Berrisford, P., Kållberg, P., Kobayashi, S., Dee, D., Uppala, S., Simmons, A., Poli, P., and Sato, H. (2011). Atmospheric conservation properties in ERA-Interim. *Q. J. R. Meteorol. Soc.* In press.

Bischof, W., Borchers, R., Fabian, P., and Kruger, B. (1985). Increased concentration and vertical distribution of carbon dioxide in the stratosphere. *Nature*, **316**, 708–710.

Bott, A. (1989). A positive definite scheme obtained by nonlinear renormalization of the advective fluxes. *Mon. Weather Rev.*, **117**, 1,006–1,015.

Bott, A. (1992). Monotone flux limitation in the area-preserving flux-form advection algorithm. *Mon. Weather Rev.*, **120**, 2,592–2,602.

Bott, A. (2010). Improving the time-splitting errors of one-dimensional advection schemes in multidimensional applications. *Atmos. Res.*, **97**, 619–631.

Brasseur, G., Hauglustaine, D., Walters, S., Rasch, P., Müller, J.-F., Granier, C., and Tie, X. (1998). MOZART, a global chemical transport model for ozone and related chemical tracers 1. Model description. *J. Geophys. Res.*, **103**, 28,265–28,289.

Bregman, A., van den Broek, M., Carslaw, K., Muller, R., Peter, T., Scheele, M., and Lelieveld, J. (1997). Ozone depletion in the late winter lower Arctic stratosphere: Observations and model results. *J. Geophys. Res.*, **102**, 10,815–10,828.

Bregman, B., Segers, A., Krol, M., Meijer, E., and van Velthoven, P. (2003). On the use of mass-conserving wind fields in chemistry-transport models. *Atmos. Chem. Phys.*, **3**, 447–457.

Bregman, B., Meijer, E., and Scheele, R. (2006). Key aspects of stratospheric tracer modeling using assimilated winds. *Atmos. Chem. Phys.*, **6**, 4,529–4,543.

Bühler, O. and Haynes, P. (1999). Constraints on the Mean Transport across Potential Vorticity Contours. *J. Atmos. Sci.*, **56**, 942–947.

Butchart, N. and Remsberg, E. (1986). Area of the stratospheric polar vortex as a diagnostic for tracer transport on an isentropic surface. *J. Atmos. Sci.*, **43**, 1319–1339.

Cain, M. (2009). *Transport and processing of ozone over the North Atlantic and in the West African monsoon.* Ph.D. thesis, The University of Reading. Chapter 3.

Cariolle, D. and Déqué, M. (1986). Southern hemisphere medium-scale waves and total ozone disturbances in a spectral general circulation model. *J. Geophys. Res.*, **91**, 10,825–10,846.

Cariolle, D. and Teyssédre, H. (2007). A revised linear ozone photochemistry parameterization for use in transport and general circulation models: Multi-annual simulations. *Atmos. Chem. Phys.*, **7**, 2,183–2,196.

Chipperfield, M. (1999). Multiannual simulations with a three-dimensional chemical transport model. *J. Geophys. Res.*, **104**, 1781–1805.

Chipperfield, M. (2006). New version of the TOMCAT/SLIMCAT off-line chemical transport model: Intercomparison of stratospheric tracer experiments. *Q. J. R. Meteorol. Soc.*, **132**, 1179–1203.

Chipperfield, M., Feng, W., and Rex, M. (2005). Arctic ozone loss and climate sensitivity: Updated three-dimensional model study. *Geophys. Res. Lett.*, **32**, L11813, doi:10.1029/2005GL022674.

Clarisse, L., Coheur, P.-F., Prata, A., Hurtmans, D., Razavi, A., Phulpin, T., Hadji-Lazaro, J., and Clerbaux, C. (2008). Tracking and quantifying volcanic SO_2 with IASI, the September 2007 eruption at Jebel at Tair. *Atmos. Chem. Phys.*, **8**, 7,723–7,734.

Clerbaux, C., Boynard, A., Clarisse, L., George, M., Hadji-Lazaro, J., Herbin, H., Hurtmans, D., Pommier, M., Razavi, A., Turquety, S., Wespes, C., and Coheur, P.-F. (2009). Monitoring of atmospheric composition using the thermal infrared IASI/MetOp sounder. *Atmos. Chem. Phys.*, **9**, 6,041–6,054.

Crutzen, P. and Arnold, F. (1986). Nitric acid cloud formation in the cold Antarctic stratosphere: a major cause for the springtime 'ozone hole'. *Nature*, **324**, 651–655.

Cullen, M. (1993). The unified forecast/climate model. *Met. Mag.*, **122**, 81–94.

Dahlberg, S. and Bowman, K. (1994). Climatology of large-scale isentropic mixing in the arctic winter stratosphere from analyzed winds. *J. Geophys. Res.*, **99**, 20,585–20,599.

Dee, D. (2009). ECMWF reanalyses: Diagnosis and application. In *ECMWF Seminar on Diagnosis of Forecasting and Data Assimilation Systems*, pages 111–119.

Dee, D., Uppala, S., Simmons, A., Berrisford, P., Poli, P., Kobayashi, S., Andrae, U., Balmaseda, M., Balsamo, G., Bauer, P., Bechtold, P., Beljaars, A., van de Berg, L., Bidlot, J., Bormann, N., Delsol, C., Dragani, R., Fuentes, M., Geer, A., Haimberger, L., *et al.* (2011). The ERA-Interim reanalysis: configuration and performance of the data assimilation system. *Q. J. R. Meteorol. Soc.*, **137**, 553–597.

DeMore, W., Sander, S., Golden, D., Hampson, R., Kurylo, M., Howard, C., Ravishankara, A., Kolb, C., and Molina, M. (1997). Chemical kinetics and photochemical data for use in stratospheric modeling. *Tech. Rep.*, **97-4**, Jet Propulsion Lab., Pasadena, Calif.

Dessler, A. (2000). *The chemistry and physics of stratospheric ozone*. Academic Press.

Durran, D. (1999). *Numerical methods for wave equations in geophysical fluid dynamics*. Springer.

Easter, R. (1993). Two modified versions of Bott's positive-definite numerical advection scheme. *Mon. Weather Rev.*, **121**, 297–304.

Eluszkiewicz, J., Hemler, R., Mahlman, J., Bruhwiler, L., and Takacs, L. (2000). Sensitivity of age-of-air calculations to the choice of advection scheme. *J. Atmos. Sci.*, **57**, 3,185–3,201.

Eyring, V., Shepherd, T., and Waugh, D., editors (2010). *SPARC CCMVal: Report on the Evaluation of Chemistry-Climate Models*.

Farman, J., Gardiner, B., and Shanklin, J. (1985). Large losses of total ozone in Antarctica reveal seasonal ClO_x/NO_x interaction. *Nature*, **315**, 207–210.

Fels, S., Mahlman, J., Schwarzkopf, M., and Sinclair, R. (1980). Stratospheric sensitivity to perturbations in ozone and carbon dioxide: Radiative and dynamical response. *J. Atmos. Sci.*, **37**, 2265–2297.

Flemming, J. and Huijnen, V. (2011). IFS Tracer Transport Study. Technical report, ECMWF.

Fortuin, J. and Kelder, H. (1998). An ozone climatology based on ozonesonde and satellite measurements. *J. Geophys. Res.*, **31**, 31,709–31,734.

Fortuin, J. and Langematz, U. (1994). An update on the global ozone climatology and on concurrent ozone and temperature trends. *Proceedings SPIE, Vol.2311, Atmospheric Sensing and Modeling*, pages 207–216.

Geer, A., Lahoz, W., Jackson, D., Cariolle, D., and McCormack, J. (2007). Evaluation of linear ozone photochemistry parameterizations in a stratosphere-troposphere data assimilation system. *Atmos. Chem. Phys.*, **7**, 939–959.

Gravel, S. and Staniforth, A. (1994). A Mass-Conserving Semi-Lagrangian Scheme for the Shallow-Water Equations. *Mon. Weather Rev.*, **122**, 243–248.

Gregory, A. and West, V. (2002). The sensitivity of a model's stratospheric tape recorder to the choice of advection scheme. *Q. J. R. Meteorol. Soc.*, **128**, 1,827–1,846.

Hall, T. and Plumb, R. (1994). Age as a diagnostic of stratospheric transport. *J. Geophys. Res.*, **99**, 1059–1070.

Haynes, P. and Anglade, J. (1997). The vertical-scale cascade in atmospheric tracers due to large-scale differential advection. *J. Atmos. Sci.*, **54**, 1121–1136.

Haynes, P. and Shuckburgh, E. (2000). Effective diffusivity as a diagnostic of atmospheric transport 1. Stratosphere. *J. Geophys. Res.*, **105**, 22,777–22,794.

Haywood, J., Jones, A., Clarisse, L., Bourassa, A., Barnes, J., Telford, P., Bellouin, N., Boucher, O., Agnew, P., Clerbaux, C., Coheur, P., Degenstein, D., and Braesicke, P. (2010). Observations of the eruption of the Sarychev volcano and simulations using the HadGEM2 climate model. *J. Geophys. Res.*, **115**, D21212, doi:10.1029/2010JD014447.

Hoppel, K., Bevilacqua, R., Nedoluha, G., Deniel, C., Lefèvre, F., Lumpe, J., Fromm, M., Randall, C., Rosenfield, J., and Rex, M. (2002). PAOM III observations of arctic ozone loss for the 1999/2000 winter. *J. Geophys. Res.*, **107**, 8262, doi:10.1029/2001JD000476.

Houghton, J. (1986). *The physics of atmospheres (2nd edition)*. Cambridge University Press.

Hsu, J., Prather, M., and Wild, O. (2005). Diagnosing the stratosphere-to-troposphere flux of ozone in a chemistry transport model. *J. Geophys. Res.*, **110**, D19305, doi:10.1029/2005JD006045.

Hu, Y. and Pierrehumbert, R. (2001). The advection-diffusion problem for stratospheric flow. Part I: Concentration probability distribution function. *J. Atmos. Sci.*, **58**, 1,493–1,510.

Hubbard, M. and Nikiforakis, N. (2003). A three-dimensional, adaptive, Godunov-type model for global atmospheric flows. *Mon. Weather Rev.*, **131**, 1,848–1,864.

Hundsdorfer, W. and Spee, E. (1995). An efficient horizontal advection scheme for the modeling of global transport of constituents. *Mon. Weather Rev.*, **123**, 3,554–3,564.

Iwasaki, T., Hamada, H., and Miyazaki, K. (2009). Comparisons of Brewer-Dobson circulations diagnosed from reanalyses. *J. Meteorol. Soc. Japan*, **87**, 997–1006.

Jöckel, P., von Kuhlmann, R., Lawrence, M., Steil, B., Brenninkmeijer, C., Crutzen, P., Rasch, P., and Eaton, B. (2001). On a fundamental problem in implementing flux-form

advection schemes for tracer transport in 3-dimensional general circulation and chemistry transport models. *Q. J. R. Meteorol. Soc.*, **127**, 1,035–1,052.

Jones, A., Roberts, D., Woodage, M., and Johnson, C. (2001). Indirect sulphate aerosol forcing in a climate model with an interactive sulphur cycle. *J. Geophys. Res.*, **106**, 20,293–20,310.

Kaas, E. (2008). A simple and efficient locally mass conserving semi-Lagrangian transport scheme. *Tellus*, **60A**, 305–320.

Kållberg, P., Berrisford, P., Hoskins, B., Simmons, A., Uppala, S., Lamy-Thépaut, S., and Hine, R. (2005). *ECMWF Re-Analyses: Project Report Series*, volume 19. ECMWF.

Karagulian, F., Clarisse, L., Clerbaux, C., Prata, A., Hurtmans, D., and Coheur, P. (2010). Detection of volcanic SO_2, ash, and H_2SO_4 using the Infrared Atmospheric Sounding Interferometer (IASI). *J. Geophys. Res.*, **115**, D00L02, doi:10.1029/2009JD012786.

Karpetchko, A., Kyrö, E., and Knudsen, B. (2005). Arctic and Antarctic polar vortices 1957-2002 as seen from the ERA-40 reanalyses. *J. Geophys. Res.*, **110**, D21109, doi:10.1029/2005JD006113.

Konopka, P., Gunther, G., Müller, R., dos Santos, F., Schiller, C., Ravegnani, F., Ulanovsky, A., Schlager, H., Volk, C., Viciani, S., Pan, L., McKenna, D., and Riese, M. (2007). Contribution of mixing to upward transport across the tropical tropopause layer (TTL). *Atmos. Chem. Phys.*, **7**, 3285–3308.

Labitzke, K. and van Loon, H. (1999). *The Stratosphere; Phenomena, History and Relevance*. Springer.

Lait, L. (1994). An alternative form for potential vorticity. *J. Atmos. Sci.*, **51**, 1754–1759.

Lary, D. (1997). Catalytic destruction of stratospheric ozone. *J. Geophys. Res.*, **102**, 21,515–21,526.

Lary, D., Chipperfield, M., Pyle, J., Norton, W., and Riishojgaard (1995). Three-dimensional tracer initialization and general diagnostics using equivalent PV latitude-potential-temperature coordinates. *Q. J. R. Meteorol. Soc.*, **121**, 187–210.

Lee, Y.-Y., Kao, W.-C., and Lee, Y.-P. (1990). Kinetics of the reaction OH+SO2 in He, N2, and O2 at low pressure. *J. Phys. Chem.*, **94**, 4535–4540.

Legras, B., Pisso, I., Berthet, G., and Lefèvre, F. (2005). Variability of the Lagrangian turbulent diffusion in the lower stratosphere. *Atmos. Chem. Phys.*, **5**, 1605–1622.

Leonard, B., Lock, A., and Macvean, M. (1995). The NIRVANA scheme applied to one-dimensional advection. *International Journal of Numerical Methods for Heat and Fluid Flow*, **5**, 341–377.

Leu, M.-T. (1982). Rate constants for the reaction of OH with SO2 at low pressure. *J. Phys. Chem.*, **86**, 4558–4562.

Li, Y. and Chang, J. (1996). A mass-conservative, positive-definite, and efficient Eulerian advection scheme in spherical geometry and on a nonuniform grid system. *Journal of Applied Meteorology*, **35**, 1897–1913.

Lin, S. and Rood, R. (1996). Multidimensional flux-form semi-Lagrangian transport schemes. *Mon. Weather Rev.*, **124**, 2046–2070.

Lin, S. and Rood, R. (1997). An explicit flux-form semi-Lagrangian shallow-water model on the sphere. *Q. J. R. Meteorol. Soc.*, **123**, 2477–2498.

Liu, Y., Fueglistaler, S., and Haynes, P. (2010). Advection-condensation paradigm for stratospheric water vapor. *J. Geophys. Res.*, **115**, doi:10.1029/2010JD014352.

McIntyre, M. (1980). Towards a Lagrangian-mean description of stratospheric circulations and chemical transports. *Philos. Trans. Roy, Soc. London*, **A296**, 251–266.

McKenna, D., Konopka, P., Grooß, J., Günther, G., and Müller, R. (2002). A new Chemical Lagrangian Model of the Stratosphere (CLaMS) 1.Formulation of advection and mixing. *J. Geophys. Res.*, **107 (D16)**, 4309, 10.1029/2000JD000114.

McRae, G., Goodin, W., and JH, S. (1982). Numerical solution of the atmospheric diffusion equation for chemically reacting flows. *J. Comput. Phys.*, **45**, 1–42.

Methven, J. (2003). The influence of PV inversion on polar-vortex dynamics and passive-tracer simulations in atmosphere-like regimes. *Q. J. R. Meteorol. Soc.*, **129**, 1191–1215.

Molina, M. and Rowland, F. (1974). Stratospheric sink for chlorofluoromethanes: chlorine atomic-catalysed destruction of ozone. *Nature*, **249**, 810–812.

Monge-Sanz, B., Chipperfield, M., Simmons, A., and Uppala, S. (2007). Mean age of air and transport in a CTM: Comparison of different ECMWF analyses. *Geophys. Res. Lett.*, **34**, L04801, doi:10.1029/2006GL028515.

Monge-Sanz, B., Chipperfield, M., Cariolle, D., and Feng, W. (2010). Results from a new linear O_3 scheme with embedded heterogeneous chemistry compared with the parent full-chemistry 3-D CTM. *Atmos. Chem. Phys. Discuss.*, **10**, 12,993–13,027.

Moore, F., Elkins, J., EA, R., Dutton, G., Dunn, R., Fahey, D., McLaughlin, R., Thompson, T., Romashkin, P., Hurst, D., and Wamsley, P. (2003). Balloonborne in situ gas chromatograph for measurements in the troposphere. *J. Geophys. Res.*, **108**, doi:10.1029/2001JD000891.

Morgenstern, O., Pyle, J., Iwi, A., Norton, W., Elkins, J., Hurst, D., and Romashkin, P. (2002). Diagnosis of mixing between middle latitudes and polar vortex from tracer-tracer correlations. *J. Geophys. Res.*, **107**, doi:10.1029/2001JD001224.

Mote, P., Rosenlof, K., McIntyre, M., Carr, E., Gille, J., Holton, J., Kinnersley, J., Pumphrey, H., Russell, J., and Waters, J. (1996). An atmospheric tape recorder: The imprint of tropical tropopause temperatures on stratospheric water vapour. *J. Geophys. Res.*, **101**, 3989–4006.

Mote, P., Dunkerton, T., McIntyre, M., Ray, E., Haynes, P., and Russell, J. (1998). Vertical velocity, vertical diffusion, and dilution by midlatitude air in the tropical lower stratosphere. *J. Geophys. Res.*, **103**, 8651–8666.

Nair, R. (2004). Extension of a conservative cascade scheme on the sphere to large Courant numbers. *Mon. Weather Rev.*, **132**, 390–395.

Nair, R. and Machenhauer, B. (2002). The mass conservative cell-integrated semi-Lagrangian advection scheme on the sphere. *Mon. Weather Rev.*, **130**, 649–667.

Nair, R., Côté, J., and Staniforth, A. (1999). Cascade interpolation for semi-Lagrangian advection over the sphere. *Q. J. R. Meteorol. Soc.*, **125**, 1445–1468.

Nair, R., Scroggs, J., and Semazzi, F. (2002). Efficient conservative global transport schemes for climate and atmospheric chemistry models. *Mon. Weather Rev.*, **130**, 2059–2073.

Nakamura, N. (1996). Two-dimensional mixing, edge formation, and permeability diagnosed in an area coordinate. *J. Atmos. Sci.*, **53**, 1524–1537.

Nakamura, N. (2004). Quantifying asymmetric wave breaking and two-way transport. *J. Atmos. Sci.*, **61**, 2735–2748.

Neu, J. and Plumb, R. (1999). Age of air in a "leaky pipe" model of stratospheric transport. *J. Geophys. Res.*, **104**, 19,243–19,255.

Norton, W. (1994). Breaking Rossby waves in a model stratosphere diagnosed by a vortex-following coordinate system and a technique for advecting material contours. *J. Atmos. Sci.*, **51**, 654–673.

Paraskevopoulos, G., Singleton, D., and Irwin, R. (1983). Rates of OH radical reactions - The reaction OH+SO2+N2. *Chem. Phys. Lett.*, **100**, 83–87.

Piani, C., Norton, W., Iwi, A., Ray, A., and Elkins, J. (2002). Transport of ozone-depleted air on the breakup of the stratospheric polar vortex in spring/summer 2000. *J. Geophys. Res.*, **107**, 8270, doi:10.1029/2001JD000488.

Ploeger, F., Konopka, P., Günther, G., Grooß, J.-U., and Müller, R. (2010). Impact of the vertical velocity scheme on modeling transport in the tropical tropopause layer. *J. Geophys. Res.*, **115**, D03301, doi:10.1029/2009JD012023.

Plumb, R. (2002). Stratospheric transport. *J. Meteor. Soc. Japan*, **80**, 793–809.

Plumb, R. (2007). Tracer interrelationships in the stratosphere. *Rev. Geophys.*, **45**, 10.1029/2005RG000179.

Plumb, R., Waugh, D., and Chipperfield, M. (2000). The effects of mixing on tracer relationships in the polar vortices. *J. Geophys. Res.*, **105**, 10,047–10,062.

Prather, M. (1986). Numerical Advection by Conservation of Second-Order Moments. *J. Geophys. Res.*, **91**, 6671–6681.

Prather, M. (1994). Lifetimes and eigenstates in atmospheric chemistry. *Geophys. Res. Lett.*, **21**, 801–804.

Prather, M. and Jaffe, A. (1990). Global impact of the Antarctic ozone hole: Chemical propagation. *J. Geophys. Res.*, **95**, 3473–3492.

Prather, M., McElroy, M., Wofsy, S., Russell, G., and Rind, D. (1987). Chemistry of the global troposphere: Fluorocarbons as tracers of air motion. *J. Geophys. Res.*, **92**, 6579–6613.

Purser, R. and Leslie, L. (1991). An efficient interpolation procedure for high-order three-dimensional semi-Lagrangian models. *Mon. Weather Rev.*, **119**, 2492–2498.

Rasch, P. and Williamson, D. (1990). Computational aspects of moisture transport in global models of the atmosphere. *Q. J. R. Meteorol. Soc.*, **116**, 1071–1090.

Rasch, P. and Williamson, D. (1991). Sensitivity of a general circulation climate model to the moisture transport formulation. *J. Geophys. Res.*, **96**, 13,123–13,137.

Rind, D. (2009). The use of tracers as diagnostics for model development. In *ECMWF Seminar on Diagnosis of Forecasting and Data Assimilation Systems*, pages 205–219.

Rotman, D., Tannahill, J., Kinnison, D., Connell, P., Bergmann, D., Proctor, D., Rodrigues, J., Lin, S., Rood, R., Prather, M., Rasch, P., Considine, D., Ramaroson, R., and Kawa, S. (2001). Global Modeling Initiative assessment model: Model description, integration, and testing of the transport shell. *J. Geophys. Res.*, **106**, 1669–1691.

Simmons, A. and Burridge, D. (1981). An energy and angular-momentum conserving vertical finite-difference scheme and hybrid vertical coordinates. *Mon. Weather Rev.*, **109**, 758–766.

Smolarkiewicz, P. and Rasch, P. (1991). Monotone advection on the sphere: An Eulerian versus semi-Lagrangian approach. *J. Atmos. Sci.*, **48**, 793–810.

Solomon, S., Garcia, R., Rowland, F., and Wuebbles, D. (1986). On the depletion of the Antarctic ozone. *Nature*, **321**, 755–758.

Somnitz, H. (2004). Quantum chemical and dynamical characterisation of the reaction OH + $SO_2 \rightleftharpoons HOSO_2$ over an extended range of temperature and pressure. *Phys. Chem. Chem. Phys.*, **6**, 3844–3851.

Sparling, L., Kettleborough, J., Haynes, P., McIntyre, M., Rosenfield, J., Schoeberl, M., and Newman, P. (1997). Diabatic cross-isentropic dispersion in the lower stratosphere. *J. Geophys. Res.*, **102**, 25,817–25,829.

Takewaki, H. and Yabe, T. (1987). Cubic interpolated pseudo particle (CIP) method - Application to nonlinear or multi-dimensional problems. *J. Comput. Phys.*, **70**, 355–372.

Takewaki, H., Nishiguchi, A., and Yabe, T. (1985). The cubic-interpolated pseudo-particle (CIP) method for solving hyperbolic-type equations. *J. Comput. Phys.*, **61**, 261–268.

Thuburn, J. (2008). Some conservation issues for the dynamical cores of NWP and climate models. *J. Comput. Phys.*, **227**, 3715–3730.

Thuburn, J. and Lagneau, V. (1999). Eulerian mean, contour integral, and finite-amplitude wave activity diagnostics applied to a single-layer model of the winter stratosphere. *J. Atmos. Sci.*, **56**, 689–710.

Tremback, C., Powell, J., Cotton, W., and Pielke, R. (1987). The forward-in-time upstream advection scheme: Extension to higher orders. *Mon. Weather Rev.*, **115**, 540–555.

Trenberth, K. and Smith, L. (2004). The mass of the atmosphere: A constraint on global analyses. *J. Climate*, **18**, 864–875.

van Peet, J., van der A, R., de Laat, A., Tuinder, O., König-Langlo, G., and Wittig, J. (2009). Height resolved ozone height structure as observed by the Global Ozone Monitoring Experiment-2. *Geophys. Res. Lett.*, **36**, L11816, doi:10.1029/2009GL038603.

von Glasow, R. (2010). Atmospheric chemistry in volcanic plumes. *PNAS*, **107**, 6,594–6,599.

Walcek, C. (2000). Minor flux adjustment near mixing ratio extremes for simplified yet highly accurate monotonic calculation of tracer advection. *J. Geophys. Res.*, **105**, 9335–9348.

Wallace, J. and Hobbs, P. (2006). *Atmospheric science: An introductory survey (2nd edition)*. Elsevier/Academic Press.

Wang, Y. and Jacob, D. (1998). Anthropogenic forcing on tropospheric ozone and OH since preindustrial times. *J. Geophys. Res.*, **103**, 31,123–31,135.

Waugh, D. and Hall, T. (2002). Age of stratospheric air: Theory, observations and models. *Rev. Geophys*, **40**, 1010, doi:10.1029/2000RG000101.

Waugh, D. and Randel, W. (1999). Climatology of the Arctic and Antarctic polar vortices using elliptical diagnostics. *J. Atmos. Sci.*, **56**, 1594–1613.

Waugh, D., Plumb, R., Elkins, J., Fahey, D., Boering, K., Dutton, G., Volk, C., Keim, E., Gao, R.-S., Daube, B., Wofsy, S., Loewenstein, M., Podolske, J., Chan, K., Proffitt, M., Kelly, K., Newman, P., and Lait, L. (1997). Mixing of polar vortex air into middle latitudes as revealed by tracer-tracer scatterplots. *J. Geophys. Res.*, **102**, 13,119–13,134.

Wayne, R. (1991). *Chemistry of atmospheres (2nd edition)*. Clarenden.

Wayne, R. (2000). *Chemistry of atmospheres (3rd edition)*. Oxford University Press.

Wild, O. and Prather, M. (2000). Excitation of the primary tropospheric chemical mode in a global three-dimensional model. *J. Geophys. Res.*, **105**, 24,647–24,660.

Wild, O. and Prather, M. (2006). Global tropospheric ozone modeling: Quantifying errors due to grid resolution. *J. Geophys. Res.*, **111**, D11305, doi:10.1029/2005JD006605.

Williamson, D., Drake, J., Hack, J., Jakob, R., and Swarztrauber, P. (1992). A standard test set for numerical approximations to the shallow water equations in spherical geometry. *J. Comput. Phys.*, **102**, 211–224.

Wine, P., Thompson, R., Ravishankara, A., Semmes, D., Gump, C., Torabi, A., and Nicovich, J. (1984). Kinetics of the reaction OH+SO2+M→HOSO2+M: Temperature and pressure dependence in the falloff region. *J. Phys. Chem.*, **88**, 2095–2104.

Wood, N., Staniforth, A., and White, A. (2009). Determining near-boundary departure points in semi-Lagrangian models. *Q. J. R. Meteorol. Soc.*, **135**, 1890–1896.

Yabe, T., Tanaka, R., Nakamura, T., and Xiao, F. (2001). An Exactly Conservative Semi-Lagrangian Scheme (CIP-CSL) in One Dimension. *Mon. Weather Rev.*, **129**, 332–344.

Zdunkowski, W. and Bott, A. (2003). *Dynamics of the Atmosphere*. Cambridge University Press.

Zerroukat, M., Wood, N., and Staniforth, A. (2002). SLICE: A semi-Lagrangian inherently conserving and efficient scheme for transport problems. *Q. J. R. Meteorol. Soc.*, **128**, 2801–2820.

Zerroukat, M., Wood, N., and Staniforth, A. (2004). SLICE-S: A semi-Lagrangian inherently conserving and efficient scheme for transport problems on the sphere. *Q. J. R. Meteorol. Soc.*, **130**, 2649–2664.

Zerroukat, M., Wood, N., and Staniforth, A. (2005). A monotonic and positive-definite filter for a Semi-Lagrangian Inherently Conserving and Efficient (SLICE) scheme. *Q. J. R. Meteorol. Soc.*, **131**, 2923–2936.

Zerroukat, M., Wood, N., and Staniforth, A. (2009). An improved version of SLICE for a conservative monotonic remapping on a C-grid. *Q. J. R. Meteorol. Soc.*, **135**, 541–546.